2-29-2016

Investigation of the Structural and Functional Dynamics of the TIM23 Protein Import Machinery

Ketan Malhotra
University of Connecticut, ketanmalhotra@gmail.com

Investigation of the Structural and Functional Dynamics of the TIM23 Protein Import Machinery

Ketan Malhotra, Ph.D.
University of Connecticut, 2016

The biogenesis of the majority of mitochondrial proteins depends on the efficient functioning of the Translocase of the Inner Mitochondrial Membrane 23 (TIM23) complex. In this body of work, we investigate the structure, interactions, and functional dynamics of the subunits involved in the initial steps of precursor protein transport: the central channel-forming component Tim23 and the central receptor Tim50. Using a combination of *in organello* analyses and model membrane systems, this work uncovers a central role for the anionic phospholipid cardiolipin in regulating site-specific Tim23-Tim50 interactions. Moreover, using fluorescence-based and other biochemical and biophysical approaches, we show that the receptor domain of Tim50 ($Tim50^{IMS}$) displays an inherent affinity for cardiolipin-containing membrane bilayers, where we identify the importance of a conserved β-hairpin loop in mediating the membrane insertion activity of $Tim50^{IMS}$. Further analyses of the $Tim50^{IMS}$-cardiolipin interaction reveal membrane-mediated structural changes in the receptor domain of Tim50. Additionally, by performing small-angle X-ray scattering analysis, we also generate the first envelope structure of the full-length $Tim50^{IMS}$. Homology modeling and molecular dynamics simulations based on our structural insights suggest bilayer-interactive sites that are confirmed experimentally. High-

resolution fluorescence mapping shows membrane potential ($\Delta\Psi_m$)-dependent structural changes and aqueous exposure of the channel-facing transmembrane segment (TMS) 2 of Tim23. Finally, using crosslinking-based approaches, this study also compares the substrate-regulated Tim23-Tim50 interactions both *in organello* and in model-membrane systems. Together, these findings demonstrate the roles played by the $\Delta\Psi_m$ and by cardiolipin in maintaining the structural and functional integrity of the core subunits of the TIM23 complex, thereby providing unique insights on the mechanisms of Tim23 channel gating and polypeptide transport.

Investigation of the Structural and Functional Dynamics of the TIM23 Protein Import Machinery

Ketan Malhotra

M.Sc. The Maharaja Sayajirao University of Baroda, 2009

A Dissertation

Submitted in Partial Fulfillment of the

Requirements for the Degree of

Doctor of Philosophy

at the

University of Connecticut

2016

APPROVAL PAGE

Investigation of the Structural and Functional Dynamics of the TIM23 Protein Import Machinery

Presented by

Ketan Malhotra, M.Sc.

Major Advisor_____

Nathan N. Alder

Associate Advisor_____

Arlene Albert

Associate Advisor_____

Victoria Robinson

Associate Advisor_____

Eric May

Associate Advisor_____

Adam Zweifach

University of Connecticut

2016

Acknowledgements

As I reach the final stage of my dissertation, I would like to thank people who have been with me through this wonderful journey and without whose constant guidance and support this work would have not been possible.

First and foremost, I would like to thank my advisor Prof. Nathan Alder for inducting me into your group and giving me some wonderful projects. Your work ethic and enthusiasm for science is something I have always admired and strived for. Thank you for being a pillar of support throughout and for never shying away whenever I asked to perform a new experiment or proposed a crazy hypothesis to be tested. You made every effort to mold me into a good researcher. Moreover, thank you for your guidance and for very stimulating discussions we had about the field of membrane biophysics. I feel privileged to have you as a mentor.

I would also like to thank all my committee members, Prof. Eric May, Prof. Victoria Robinson, Prof. Adam Zweifach and Prof. Arlene Albert for your constant guidance. This work would have not been possible without your unending support.

To Prof. Eric May, Prof. Dejana Mokranjac and Prof. Victoria Robinson for providing valuable insights and resources towards this work and for being excellent collaborators.

To all the past and present members of the Alder lab, including Dr. Judith Landin, Ashley Long, Dr. Christine Schwall, Victoria Greenwood, Matthew Greenwood, Murugappan Sathappa, Dylan Laprise, Melissa Skoryk, Dr. Arnab Modak, Sally Chamberland, Adrian Coscia, Margaret Mayer and Tess Decater. I would like to especially thank Dr. Judith Landin for your co-mentorship during my first three years in the lab, and for making sure that things ran smoothly. Thank you also to Dylan and Melissa for making thesis writing a less stressful affair and to Melissa for some intriguing ideas for my thesis.

I would like to thank all the members of the 2nd floor BPB building for all the resources and guidance I have received from you time to time. Noteworthy are people, including Dr. Nadia D'Lima, Dr. Katherine Launer-Felty, Prof. Carol Teschke, Prof. Jim Cole, Tyler Daman, Ala Shaqra, Dr. Tina Motwani, Chris Mayo, Rebecca Newcomer and Kunica Asija.

To my parents, Anil Malhotra and Neelam Malhotra, for all the unconditional love that you have given me throughout my existence, and most importantly, believing in me in all the endeavors that I have undertaken. Thank you for your unwavering support. You are my role models. To my sister, Aneesha Malhotra, for being a

wonderful human being and a friend. I have always admired and envied your patience and evergreen positive outlook in life.

To Cassie Zerbe, for being such an amazing person and scientist. You have always inspired me with your dedication to work and never-say-die attitude. Thank you for all the stimulating scientific discussions we have had, and for making me learn so many new things. Most importantly, thank you for your wonderful company, and for being there whenever and wherever I need it. You made sure that my journey through this critical phase of life was as smooth and fun as possible.

Finally, I would like to thank my spiritual guru, Sant Shri Asaramji Bapu, for all the deep knowledge about yoga and meditation I have gained from you, which have helped me leap through all the obstacles that I have faced. I will forever be indebted for the teachings and values that you have instilled in me.

Table of Contents

List of Figures and Tables

Chapter 1

Chapter 2

Chapter 3

Chapter 4

Chapter 5

Chapter 6

Chapter 1

Introduction: Mitochondrial Protein and Cardiolipin Biogenesis

1.1 Protein Import Pathways of Mitochondria

Organelles are the membrane-bound subcompartments of eukaryotic cells that impart specificity and division of multiple cellular functions. Moreover, if we think of organelles as individual “factories” then proteins would be considered as the “workers”. More than half of the proteins synthesized in the cytosol are transported into or across the membranes to reach their final destination **(Schmidt et al., 2010)**. Therefore, it is imperative to understand the mechanisms that operate to make sure the proteins reach their final destination correctly. The Mitochondrion (plural mitochondria), also popularly known as the “energy factory”, imports more than 99% of its proteins (~1000 in yeast and ~1500 in humans), which are encoded by nuclear DNA and synthesized on cytosolic ribosomes **(Chacinska et al., 2009)**. The dependence of mitochondria on the supply of proteins from the cytosol is widely attributed to its prokaryotic origin, which resulted in the transfer of most of its protein-encoding genes to the nuclear genome **(Dolezal et al., 2006)**. Moreover, morphing of the “bacterial endosymbiont” to the present day “mitochondrion” meant retaining the double membrane character typical of gram-negative bacteria. To carry out the process of protein import in an efficient manner, mitochondria have evolved complex protein translocating machineries that reside in its two membranes, namely the Translocase of the Outer Membrane (TOM) complex and the Translocase of the Inner Membrane (TIM) complexes.

Broadly, the protein import pathways in mitochondria can be divided into four types. The TOM complex of the outer membrane (OM) forms the common entry gate for the majority of precursor proteins before they follow specialized routes to reach their final destination (**Figure 1.1**). The four pathways can be described as follows:

Presequence Translocase Pathway

The presequence translocase pathway is responsible for importing the majority of mitochondrial proteins **(Mokranjac & Neupert, 2010)**. Proteins imported by the presequence translocase pathway are characterized by the presence of a cleavable presequence that acts as a signaling element. The inner membrane (IM) machinery of this pathway is formed by the TIM23 complex, from where the preproteins are either laterally inserted into the IM or transported across the bilayer into the mitochondrial matrix. The latter process also requires the presence of the Presequence translocase-Associated Motor (PAM) complex (**Figure 1.1-1.2**). Moreover, a couple of recent investigations into the import of helical membrane proteins in the OM implicated the presequence translocase pathway for its involvement **(Song et al., 2014; Wenz et al., 2014)**.

Carrier Pathway to the Inner Membrane

Proteins imported through the carrier pathway contain multiple transmembrane segments (TMSs) that are chaperoned by the Hsp70 and Hsp90 proteins in the cytosol and by the Tim9-Tim10 complex of the intermembrane space (IMS). The final insertion of proteins being transported through this route is mediated by the TIM22 complex of the IM (**Figure 1.1**). The main group of proteins following the carrier pathway is formed by the metabolite carriers such as ADP and ATP carrier (AAC) **(Schmidt et al., 2010)**.

Transport Pathways for the Outer Membrane Proteins

Outer membrane proteins fall into two main class of proteins, β-barrel and α-helical as compared to the presence of only α-helical proteins in the IM. The OM proteins are synthesized as non-cleavable precursors carrying internal targeting signals. Amongst them, the α-helical proteins mostly act as receptors and are membrane-anchored by one or more TMSs. The β-barrel proteins or the pore-forming proteins comprise of multiple TMS β-strands. The import pathway for β-barrel proteins have been well characterized and involve the TOM complex, IMS chaperones and the Sorting and Assembly Machinery (SAM) complex of the OM. Insertion of the OM proteins with multiple α-helical proteins is facilitated by Mim1 together with Mim2 (**Figure 1.1**). As pointed out earlier, insertion of at least some of the single-pass α-helical membrane proteins is catalyzed by the presequence translocase machinery of the IM along with subunits of the TOM complex **(Endo et al., 2011; Schulz et al., 2015)**.

Redox-Mediated Pathway of the Intermembrane Space

Proteins destined to the IMS contain characteristic cysteine motifs and are transported mostly through the oxidative Mitochondrial Intermembrane space Assembly (MIA) machinery (**Figure 1.1**). The MIA pathway involves oxidation of cysteine residues to form an intermediate disulfide-linked precursor-Mia40 complex before releasing the mature folded form of proteins into the IMS **(Chacinska et al., 2009)**.

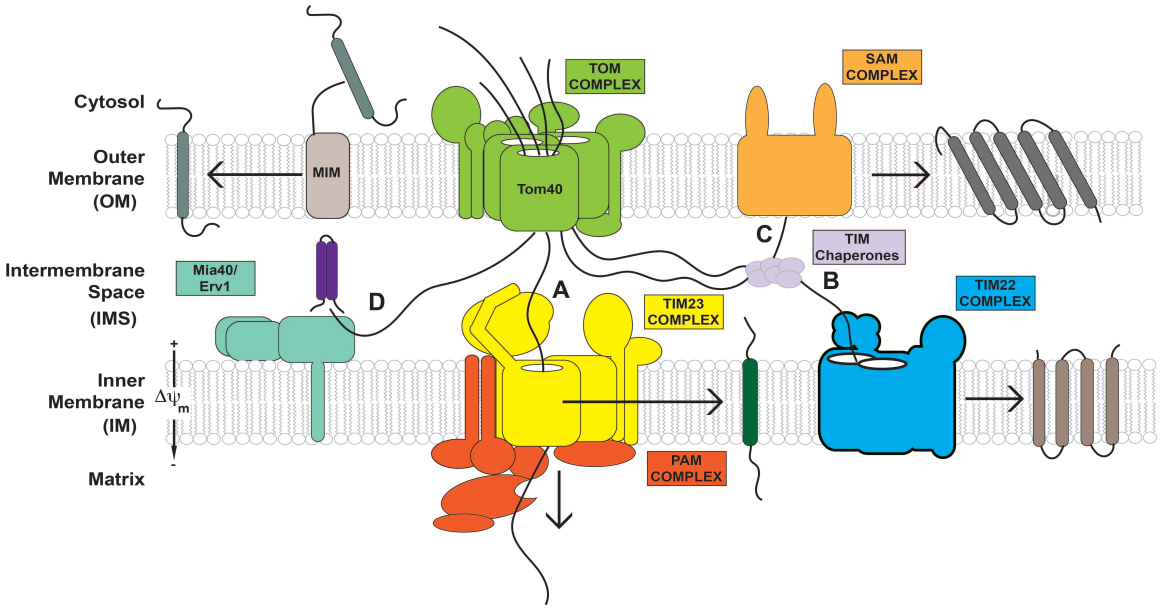

Figure 1.1 *Protein Import Pathways of Mitochondria*

The four major mitochondrial protein import pathways are depicted as (A-D) along with the partially characterized pathway for the OM α-helical proteins using the mitochondrial import (MIM) complex (gray) of the OM. Most of the preproteins enter mitochondria through the TOM complex via channel-forming Tom40 (green). From there preproteins take different sorting routes. TIM23 complex (yellow) is the IM machinery for the presequence translocase pathway (A), which is involved in either lateral insertion of membrane proteins or transport of soluble proteins across the IM along with the PAM complex (orange) (discussed in more detail in **Figure 1.2**). The carrier pathway (B)

imports proteins with multiple TMSs into the IM. The hydrophobic TMSs of preproteins are chaperoned in the IMS by the small TIMs (light purple) (Tim9-Tim10 and Tim8-Tim13). Finally, these proteins are inserted into the IM by the $\Delta\Psi_m$-dependent carrier translocase of the IM, TIM22 complex (blue). The precursors of the outer membrane β-barrel proteins are imported by the TOM complex and TIM chaperones, and are inserted into the OM by the sorting and assembly machinery (SAM) complex of the OM (orange, C). Cysteine-rich substrates are translocated in a reduced conformation and imported by the mitochondrial IMS import and assembly (MIA) machinery together with Erv1 into the IMS (light green, D) **(Harbauer et al., 2014)**.

1.2 The Presequence Translocase Machinery of the IM or the TIM23 Complex

The presequence translocase of the IM (TIM23 complex) (**Figure 1.2**) is considered the most modular of all the translocases present in mitochondria, as it is found to associate with protein complexes from three out of four mitochondrial subcompartments; the TOM complex of the OM, the PAM complex and the Oxa machinery in the matrix, and the AAC complex as well as respiratory chain complexes III and IV of the IM **(Mokranjac & Neupert, 2010)**. Moreover, the TIM23 complex is also known to utilize two different energy sources, namely the membrane potential ($\Delta\Psi_m$) across the IM and matrix ATP to carry out its protein import activity. Hence, it does not come as a surprise that the TIM23 machinery is also considered as one of the most complicated translocase machineries in mitochondria.

The TIM23 complex is involved in the import of most of the matrix-directed as well as inner membrane proteins, and mainly recognizes preproteins with an amphipathic presequence at the amino-terminus (**Figure 1.2**). These cleavable presequences are also considered as the classical type of mitochondrial targeting sequences. Their typical length varies from 15 to 50 residues and are amphipathic, with one face primarily composed of positively charged amino acid residues while the other dominated by hydrophobic residues. Overall they carry a net charge of +3 to +6. The presence of positively charged residues in the presequences is known to be critical for the electrophoretic pulling effect exerted by the $\Delta\Psi_m$ across the IM (matrix negative) **(Turakhiya et al., 2016)**. Moreover, the amphipathicity imparts signature properties to the preproteins that are recognized by the receptor proteins of the TOM and TIM23 translocases. Presequences directed towards the mitochondrial matrix are proteolytically removed by the dimeric mitochondrial processing peptidase (MPP) upon their import. Preproteins directed towards the IM on the other hand contain an additional stop-transfer signal, which is also the transmembrane segment of the mature protein. The stop-transfer signal is 16-18 residues long found adjacent to the matrix-targeting signal, which arrests translocation in the IM with the preproteins being laterally released into the lipid phase. In such cases, the matrix-targeting signal is cleaved by MPP following the integration of proteins into the IM **(Chacinska et al., 2009)**.

The core subunits of the TIM23 complex comprise three essential membrane-embedded proteins: Tim50, Tim23, and Tim17 (**Figure 1.1-1.2**). Tim50 is a receptor protein with a C-terminal receptor domain that faces the IMS ($Tim50^{IMS}$). Tim50 is the first component of the IM to receive the emerging preproteins from the TOM complex of the OM **(Rahman et al., 2014)**. Moreover, the association of $Tim50^{IMS}$ with the $Tim23^{IMS}$ receptor domain is known to enhance the protein transport function of the TIM23 translocase **(Gevorkyan-Airapetov et al., 2009; Mokranjac et al., 2009; Tamura et al., 2009b)**. Tim23 is the central component of the TIM23 complex, which also contributes to the channel formation along with Tim17 **(MALHOTRA et al., 2013)**. Additionally, recent evidence has shown that another IM-embedded subunit of the presequence translocase, Mgr2, is capable of interacting with precursor proteins triggering speculation of its involvement in the channel formation **(Ieva et al., 2014)**. Gating of the presequence translocase channel is necessary to maintain the permeability barrier of the IM, which in turn helps maintain the electrochemical potential ($\Delta\mu_{H+}$) across the IM. The process of gating the IM channel is intricate and tightly regulated, and is performed by the collective action of several factors, including the $\Delta\Psi_m$ across the IM, as well as interactions with Tim50 and Tim17. Additionally, the presequence-carrying substrates are also known to gate the channel, where there presence elicits the opening of the conduction pore **(Meinecke, 2006; Truscott et al., 2001)**.

The highly modular character of the TIM23 translocase is best characterized by its ability to exist in two different translocation competent states. $TIM23^{SORT}$ refers to the Tim21-containing core complex, which directs preproteins to be laterally inserted into the IM. Additionally, Tim21 is also required for the coupling of the TIM23 translocase with the TOM complex of the OM as well with respiratory chain complexes III and IV **(Chacinska et al., 2010; 2005)**. Moreover, it was shown that Mgr2 is required for binding of Tim21 to the core complex, imparting regulation to the process of membrane sorting of preproteins as well as TIM23-TOM coupling **(Gebert et al., 2012)**. The second state called the $TIM23^{MOTOR}$ or TIM23-PAM is associated with subunits of the PAM complex, but lacks Tim21. The function of this particular translocation state is to transfer hydrophilic proteins into the mitochondrial matrix driven by the ATP powered motor complex in the mitochondrial matrix **(Chacinska et al., 2009)**. On the contrary, there have been reports that suggest the existence of the TIM23 translocase machinery as a single entity associated with the motor machinery **(Popov-Čeleketić et al., 2008)**. It is also possible that the two translocation-competent states exist in a state of equilibrium, where the $Tim23^{SORT}$ complex is used for the transfer of preproteins from the TOM complex and then the TIM23-PAM machinery is used for translocation into the matrix **(Schmidt et al., 2010)**.

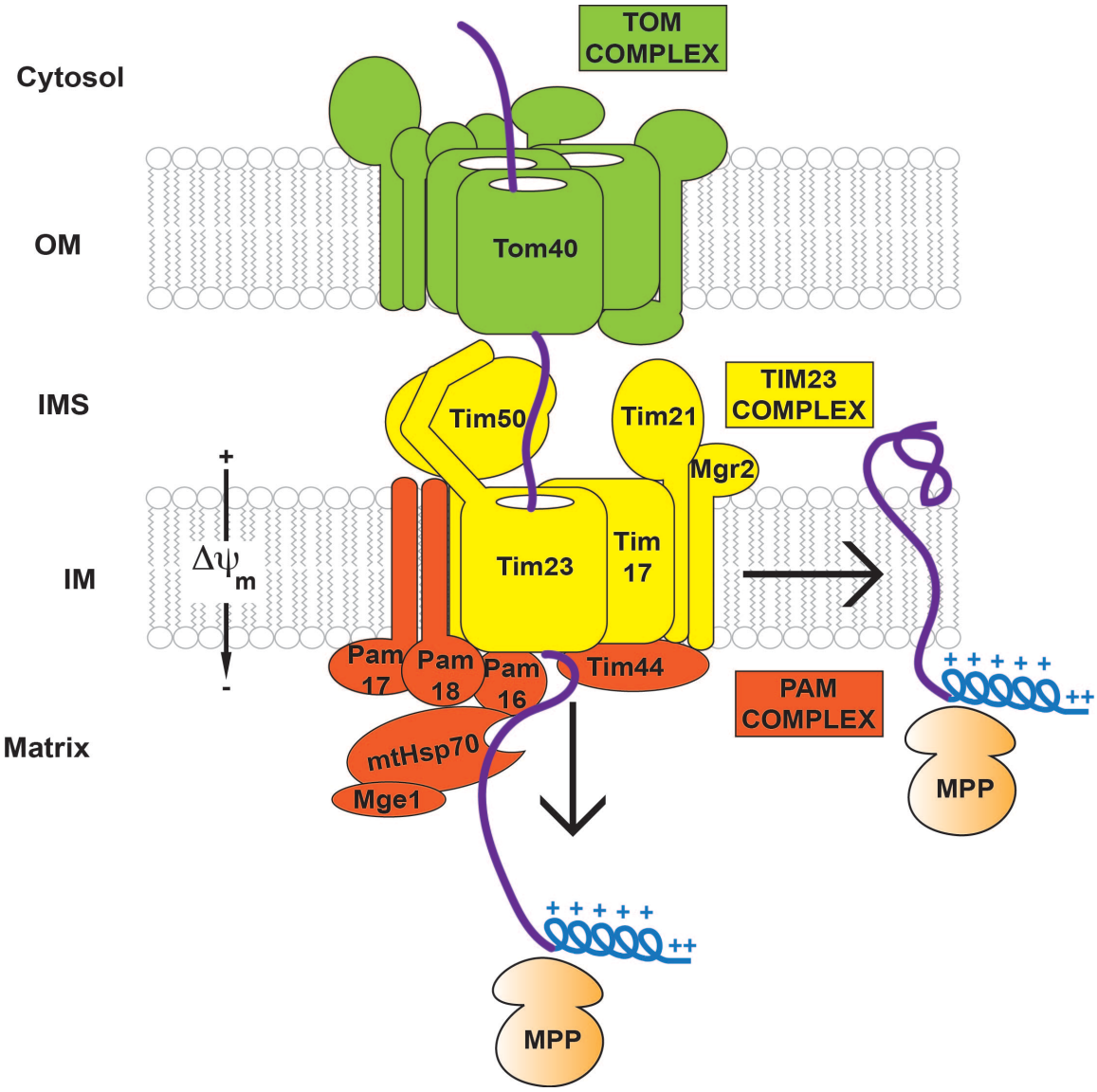

Figure 1.2 *Protein Import by the The Presequence Translocase Pathway*

Preproteins (purple string) carrying a positively charged amphipathic presequence (blue) at the N-terminus pass through the TOM complex, which acts as a common entry route for most of the mitochondrial proteins. Tom40 is the pore-forming subunit of the TOM complex. Once the presequence-carrying preproteins enter the TIM23 channel in the inner membrane, they are either laterally inserted into the IM (membrane proteins) or transported across the IM into the matrix (soluble proteins). Lateral insertion of preproteins requires presence of just the $\Delta\Psi_m$ across the IM as energy source. For transport of soluble proteins, TIM23 requires an additional action of ATP-coupled PAM machinery. The amphipathic presequences for both membrane and

soluble proteins are finally cleaved by mitochondrial processing peptidase (MPP) **(Chacinska et al., 2009)**.

1.3 Interactive Sites on Tim23

Tim23 has a bipartite domain organization comprising a soluble intrinsically disordered receptor domain facing the IMS ($Tim23^{IMS}$) and a well-folded C-terminus membrane-resident channel domain. The C-terminal domain of Tim23 is divided into four TMSs forming a substrate- and voltage-sensitive channel, where TMS1 and TMS2 have been shown to interact with preproteins in transit through the aqueous lumen **(Alder et al., 2008a; Alder et al., 2008b)**. Moreover, a high-resolution fluorescence-based approach identified TMS2 as one of the helices facing the aqueous lumen of the protein-conducting channel **(Alder et al., 2008a)**. As a central receptor- and channel-forming component, Tim23 is involved in a host of interactions both within the complex and outside the complex via its different segments. Here we make an attempt to build a map of the interactive partners of different Tim23 regions, as well as provide residue level information of those interactions wherever possible (**Figure 1.3**).

IMS Domain

The receptor domain of Tim23 in *Saccharomyces cerev*isiae consists of the N-terminal 96 residues of Tim23 and is probably the most promiscuous of all the Tim23 regions. The $Tim23^{IMS}$ is intrinsically disordered as was demonstrated by nuclear magnetic resonance (NMR) studies **(Ia Cruz et al., 2010)**, and its flexibility enables it to interact with multiple binding partners of the protein import machineries as well as the myriad substrates that it recognizes. This inherent flexible nature makes $Tim23^{IMS}$ well suited to carry out receptor functions. A prominent role for the $Tim23^{IMS}$ was discovered when it was found that it is essential for protein import and forms a dimer via heptad leucine repeat motif present in the C-terminus (residues: 50-96) in the presence of the $\Delta\Psi_m$. This $Tim23^{IMS}$ dimer was then proposed to act as a receptor for the incoming preproteins, dissociating upon contacting the presequences **(Bauer et al., 1996)**. Moreover, by using cysteine substitution analysis another study reported crosslinking-detected dimerization of imported monocysteine Tim23 (N43C) with endogeneous Tim23 proteins **(Alder et al., 2008b)**. The N-terminal region of $Tim23^{IMS}$ (residues: 1-50) was found to be exposed at the surface of the OM, giving rise to a two-membrane spanning model for Tim23, which could in principle form translocation contact sites with the TOM complex **(Donzeau et al., 2000)**. Indeed, $Tim23^{IMS}$ was found to interact with Tom22 by *in vivo* crosslinking analysis at position 41 **(Tamura et al., 2009b)**. NMR analysis confirmed the interaction between the IMS domains of Tim23 and Tom22, where residues 53 and 58-61 on the $Tim23^{IMS}$ were found to experience chemical shifts in the presence of $Tom22^{IMS}$ **(Bajaj et al., 2014a)**.

In the IM, Tim23^{IMS} is reported to interact with both Tim50^{IMS} and Tim21^{IMS} of the TIM23 complex. The predicted coiled-coil region in the Tim23^{IMS} (residues: 61-83) **(Bauer et al., 1996)** is known to play a critical role in mediating interactions with the partner receptor domain of Tim50, where residues 64, 71 and 78 comprising the hydrophobic face of the putative coiled-coil on the Tim23^{IMS} were shown to be directly involved in mediating Tim23's interaction with Tim50 **(Tamura, et al., 2009b)**. Moreover, mutation of residues Y70 and L71 to alanine was found to abrogate Tim23-Tim50 interaction **(Gevorkyan-Airapetov et al., 2009)**. Similarly, crosslinking-based interaction analysis *in organello* found Tim23 residue 80 to be proximal to Tim50 **(Alder et al., 2008b)**. NMR-detected shifts in the Tim23^{IMS} in the presence of Tim50 construct comprising the core and the presequence binding domain (residues: 164-476) found residues 1-7 and 56-92 on the Tim23^{IMS} to be Tim50 interactive **(Bajaj et al., 2014a)**.

According to a recent NMR analysis, the Tim21 interactive sites on Tim23^{IMS} are broadly mapped to three distinct regions, residues 1-7, 68-74, and 90-96, all of which carry an aspartic residue positioned two residues downstream from an aromatic residue **(Bajaj et al., 2014a)**. As a receptor domain, Tim23^{IMS} engages with presequence-carrying preproteins either alone or in complex with the Tim50^{IMS} **(Schulz et al., 2015)**. The presequence binding sites on Tim23^{IMS} were found to lie in the C-terminal half of the receptor domain (residues: 51-96), the same region that mediates Tim23 dimerization (**Bauer et al., 1996)**. This was confirmed by NMR analysis, which mapped the presequence binding domain from residues 71-96 **(la Cruz et al., 2010)**. However,

crosslinking-based interaction between $Tim23^{IMS}$ and model substrate pSu9-DHFR revealed binding of substrate to almost the entire surface of the receptor domain **(Alder, Jensen, & Johnson, 2008a)**.

In addition to the binding partners described above, the $Tim23^{IMS}$ domain has also been shown to mediate interaction with Tim17 of the TIM23 complex, where Tim50 interactive residues 64, 71, and 78 were also found to be crosslinked to Tim17 **(Tamura et al., 2009b)**. Moreover, NMR analysis also found the Tim23 receptor domain to be membrane-interactive in a cardiolipin-dependent manner, where signals from N-terminal residues 1-12 and 29-46 were highly attenuated in the presence of cardiolipin-containing membrane bilayers **(Bajaj et al., 2014b)**.

TMSs 1 and 2

The membrane-bound TMS1 and TMS2 have been shown to interact with presequence-carrying preproteins where crosslinking analysis using substituted cysteines along the entire surface of the two TMSs were mapped proximal to the substrate in transit **(Alder et al., 2008a)**. Additionally, fluorescence-based approaches identified the channel-facing residues 152-153, 155-156, 160, and 163-164 in TMS2 moving to a more non-polar environment in the presence of substrate **(Alder et al., 2008a)**. Therefore this face of the helix appears to face the aqueous channel lumen and be in contact with translocating polypeptides. Moreover, by performing mutational

analysis, residues 105, 107, 109 and 111 of TMS1 were found to be important for Tim23 homodimerization as well as substrate interaction, highlighting for the first time role of TMS1 in promoting self-association **(Pareek et al., 2013)**. Interestingly, the N-terminus of TMS1 was also found to interact with the soluble receptor domain of Tim50 where the same study also identified a specific helical face of TMS1 to be interacting with Tim17 **(Alder et al., 2008b)**. Finally, using coimmunoprecipitation-based detection method, residues 149 and 153 on TMS2 were found to be important for Tim17 association and substrate interaction **(Pareek et al., 2013)**.

Matrix- and IMS-Facing Loops

Coimmunoprecipitation- and crosslinking-based interaction analysis identified matrix-facing loop1 between TMS1 and TMS2 to be involved in mediating interactions with the components of the motor machinery, where position 127 on loop1 was found to be proximal to Tim44 **(Banerjee et al., 2015; Ting et al., 2014)**. Additionally, positions 138-139 were shown to be important for recruitment of Tim17 and Tim21 to the core complex. Similarly, IMS-facing loop2 and extreme C-terminus were found to be important for the association of Tim21 to the core complex **(Pareek et al., 2013**).

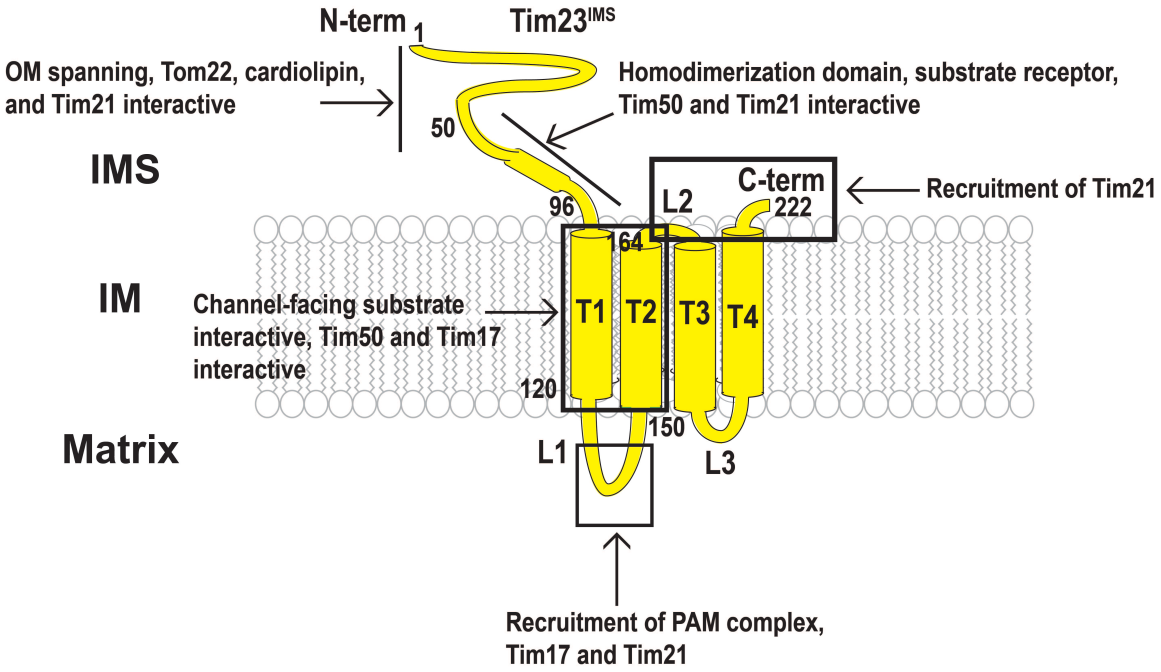

Figure 1.3 *Tim23 Interactome*

Topology diagram of Tim23 (yellow) in the mitochondrial inner membrane. Tim23 is divided into distinct regions broadly comprising of the soluble receptor domain ($Tim23^{IMS}$, residues: 1-96 in *S.cerevisiae*) and membrane bound C-terminus (residues: 97-222), which is further divided into four transmembrane segments (T1-T4) and matrix- and IMS-facing loops (L1-L3, C-term). The interactive partners of Tim23 are mentioned corresponding to the specific Tim23 binding site.

1.4 Cardiolipin and Mitochondrial Function

Cardiolipin (CL; 1,3-*bis*(*sn*-3' -phosphatidyl)-*sn*-glycerol) is an anionic phospholipid found in the energy-conserving membranes of bacteria and eukaryotes that couple the proton-motive force generated by the proton pumping activity of the complexes of the electron transport chain with endergonic processes such as ATP synthesis and substrate transport **(Paradies et al., 2014)**. The dimeric structure of CL makes it unique amongst most of glycerophospholipids, containing two negatively charged phosphatidate head groups joined together by a central glycerol moiety and four acyl chains instead of two (**Figure 1.4**). As a major anionic lipid of energy-transducing membranes, its contribution to the process of energy conversion appears to be manifold. First, it is involved in the stabilization of complexes involved in oxidative phosphorylation and their assembly into higher-order supercomplexes, which in turn leads to efficient ATP production **(Arias-Cartin et al., 2012; Chaban, Boekema, & Dudkina, 2014; Mileykovskaya & Dowhan, 2014; Paradies et al., 2014)**. Second, due to its anionic character and appreciable content in the energy-conserving membranes, it also contributes to the interfacial surface potential (Ψ_o) of the bilayers in which it resides. Therefore, cardiolipin is a critical component of the electrostatic profile of the membrane. Third, the ability of the two phosphatidyl headgroups in CL to form a resonance-stabilized acid-anion pair through hydrogen bonding with the 2'-hydroxyl of the central glycerol bridge is suggested to allow CL to act as a proton trap in the bilayer, which in turn can buffer the proton pool across the energy-conserving membranes contributing to the membrane potential ($\Delta\Psi_m$) **(Haines, 2009)**. Thus, CL is an important

constituent of the energy-transducing membranes where it helps maintain the transmembrane $\Delta\mu_{H+}$ in bacteria as well as eukaryotes.

Most of the CL in a eukaryotic cell is associated with mitochondrial membranes, especially the IM where its biosynthesis takes place **(Claypool & Koehler, 2012)**. For this reason, CL is called the signature phospholipid of mitochondria where it is present at a concentration of ~15-20 mol% of total lipids **(Alder NN, 2011)**. In addition to the involvement of CL in the energy transduction process in mitochondria, it also plays important roles in regulating several mitochondrial processes such as apoptosis, mitophagy, iron-sulfur cluster biogenesis, translocation by mitochondrial creatine and nucleoside diphosphate kinases, and preprotein translocation **(Böttinger et al., 2015; Claypool & Koehler, 2012; Joshi et al., 2009; Li et al., 2015; Mileykovskaya & Dowhan, 2009; Planas-Iglesias et al., 2015)**. Moreover, biogenesis of several membrane proteins in the IM as well as the OM is known to be dependent on the presence of CL **(Brandner et al., 2005; Claypool et al., 2008; Gebert et al., 2009)**. Many studies have also implicated CL in regulating mitochondrial dynamics by controlling processes such as fission and fusion **(Ban et al., 2010; DeVay et al., 2009; Montessuit et al., 2010)**. CL has also been shown to be important for maintaining mitochondrial cristae morphology by regulating the assembly of ATP synthase into higher order oligomers, as well as the assembly of a conserved mitochondrial contact site and cristae organizing system (MICOS) complex in the IM **(Acehan et al., 2011; Friedman et al., 2015)**. Moreover, CL is important for maintaining mitochondrial DNA stability especially under stressful conditions **(Luévano-Martínez et al., 2015)**. In all its

roles, CL specifically interacts with a range of integral and peripheral membrane proteins where recent structural and computational studies have made significant progress in elucidating the nature of protein binding sites that interact with the headgroup and acyl chain region of CL **(Planas-Iglesias et al., 2015)**. Due to its involvement in a myriad of mitochondrial processes, aberrant CL metabolism results in various diseases, including diabetes, cardiovascular disease, neurodegenerative disease, and the multisystem disorder called Barth Syndrome **(Chicco & Sparagna, 2007; Gaspard & McMaster, 2015; Jefferies, 2013)**.

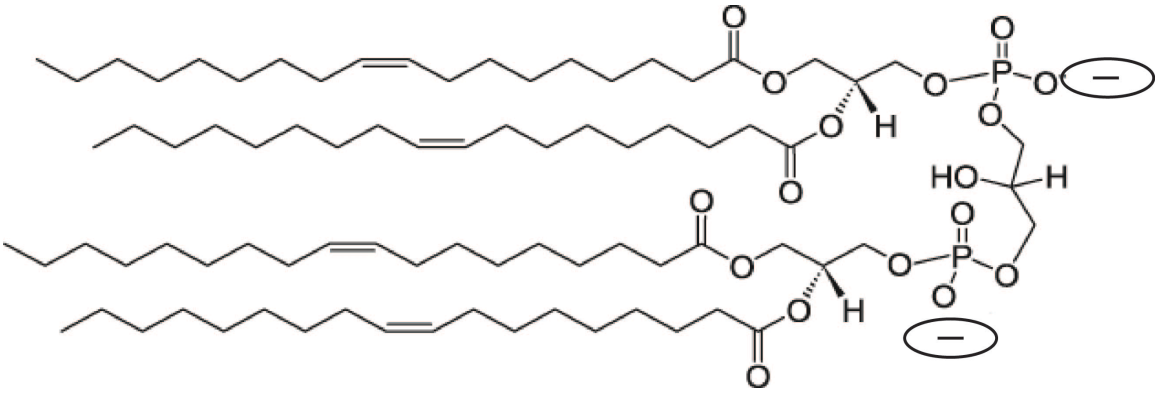

Figure 1.4 *Chemical Structure of Cardiolipin*

Chemical structure of tetraoleoyl cardiolipin (TOCL, 1′,3′-bis[1,2-dioleoyl-*sn* -glycero-3-phospho]-*sn* -glycerol). Cardiolipin has a unique structure with two 1,2-diacyl phosphatidate moieties esterified to the *sn*-1 and *sn*-3 positions of a central glycerol bridge. As a result, each CL molecule has four acyl chains and two ionizable phosphate headgroups at physiological pH.

1.5 Cardiolipin Structure and Physiochemical Properties

Unlike other naturally occurring glycerophospholipids, CL has a unique dimeric structure with four fatty acids linked to the peripheral hydroxyl groups of a 1,3-bis(glycerol-3'-phosphoryl)-glycerol backbone (**Figure 1.4**). Despite the apparent symmetry of structure, cardiolipin has two chemically distinct phosphatidyl moieties, owing to the two chiral centers in the headgroup glycerol, each of which is in the *R* configuration **(Schlame, Rua, & Greenberg, 2000)**. As a result, the two phosphate groups have different chemical environments as was demonstrated by ^{31}P-NMR resonance spectra **(Powell & Jacobus, 1974)**. Hence, the dimeric structure of CL helps confer unique physical and chemical properties that are vital for its function.

The CL polar head group contains two phosphodiester moieties, which, in principle, should both be negatively charged at physiological pH. However, a model by Haines and colleagues point to the presence of a resonance-stabilized acid-anion headgroup structure in which the protonated state of one phosphate oxygen atom is stabilized by hydrogen bond interactions with the secondary hydroxyl of the central glycerol (**Figure 1.5**) **(Haines, 1983)**. This model has implications for the function of CL as a component of the energy-conserving membranes where the headgroup region of CL can act as a proton reservoir for proton-pumping respiratory enzymes. The support for this model came from comparisons of pH titrations between CL and its 2'-deoxy form (lacking the 2'-hydroxyl group), which revealed disparate ionization constants for the two phosphates (pK_1~2-4 and pK_2>8.5) **(Kates et al., 1993)**. Moreover, it was

hypothesized that equal lengths of the four acyl chains could stabilize the bicyclic structure **(Haines, 2009)**. However, ^{2}H-NMR spectroscopic studies on CL within the bilayer indicate that the headgroup glycerol of CL is parallel to the bilayer surface, and is motionally constrained to engage in inter- and intra-molecular hydrogen bonding interactions except with water and ions present at the surface of the lipid membranes **(Allegrini, Pluschke, & Seelig, 1984)**. This has given credence to the second model where experimental evidence from several laboratories (including our laboratory; **Sathappa and Alder**, *unpublished*) has shown that that the two phosphodiester moieties in CL are negatively charged under physiological conditions (**Figure 1.4**) **(Lewis & McElhaney, 2009; Malyshka & Pandiscia, 2014; Olofsson & Sparr, 2013; Tarahovsky, Arsenault, & MacDonald, 2000)**. The presence of two negative charges on CL in turn has implications on controlling processes such as polymorphic phase behavior, establishment of membrane curvature, charge-charge interactions with peripheral and integral membrane proteins, and headgroup coordination of ions.

The sharing of a single glycerol molecule by two phosphatidyl moieties imparts structural features in CL, which distinguishes it from other glycerophospholipids. Because of the sharing of the central glycerol moiety by two phosphatidate head group, the cross-sectional area of the headgroup relative to the area occupied by the acyl chains is significantly smaller than those of diacyl glycerophospholipids such as POPC (PC, 1-palmitoyl-2-oleoyl-*sn*-glycero-3-phosphocholine), POPS (PS, 1-palmitoyl-2-oleoyl-*sn*-glycero-3-phospho-L-serine) and PG. The small size of the polar headgroup in turn leads to an increase in the lateral pressure and transition temperature **(Lewis &**

McElhaney, 2009). It also confers CL the propensity to form inverted hexagonal II (HII) phase structures under cerain conditions, including low pH, presence of divalent cations and binding to basic proteins. The HII phase is a hallmark for non-bilayer forming lipids with a conical geometry **(van den Brink et al., 2004)**. Under physiological conditions, the possibility of existence of non-bilayer structures in lipid bilayer diminishes due to the repulsive forces acting between the anionic headgroups **(Tarahovsky et al., 2000**). However, under certain conditions like the ones stated above there is a possibility for the formation of non-lamellar structures. Besides the CL headgroup, the volume occupied by the hydrophobic acyl chains also plays a determining factor in the phase behavior of CL, where addition of one acyl chain to CL produces acylcardiolipin, which strongly favors the HII phase, whereas removal of one acyl chain produces monolysocardiolipin (MLCL), which favors the lamellar phase **(Powell & Marsh, 1985**). Moreover, the conversion of cardiolipin from lamellar to non-lamellar phase is speculated to be involved in modulation of cristae structure leading to the formation of membrane contact sites **(Friedman et al., 2015; Kim et al., 2004)**. This has implications for mitochondrial functions such as apoptosis and protein transport **(Epand et al., 2002; Horvath et al., 2015)**.

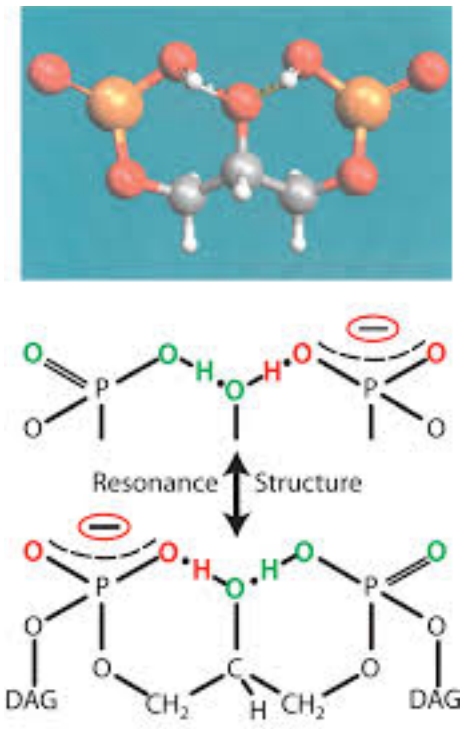

Figure 1.5 *Resonance-Stabilized Headgroup of Cardiolipin*

Model of the bicyclic resonance-stabilized headgroup structure of cardiolipin proposed by Haines and colleagues **(Haines, 2009)**. According to this model, the 2'-hydroxyl group engages in strong hydrogen bonding interactions with phosphate moieties resulting in distribution of a single negative charge in the headgroup region under physiological conditions. Figure adapted from **(Haines, 2009)**.

1.6 Cardiolipin Biosynthesis and Remodeling in Yeast

In yeast, CL biosynthesis occurs through several steps of conversion and modification of phosphatidic acid (PA) by a chain of enzymes located in the IM (**Figure 1.6**). PA, synthesized in the Mitochondrial Associated Membrane (MAM) of the endoplasmic reticulum (ER), is trafficked across the IMS via the Mdm35-stabilized Ups1 lipid transfer protein into the IM **(Watanabe et al., 2015; Yu et al., 2015)**. Following its transfer, *de novo* synthesis of CL is initiated by the conversion of PA is to CDP-diacylglycerol (CDP-DAG) by the cytidylyltransferase Tam41 **(Tamura et al., 2013)**. Alternatively, CDP-DAG can be synthesized by Cds1 in the ER that is then transported to the IM though the contribution of this route to CL synthesis is considered to be miniscule **(Kuchler et al., 1986)**. CDP-DAG and glycerol 3-phosphate are then converted to PG phosphate (PGP) by Pgs1 and then to PG via dephosphorylation by Gep4 **(Chang, Heacock, & Clancey, 1998; Osman et al., 2010)**. Both these enzymes are predicted to be located on the matrix-facing side of the IM. Moreover, their location is in agreement with the proposed initiation of CL synthesis on the matrix-exposed leaflet of the IM **(Joshi et al., 2009)**. The synthesis of immature form of cardiolipin, characterized by random assortment of saturated acyl chains, is initiated by cardiolipin synthase Crd1, which performs the condensation of PG and CDP-DAG **(Schlame & Haldar, 1993)**. This is followed by the remodeling cycle to produce mature form of CL, and is performed by CL-specific phospholipase Cld1, which removes an acyl chain to generate a remodeling intermediate monolyso-CL (MLCL) **(Beranek et al., 2009)**. The acyl-CoA independent transacylase tafazzin (Taz1) then transfers an acyl chain from

donor phospholipid, usually PC or POPE (PE, 1-palmitoyl-2-oleoyl-*sn*-glycero-3-phosphoethanolamine), to MLCL to regenerate the tetraacyl CL **(Xu et al., 2006)**. It has been shown experimentally that all fatty acyl chains in CL are amenable to remodeling **(Xu et al., 2003)**. Moreover, cycles of deacylation and reacylation yield CL with an acyl chain composition that is species- and tissue-specific and enriched in unsaturated fatty acids, predominantly palmitoleyl (16:1) and oleoyl (18:1) **(Schlame et al., 2005)**.

In wild-type yeast 90% of CL fatty acyl chains are unsaturated **(Baile, Whited, & Claypool, 2013)**. Moreover, despite the diversity of fatty acid combinations possible for this tetraacyl lipid, only a few types of unsaturated acyl groups are actually represented for CL within a given organism or tissue type **(Schlame et al., 2005)**. Furthermore, the importance of the tafazzin-mediated remodeling process is underscored by the fact that mutations affecting the X-linked *TAZ* gene in humans cause a multisystem disorder called Barth syndrome. To date, approximately 150 nonsense or missense mutations have been identified in the *TAZ* gene that cause Barth syndrome characterized by cardiac and skeletal myopathies, cyclic neutropenia, growth disturbance, and fatalities in young males **(Clarke et al., 2013)**. Mutations or knockout of the *TAZ* gene affects the level of unsaturated CL species, where it has been shown to cause 75% decrease in CL content with a subsequent increase in the level of MLCL **(Baile, Lu, & Claypool, 2014a; Gaspard & McMaster, 2015)**. As a result, Barth syndrome patients are found to have abnormal mitochondrial ultrastructure and destabilized respiratory supercomplexes **(Gu et al., 2004; McKenzie et al., 2006)**. However, it was shown in yeast that halting the remodeling process at the initiation stage resulting in accumulation

of unremodeled form of CL did not show any apparent mitochondrial defects compared to the wild-type species with remodeled CL **(Baile, Lu, & Claypool, 2014a)**. Hence, the physiological importance of CL remodeling remains poorly understood.

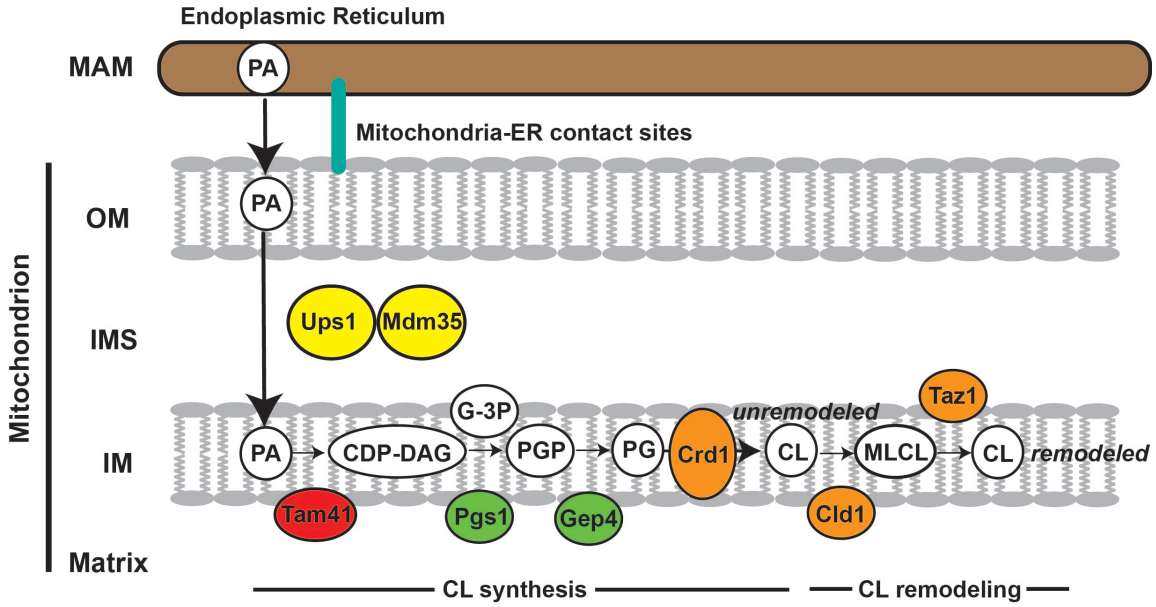

Figure 1.6 *Cardiolipin Biosynthesis and Remodeling in Yeast*

The synthesis of CL in the mitochondrion is initiated as phosphatidic acid (PA), synthesized in the Mitochondrial Associated Membrane (MAM) of the endoplasmic reticulum (ER), is trafficked across the IMS via membrane contact sites between mitochondria and ER (Mitochondria-ER contact sites) and Mdm35-stabilized Ups1 lipid binding protein. The *de novo* synthesis of CL in yeast mitochondrial IM includes enzymatic steps involved in the synthesis of unremodeled form of CL followed by a remodeling pathway to generate a remodeled and mature form of CL. Tam41 (red) is localized towards the matrix-facing side of the IM and catalyzes the conversion of PA to cytidine diphosphate-diacylglycerol (CDP-DAG), and was first reported to be involved in maintaining the integrity of the TIM23 complex **(Tamura et al., 2006)**. This is followed by the formation of phosphatidylglycerolphosphage (PGP) from CDP-DAG and glycerol 3-phosphate by Pgs1. Further, dephosphorylation of PGP by Gep4 yields phosphatidylglycerol (PG). PG then enters the step for the synthesis of unremodeled form of CL catalyzed by cardiolipin synthase (Crd1) followed by remodeling pathway

initiated by the CL-specific lipase Cld1, which removes an acyl chain to generate mololyso-CL (MLCL). The acyl-CoA independent transacylase Taz1 then transfers an acyl chain from a donor phospholipid to MLCL, thereby regenerating the tetraacyl CL. Cycles of deacylation and reacylation yield CL with an acyl chain composition that is species- and tissue-specific and enriched in unsaturated fatty acids. Synthesis and remodeling enzymes in orange indicate those subject to genetic knockouts in this study (**Chapter 4**).

1.7 Cardiolipin and Mitochondrial Protein Import

The first experimental evidence suggesting a role for CL in mitochondrial protein import came from studies demonstrating the importance of anionic phospholipids in unfolding of precursor proteins and subsequent transport, as well as inhibition of protein import in yeast cells treated with doxorubicin, a drug targeting anionic phospholipids **(Eilers, Endo, & Schatz, 1989; Endo & Schatz, 1988; Endo, Eilers, & Schatz, 1989)**. Subsequently, it was shown that yeast cells lacking cardiolipin synthase (Δ*crd1*) were partially defective in protein import in both fermentable as well as non-fermentable media **(Jiang et al., 2000)**. This finding was considered to be significant for CL-mediated protein import, as even the increased levels of PG in yeast grown in non-fermentable media could not overcome the protein import defects seen in the *Δcrd1* strain **(Jiang et al., 2000)**. However, the study also detected a decrease in the $\Delta\Psi_m$ in the absence of CL, which plays a direct role in mediating preprotein transport **(MALHOTRA et al., 2013)**. A more direct role for CL in the functioning of the TIM23 complex was established by later studies using *in vitro* reconstitution methods where it was shown that the reconstitution of a functional motor-free form of presequence

translocase ($TIM23^{SORT}$) in liposomes required the presence of cardiolipin **(van der Laan et al., 2007)**.

In the past few years several studies have suggested an intimate link between the biogenesis of mitochondrial phospholipids and proteins **(Gohil & Greenberg, 2009)**. By performing initial screening of essential mitochondrial proteins with unknown functions, it was revealed that translocator assembly and maintenance protein 41 (Tam41) plays an important role in the assembly and functioning of the TIM23 machinery (**Figure 1.6-1.7**) **(Gallas et al., 2006; Tamura et al., 2006)**. Interestingly, closer examination of Δ*tam41* mutant yeast cells displayed phenotype similar to the one known for cells deficient in CL synthesis (Δ*crd1*) **(Kutik et al., 2008)**. Subsequently, it was revealed that Δ*tam41* mutant cells lack the presence of both CL and PG, suggesting regulation of Tam41 in the biosynthesis pathway of CL at the level of CDP-DAG synthase **(Kutik et al., 2008)**. Altogether, these findings suggest that Tam41 is involved in protein import via its regulation of CL synthesis in yeast cells. Moreover, later studies also implicated IMS proteins, Ups1p and Ups2p, in regulating CL levels in an antagonistic manner. Consequently, it was shown that defects in Ups1p expression, which acts as a transport protein for CL precursor PA, lead to defects in mitochondrial protein import via altered assembly of the subunits of the TIM23 complex and its aberrant association with the PAM machinery of the mitochondrial matrix (**Figure 1.6-1.7**) **(Tamura, 2009a)**. Moreover, lipid-binding analysis performed on TIM23 subunits have revealed inherent affinities for the matrix-facing Tim44 as well as for the IMS-facing Tim23 receptor domain for CL-containing bilayers (**Figure 1.7**) **(Bajaj et al.,**

2014b; Marom et al., 2009; Weiss et al., 1999). Thus, growing evidence suggests direct involvement of constituents of the CL biosynthesis pathway and mitochondrial protein import via CL binding and stabilization of the components of the presequence translocase machinery.

Even though CL is synthesized in the IM and is present in appreciable quantities, there have been reports that identified the presence of CL in the OM **(Gebert et al., 2009; Alder NN, 2011)**. Interestingly, CL was also shown to be involved in the biogenesis of proteins of the OM, where it was demonstrated that CL deficiency altered the assembly of the OM protein import complexes **(Gebert et al., 2009)**. Moreover, a link between defect in protein transport and Barth syndrome was revealed by the identification of Barth syndrome-like illness known as dilated cardiomyopathy with ataxia (DCMA). DCMA is caused by mutations in the DNAJC19 gene that shares similarity with fungal Pam18 involved in protein import as a component of the motor machinery on the matrix side of the IM **(MacKenzie & Payne, 2007)**. Just like patients afflicted with Barth syndrome, patients with DCMA are known to suffer from debilitating conditions like cardiomyopathy, cerebral ataxia and elevated levels of 3-methylglutaconic acid. This similarity with clinical phenotypes of Barth syndrome patients suggests that defects in Tim23-mediated protein import and defects in CL remodeling have similar effects at the molecular level. Future studies involving comprehensive structural and functional analyses of the components involved in the biogenesis of mitochondrial proteins and phospholipids will help paint a better picture of the intricate relationship between the two seemingly different pathways. Moreover, a solid knowledge base of the relationship

between the two systems will help in the diagnosis of different pathological conditions associated with defective protein and lipid transport.

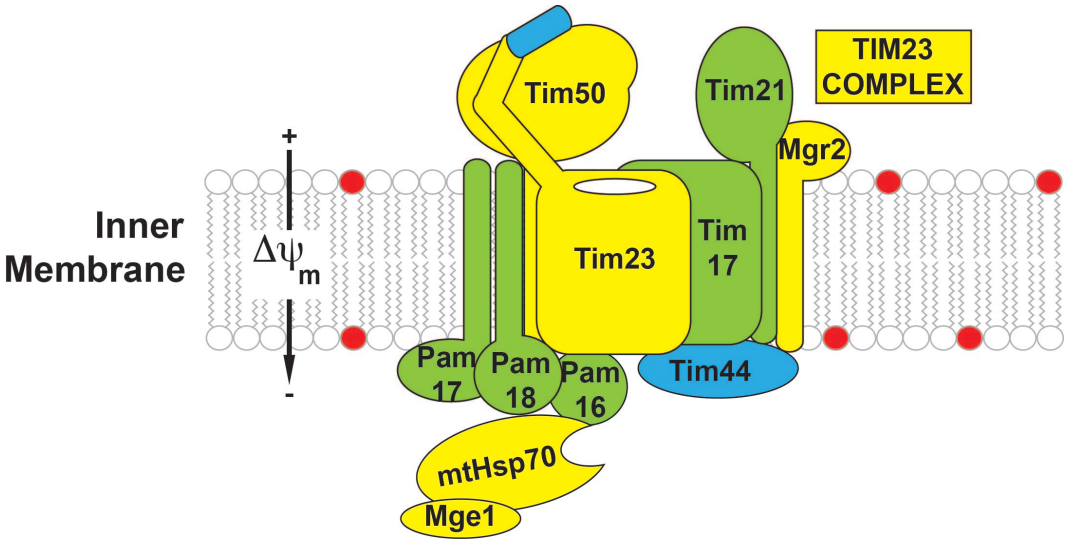

Figure 1.7 *Cardiolipin-Regulated Interactions of the Mitochondrial Presequence Translocase*

Yeast deficient in cardiolipin (red) has been shown to affect the interaction between Tim23 and other complex subunits (green), including the PAM machinery on the matrix-facing side of the inner membrane and Tim17 and Tim21 in the inner membrane **(Gallas et al., 2006; Kutik et al., 2008; Tamura et al., 2006; Tamura et al., 2009a)**. Additionally, the C-terminus of Tim44 and the extreme N-terminus of Tim23 receptor domain (blue) are known to directly interact with CL-containing membrane bilayers **(Bajaj et al., 2014b; Marom et al., 2009; Weiss et al., 1999).**

Chapter 2

Introduction: Advances in the Use of Nanoscale Bilayers to Study Membrane Protein Structure and Function

Derived from: Malhotra K.M. and Alder N.N. (2014) Advances in the use of nanoscale bilayers to study membrane protein structure and function. *Biotechnol. Genet. Eng. Rev.* (1-2): 79-93, doi: 10.1080/02648725.2014.921502.

2.1 Introduction

Eukaryotic cells are complex and highly organized entities designed to perform specialized functions. In order to carry out its activities while maintaining cellular homoeostasis, the cell contains defined boundaries surrounding its surface and the subcellular organelles called membranes. In addition to maintaining numerous microenvironments by tightly regulating the transport of materials within and across the semi-permeable bilayer, biological membranes are also sites of many cellular activities ranging from signaling to energy production. Hence, it does not come as a surprise that much of the cellular energy produced is used to help maintain various membrane components, which gives membranes their unique character.

Biological membranes are distinct within a eukaryotic cell, which provides them with the ability to support a wide array of specialized functions. They are dynamic and inherently complex, contains a host of biomolecules that interact with each other in a controlled manner to translate into a particular function. The lamellar bilayer of biological membranes is an aggregate of lipids stabilized by noncovalent interactions. A given biomembrane is composed of a defined collection of lipids, each with distinct features, including molecular geometry (cylindrical, cone, and inverted cone), head group identity (variable size and charge distribution), and acyl chain properties (variable lengths and degrees of saturation). Together, these attributes define fundamental features of the bilayer such as lateral pressure, polarity, and lipid tail mobility profiles (**Figure 2.1**) as well as elastic properties, curvature, and polymorphic behavior. The lipid bilayer is also

the natural milieu of integral membrane proteins (IMPs). IMPs comprise almost 30% of all gene products and active targets of nearly half of current pharmaceutical drugs **(Wallin & Heijne, 1998)**. Despite their importance, the underlying mechanistic aspect of many of the IMPs remains enigmatic due to difficulties in purifying them in large amounts and in a soluble form, making them recalcitrant to solution based biophysical techniques. Owing to the inherent complex nature of the membrane environment, it is extremely difficult to study the role of individual interactions within the context of native biological membranes. The advent of artificial model-membranes offers an attractive solution to those problems. By offering conditions closely mimicking that of native membranes sans the complexity, model-membranes have been widely used to study a range of membrane residing interactions, which mainly include protein-protein and lipid-protein interactions. The field of model-membrane systems has evolved considerably over the years offering an extensive insight into the behavior of membrane components under different conditions. Both conventional and non-conventional membrane systems have been employed to study specific or different roles adopted by those components.

The solubilization of membranes with nonionic surfactants (detergents in the vernacular) has traditionally been the means by which IMPs were isolated and characterized. Detergents commonly used for this purpose include DDM, Triton X-100, and those of the Brij series. Indeed, the nonpolar domains of detergents shield the aggregation-sensitive regions of IMPs; however, the resulting micellar structures do not recapitulate the physiochemical properties of the lamellar bilayer from which the proteins were extracted (**Figure 2.1**). Hence, IMPs in detergent micelles are prone to altered conformational dynamics, misfolding, and loss of function **(Seddon, Curnow, &**

Booth, 2004). By contrast, liposomes, vesicles composed of synthetic lipid bilayers, are good mimetics of the native lamellar membrane. However, the large size of proteoliposomes (IMP-containing liposomes) makes them unsuitable for many spectroscopic techniques due to light scatter and low rotational mobility; they offer poor control over the oligomeric state of the IMPs, leading to inhomogeneous samples; and their vesicular nature precludes experimental access to both sides of the bilayer. To circumvent these issues, researchers have employed bicelles, phospholipid bilayers encircled by a rim of high-curvature short chain lipids or surfactants. Bicelles provide the lamellar environment of a native membrane while being small enough for techniques such as solution NMR. However, bicelles can be inherently unstable and the specific combination of lipids required for their synthesis may not be commensurate with the lipid requirements of the reconstituted IMPs.

The most recent advances in the development of model membrane systems have been with nanoscale bilayers that are stabilized by annuli of amphipathic proteins or copolymers. These experimental systems allow for the reconstitution of IMPs and protein complexes into stable and monodisperse lamellar bilayers of precisely defined lipid composition. In this chapter, we review progress in the development of these nanoscale bilayers and highlight key examples of their use in the investigation of IMP structure and function using solution-based biochemical and biophysical techniques.

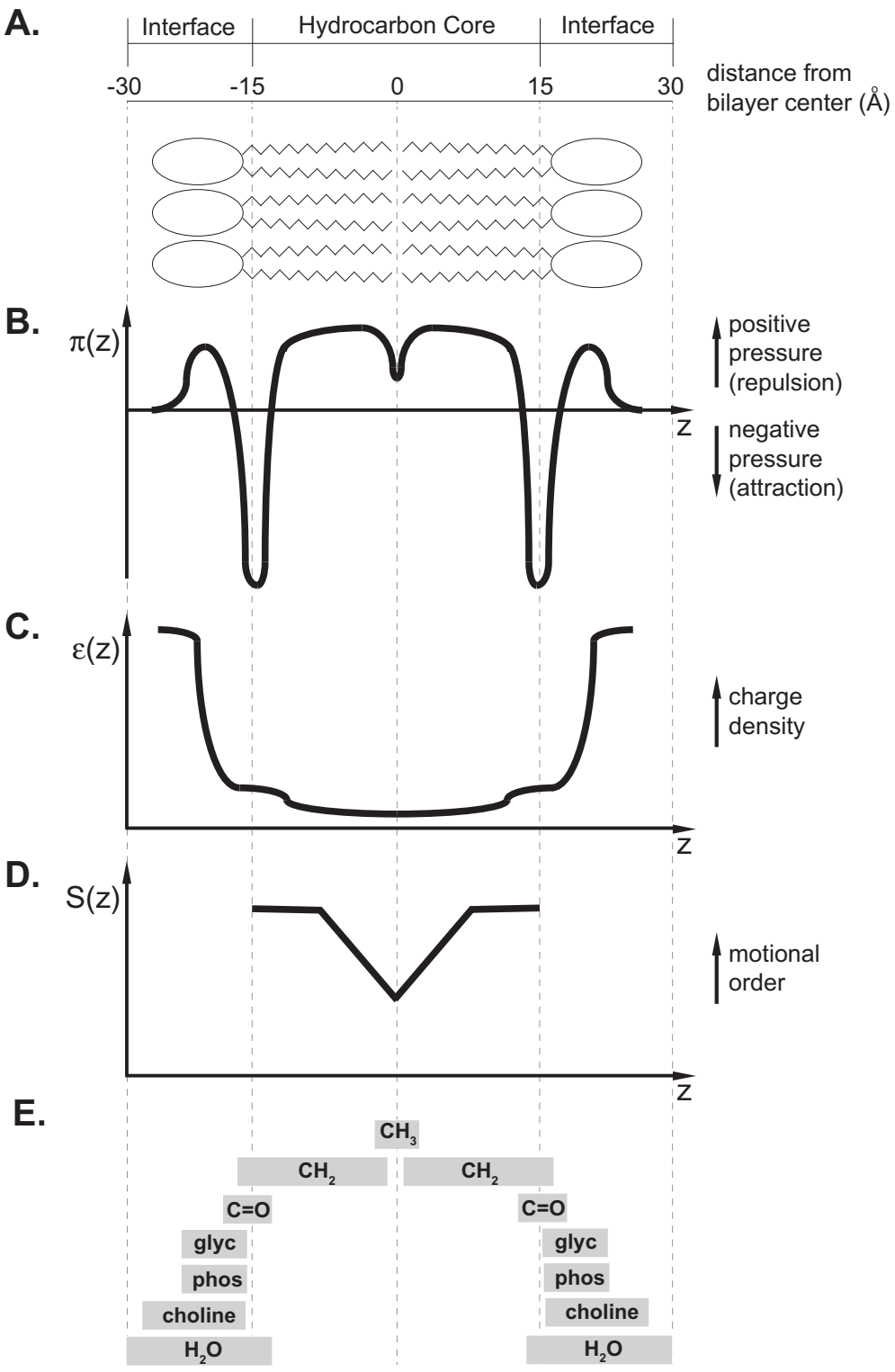
A.
Interface
Hydrocarbon Core
Interface
-30
-15
0
15
30
distance from bilayer center (Å)
B.
π(z)
z
positive pressure (repulsion)
negative pressure (attraction)
C.
ε(z)
z
charge density
D.
S(z)
z
motional order
E.
CH3
CH2
CH2
C=O
C=O
glyc
glyc
phos
phos
choline
choline
H2O
H2O

Figure 2.1 *Physiochemical Properties of Lamellar Bilayer*

The lamellar lipid bilayer of biological membranes is an anisotropic arrangement of lipid monolayers with many physiochemical gradients along the bilayer normal (z-axis), as shown for this representation of a phosphatidylcholine bilayer. A. Bilayer dimensions. The thickness of a typical hydrocarbon core, defined by the alkyl chains of both leaflets, is ~ 3 nm. The thermal thickness of the combined interfacial regions (polar head groups and waters of hydration) comprise roughly half of the bilayer thickness, B. Lateral pressure profile. Bilayer pressure (π) is composed of repulsive lateral pressure profiles in the headgroup and acyl chain regions and interfacial tension at the polar/nonpolar interface originating from the hydrophobic effect **(Marsh, 2007)**. C. Dielectric profile. The multilayer dielectric (ε) profile includes a very low dielectric core in the hydrocarbon center flanked by regions of intermediate dielectric followed by a steep gradients in the polar headgroup region toward high ε values similar to bulk water **(Nymeyer & Zhou, 2008)**, D. Acyl chain order profile of hydrocarbon chains. Measurements of segmental order parameter (S) reveal consistently high order for several chain segments near the headgroup followed by progressively greater disorder (lower anisotropy) toward the bilayer center **(Seelig & Seelig, 1974)**, and E. Time-averaged probability distributions of water and principal lipid structural groups for the thermally disordered fluid bilayer in the liquid crystalline phase, based on X-ray and neutron scattering profiles (phos, phosphate; glyc, glycerol backbone) **(White, 2001)**. Figure adapted from **(MALHOTRA & Alder, 2014)**.

2.2 Nanodiscs

Nanodiscs are soluble nanoscale phospholipid bilayers that were first synthesized in the lab of Stephen Sligar **(Bayburt, Grinkova, & Sligar, 2002)**, and have been used ever since as the membrane system of choice by many for carrying out biophysical characterization of IMPs. Nanodiscs are modeled on the structure of high-density lipoprotein (HDL) particles, which comprise of a scaffolding protein surrounding the phospholipid bilayer and function to transport mainly cholesterol from living tissues to liver for excretion **(Atkinson & Small, 1986)**. The major protein component of HDL particles is apolipoprotein A-I (apoA-I), which binds to phospholipid bilayer *via* its C-

terminal lipid-binding domain rich in amphipathic α-helices. Two copies of this protein wrap around the serum phospholipids to form scaffolds of disc like structures ~10 nm in diameter. ApoA-I has also been shown to form discoidal particles with synthetic phospholipids. Similar to the HDL particles, nanodiscs contain membrane scaffolding protein (MSP) derived from apoA-I, retaining only its C-terminal lipid-binding region, which is able to form a belt like structure around the phospholipid bilayer **(Segrest et al., 1999)**. Specifically, two molecules of MSP1 or one molecule of its fusion product, MSP2, was shown to give rise to disc like bilayer structures of roughly the same size as HDL particles (~ 10 nm in diameter) enclosing 160 phospholipid molecules (80 lipid molecules per leaflet) (**Figure 2.2A**).

The process of nanodisc assembly begins with mixing cholate-dissolved phospholipids with MSP of desired length. This is followed by detergent removal either with the help of adsorbent hydrophobic beads (Bio-Beads SM-2, BioRad or Amberlite XAD-2, Sigma-Aldrich) or dialysis against an appropriate buffer. As the detergent is being removed around the phospholipids, the hydrophobic regions of the amphipathic MSP start interacting with the lipids leading to the formation of soluble nanoscale lipid bilayers **(Bayburt et al., 2002)**. For membrane protein reconstitution into the nanodiscs, the protein of interest is solubilized with the detergent of choice and added to the MSP and phospholipid mix as described above, followed by detergent removal **(Bayburt & Sligar, 2010)**. Alternatively, cell-free synthesis of IMPs in the presence of nanodisc particles have also lead to their successful incorporation **(Lyukmanova et al., 2012)**.

Target protein reconstitution *via* detergent removal is mostly derived by protein-lipid interaction and lipid-lipid interaction as the detergent is being removed.

One of the numerous advantages of using nanodiscs as membrane system is that it offers unhindered access to both the leaflets, allowing molecules in the solution to interact with both sides of the reconstituted membrane components. This is in contrast to other conventional membrane systems like liposomes or supported-bilayers, which allow access to only the *cis* side of the membrane. The presence of a protein scaffold, MSP, forming the boundary of these nanoscale particles offers numerous other advantages. The presence of MSP helps confer stability to the system, which is an additional bonus over conventional membrane systems like liposomes that are inherently unstable. It also ensures that the nanodisc preparations are homogenous, precise and reproducible over a wide range. The size of the discoidal particle is dependent on the size of the protein scaffold. Denisov *et al.* showed this by designing MSP variants of different lengths that resulted in nanodiscs of different diameters ranging from 9.5 to 12.8 nm. This technical advancement has enabled researchers to study membrane proteins of various sizes using this system. In fact, it has also been shown that the monomeric or multimeric state of membrane proteins reconstituted into nanodiscs can be controlled using MSPs of different sizes. The presence of scaffold protein contacting the lipids in the outer rim of the discs also gives rise to boundary lipids, which help them closely mimic the gel-to- liquid phase transitions seen in biological membranes **(Shaw, McLean, & Sligar, 2004)**. Thus, reconstitution of membrane proteins into nanodiscs helps keep the protein in solution and provide a

native-like membrane environment with a control over the oligomerization state of the protein.

Nanodisc reconstitutions have been used for two-dimensional solution NMR-based studies on the structures and functional dynamics of many IMPs, including the voltage-sensing domain of the potassium channel KvAP **(Shenkarev & Lyukmanova, 2010)**, the mitochondrial voltage-dependent anion channels VDAC-1 **(Raschle et al., 2009)** and VDAC-2 **(Yu et al., 2012)**, and the membrane-spanning segment of the CD4 receptor **(Glück et al., 2009)**. In an effort to further improve the quality of NMR spectra of nanodisc-reconstituted samples, recent work has been aimed toward engineering smaller bilayers by systematic reduction of the MSP belt size, resulting in discs with shorter rotational correlation times. The truncation of MSP1D1 by selective removal of internal helices allowed for the reconstitution of bR and the β-barrel OmpX into nanodiscs as small as 6.3 nm in diameter, making them accessible to multidimensional NMR analysis and higher resolution structure determination **(Hagn et al., 2013)**. In a related study, C-terminal truncations of MSP down to seven helical repeats rendered improved ^{15}N TROSY-HSQC spectral quality of integrin α_{IIB} incorporated into nanodiscs, particularly for transmembrane residues **(Puthenveetil & Vinogradova, 2013)**. Interestingly, both studies identified lower size limits for nanodiscs: below a certain MSP length threshold, discs lacked stability or began to form heterogeneous samples containing larger particles.

Nanodiscs have also been extensively used to study the lipid-dependent activity of membrane-bound oxidoreductases. For example, mitochondrial succinate:quinone oxidoreductase reconstituted into nanodiscs of different lipid composition revealed a critical role for the anionic phospholipid cardiolipin in promoting holoenzyme stability and redox activity **(Schwall, Greenwood, & Alder, 2012)**. Another complex of the electron transport chain, cytochrome c oxidoreductase, was reconstituted into nanodiscs and subjected to microsecond resolution measurements of proton-coupled electron transfer, revealing an accelerated rate of proton uptake in comparison to detergent-solubilized enzymes **(Öjemyr et al., 2012)**. Several studies have also examined electron transfer mechanisms of the diflavin cytochrome P450 reductase (CPR) and its native redox partner CYP3A4, a drug-metabolizing member of the cytochrome P450 superfamily. These monotopic IMPs of the endoplasmic reticulum mediate the transfer of electrons from NADPH to organic substrates. Using spectroelectrochemical titrations, Sligar and co-workers analyzed the redox potentials of microsomal CYP3A4 and CPR reconstituted into nanodiscs of different lipid composition, finding that membrane insertion shifted the midpoint potentials of the FAD/FMN (CPR) and heme (CYP3A4) to significantly more positive values in a manner that was influenced by the presence of anionic phospholipids **(Das & Sligar, 2009; Das, Grinkova, & Sligar, 2007)**. These studies demonstrated that the electrostatic field of the bilayer is critical in tuning the redox potentials of these enzymes to make electron transfer thermodynamically feasible. This effect may underpin the recently reported increase in CYP3A4 coupling when reconstituted in the presence of anionic phospholipids **(Grinkova et al., 2013)**. As another experimental approach, neutron

reflectometry was employed to monitor redox-dependent structural transitions of nanodisc-bound CPR aligned at the water–silica interface, suggesting that NADPH reduction promoted a compact conformation as a potential mechanism to prevent off-pathway electron transfer **(Wadsäter et al., 2012)**. Technical advances in monitoring individual enzyme turnover events of nanodisc-bound CPR **(Laursen et al., 2014)** forecast future single molecule strategies using nanodics to explore discrete functional states of such oxidoreductases and other MPs.

Taken together, these studies demonstrate that nanodiscs are excellent platforms for solution-based structural studies and for precisely determining the effects of different lipids on IMP structure and function. They also serve to emphasize the point that lipid composition is a critical component in the experimental design of such model membrane-based analysis.

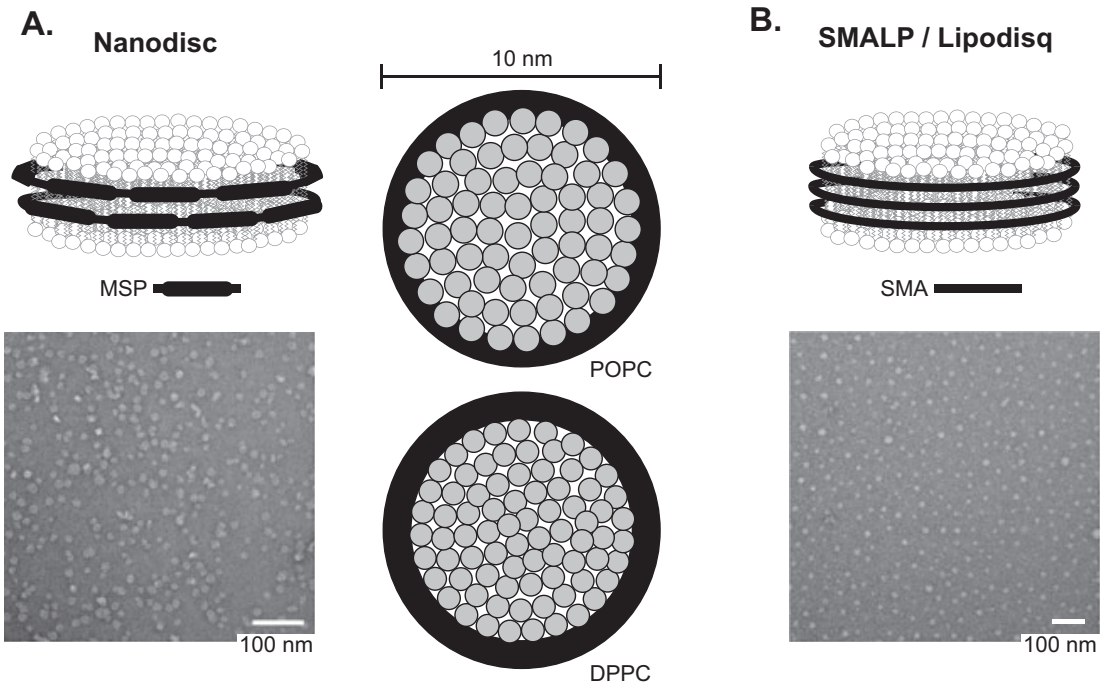

Figure 2.2 *Nanoscale Lipid Bilayers*

A. Nanodiscs (left, upper panel) are lipid discoids bound by two copies of the MSP polypeptide, each one containing amphipathic α-helices (11 or 22 residues in length) that are separated by proline and glycine residues. Commonly used MSP variants include MSP1 (with 10 amphipathic helices, Ø = 9.8 nm) and MSP1E1 (Ø = 10.6 nm), MSP1E2 (Ø =11.9 nm), and MSP1E3 (Ø = 12.9 nm), containing one, two, and three 22-mer helical inserts in the center of the MSP1 unit, respectively **(Denisov et al., 2004; Schuler et al., 2013)**. Left, lower panel, electron micrograph of MSP1E3-bound nanodiscs at a magnification of 180,000 x **(Schwall et al., 2012)**. Right panels, top-down schematics showing that the number of lipids per nanodisc depends on the MSP length and the cross-sectional area occupied by each lipid. MSP1 nanodiscs are approximately 10 nm in diameter, producing a lipid bilayer disc with a diameter of 8 nm (bilayer area = 50.2 nm^2). In the liquid crystalline phase, the disaturated lipid 1,2-dipalmitoyl-sn-glycero-3-phosphocholine (DPPC, 16:0/16:0 PC) has an area of 0.54 nm^2 and the monounsaturated lipid 1-palmitoyl-2-oleoyl-sn-glycero-3-phosphocholine (POPC, 16:0/18:1 PC) has an area of 0.70 nm^2. In agreement with experimental measurements, MSP1 discs contain approximately 78 DMPC lipids and 68 POPC lipids per leaflet. The bilayer thickness of nanodiscs containing DPPC or POPC, measured by SAXS, is ~5.6 nm and ~4.6 nm, respectively, and B. SMALPs/Lipodisqs® (upper panel) are lipid discoids bound by the styrene maleic acid copolymer containing styrene and maleic acid groups in molar ratios of 3:1 or 2:1. Lower panel, electron micrograph of 3:1 SMA-bound discs at a magnification of 120,000Å~ **(Long et al., 2013)**. Figure adapted from **(MALHOTRA & Alder, 2014)**.

2.3 SMALP's/Lipodisq®

More recently, lipid bilayers stabilized by rings of the copolymer styrene maleic acid (SMA) have been developed under the nomenclature styrene maleic acid lipid particles [SMALPs **(Knowles, Finka, Smith, & Lin, 2009)**] or Lipodisqs® **(Orwick, Judge, & Procek, 2012; Orwick-Rydmark, Lovett, & Graziadei, 2012)** (**Figure 2.2B**). Lipodisq® technology is based on nanosized lipid-polymer assembly, which as a proprietary of Malvern Cosmeceutics Ltd., is used as a biodegradable method to target hydrophobic compounds to dermal tissues **(Tonge SR, Patent GB2426703)**. This novel technology has also recently found its way for application in membrane protein solubilization and characterization. The lipid-polymer particle assembly is based on the property of amphipathic polymers (amphipols) to associate hydrophobically when the pH of the environment is changed, which in turn brings about conformational changes in the polymer structure **(Tonge & Tighe, 2001)**. Those changes are known to promote formation of secondary structures, with hydrophobic and hydrophilic moieties occupying opposite faces in the polymers, an effect known as hypercoiling **(Popot, 2010)**. This structural heterogeneity of amphipols can be brought to use as a surfactant detergent molecule or lipid associating amphipathic protein (e.g. MSP), which can bind around the membranes leading to the formation of nanometer sized lipid assemblies. The ability of amphipols to form such assemblies was probably first demonstrated in the case of Poly(2-ethacrylic acid) (PEAA), which was found to bind to the surface of dipalmitoyl-*sn*-phosphatidylcholine (DPPC) liposomes **(Kusonwiriyawong et al., 2003)**.

SMALPs/Lipodisq® preparation was described to result from mixing of a copolymer prepared from a 3:1 molar ratio of styrene to maleic acid (3:1 SMA) (**Figure 2.3**), and dimyristoyl-*sn*-phosphatidylcholine (DMPC) in a ratio of 1.25:1.0 (w/w) that resulted in a population of monodispere particles having an average size of 9 nm **(Orwick et al., 2012)**. Characterization of properties of lipid molecules within Lipodisq® particles revealed a non co-operative gel to liquid crystalline phase transition, most likely due to the lateral pressure exerted by the copolymer on the lipid molecules. Further, EPR studies showed the pressure being exerted mostly on lipid tail molecules while the molecules at the center were free from any restrictions.

Amphipols were originally designed to keep the membrane proteins in a soluble form after their detergent extraction from biological membranes. Since then, they have been widely used to maintain the solubility and activity of a variety of membrane proteins. As a means of reconstituting IMPs into soluble discs, the SMA copolymer has been shown to extract both α-helical and β-barrel proteins directly from DMPC vesicles into polymer-bound particles that contained both the protein and lipid, and retained native protein function **(Knowles et al., 2009; Orwick et al., 2012; Orwick-Rydmark et al., 2012)**. This approach allows for the single-step extraction of IMPs directly from bilayers in a manner that obviates the requirement for detergents; therefore, there is no potentially problematic step involving detergent removal prior to disc formation. Moreover, because bilayers are stabilized by polymer, not polypeptide, there is no additional protein signal that must be deconvoluted from the target protein during analysis. On the other hand, in contrast to nanodiscs, the lipid content of the polymer-

bound discs is constrained to that of the originating membrane. Moreover, as of yet, there is no clear means of systematically adjusting the diameters of SMA-bound particles based on polymer size alone.

A further application of this technology is the reconstitution of IMPs from native cellular membranes directly into SMA-bound particles. It was recently reported that the SMA copolymer solubilized mitochondrial membranes, enabling the reconstitution of the multisubunit respiratory complex IV into polymer-bound lipoprotein particles in a manner that retained the redox activity of the holoenzyme **(Long et al., 2013)**. Subsequently, SMA has been shown to extract a wide range of IMPs, including photoreaction center, tetrameric potassium channel, KcSA, and ATP-binding-cassette (ABC) transporters from the membranes of prokaryotic as well as eukaryotic expression systems **(Dörr et al., 2014; Gulati et al., 2014; Swainsbury et al., 2014)**. In all the cases, IMPs reconstituted in SMALPs were found to be more stable than in detergent micelles.

Spectroscopic techniques such as Pulsed EPR double electron-electron (DEER) resonance spectroscopy provide distance measurements between paramagnetic centers up to 80 Å apart. bR and KCNE1 reconstituted into SMALPs/Lipodisqs® revealed high-quality DEER-detected distance distributions between selectively incorporated spin labels **(Orwick-Rydmark et al., 2012; Sahu et al., 2013)**, forecasting the applicability of this technique to other IMPs in obtaining distance constrains for modeling, and in determining structural dynamics and ligand associations. Recent advances in the electron microscopy (EM) detection technology have transformed it as a forefront technique for determining structure of membrane proteins at near atomic resolution **(Callaway, 2015)**. The use of SMALPs to purify membrane proteins offers an

excellent opportunity to carry out structural studies of IMPs in a native-like membrane environment. Recent negative stain-and cryo-EM analysis of SMALP-bound membrane transporters, Pgp and AcrB **(Gulati et al., 2014; Postis et al., 2015)**, testifies the currently untapped potential of combination of these two techniques. EM-based structural analysis of SMALP-solubilized IMPs offers a lucrative alternative to X-ray crystallography, especially for membrane proteins that have resisted years of crystallization efforts. Moreover, it offers an opportunity to look at structural changes in membrane proteins accompanying changes in the lipid composition.

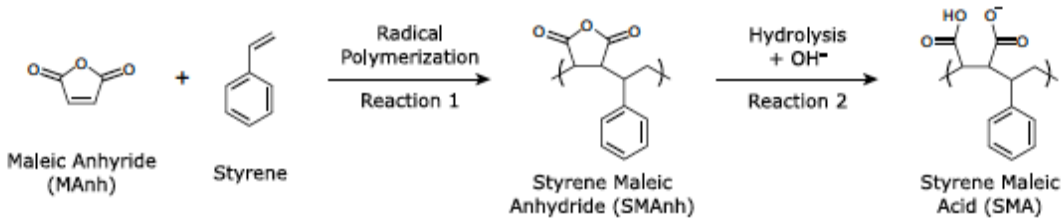

Figure 2.3 *Synthesis of SMA Copolymer*

Schematic representation of the synthesis of styrene-maleic acid anhydride (Reaction 1) and the preparation of styrene-maleic acid (Reaction 2). The 3:1 SMA copolymer results from forging together hydrophobic styrene and hydrophilic maleic acid groups. Figure adapted from **(Dörr et al., 2016)**.

2.4 Conclusions

Nanoscale bilayers represent the next frontier in the study of MP structure and function. The solubility, stability, and monodispersity of these model membranes coupled with their facile synthesis make them widely applicable to solution-based studies of IMPs that have a broad range of structural complexities. This point is confirmed by the recent studies on IMP structure, protein– protein interactions, and protein– lipid interactions that have been covered in this chapter. Nanodiscs, having been in development for over a decade, have the proven ability to functionally reconstitute IMPs in a controllable oligomeric state and with a user-defined lipid composition. The SMALP/Lipodisq® system as a means of detergent-free IMP reconstitution is, by contrast, a relatively nascent technology whose full range of applications has yet to be explored. In this regard, future modifications of the SMA copolymer (size, pendant group stoichiometry and functionalization with molecular tags) will likely be useful in the development of novel experimental applications. In addition to their utility in basic research, these nanoscale bilayers have vast potential for applied technologies, including the development of biocompatible systems for hydrophobic drug delivery and diagnostic applications **(Murakami, 2012; Ng et al., 2013; Numata et al., 2013)**, nanoelectronic devices **(Goldsmith et al., 2011; Ham et al., 2010)**, and multiplexed sensor arrays to detect protein interactions **(Sloan et al., 2013)**.

Chapter 3

Reconstitution of Tim23 into Nanodiscs Using Cell-Free Expression-Based Approaches

Derived from: Malhotra K. and Alder N.N. (*in revision*) Reconstitution of mitochondrial membrane proteins into nanodiscs by cell-free expression. *Methods in Molecular Biology*.

3.1 Abstract

The TIM23 complex is highly intricate machinery, composed of 11 known subunits that come together to perform protein import in the IM of mitochondria. Tim23 is the central component of the TIM23 complex, whose functions as a receptor and a protein-conducting channel are under tight control via interactions with the subunits within the complex as well as multiple factors outside the complex. So far, the studies on the Tim23 protein have focused on its interactions and functions in the context of an active complex in mitochondria, precluding more detailed information about the contribution of individual mitochondrial components on the functioning of this protein. In this study, we present optimized methods for reconstituting full-length Tim23 in model membranes, termed nanodiscs. This reductionist system is used for characterizing Tim23 interactions with the components within the TIM23 complex as well as outside the complex in the mitochondrial IM. We show that cell-free translated Tim23 is capable of reconstitution into nanodiscs in both co-translational and post-translational manner, and that this protein assumes a proper topology upon reconstitution. By reconstituting an *in vitro* translated membrane protein into nanodiscs, this methodology offers a platform for directly characterizing membrane protein functions in isolation, and its interactions with the individual membrane-resident components.

3.2 Introduction

Integral membrane proteins are one of the most sought after drug targets in the pharmaceutical market **(Sanders & Myers, 2004)** while also being the least understood and most challenging class of proteins for structural and functional studies. One of the major bottlenecks in the study of membrane proteins is to recreate the lipid bilayer; a highly dynamic and chemically complex two-dimensional amphipathic environment, which imparts stability to the overall structure of membrane proteins. Most of the membrane proteins are produced in very low amounts within a cell, thus making it difficult to carry out structural and functional studies within their endogenous milieu. On the other hand, overexpression of recombinant membrane proteins often results in cytotoxicity, misfolding and aggregation. Moreover, conventional methods for membrane protein purification are dependent on the use of detergents, which can destabilize membrane proteins, thereby affecting their function. This chapter describes procedures that leverage the technical advantages of cell free biosynthetic systems with advances in the use of nanoscale lipid bilayers for the expression and functional reconstitution of a mitochondrial membrane protein.

Cell-free protein translation systems are based on biosynthetic machinery that is isolated from metabolically active cells with relatively low amounts of endogenous messenger RNA (mRNA). The most commonly used lysates include those from rabbit reticulocytes, from bacterial cells, and from wheat germ embryos. These lysates include the components essential for translation: ribosomes, transfer RNA (tRNA), aminoacyl tRNA synthetases, and translation initiation and elongation and termination factors. In

cell-free translation reactions, these lysates are supplemented with mixtures that enhance protein translation, including energy generating systems and amino acids. Some systems entail programming the reaction with plasmid or linear DNA that encodes the protein of interest and from which mRNA transcripts are synthesized by endogenous RNA polymerases. In other systems, purified mRNA transcripts that are prepared during a separate *in vitro* transcription reaction are added to the cell-free translation.

Cell-free protein synthesis reactions confer several advantages over conventional expression systems (e.g., in live *Escherichia coli*, yeast, or insect cells), particularly for the expression of membrane proteins. Most notably, because living cells are not involved in the reaction, cell free systems avoid the potential cytotoxicity of expressing hydrophobic proteins, plasmid instability, and issues associated with cellular protein trafficking and membrane integration, all of which can result in low protein yield **(Junge et al., 2011; Sachse et al., 2014)**. Moreover, because cell-free expression systems are open, they allow for unrestricted experimental access to the reaction for the inclusion of additives such as cofactors and probes for site-specific protein labeling (e.g., with fluorescent or EPR probes). Of course, the native milieu of a membrane protein is a lipid bilayer, and several strategies have been utilized that provide additives that mimic the nonpolar membrane environment within cell-free systems for proper folding and stability of translated proteins. By one approach, reactions contain mild nonionic detergents that are compatible with the biosynthetic machinery and allow for the cotranslational stabilization of membrane proteins in proteo-micelle complexes **(Junge et al., 2011; Klammt et al., 2005)**. In addition, synthetic surfactants including organic amphipathic polymers (amphipols), fluorinated surfactants, and designed

peptide surfactants have been shown to stabilize membrane proteins produced by cell-free translation **(Bazzacco et al., 2012; Blesneac et al., 2012; Corin et al., 2011; Wang et al., 2012)**.

Recent advances in model membrane systems have provided new mechanisms for the reconstitution of membrane proteins into a lipidic environment. By comparison with the above hydrophobic additives, such model membranes allow proteins to fold into physiologically relevant lamellar lipid bilayers and can satisfy requirements of specific lipid interactions for membrane protein function **(Andersen & Koeppe, 2007; Cross et al., 2013; Lee, 2004)**. Cell-free reconstitution strategies for membrane proteins have been reported using liposomes, spherical lipid vesicles of different diameter **(Hovijitra et al., 2009; Kalmbach et al., 2007; Long et al., 2012; Moritani et al., 2010)** and bicelles, discoidal assemblies of lipids with outer edges of short-chain lipid or detergent **(Dürr et al., 2012; Lyukmanova et al., 2012; Uhlemann et al., 2012)**. However, nanoscale lipid bilayers belted by rings of amphipathic protein or co-polymers have emerged as excellent membrane mimetics for experimentation due to their small size, stability, monodispersity, and wide range of compatible lipids **(MALHOTRA & Alder, 2014; Chapter 2 of this study)**. Most notable for cell-free translation systems, nanodiscs – discoidal nanoscale lipid bilayers that are stabilized by annuli of amphipathic polypeptides – allow for the reconstitution of membrane proteins into lamellar bilayer systems that are amenable to solution-based biochemical, biophysical and structural analysis. Developed originally by Sligar and colleagues, nanodiscs comprise bilayers of synthetic or naturally derived lipids enclosed by engineered variants of apolipoprotein A-1, termed membrane scaffold protein (MSP) **(Bayburt et**

al., 2002; Bayburt & Sligar, 2003; Denisov et al., 2004). Nanodiscs have most widely been used for the reconstitution of overexpressed and purified membrane proteins, as recently reviewed **(Schuler et al., 2013)**. However, several groups have recently shown the utility of nanodiscs in the reconstitution of membrane proteins synthesized by cell-free systems **(Cappuccio et al., 2008; Henrich et al., 2015; Katzen et al., 2008; Lyukmanova et al., 2012; Proverbio et al., 2013; Roos et al., 2012; Yang et al., 2011)**. In this regard, multiple reconstitution strategies have been reported, including the cotranslational insertion of membrane proteins into pre-assembled nanodiscs added to the translation reaction and the simultaneous formation of nanodiscs and the target membrane protein.

In this chapter, we discuss the cell-free synthesis and nanodisc reconstitution of Tim23, the central subunit of the TIM23 protein transport complex of the mitochondrial inner membrane. We provide procedures and results for co-translational assembly of Tim23-containing nanodiscs (wherein Tim23 is synthesized in the presence of pre-formed nanodiscs) as well as for post-translational assembly (wherein pre-synthesized Tim23 is added to nanodisc assembly reactions). Moreover, using fluorescence spectroscopy-based approaches, we show that the conformation of Tim23 assembled into nanodiscs is a topologically correct one.

3.3 Results

Tim23 Reconstitution into Nanodiscs

To carry out nanodiscs reconstitution of the integral membrane protein Tim23 using different approaches, a series of steps were followed (**Figure 3.1**). The preliminary steps involved PCR amplification of Tim23 DNA coding regions using plasmid selected from our SP6-based plasmid library encoding for the full-length Tim23 (wild-type or monocysteine mutants) from *Saccharomyces cerevisiae* (**Appendix A, Table A.1**). This was followed by *in vitro* transcription to generate Tim23 mRNAs (**Appendix A, Table A.2**), as well as purification of membrane scaffolding protein, MSP1E3D1, for nanodisc preparation (**Figure 3.1**). For the post-translational mode of Tim23 integration, first, mRNA encoding for the full-length wild-type Tim23 protein was used to program wheat germ-based *in vitro* translation reactions in the presence of energy generating system and all twenty amino acids, where methionine was replaced with radiolabeled [^{35}S] methionine (**Appendix A, Table A.5**). This was followed by addition of the translation mix to a reaction containing components for nanodisc preparation *i.e.* 6X-histidine tagged membrane scaffold protein (MSP) and detergent-solubilized native lipid mix containing either 100 mol% POPC (16:0/18:1) or 80 mol% POPC and 20 mol% CL (18:1) (**Appendix A, Table A.7**). Following detergent removal via BioBeads, the nanodiscs were eluted using Ni^{2+}-NTA affinity chromatography (**Appendix A, Table A.4**) and the different fractions were analyzed using SDS-PAGE. The presence of MSP in the coomassie blue stained gel fractions was used as a

diagnostic tool for the presence of nanodiscs in those fractions as shown by earlier studies **(Schwall et al., 2012)**. This was followed by autoradiography to detect the presence of [^{35}S]Tim23.

For our co-translational approach, the translation reaction was carried out in the presence of preformed nanodiscs (**Appendix A, Table A.5**), and subjected to a second round of affinity purification followed by SDS-PAGE analysis (**Figure 3.1**). For both the co-translational and the post-translational mode of [^{35}S]Tim23 incorporation, we saw [^{35}S]Tim23 co-eluting with MSP1E3D1, indicating that Tim23 does get incorporated into nanodiscs (**Figure 3.2**). Moreover, omission of MSP from the reaction resulted in >90% of [^{35}S]Tim23 falling off the affinity column into the flow-through (**Appendix A, Table A.3; Figure 3.3**). These results indicate that elution of Tim23 is indeed dependent on the formation of MSP-derived discoidal-bilayer structures. The assembled structure of Tim23 into nanodiscs will henceforth be denoted as Tim23-ND.

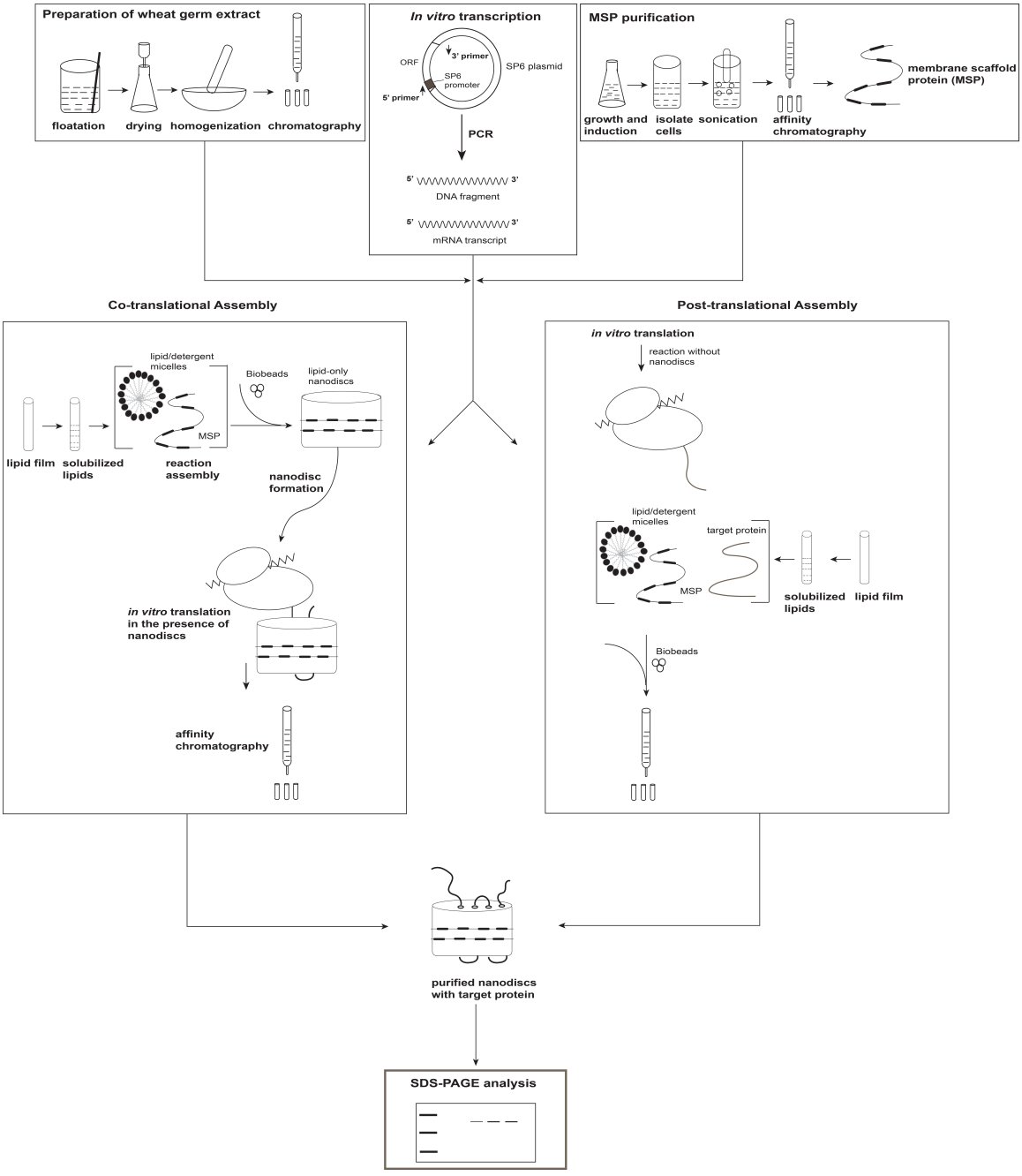

Figure 3.1 *Protocol Flowchart for the Assembly of Tim23 into Nanodiscs*

Flowchart depicting steps for the reconstitution of Tim23 into nanodiscs using *in vitro* translation including: Preparation of wheat germ extract, *In vitro* transcription, Preparation of MSP, Co- and post-translational nanodiscs assembly, and SDS-PAGE analysis.

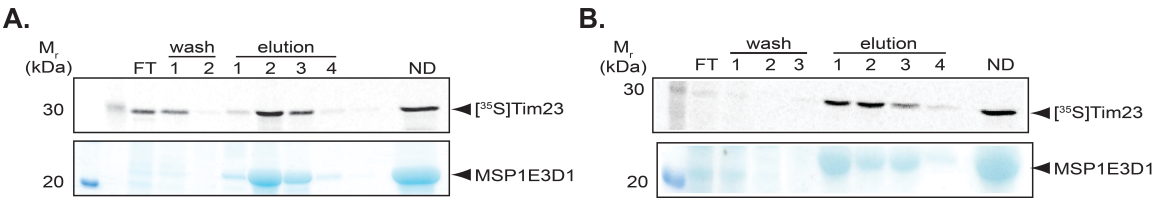

Figure 3.2 *Tim23 Co-Elutes with MSP*

Analysis of nanodisc assembly and purification for A. post-translational assembly, and B. co-translational assembly. Samples were resolved by SDS-PAGE on 12% gels and visualized by radioisotope scanning (upper gels) to image [^{35}S]Tim23 and by coomassie staining (lower gels) to detect MSP. Individual flow through, wash, and elution fractions are indicated. ND denotes the final combined fraction (elution 1 + elution 2), concentrated to 500 µl.

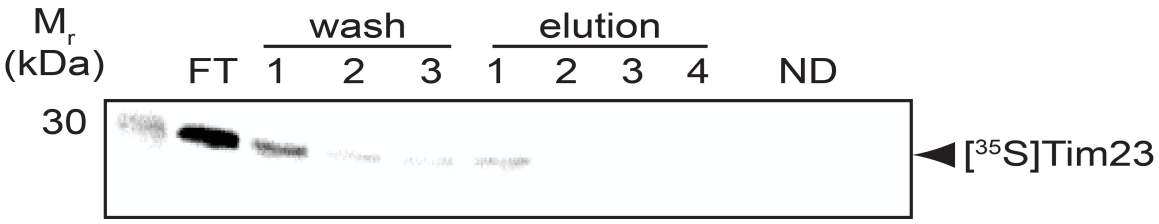

Figure 3.3 *Lipid-Only Nanodiscs [^{35}S]Tim23 Reconstitution*

Loading the reaction on a Ni^{2+}-NTA column resulted in >90% [^{35}S]Tim23 falling off the column in the flow-through ("FT") in the absence of MSP protein. This control demonstrates the specificity of the Tim23 reconstitution reaction.

Tim23 Assumes Correct Topology in Nanodiscs

After confirming the reconstitution of Tim23 into nanodiscs, we went further and asked whether Tim23 assembles within the nanoscale discoidal bilayer in a proper topological fashion. To address that question, we used our cell-free fluorescence labeling approach **(Alder et al., 2008a; MALHOTRA et al., 2013; Chapter 5 of this study)** to label Tim23 with the environment-sensitive probe, NBD, at specific sites (**Figure 3.4A**). Specifically, we used monocysteine Tim23 mRNA constructs, encoding for cysteine at position 24 (IMS) and position 111 (TMS1), to program our *in vitro* translation reactions in the presence of NBD-Cys-tRNA^{cys} (**Appendix A, Table A.6**). Following the post-translational reconstitution method for incorporating Tim23 into nanodiscs, we monitored the emission spectra of the NBD fluorophore at those two positions independently. NBD is used as an excellent probe, to report the microenvironment of a specific site (**Alder *et al.*, 2008; Malhotra *et al.*, 2013; Chapter 5 of this study**). The spectral properties of NBD are dependent on the polarity of the environment, wherein an aqueous environment NBD shows a lower steady-state emission intensity and red shift in its wavelength of maximum emission ($\lambda_{em\ max}$) compared to when it is in a non-polar medium. Monitoring the emission spectrum of NBD at the two Tim23 residues revealed about ~2.5X higher emission intensity of the probe positioned in TMS1 compared to the probe facing the aqueous IMS domain. Moreover, NBD at the membrane-exposed site displayed a blue shift in $\lambda_{em\ max}$ relative to the probe in the IMS site (**Figure 3.4B**). These results suggest that Tim23 assumes a proper topology in nanodiscs after reconstitution.

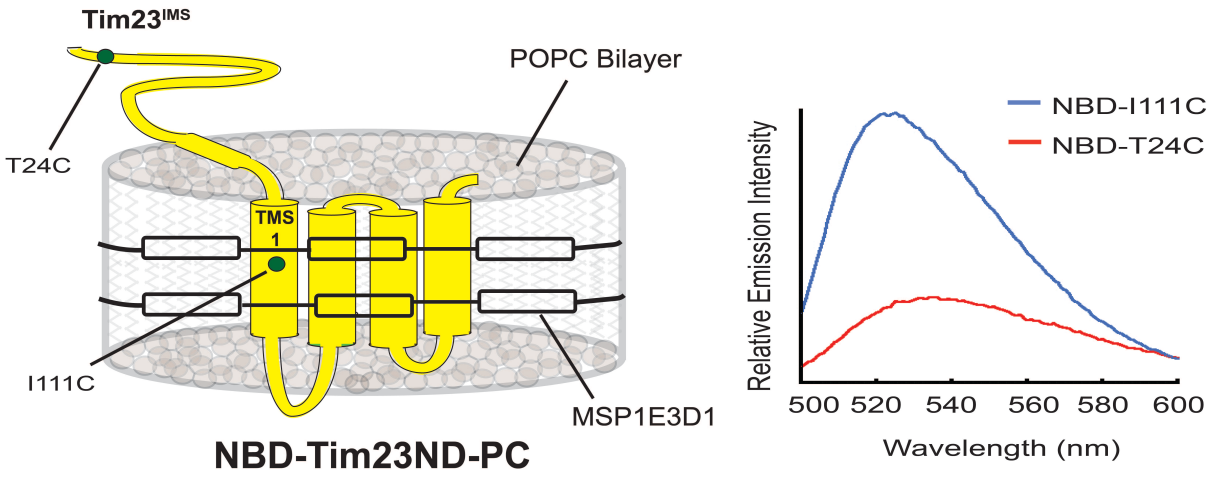

Figure 3.4 *Tim23 Assumes a Proper Topology in Nanodiscs*

A. Topology diagram of NBD labeled Tim23 reconstituted into POPC NDs bound by MSP1E3D1. Sites bearing NBD are indicated (green circles). B. Corrected emission spectrum of NBD-Tim23. NBD positioned at I111C (TMS1) displayed ~2.5X higher emission intensity than NBD at position T24C (IMS) in Tim23 after reconstitution into NDs. The $\lambda_{em\ max}$ also showed a blue shift for NBD-I111C relative to NBD-T24C, confirming right topology of Tim23 reconstituted into NDs.

3.4 Discussion

The TIM23 complex is an extraordinarly versatile machinery. Eleven subunits of the complex have so far been identified, a number that has seen a steady rise over the past decade. Even with eleven subunits, only three integral membrane proteins, Tim23, Tim17, and Tim50 define the core of the complex. Besides forming an intra-protein interactive network, the subunits are also known to make extensive contacts with protein components outside the TIM23 complex. For example, the IMS-facing domains of Tim23, Tim50 and Tim21 are known to interact with Tom22 of the outer membrane translocase machinery, contributing to the initial stages of preprotein translocation **(Chacinska et al., 2010; Shiota et al., 2011; Tamura, et al., 2009b)**. The importance of TIM23 contacts with the OM is also highlighted by a recent finding that the presequence translocase is involved in the biogenesis of OM proteins **(Song et al., 2014; Wenz et al., 2014)**. Closer to its native protein-rich mitochondrial inner membrane, the complex is known to be in a close association with the respiratory chain complexes III and IV, which is presumed to help the protein import process under low $\Delta\Psi_m$ conditions **(Dienhart & Stuart, 2008; Mick et al., 2012; van der Laan et al., 2006; Wiedemann et al., 2007)**. A recent study also identified that the IM ADP/ATP carrier associates with the presequence translocase in a 1:1 ratio **(Mehnert et al., 2014)**. From the matrix side, the core subunits of the translocase machinery associate with presequence associated motor (PAM) complex to carry out the process of protein transport across the IM **(Schulz & Rehling, 2014; Ting et al., 2014)**. Finally, the TIM23 complex cooperates with Oxa1 machinery for integration of multispanning membrane proteins into the IM **(Bohnert et al., 2010)**.

Most of the interactions described above have been characterized within the context of the highly complex mitochondrial environment, obscuring information about residue-level contacts forged directly between different subunits, and the role played by various mitochondrial components in mediating those interactions. On the other hand, reconstitution-based *in vitro* procedures have been employed successfully to investigate not only membrane protein dynamics, but also various cellular processes. Nanodiscs are nanoscale bilayers that have been employed extensively to study integral membrane proteins **(Chapter 2 of this study)**. In this chapter, we describe an efficient way of reconstituting the central component of the TIM23 complex, Tim23, into nanoscale bilayers, providing an opportunity to characterize Tim23 interactome in a native-like membrane bilayer environment. We show that cell-free translated Tim23 can be incorporated into nanodiscs in both co-translational and post-translational manner and assumes a proper topology upon reconstitution. Moreover, by performing Tim23 reconstitution in the presence of only lipids, we show that co-isolation of Tim23 is strictly dependent on the presence of the scaffolding protein involved in the formation of nanodiscs.

3.5 Materials and Methods

For details, refer to Appendix A

Chapter 4

Cardiolipin-Mediated Interactions of the Mitochondrial Presequence Translocase Channel and Receptor

Derived from: Malhotra K., Nangia S., Daman T., Robinson V., Mokranjac D., May E., and Alder N.N. (*in preparation*) Cardiolipin-mediated interactions of the mitochondrial presequence translocase channel and receptor.

4.1 Abstract

Tim50, a component of the core machinery of the TIM23 complex, is involved in the early stages of recognition and transport of preproteins in the mitochondrial inner membrane. The intermembrane space-facing domain of Tim50 ($Tim50^{IMS}$), together with the intrinsically disordered Tim23 N-terminus ($Tim23^{IMS}$), constitutes the presequence recognizing receptor complex. The $Tim50^{IMS}$ is also known to interact with a channel-facing transmembrane segment of Tim23, but how the soluble receptor domain binds to the membrane-embedded channel remains poorly understood. Moreover, there is no information on the effect of the lipid composition of the mitochondrial inner membrane (IM) on the interaction between Tim50 and the individual domains of Tim23. By combining crosslinking and fluorescence-based approaches *in organello* and in model-membrane systems, we uncover the role of the IM-resident phospholipid, cardiolipin, in mediating site-specific interactions between Tim50 and Tim23. Moreover, we show that the IMS domain of Tim50 has an inherent affinity for CL-containing membrane bilayers. Additionally, by performing small-angle X-ray scattering analysis, we also generate the first envelope structure of the full-length $Tim50^{IMS}$. By allowing investigation of the two central components of the TIM23 complex using a wide array of systems and solution-based biophysical techniques, this study offers novel insights into the early stages of preprotein translocation in mitochondria.

4.2 Introduction

The proteomic pool of mitochondria is comprised of ~1000 proteins in yeast and ~1500 proteins in humans. Almost 99% of these proteins are encoded in nuclear DNA, translated on cytosolic ribosomes, and then targeted to one of the four specialized mitochondrial subcompartments: the outer membrane (OM), the inner membrane (IM), the intermembrane space (IMS), and the matrix **(Chacinska et al., 2009; Dolezal et al., 2006; Harbauer et al., 2014; Mokranjac & Neupert, 2010; Neupert & Herrmann, 2007; van der Laan et al., 2010)**. The sorting of such a large volume of proteins requires the coordinated action of multiprotein complexes, including the membrane-associated Translocase of the Outer Mitochondrial Membrane (TOM) complex of the OM, and the Translocase of the Inner Mitochondrial Membrane (TIM) complexes of the IM **(Neupert & Herrmann, 2007)** (**Figure 1.1-1.2**).

The TIM23 complex of the IM is mainly involved in the biogenesis of preproteins carrying an amphipathic targeting presequence at the N-terminus, either laterally inserting them into the IM or transporting them across the lipid bilayer into the matrix **(Mokranjac & Neupert, 2010)**. The transport function of the TIM23 complex is largely dependent on the presence of the membrane potential ($\Delta\Psi_m$) across the IM that drives the translocation of positively charged presequences and activates the voltage-gated channel **(Alder et al., 2008a; Bauer et al., 1996; MALHOTRA et al., 2013)**. Additionally, the transport of the matrix-targeted soluble proteins requires the action of the ATP-coupled PAM (Presequence translocase Associated Motor) complex, on the

matrix side of the IM **(Lytovchenko et al., 2013; Marom et al., 2011b; Popov-Čeleketić et al., 2008; Schulz & Rehling, 2014; Ting et al., 2014)**. The TIM23 complex is composed of five integral membrane proteins: Tim23, Tim50, Tim17, Mgr2 and Tim21, of which Tim23 functions as the central component and forms a part of the protein-conducting channel **(Gebert et al., 2012; Ieva et al., 2014)** (**Figure 1.2**). The heterogeneous architecture of Tim23 allows it to assume different roles to carry out preprotein transport. The intrinsically disordered N-terminus in the IMS ($Tim23^{IMS}$), along with the soluble domain of Tim50 ($Tim50^{IMS}$) forms the receptor complex to recognize the presequence of the TIM23 complex preproteins **(Gevorkyan-Airapetov et al., 2009; la Cruz et al., 2010; Mokranjac et al., 2009; Tamura et al., et al., 2009b)**. This $Tim23^{IMS}$-$Tim50^{IMS}$ interaction is likely mediated by a coiled-coil interaction between in the two IMS domains. Indeed, specific mutations in the predicted heptad leucine repeat regions of the $Tim23^{IMS}$ and $Tim50^{IMS}$ are known to abrogate Tim23-Tim50 interaction **(Gevorkyan-Airapetov et al., 2009; Tamura, et al., 2009b)**. After precursor recognition by the $Tim23^{IMS}$-$Tim50^{IMS}$ receptor complex, the preproteins are then directed to a substrate- and voltage- sensitive IM channel formed in part by the membrane-bound C-terminus of Tim23, comprising transmembrane segments (TMSs) 1-4 **(Alder et al., 2008a; MALHOTRA et al., 2013; Truscott et al., 2001)**. Both TMS1 and TMS2 have been shown to be important for the structural integrity of the TIM23 complex **(Demishtein-Zohary et al., 2015; Pareek et al., 2013)**. Moreover, both TMS1 and TMS2 are also known to interact with the incoming preproteins, where TMS2 was shown to face the protein-conducting IM channel **(Alder et al., 2008a; Pareek et al., 2013)**. Additionally, TMS1 is known to interact with $Tim50^{IMS}$ **(Alder et al., 2008b)**.

Tim50^{IMS} also plays a regulatory role in gating the Tim23 channel, although its molecular mechanism remains unknown **(Meinecke, 2006)**.

Mitochondrial lipidome is known to influence the structure and function of protein complexes residing in the two mitochondrial membranes **(Böttinger et al., 2015; Gebert et al., 2011; Gohil, 2004; Horvath & Daum, 2013; Osman et al., 2011)**. Cardiolipin (CL) is a structurally unique anionic phospholipid of mitochondria and plays an important role in mitochondrial protein biogenesis of proteins of the mitochondrial membranes **(Brandner et al., 2005; Claypool & Koehler, 2012; N. Gebert et al., 2009; Schlame et al., 2000)**. CL is also involved in efficient functioning of numerous other mitochondrial processes, including oxidative phosphorylation, maintaining cristae morphology, mitochondrial fission and fusion, protein import, and apoptosis **(Baile, et al., 2014b; Claypool & Koehler, 2012; Jiang et al., 2000; Kutik et al., 2008; Tamura et al., 2006; Tamura et al., 2009a)**. It has been shown that functional reconstitution of TIM23 in proteoliposomes requires the presence of CL **(van der Laan et al., 2007)**. Additionally, the presence of CL is important for the stability of the TIM23 translocase and its association with the PAM machinery **(Gallas et al., 2006; Kutik et al., 2008; Tamura et al., 2006; Tamura et al., 2009a)**. Moreover, CL has also been shown for lipid bilayer interactions of both the matrix-exposed C-terminal domain of Tim44, as well as the IMS facing soluble domain of Tim23 **(Bajaj et al., 2014b; Marom et al., 2009; Weiss et al., 1999)**.

In this study, we looked at the role of CL in membrane association of Tim50 and the implication this has for its interaction with Tim23. By performing site-specific chemical crosslinking both *in organello* and in model-membrane systems, we demonstrated that the presence of CL is required for regulating interactions between Tim50 and Tim23. *In vitro* liposome binding experiments with the receptor domain of Tim50 further revealed inherent affinity of the $Tim50^{IMS}$ for CL-containing membrane bilayers. Furthermore, we also generated an *ab initio* small-angle X-ray scattering (SAXS) solution structure of $Tim50^{IMS}$, to which a homology model for the full-length $Tim50^{IMS}$ was aligned. This $Tim50^{IMS}$ homology model was then used to perform *in silico* analysis of the $Tim50^{IMS}$-CL interaction. Taken together, these results provide mechanistic and molecular insights into the role of CL in regulating the interaction between the Tim50 receptor and the channel region of Tim23, thus regulating the early stages of pre-protein translocation.

4.3 Results

Cardiolipin-Regulated Interactions Between Tim50 and Tim23 In Organello

To probe the role played by CL in mediating Tim23-Tim50 interaction in detail, we employed a previously developed chemical crosslinking-based approach **(Alder et al., 2008b)** wherein *in vitro* translated [^{35}S]Tim23 monocysteine mutants ([^{35}S]Tim23C) were imported into mitochondria isolated from yeast strain YPH499 deficient in specific steps of the CL biosynthesis and remodeling pathway (provided by Prof. D. Mokranjac,

LMU, Munich). It has been amply demonstrated that by this approach *in vitro* translated Tim23 can properly integrate into the mitochondrial IM and assemble with endogenous TIM23 complex subunits **(Alder et al., 2008a; Alder et al., 2008b; Dekker et al., 1997)**. Using limited proteolysis as a diagnostic tool **(Alder et al., 2008b; Davis et al., 1998; Demishtein-Zohary et al., 2015)**, we first checked the import and integration of wild-type [^{35}S]Tim23 ([^{35}S]Tim23wt) into mitochondria with altered CL composition and compared it against mitochondria with a normal CL background. Mitochondria from yeast lacking cardiolipin synthase (*Δcrd1*) are devoid of CL and have increased concentration of its biosynthetic precursor, phosphatidylglycerol (PG). Mitochondria from yeast lacking CL-specific deacylase (*Δcld1*) contain unremodeled CL with acyl chains more saturated and heterogeneous compared to remodeled CL. And mitochondria from yeast lacking the transacylase tafazzin (*Δtaz1*) contain CL that is at a decreased concentration and contain unremodeled acyl chain composition, as well as accumulation of remodeling intermediate monolysocardiolipin (MLCL) (**Figure 1.6**). Under fully energized conditions and intact mitochondria, [^{35}S]Tim23wt showed almost equal protection against externally added Proteinase K for all the strains tested (**Figure 4.1**, lanes 2,7,12 and 17), confirming its import. When the OM was disrupted by hypotonic swelling prior to proteinase K digestion (yielding “mitoplasts”), imported [^{35}S]Tim23wt in all the strains displayed a protected fragment (~13-kDa) corresponding to the IM-bound region of Tim23 **(Alder et al., 2008b; Demishtein-Zohary et al., 2015)** (**Figure 4.1**, lanes 3,8,13 and 18), confirming the proper integration of [^{35}S]Tim23 into the IM irrespective of the CL background.

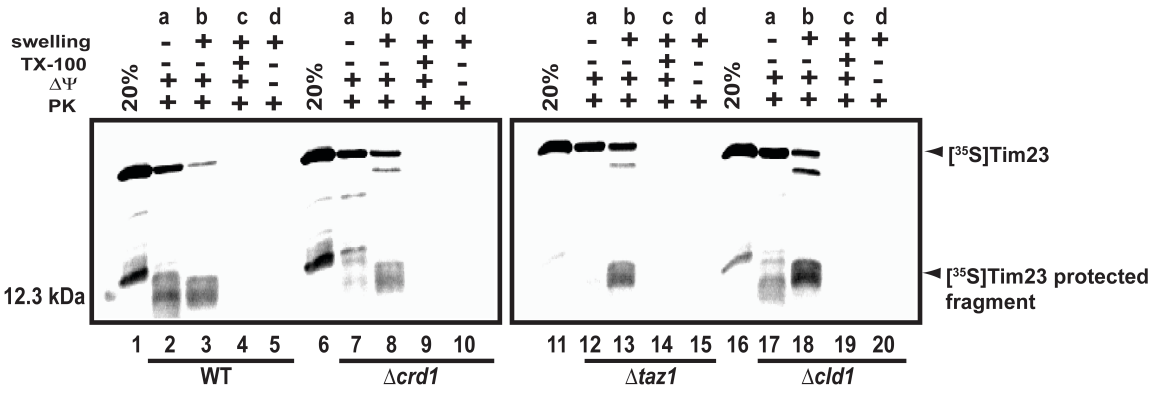

Figure 4.1 *Import and Membrane Integration of Tim23*

Wild-type [^{35}S]Tim23 incubated with mitochondria isolated from *S. cerevisiae* with different CL backgrounds [Wild-type (WT), Δ*crd1*, Δ*taz1*, and Δ*cld1*), was subjected to proteinase K treatment under energized conditions as follows: a. addition of protease to intact mitochondria (lanes 2,7,12 and 17), b. addition of protease to mitochondria treated with hypotonic media to generate mitoplasts with no OM ("swelling", lanes 3,8,13 and 18). Mitoplasts treated with proteinase K will give rise to a membrane-protected fragment (~13-kDa) as an indication of proper integration of Tim23 into the IM. c. Detergent Triton X-100 was used to solubilize the membranes after protease treatment ("TX-100", lanes 4,9,14 and 19). d. As a control for Tim23 import and membrane integration, $\Delta\Psi_m$ was dissipated using 1 μM valinomycin prior to protease treatment to intact mitochondria ("-$\Delta\Psi_m$", lanes 5,10,15 and 20).

Next, we used site-specific thiol-thiol chemical crosslinking to analyze the interaction between different [^{35}S]Tim23 monocysteine variants and endogenous Tim50, which in yeast has a single encoded cysteine at position 268. Drawing from our Tim23 monocysteine mutant library, we specifically looked at the interactions of Tim50 with the receptor domain (Tim23^{IMS}) as well as the channel-facing TMSs (TMS1 and TMS2) of Tim23 in different CL backgrounds (**Figure 4.2A**). Using the same approach, Tim50 was previously shown to interact with the Tim23^{IMS} and TMS1 of Tim23 **(Alder et al., 2008b)**. The Y70 and L71 residues on the heptad leucine repeat motif of Tim23^{IMS} are

known to be critical for mediating Tim23-Tim50 interaction, where mutating them both to alanine blocks the Tim23-Tim50 interaction **(Gevorkyan-Airapetov et al., 2009)**. Therefore, we also analyzed the effect of mutating those residues on the crosslinking-detected interaction between different Tim23 regions and Tim50 by our crosslinking-and IP-based approach. In mitochondria with a normal CL background, the IMS domain of [^{35}S]Tim23 with cysteine at position 80 formed two crosslinked adducts: a prominent band at ~97-kDa and a weaker band at ~70-kDa that likely represents proteolysis product (**Figure 4.2B**, lane 1). Both adducts were confirmed to be crosslinked [^{35}S]Tim23 and Tim50 using anti-Tim50 antibodies (**Figure 4.2B**, lane 9), as has been reported earlier **(Alder et al., 2008b)**. Mutating residues Y70 and L71 on Tim23^{IMS} to alanine (YL mutant), abrogated interaction with Tim50 (**Figure 4.2B**, lanes 2 and 10), as has been shown earlier **(Gevorkyan-Airapetov et al., 2009)**. Interestingly, the loss of cardiolipin synthase (Crd1p) as well as cardiolipin remodeling enzymes, Taz1p and Cld1p, resulted in an increase in interaction between the two receptor domains compared to mitochondria with a normal CL background (**Figure 4.2B**, compare lane 1 with lanes 3, 5 and 7 and compare lane 9 with lanes 11, 13 and 15). In Tim23 constructs containing the YL mutations, the interaction between Tim23^{IMS} and Tim50 was extremely low, regardless of the CL composition (**Figure 4.2B**, compare lane 2 with lanes 4, 6 and 8 and compare lane 10 with lanes 12, 14 and 16).

Crosslinking-based analysis of the interaction between Tim50^{IMS} and TMS1 and TMS2 of Tim23 (**Figure 4.2C**) revealed that Tim50 potentially interacts with specific faces of each transmembrane helix (**Figure 4.2D**). Henceforth, residue F114C of TMS1 and residue A156C of TMS2 were used to represent the channel-facing TMSs to probe their interaction with Tim50 in different cardiolipin mutant strains in the presence and absence of Tim23 YL mutations. Interestingly, we found that as compared to almost no interaction seen between Tim50 and Tim23^{IMS} YL mutant, Tim50 maintained its interaction with the channel facing TMSs even in the presence of mutations in the coiled-coil region (**Figure 4.2E**, lanes 2 and 10, compare with lanes 2 and 10 of **Figure 4.2B**), albeit with less efficiency (**Figure 4.2E-F**; **Figure 4.2H-I**). When we characterized the interaction of Tim50 with the TMS1 in CL compromised strains, we found that CL deficient (Δ*crd1*) mitochondria displayed less crosslinking efficiency with Tim50 in comparison with wild-type Tim23 (**Figure 4.2E**, lane 3; **Figure 4.2H**). When the Tim23 YL mutant was introduced, there was even further decrease in interaction between Tim50 and TMS1 of Tim23 as compared to wild-type CL-containing mitochondria (**Figure 4.2E**, compare lanes 2 and 4; **Figure 4.2H**), pointing to the important role played by CL in mediating contact between Tim50 and the channel facing TMS1. Similar results were obtained with Tim23 YL mutant in mitochondria isolated from the Δ*taz1* strain with an up-regulated MLCL content and general decrease in CL content (**Figure 4.2E**, compare lanes 4 and 6; **Figure 4.2H**). Mitochondria with unremodeled CL isolated from the Δ*cld1* strain showed Tim23-Tim50 crosslinking efficiency similar to that of wild-type mitochondria (**Figure 4.2E**, compare lanes 7 and 8 with lanes 1 and 2; **Figure 4.2H**). This is not surprising considering both unremodeled and remodeled CL

have been shown to be functionally indistinguishable in yeast **(Baile et al., 2014b)**. Abnormal CL content in *Δcrd1* and *Δtaz1* strains caused Tim50 –TMS2 interaction defects as well (**Figure 4.2F**, lanes 9-16; **Figure 4.2I**). Overall, the results indicate that *in organello*, compromising CL content or composition affects Tim50's interaction with Tim23 in a site-specific manner.

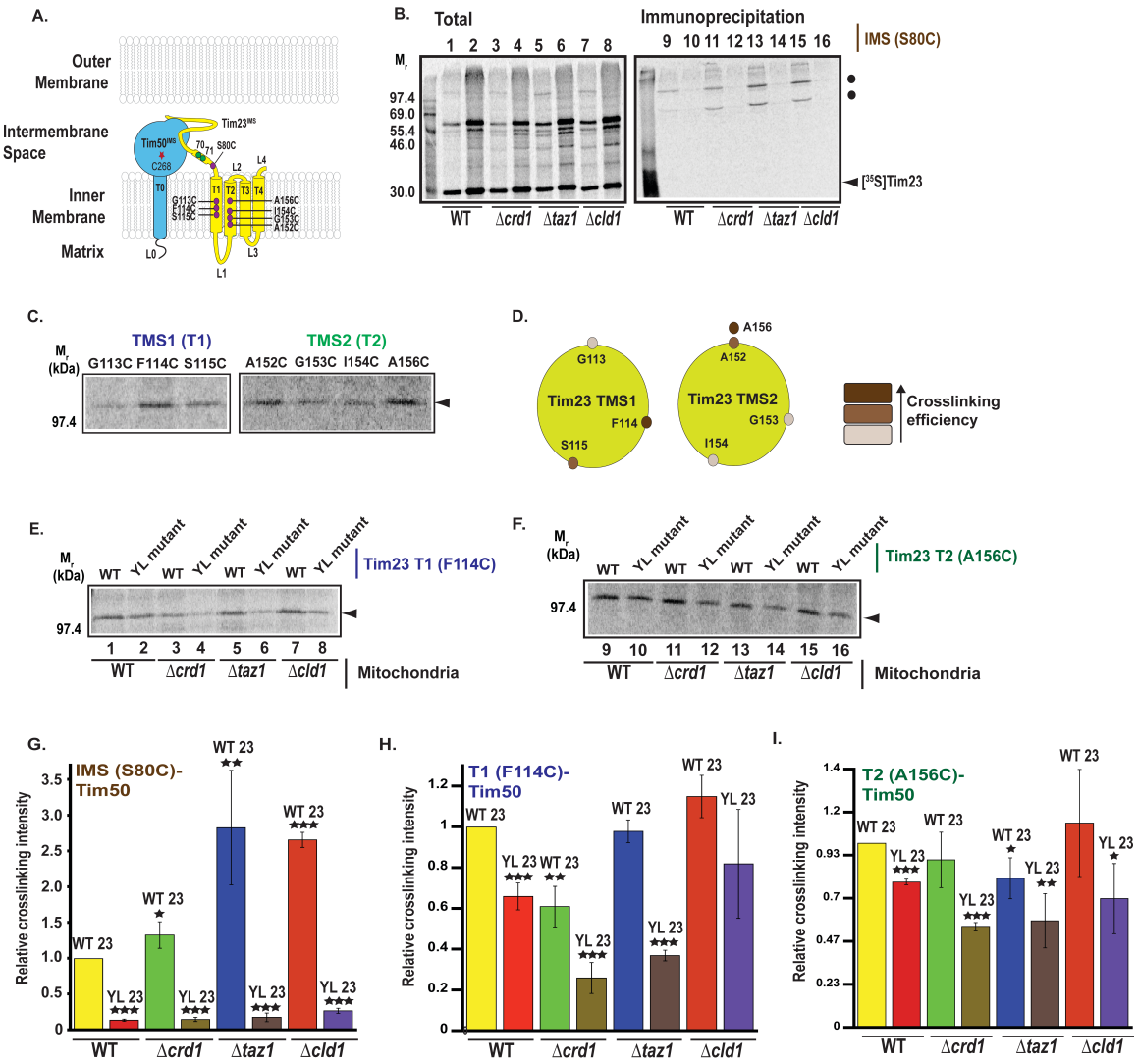

Figure 4.2 *Crosslinking-Based Analysis of Tim23-Tim50 Interactions In Organello*

A. *Topology diagram of Tim23 and Tim50 in the IM*. Tim50 (blue) contains a C-terminus soluble domain (Tim50^{IMS}) with a single TMS (T0) and a matrix-facing region (L0). Tim23 (yellow) contains an IMS-facing domain (Tim23^{IMS}) and a membrane bound C-terminus with 4 TMSs (T1-T4), and matrix-and IMS-facing loops (L1-L4). Cysteines introduced at specific sites in Tim23 are depicted as circles (magenta), and that used for crosslinking with a single encoded cysteine of Tim50 (red asterisk). The Y70 and L71 residues in the Tim23^{IMS} are highlighted as green circles.
B. *Crosslinking and immunoprecipitation (IP)-detected interaction between Tim23 and Tim50*. [^{35}S]Tim23(S80C) and [^{35}S]Tim23(S80C) Y70A L71A mutants imported into mitochondria isolated from yeast strain YPH499 with varying CL backgrounds were probed for their proximity to the cysteine at position 268 in Tim50 using a thiol-reactive chemical crosslinker BMOE (50 μM). Mitochondria isolated from baker's yeast with a

normal cardiolipin (CL) biosynthesis pathway ("WT"), or with a defective biosynthesis pathway with no cardiolipin synthase ("*Δcrd1*"), no CL-specific deacylase ("*Δcld1*"), and no transacylase ("*Δtaz1*") were used. Different crosslinked products were detected by running the crosslinked samples on SDS-PAGE followed by autoradiography ("Totals", lanes 1-8). The Tim23-Tim50 crosslinked adduct was detected by immunoprecipitation (IP) using polyclonal anti-mouse antibodies against Tim50 ("Immunoprecipitation", lanes 9-16). Crosslinked adducts detected by immunoprecipitation are indicated by black circles.
C. Crosslinking-and IP-detected interaction between Tim50 and [^{35}S]Tim23 channel-facing TMSs, T1 (left) and T2 (right)
D. Helical wheel representation of Tim23 TMS1 and TMS2 showing all cysteine substitutions used in T1 and T2 for crosslinking with Tim50 (left). Crosslinking efficiency of different residues to Tim50 is ranked as indicated (right).
E. and F. *CL-regulated interaction between Tim50 and the channel region of Tim23*. Crosslinking-and IP-detected interaction between Tim50 and [^{35}S]Tim23 T1 (F114C), and T2 (A156C) ["WT 23"] and the corresponding Y70A L71A mutant ("YL 23"), in mitochondria with different CL backgrounds.
G., H., and I. Quantification of IP-detected crosslinking efficiency between Tim50 and [^{35}S]Tim23 S80C (B.) F114C (E.), and A156C (F.) respectively, in mitochondria with different CL backgrounds. Crosslinked adduct between [^{35}S]Tim23C and Tim50 in wild-type ("WT") CL background was used as control to normalize values, with standard deviations from 3 independent experiments.
The asterisks on the bar graphs indicate a significant difference from the corresponding control experiment (WT Tim23, WT mitochondria) by student's t-test. *$p < 0.05$; **$p < 0.01$; ***$p < 0.0001$

Cardiolipin Mediates a Direct Effect on the Tim23-Tim50 Interaction

To investigate the direct role of CL, and to rule out any secondary effects of mutations in the CL biosynthesis pathway on Tim23-Tim50 interaction, we recapitulated the interactions of the IM *in vitro* using the model-membrane system, nanodiscs (ND) (**Figure 4.3A**). ND are nanoscale discoidal bilayers surrounded by an amphipathic belt of membrane scaffolding protein (MSP), and are widely used as the model membrane of choice to investigate the functional dynamics of membrane proteins (**MALHOTRA &**

Alder, 2014). In this study, we used ND to reconstitute Tim23 in its entirety to make Tim23 amenable to solution-based experiments (*e.g.* crosslinking) and to reconstitute Tim23 in a desired lipid environment. ND-containing 1-palmitoyl-2-oleoyl-*sn*-glycero-3-phosphocholine or POPC (ND_PC) as the sole bilayer forming lipid were used to functionally reconstitute *in vitro* translated [^{35}S]Tim23 as described in **Chapter 3**. As initial tests to probe the accessibility of cysteine sites in different positions of Tim23 reconstituted into ND, we analyzed modification of different sites with the membrane impermeant thiol-reactive probe (Methyl-PEG_{12})$_3$-PEG_4-Maleimide [$TMM(PEG)_{12}$] **(Figure 4.4A)**. Analysis of substituted cysteine accessibility using thiol-specific chemical reagents is a widely used technique to study the topology of membrane proteins **(Bogdanov et al., 2005)**, as well as to map membrane-spanning segments that line an aqueous channel **(Liapakis et al. 2001)**. As mentioned, both TMS1 and TMS2 of Tim23 are known to interact with translocating TIM23 substrate polypeptide, where TMS2 has been experimentally shown to face the protein-conducting channel in the IM **(Alder et al., 2008a)**. Moreover, using cysteine substitution methodology, specific sites within the same membrane-spanning segments were shown to be partially reactive to a thiol-active reagent, 4-acetamido-4'-[(iodoacetyl)amino] stilbene-2,2'-disulfonic acid (IASD), under fully-energized conditions in mitochondria **(Alder et al., 2008b; MALHOTRA et al., 2013)**. The reactivity of cysteines positioned in the aqueous-facing Tim23 N-terminus (S80C) in ND_PC towards $TMM(PEG)_{12}$ displayed a slow migrating labeled product on SDS-PAGE and ~65% labeling efficiency (**Figure 4.4A**, lane 4). As negative controls, upon pretreatment with the reducing agent dithiothrietol (DTT) (**Figure 4.4A**, lane 3), or using Tim23 with no cysteine (Δcys) (**Figure 4.4A**, lane 2), no modified

[^{35}S]Tim23 was observed confirming the specificity of this reaction. Interestingly, probing the reactivity of different cysteine-substituted sites in the various membrane-spanning segments of Tim23-ND_PC towards TMM(PEG)$_{12}$, showed enhanced labeling of all the three sites in TMS1 compared to TMS2 and TMS4 (**Figure 4.4A**, compare lanes 6, 8 and 10 with lanes 12, 14, 16 and 18, **Figure 4.4B**). The labeling efficiency of different sites in TMS1 were, however, significantly lower than the water-facing IMS segment of Tim23 (**Figure 4.4A**, compare lane 4 with lanes 6, 8 and 10, **Figure 4.4B**). These results support conclusions available from a previous report where sites I111C and F114C of TMS1 were found to be partially accessible to the thiol-reactive reagent IASD in active mitochondria **(Alder et al., 2008b)**, consistent with the proposal that TMS1 faces an aqueous-conducting channel. In any case, by using cysteine-accessibility methodology, we confirm that the topology of Tim23 reconstituted into ND_PC resembles that of the IM.

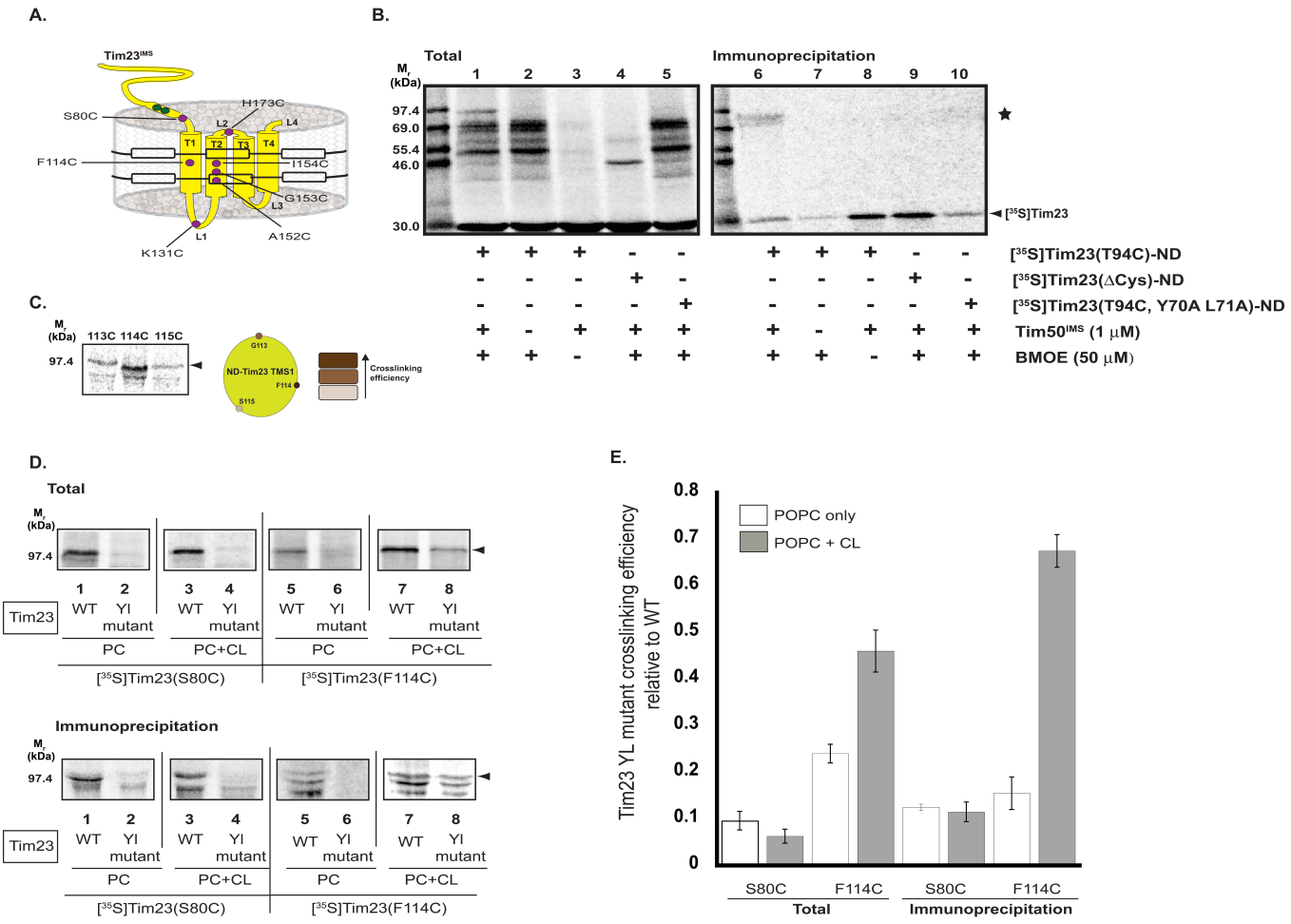

Figure 4.3 *Cardiolipin-Mediated Tim23-Tim50 Interactions*

A. *Topology diagram of Tim23-ND*. Tim23 reconstituted into ND (yellow) with indicated cysteine positions used for crosslinking-based proximity analysis to the cysteine at position 268 in the Tim50^{IMS} (blue). The cysteines used for crosslinking analysis are depicted as circles (magenta). The Y70 and L71 residues are depicted as green circles.

B. *Crosslinking and IP-detected interaction between Tim23-ND and Tim50*. Tim50^{IMS} crosslinked to [^{35}S]Tim23(T94C) in POPC nanodiscs (PC_ND) (lanes 1 and 6) with control reactions: (i.) no Tim50^{IMS} (lanes 2 and 7) (ii.) no crosslinker (lanes 3 and 8) (iii.) with [^{35}S]Tim23(ΔCys)-ND_PC (lanes 4 and 9), and (iv.) with [^{35}S]Tim23(T94C) Y70A L71A-ND_PC (lanes 5 and 10). The crosslinked adduct between [^{35}S]Tim23 and the Tim50^{IMS} is indicated by an asterisk, where position of [^{35}S]Tim23 band is indicated by an arrowhead.

C. Crosslinking-and IP-detected interaction between the Tim50^{IMS} and [^{35}S]Tim23 channel-facing TMS1 (T1) in PC_ND (left). The crosslinked adduct between [^{35}S]Tim23 and the Tim50^{IMS} is indicated by an arrowhead. Helical wheel representation of Tim23 showing all cysteine substitutions used in T1 for crosslinking with the Tim50^{IMS} (right). Crosslinking efficiency to the Tim50^{IMS} is ranked as indicated (right).

D. Crosslinking-and IP-detected interaction between the Tim50^{IMS} and [^{35}S]Tim23(S80C and F114C) ["*wt*"] and [^{35}S]Tim23(S80C and F114C, Y70A L71) ["*yl*"] constructs in PC_ND ("PC") or POPC + cardiolipin ("PC+CL") ND background. The crosslinked adduct between [^{35}S]Tim23 and the Tim50^{IMS} in "Total" and "Immunoprecipitation" samples is indicated by an arrowhead

E. Quantification of crosslinked adduct between the Tim50^{IMS} and [^{35}S]Tim23-ND "yl" mutant construct relative to the "wt" construct in PC and PC+CL ND background as shown in D. The standard deviations shown are from three independent experiments.

Tim50^{IMS} has been shown to support all the functions of the full-length Tim50 *in vivo* **(Mokranjac et al., 2009)**. To check whether Tim23-ND is capable of interacting with Tim50 in a physiologically relevant manner, crosslinking reactions of [^{35}S]Tim23(T94C)-ND_PC, bearing a single cysteine at position 94 of the Tim23^{IMS} domain, were carried out in the presence of recombinantly expressed Tim50^{IMS} (**Figure 4.4C**). Similar to the crosslinking-based interaction seen *in organello*, there was a formation of crosslinked adduct of ~97-kDa between the two IMS domains (**Figure 4.3B,** lanes 1 and 6). Negative control reactions with (i.) no Tim50^{IMS}, (ii.) no crosslinker, (iii.) [^{35}S]Tim23(ΔCys), and (iv.) [^{35}S]Tim23(T94C) Y70A L71A did not show any crosslinked product, demonstrating the specificity of the Tim23-Tim50 interactions in our ND system (**Figure 4.3B,** lanes 2-5 and lanes 7-10). Similar to the Tim50^{IMS} interaction with cysteine at position 94, Tim23 with cysteine at position 80 displayed interaction with Tim50^{IMS} (**Figure 4.3D**, lane 1, Total and Immunoprecipitation), and mutating Y70 and L71 residues on the heptad leucine repeat motif to alanine abrogated its proximity to the

Tim50^{IMS} (**Figure 4.3D**, lane 2, Total and Immunoprecipitation). [^{35}S]Tim23-ND_PC also supported the interaction between recombinant Tim50^{IMS} and TMS1 of Tim23 (**Figure 4.3C,** left). The helical analysis as performed in ND again identified cysteine at position 114 in TMS1 as the primary interactive site (**Figure 4.3C,** left). Taking position F114C as our representative site for TMS1, we proceeded to look at the effect of incorporating Y70A and L71A mutations on its interaction with the Tim50^{IMS}. However, unlike the intact Tim23 channel-Tim50 interactions seen in the IM even in the presence of Y70A and L71A mutations, incorporation of the same mutations in Tim23 showed much less of an interaction between the channel-facing TMS1 and Tim50^{IMS} in POPC-containing ND environment (**Figure 4.3D**, lane 6, Total and Immunoprecipitation; **Figure 4.3E**). Moreover, probing different sites on TMS2 for their proximity to the Tim50^{IMS} in ND_PC yielded no signs of crosslinking-based interaction, as opposed to the interaction of channel-facing sites (A152C and A156C) with Tim50 seen *in organello* (**Figure 4.4E**, upper panel). Additionally, crosslinking-based proximity mapping revealed no interaction between the Tim50^{IMS} and sites on the IMS- and matrix-facing Tim23 membrane loop segments in ND_PC (**Figure 4.4F**, upper panel).

To check the direct effect of CL on the Tim23-Tim50 interactions, we incorporated tetraoleoyl cardiolipin (TOCL, 18:1), henceforth to be named as just CL, at physiological concentration of 20 mol% to our ND system (ND_CL). Incorporation of [^{35}S]Tim23 into ND_CL did not affect its elution profile or change the amount of [^{35}S]Tim23 incorporated into ND_CL compared to ND_PC as judged by the purified [^{35}S]Tim23 band on SDS-PAGE (**Figure 4.4D**, compare upper panel with the lower panel). Moreover, crosslinking reactions of [^{35}S]Tim23(S80C)-ND_CL did not change

the interaction of Tim23 with the Tim50^{IMS} compared to our ND_PC system even in the presence of Y70A and L71A mutations (**Figure 4.3D**, compare lanes 3 and 4 with lanes 1 and 2, Total and Immunoprecipitation; **Figure 4.3E**). However, addition of CL to our ND system restored the physiological interaction seen between [^{35}S]Tim23(F114C) and Tim50 in the presence of Y70A and L71A mutations compared to our ND_PC system (**Figure 4.3D**, compare lanes 7 and 8 with lanes 5 and 6, Total and Immunoprecipitation; **Figure 4.3E**). Moreover, all three sites on TMS2 that tested negative for their interaction with the Tim50^{IMS} in ND_PC, displayed robust interaction with the receptor domain of Tim50 when reconstituted in our ND_CL system, where site A152C displayed the highest proximity to the Tim50^{IMS} (**Figure 4.4E**, compare lower panel with the upper panel). By contrast, the interaction of sites on the IMS- and matrix-facing Tim23 loops with the Tim50^{IMS} in our ND_CL system displayed only a slight change compared to our ND_PC system (**Figure 4.4F**, compare lower panel with the upper panel). Thus, the results from our crosslinking analysis in this reductionist system strongly suggest that CL mediates direct effects on Tim23-Tim50 interactions in a site-specific manner. Specifically, CL seems to stabilize the interaction between Tim50^{IMS} and the transmembrane segments of the Tim23 channel. Stated another way, the results from *in organello* and nanodiscs reactions on Tim23-Tim50 interactions reveal that both the coiled-coil region in the Tim23^{IMS} and CL play an important role in mediating interactions with the Tim50 receptor.

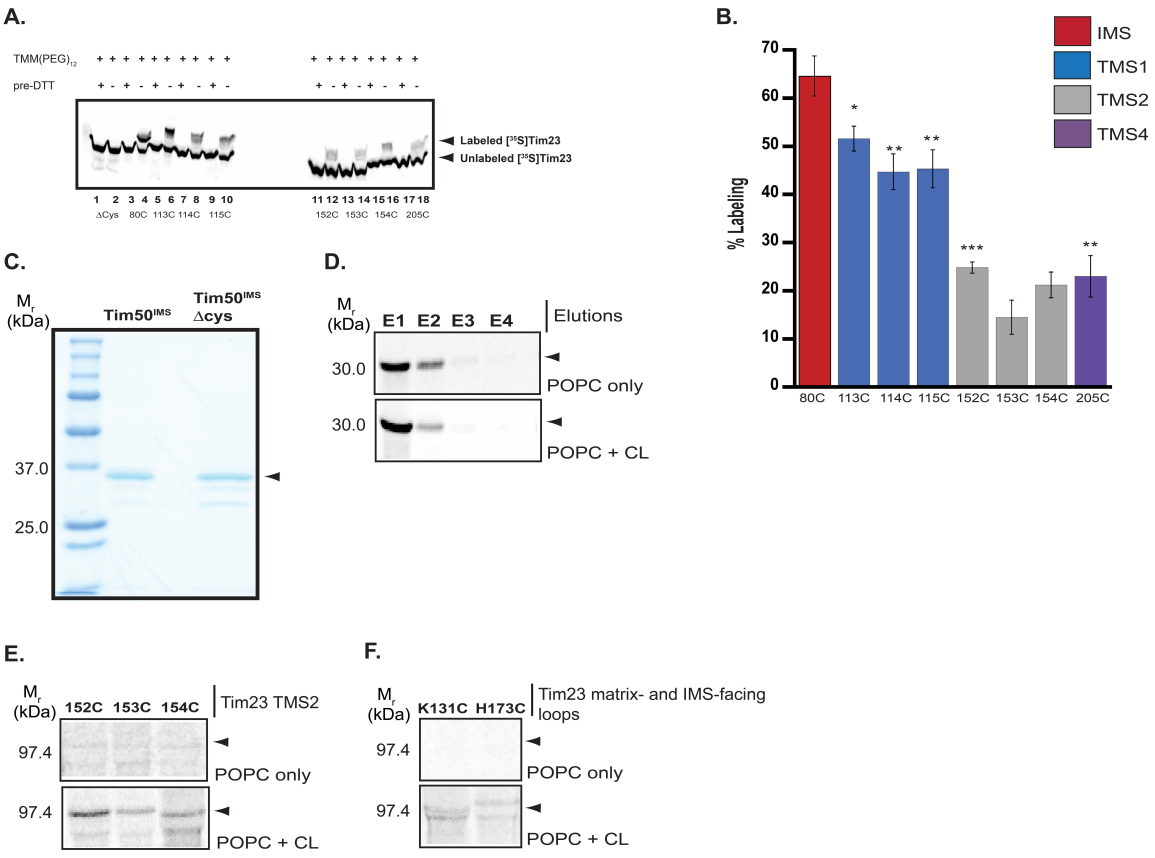

Figure 4.4 *Analysis of Tim23 Reconstituted into Nanodiscs and its Interaction with Tim50^{IMS}*

A. Monocysteine [^{35}S]Tim23 was reconstituted into POPC ND and subjected to site-specific cysteine modifications with the thiol-reactive reagent, TMM(PEG)$_{12}$. TMM(PEG)$_{12}$ is membrane impermeable and reacts with thiol groups exposed to the aqueous environment. [^{35}S]Tim23-TMM(PEG)$_{12}$ conjugates migrate slower on the gel ("labeled [^{35}S]Tim23") than the unconjugated fraction ("unlabeled [^{35}S]Tim23"). Monocysteine Tim23 constructs used include cysteine sites in the IMS (S80C), TMS1 (G113C, F114C and S115C), TMS2 (A152C, G153C and I154C), and TMS4 (V205C). As a control, reactions were exposed to DTT treatment ("pre-DTT") or reactions were carried out with cysteineless Tim23 ("[^{35}S]Tim23Δcys").
B. Amount of labeled [^{35}S]Tim23 as in A. expressed in %. Graph shows normalized values and the average ± SEM of three independent reactions. **p < 0.01, ***p < 0.0001.
C. SDS-PAGE analysis of purified recombinant soluble domain of Tim50 with ("Tim50^{IMS}") and without ("Tim50^{IMS}Δcys") cysteine at position 268. The arrowhead depicts the position of the band of purified product.

D. Elution profile of [^{35}S]Tim23-ND containing POPC or POPC + CL lipids using Ni^{2+}-NTA chromatography.
E. Crosslinking- and-immunoprecipitation detected proximity between $Tim50^{IMS}$ and [^{35}S]Tim23(TMS2) in ND containing POPC or POPC + CL as indicated. The cysteines on Tim23 were positioned at different sites on TMS2 (A152C, G153C and I154C). The crosslinked adduct between [^{35}S]Tim23 and the $Tim50^{IMS}$ is indicated by an arrowhead.
F. Crosslinking- and-immunoprecipitation detected proximity between Tim50IMS and [^{35}S]Tim23 in ND containing POPC or POPC + CL as indicated. The cysteines on Tim23 were positioned at matrix- and-IMS-facing loops (K131C and H173C respectively). The crosslinked adduct between [^{35}S]Tim23 and the $Tim50^{IMS}$ is indicated by an arrowhead.

$Tim50^{IMS}$ Binds to Cardiolipin-Containing Membrane Bilayers

The effect of CL on Tim23-Tim50 interaction prompted us to check whether the $Tim50^{IMS}$ domain has an inherent affinity for binding to CL-containing bilayers. CL is a dimeric phospholipid believed to carry a single negative charge due its resonance-stabilized headgroups **(Kates et al., 1993)**(**Figure 4.5A**), though recent findings from our laboratory strongly suggest that CL is dianionic at physiological pH (**Sathappa and Alder**, *unpublished*). The large surface area occupied by its four acyl chains compared with the cross-sectional area of the two-phosphate head groups gives CL the propensity to form nonlamellar hexagonal II (HII)-phase structures under certain conditions **(Lewis & McElhaney, 2009; Schlame et al., 2000)**. Moreover, the unique physical and chemical properties of CL have been shown to be instrumental in binding of the IMS protein cytochrome c to the IM and facilitating its peroxidase activity **(Bergstrom et al., 2013)**. Co-sedimentation analysis is a widely used technique to study the binding of peripheral membrane proteins to membrane bilayers **(Marom & Azem, 2013)**. In this technique, soluble proteins are assembled with oligosaccharide-loaded vesicles of different diameters and lipid composition, followed by separation of the protein-bound

heavy vesicles from the unbound proteins in supernatant using ultracentrifugation. SDS-PAGE analysis of the pelleted fraction (vesicles + protein) reveals the fraction of protein bound to different vesicles versus the total protein loaded in the reaction. Therefore this assay is an excellent means of testing the ability of different lipids to promote membrane interactions of proteins. Co-sedimentation analysis of $Tim50^{IMS}$ with large unilamellar vesicles (LUVs) of diameter 100 nm having POPC (PC) (**Figure 4.5B**) as the sole lipid showed negligible binding with increasing liposome concentration (**Figure 4.5C-D**). However, when CL was included with PC LUVs at a molar ratio of 20 mol% (**Figure 4.5B**), we observed a robust binding of $Tim50^{IMS}$ to the vesicles (**Figure 4.5C-D**). To address the specificity of CL in recruiting $Tim50^{IMS}$ to vesicles, we incorporated the monoanionic lipid PG instead of CL at the same molar ratio and carried out co-sedimentation analysis. PG (see above), carries a single negative charge on its headgroup and is an important constituent of the IM but actually comprises a low percentage of IM lipids **(Khalifat et al., 2014)**. Incorporation of PG to the LUVs with PC host lipids did improve binding to the $Tim50^{IMS}$ compared to LUVs containing PC alone, but did not show as strong binding to the $Tim50^{IMS}$ as displayed by CL-containing LUVs (**Figure 4.5C-D**). To determine the extent to which ionic interactions contribute to the CL-mediated $Tim50^{IMS}$ interaction with vesicles, we added increasing concentration of NaCl to screen the electrostatic interaction between the $Tim50^{IMS}$ and CL-containing LUVs. The addition of increasing concentration of NaCl in the physiological range showed a slight but not a significant increase in binding of $Tim50^{IMS}$ to CL-containing bilayers. Increasing NaCl concentration beyond the physiological range did affect binding of the $Tim50^{IMS}$ to CL-containing bilayers, but the interaction remained intact

even at high 1 M NaCl concentration (**Figure 4.5E-F**). This suggests that factors other than electrostatic forces might play a role in mediating $Tim50^{IMS}$-CL interaction as seen with cytochrome c **(Muenzner & Pletneva, 2014; Planas-Iglesias et al., 2015)**. To check the extent to which the non-bilayer property of CL might drive $Tim50^{IMS}$ interactions, we incorporated another non-lamellar phase forming phospholipid, POPE (PE), to PC LUVs at a molar ratio of 50 mol%, which is close to its physiological concentration found in the IM of yeast mitochondria **(Schwall et al., 2012)**. Interestingly, the $Tim50^{IMS}$-LUV interaction did not change upon addition of PE (**Figure 4.5C-D**). All these results support the conclusion that the $Tim50^{IMS}$ interacts specifically with vesicles containing CL and underscore a dominant role of headgroup interactions.

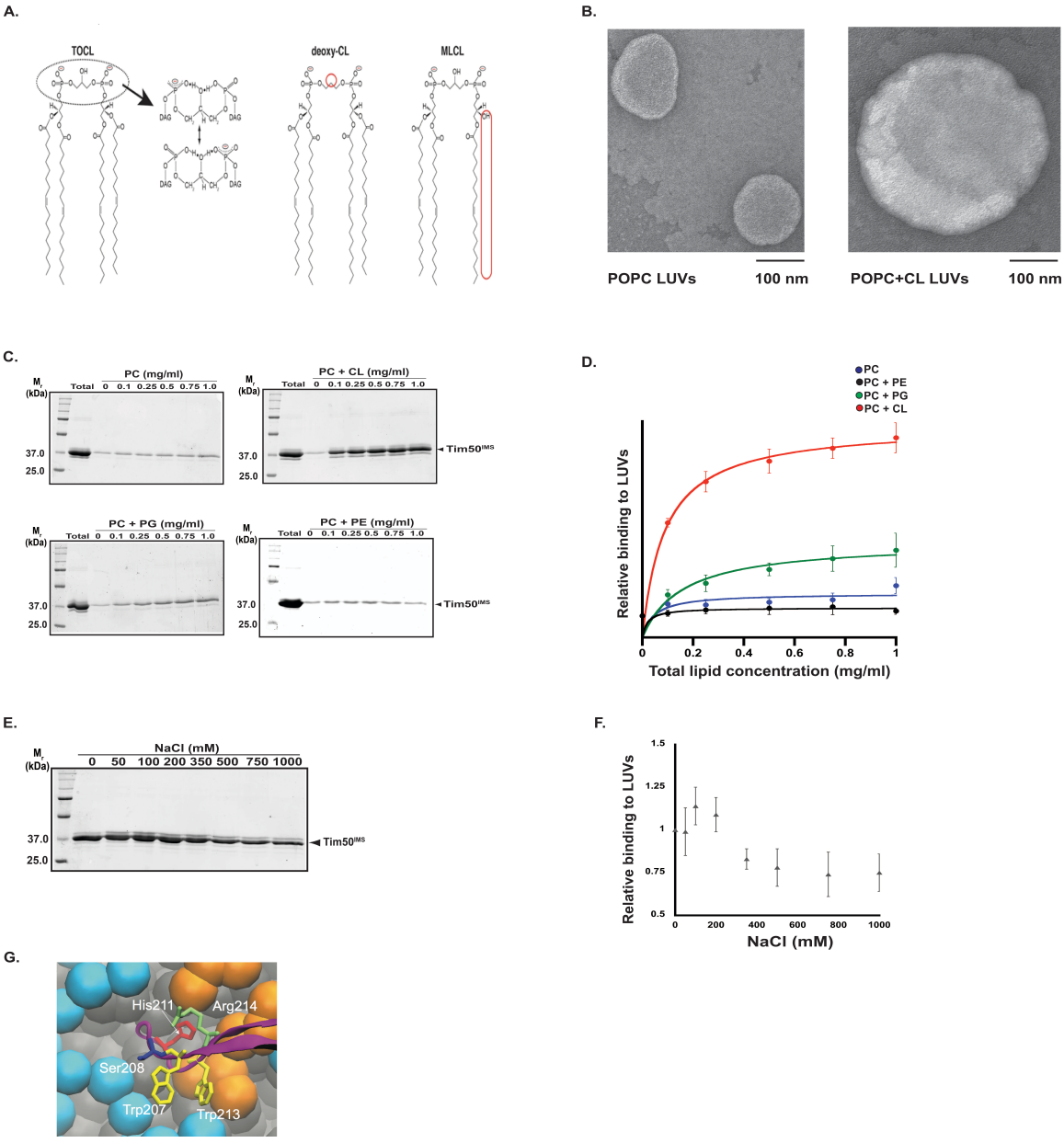

Figure 4.5 *Association of the Tim50^{IMS} with Membrane Bilayers in a Cardiolipin-Dependent Manner*

A. Chemical structures of tetraoleoyl cardiolipin (1',3' –bis[1,2-dioleoyl-*sn*-glycero-3-phospho]-*sn*-glycerol, "TOCL") and its resonance-stabilized bicyclic headgroup showing its one mode of existence, 2'-deoxycardiolipin ("deoxy-cardiolipin"), and monolysocardiolipin ("MLCL").

B. Negative stain transmission electron microscopy images of POPC only and POPC+CL LUVs at 23,000X magnification (scale bar = 100 nm)
C. Co-sedimentation analysis of the $Tim50^{IMS}$ (1 μM) in the presence of different LUVs at the indicated lipid concentration. For making LUVs, POPC was used as host lipid with 20 mol% anionic lipids, POPG and CL, or 50 mol% POPE. Samples were run on SDS-PAGE followed by SYPRO-orange staining. "Total" lane indicates the total amount of $Tim50^{IMS}$ added to each reaction. Stained band of $Tim50^{IMS}$ is indicated by an arrowhead.
D. Relative binding of $Tim50^{IMS}$ plotted as a function of total lipid concentration for LUVs of different lipid composition. Bands were quantified by densitometry based on experiments shown in panel. Data points were fit using nonlinear regression analysis in KaleidaGraph assuming 1:1 binding using the equation: $y=m1x/K_m+x$, where m1=maximum binding intensity, x=available total lipid concentration, y=binding intensity at a given total lipid concentration and K_m=total lipid concentration at ½ maximum binding intensity. The points indicated are averages ($\pm$ SEM) of three independent experiments.
E. Co-sedimentation analysis of $Tim50^{IMS}$ (1 μM) with CL-containing LUVs (0.5 mg/ml) in the presence of indicated NaCl concentration.
F. Relative binding of $Tim50^{IMS}$ plotted as a function of NaCl concentration as in panel D. The points indicated are averages ($\pm$ SEM) of three independent experiments.
G. Coarse-grained molecular dynamics simulation depicting binding of a highly conserved β-hairpin loop of the core domain of the $Tim50^{IMS}$ with a membrane bilayer containing 80 mol% POPC and 20 mol% CL. Beads representing the CL headgroups joined by central glycerol moiety are shown in orange, POPC headgroups are depicted in blue and the acyl chains are shown in gray. CL-binding sites on β-hairpin used to carry out alanine mutations (Trp207, His211, Trp213 and Arg214) and for IANBD labeling (Ser208) are shown as sticks (Figure provided by Prof. Eric May, University of Connecticut).

Coarse-grained molecular dynamics (MD)-based analysis of the interaction between $Tim50^{IMS}$ homology model (see below) and CL-containing membrane bilayers (performed by Prof. Eric May and Dr. Shivangi Nangia, University of Connecticut) strongly suggested the involvement of residues in a highly conserved β-hairpin of the $Tim50^{IMS}$ in mediating interactions with CL head groups and acyl chains (**Figure 4.5G**). To empirically test the membrane binding and insertion activity of the β-hairpin we undertook a fluorescence spectroscopy-based approach wherein a polarity-sensitive

probe was incorporated at the tip of the $Tim50^{IMS}$ β-hairpin. To this end, a $Tim50^{IMS}$Δcys construct was created (**Figure 4.4C**), followed by mutating a relatively less conserved serine at position 208 to cysteine in the loop that connects two β-strands of the $Tim50^{IMS}$ β-hairpin structure. By performing site-specific labeling of S208C using a thiol-reactive IANBD amide, we then incorporated an environment sensitive fluorophore, NBD, and monitored its emission intensity in the presence of LUVs of different lipid composition. The emission intensity of NBD is highly environment sensitive, acting as an excellent reporter for whether the probe is in a nonpolar or aqueous environment. This approach enables one to investigate the membrane binding interactions of specific sites on bilayer-interactive proteins **(Heuck et al., 2000; Johnson, 2005)**. In the presence of CL-containing LUVs, $Tim50^{IMS}$-NBD showed ~2.5X higher emission intensity than it did in the presence of PC-only LUVs (**Figure 4.6A**). Moreover, changes in the maximum fluorescence intensity (F/F_0) of NBD as a function of liposome concentration displayed robust and saturable binding in case of CL-containing vesicles but not with PC-only vesicles (**Figure 4.6B**). Interestingly, increasing the CL content in LUVs showed a cooperative behavior in binding of the $Tim50^{IMS}$-NBD to membrane bilayers (**Figure 4.6C**). Moreover, mutations of key CL-binding sites on the $Tim50^{IMS}$ β-hairpin that were identified by MD simulations decreased the $Tim50^{IMS}$-NBD binding to CL-containing LUVs, supporting the importance of the residues in this structural element in mediating $Tim50^{IMS}$-CL interactions (**Figure 4.6D**). However, lipid-binding analysis of just the “core domain” ($Tim50^{core}$, residues: 165-361) that contains the β-hairpin, or even “core domain + C-terminus” ($Tim50^{core+C\text{-}terminus}$, residues: 165-476) did not show any binding to CL-containing bilayers, suggesting that multiple binding sites, spanning

beyond the β-hairpin on the Tim50^{IMS} co-operate together to facilitate the Tim50^{IMS} binding to CL-containing membrane bilayers (**Figure 4.6D)**. Due to the labile nature of "N-terminus + core domain" (residues: 133-164), its binding to LUVs could not be tested.

To further assess the role of the physiochemical properties of CL in promoting membrane interactions of Tim50^{IMS}, we assembled LUVs containing the CL variants MLCL or deoxyCL. The chemical structure of deoxyCL lacks the secondary hydroxyl of the central glycerol, the only hydrogen bond donor in the CL headgroup, which would effectively destabilize the resonance-stabilized bicyclic structure and disrupt other intra- and inter-molecular hydrogen bonding (**Figure 4.5A**). As a result, deoxyCL is assumed to strictly exist as dianion at physiological pH **(Kates et al., 1993)**. It has been proposed by previous studies that equal lengths of the four acyl chains in CL contribute towards maintaining the bicyclic structure of the CL head group **(Haines, 2009)**. MLCL with only 3 acyl chains will not only lead to destabilization of the resonance-stabilized head group structure, but because the non polar domain has a lower cross-sectional area, MLCL will likely have less HII propensity than intact CL (**Figure 4.5A**). Incorporation of deoxyCL with two negative charges at 20 mol% to PC LUVs showed a slight increase in the Tim50^{IMS} binding to membrane bilayers compared to CL-containing LUVs. On the other hand, incorporation of MLCL displayed a strong inhibitory effect on the Tim50^{IMS} interaction with bilayers compared to when CL is present (**Figure 4.6A-B**). Overall, our results from the binding studies of NBD-Tim50^{IMS} to CL and its variants suggest that

inter-molecular hydrogen bonding with the CL headgroup as well as the propensity of CL to undergo HII phase transitions regulate the membrane binding of $Tim50^{IMS}$.

Moreover, limited proteolysis of the $Tim50^{IMS}$ in the presence of vesicles showed protection of specific $Tim50^{IMS}$ regions when CL was present in LUVs (**Figure 4.6E**). These results suggest that $Tim50^{IMS}$ may partially insert membrane interactive region into CL-containing bilayers and/or undergo a CL-dependent conformational change that protects key residues from proteolysis. Together, these results suggest an important role for hydrophobic forces in mediating the $Tim50^{IMS}$-bilayer interaction. Overall, lipid-binding studies reveal that the receptor domain of Tim50, $Tim50^{IMS}$, is a peripheral membrane-binding domain and interacts with membrane bilayers in a CL-specific manner.

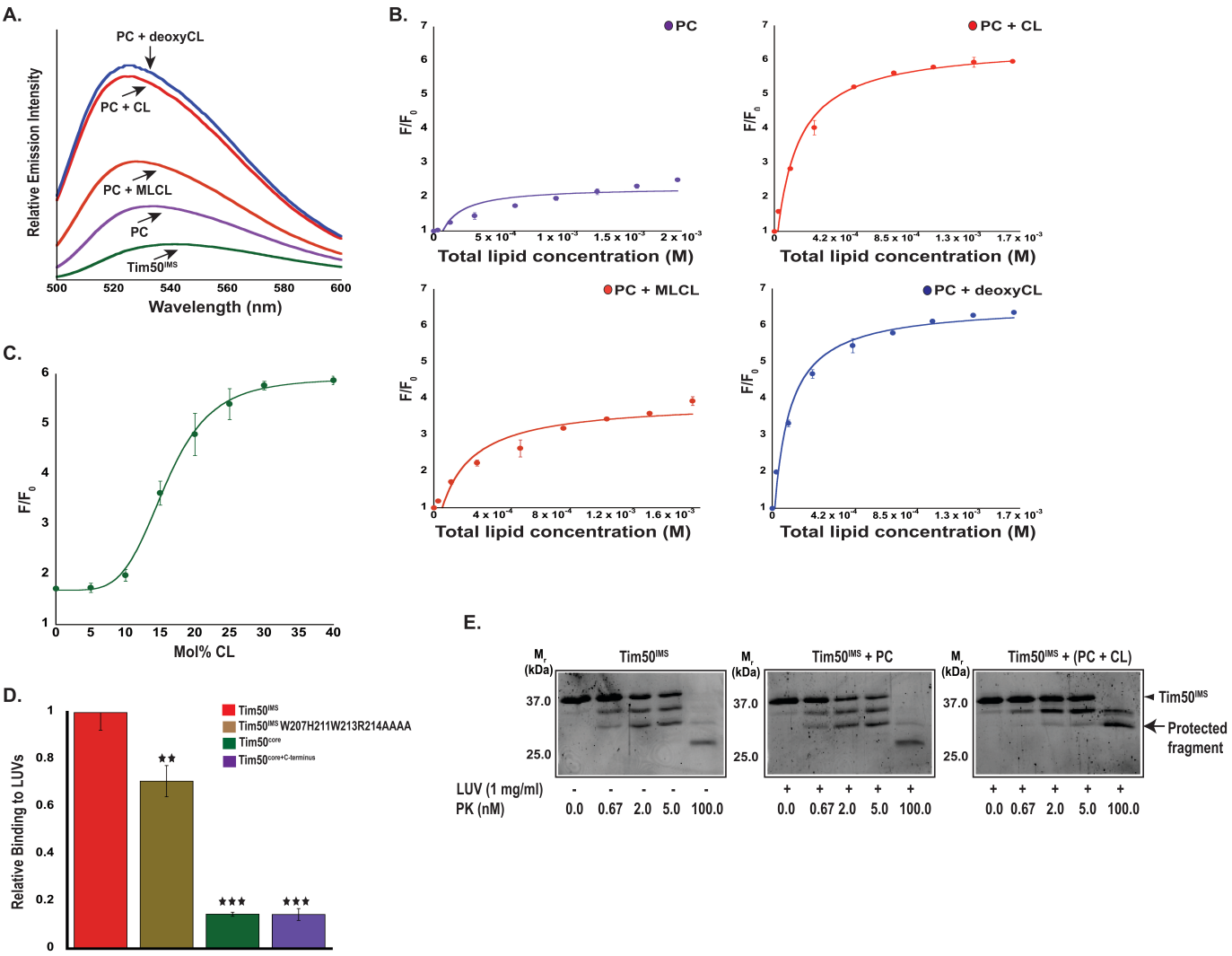

Figure 4.6 *Tim50^{IMS} Binds Specifically to Cardiolipin-Containing Membrane Bilayers*

A. Corrected emission spectrum of NBD-Tim50^{IMS} alone (Tim50^{IMS}) or in the presence of LUVs (1 mg/ml) with the following lipid composition: 100% POPC (PC), and 80% PC + 20% X (mole/mole); X= CL, MLCL and deoxyCL.
B. Maximum fluorescence intensity (F/F_0) of NBD-Tim50^{IMS} plotted as a function of total lipid concentration using LUVs described in panel A. Curves through the data points represent best fits to the data assuming a single class of binding sites in each case. Data points were fit using nonlinear regression analysis in KaleidaGraph assuming 1:1 binding using the equation: $y=m1x/K_m+x$, where $m1=F/F_0max$, x=available total lipid concentration, y=change in F/F_0 at a given total lipid concentration and K_m=total lipid concentration at ½ F/F_0max.
C. Changes in maximum fluorescence intensity (F/F_0) of NBD-Tim50^{IMS} as a function of CL concentration in LUVs containing a background of POPC (mole/mole). The total lipid concentration used was 0.5 mg/ml in each case. Curves through the data points

represent best fit to the data using the Hill equation in KaleidaGraph: m1+(m2-m1)/[1+(x+K_m)*m4], where x=mol% of CL in LUVs, y=change in F/F_0 at a given mol% of CL, m1=F/F_0max, m2=F/F_0 at x=0 mol% of CL, K_m=mol% of CL at ½ F/F_0max and m4=hill coefficient.
D. Co-sedimentation analysis of 1 μM (i) $Tim50^{IMS}$ (residues: 133-476), (ii) $Tim50^{IMS}$ mutant (W207H211W213R214AAAA), (iii) Tim50 core (residues: 165-361), and (iv) Tim50 core + C-termini (residues: 165-476) binding to CL-containing LUV's (1 mg/ml). Graph shows normalized values and the average ± SEM of three independent reactions. **p < 0.01, ***p < 0.0001.
E. Proteinase K treatment of the $Tim50^{IMS}$ (1 μM) only or in the presence of 1 mg/ml LUV's containing either 100% POPC ("PC") or 80% POPC + 20% CL ("PC + CL") (mole/mole). The intact $Tim50^{IMS}$ band is indicated by an arrowhead and the protected $Tim50^{IMS}$ band ("protected fragment", PC+CL sample) is indicated by an arrow.

Small-Angle X-ray Scattering Model of the IMS Domain of Tim50

The IMS domain of yeast Tim50 (residues: 133-476) (**Figure 4.7A**) is reported to be mostly folded with a high content of α-helices and β-sheets **(Gevorkyan-Airapetov et al., 2009)**. However, about 25% of the $Tim50^{IMS}$ sequence is predicted to be intrinsically disordered **(Li et al., 1999)** (**Figure 4.8A**). The conformational flexibility of $Tim50^{IMS}$ combined with its molecular weight (~41 KDa), makes $Tim50^{IMS}$ recalcitrant to high-resolution structural studies like X-ray crystallography or NMR spectroscopy. So far the structural analysis of Tim50 has been restricted to the relatively higher ordered and protease resistant $Tim50^{core}$ (residues: 165-361), where crystal structure of a "conserved core" region ($Tim50^{CC}$; residues: 176-361) was solved [PDB codes: 3QLE **(Qian *et al.*, 2011)**, and 4QQF **(Li and Sha, 2015)**] (**Figure 4.7B**; **Figure 4.8A**). Here we report a low-resolution structural model of the entire IMS domain of yeast Tim50 determined *ab initio* by SAXS. The Guinier regions (**Figure 4.8B, inset**) for the three different concentrations of $Tim50^{IMS}$ used were linear, indicating that the protein in

solution is monodisperse, containing single molecular species. The estimated molecular mass of Tim50^{IMS} was calculated to be 42.01± 1.4 kDa (averaged for 3 concentrations) (**Table 4.1**), and agreed closely with the value obtained from the primary sequence (40.34 kDa). Radius of gyration (R_g) values as calculated by the program GNOM **(Svergun, 1992)** (32.7±1.04 Å, averaged for 3 concentrations) (**Table 4.1**) are fairly uniform suggesting no self-association for all the concentrations tested. The pair distance distribution function *p(r)* of Tim50^{IMS} shows a maximum at ~30 Å with a tail to longer distances, suggesting the presence of flexible regions and an elongated rod-like structure with a maximum dimension (D_{max}) of ~120 Å (**Figure 4.8C**). Indeed, the low-resolution envelope of the Tim50^{IMS} generated via *ab initio* reconstructions confirmed its elongated rod-like appearance (**Figure 4.7C**). Moreover, the normalized spatial discrepancy (NSD) for the 10 independent reconstructions from DAMMIF (**Franke & Svergun, 2009)** was calculated to be 0.658 for the Tim50^{IMS} (0.5 mg/ml), suggesting high quantitative similarity between independent reconstructions.

Table 4.1 *Experimental Parameters for SAXS Sampling of the Tim50^{IMS}*

Concentration (mg/ml)	**R_g[a] (Å)**	**R_g[b] (Å)**	**D_{max} (Å)**	**MW I(O) (kDa)**
0.25	32.91	33.1	128.17	42.92
0.5	31.60	31.76	124.36	42.81
0.65	33.67	33.95	152.10	40.3

R_g[a] = R_g from Guinier analysis

R_g[b] = R_g from *p(r)* distribution analysis (Real Space)

Next, a model for the full-length Tim50^{IMS} was constructed (performed by Prof. Eric May, University of Connecticut) by combining the known coordinates of the conserved core region (residues: 176-361; PDB code: 3QLE), with homology-modeled structures of the N-terminal and C-terminal regions. The structure of the N-terminal region (residues: 133-175) and the C-terminal region (residues: 362-476), were predicted by the I-TASSER webserver **(Zhang, 2008)** to generate models of those regions. The top ranked model for the N-terminal region and the second ranked model for the C-terminal region where attached to the Tim50^{CC} by performing a local structural alignment. The second ranked model was chosen for the C-terminal region, because this model displayed a trimeric coiled-coil motif, whereas the top-ranked model was a dimeric coiled-coil motif. The dimer model was too elongated to be consistent with the SAXS envelope, and therefore the more compact trimeric model was selected. The structure was energy minimized in the CHARMM program **(Brooks et al., 2009)** using the CHARMM22 force field **(MacKerell et al., 1998)** with CMAP correction **(MacKerell et al., 2004)** to relieve local steric strains. The minimized structure was then rigidly docked into the SAXS derived density map using the SITUS package **(Wriggers & Chacón, 2001)**.

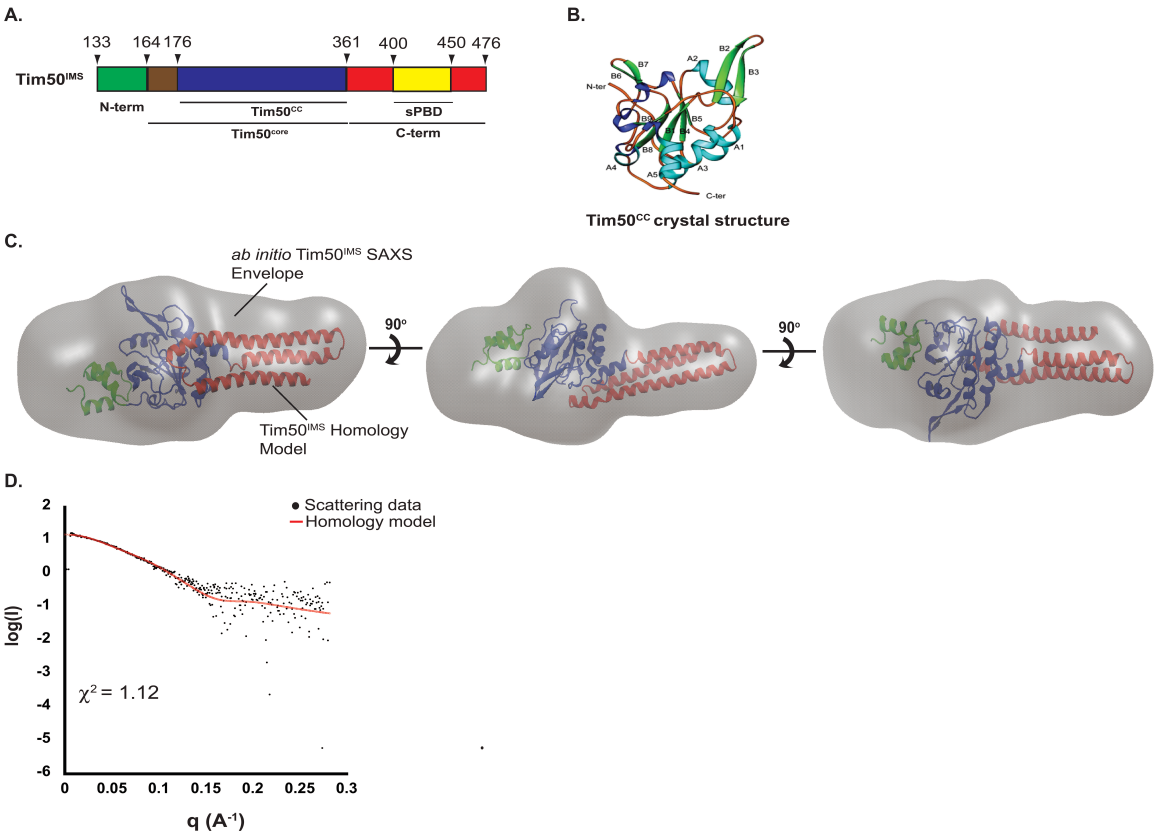

Figure 4.7 *SAXS Analysis of the Tim50^{IMS}*

A. Schematic of the different domains in Tim50^{IMS} with indicated residue numbers (arrowhead); N-terminus ("N-term") residues: 133-164; core domain ("Tim50^{core}") residues: 165-361; conserved core domain ("Tim50^{CC}") residues: 176-361; C-terminus ("C-term") residues: 362-476; small presequence binding domain ("sPBD") residues: 400-450.
B. Ribbond diagram of Tim50^{CC} (PDB ID: 3QLE; **(Qian et al., 2011)**. The β-hairpin comprises of β-strands B2 and B3 and connecting loop. Figure generated in PyMol.
C. SAXS-derived molecular envelope for 0.5 mg/ml Tim50^{IMS} (full-length). The homology model of the Tim50^{IMS} has been aligned with the SAXS envelope using the program SITUS **(Wriggers & Chacón, 2001)**. The normalized spatial discrepancy (NSD) for the 10 independent reconstructions from DAMMIF **(Franke & Svergun, 2009)** was calculated to be 0.658. The figures are rotated 90° relative to each other. Different domains in the Tim50^{IMS} homology model are colored as in A) except for the Tim50^{core} residues 165-176 and sPBD domain (residues: 400-450), which have been assimilated to to the coloring scheme of Tim50^{CC} and C-term respectively (Figure of the Tim50^{IMS} homology model aligned with the SAXS envelope provided by Prof. Eric May, University of Connecticut).
D. Fitting of the experimental scattering data for 0.5 mg/ml Tim50^{IMS} (black) to the theoretical scattering data for the Tim50^{IMS} homology model (red). The fit was

performed using the program CRYSOL **(Svergun et al., 1995)** and gave an acceptable χ^2 value of 1.12.

The theoretical scattering profile for the homology model was compared with the experimental scattering values of the Tim50^{IMS} using the program CRYSOL **(Svergun & Koch, 2003; Svergun et al., 1995)**. The model displayed an excellent fit to the experimental scattering data (χ^2=1.12) (**Figure 4.7C-D**). Moreover, the homology model suggested a coiled-coil conformation for the C-terminus of Tim50^{IMS}, which is in agreement with the predicted coiled-coil propensity of that region (**Figure 4.8D**), as well as the previously reported NMR and circular dichroism spectra of the sPBD domain of Tim50^{IMS}, which suggested preponderance of α-helical conformations for that region **(Rahman et al., 2014)**.

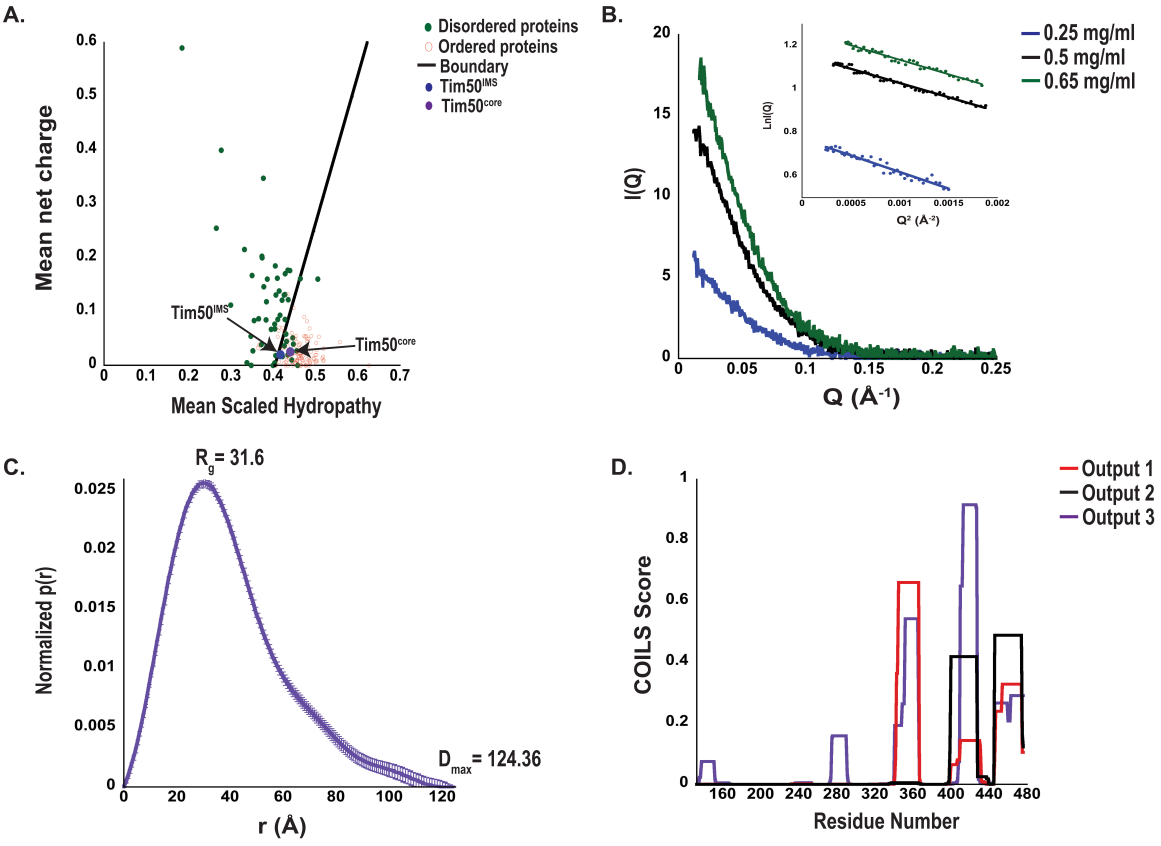

Figure 4.8 *Analysis of Tim50^{IMS} using SAXS and Prediction Programs*

A. Charge hydropathy analysis of the Tim50^{IMS} and Tim50^{core}. Tim50^{IMS} lies at the boundary region of the ordered and disordered proteins. Tim50^{core} resides more inside the ordered region than the Tim50^{IMS} by charge hydropathy analysis (Source: PONDR).
B. SAXS scattering curves for Tim50^{IMS} (from bottom to top: 0.25, 0.5. 0.65 mg/ml). Inset: Guinier curve of Tim50^{IMS} at low-q (< 1.3/R_g) for indicated concentrations. Continuous lines indicate regions used in the Guinier fit.
C. *p(r)* distribution curve for 0.5 mg/ml Tim50^{IMS} computed from the experimental data by GNOM **(Svergun, 1992)** indicating the R_g and D_{max} positions.
D. Coiled-coil analysis of the Tim50^{IMS}. The C-terminus of the Tim50^{IMS} (residues: 362-476) shows a high propensity for adopting coiled-coil structures as predicted by different output methods by the COILS server **(Lupas et al., 1991).**

In order to further validate our SAXS model for the Tim50^{IMS}, we extended our SAXS analysis to include the Tim50^{core} domain (residues: 165-361). The crystal structure of the Tim50^{CC} spanning residues 176-361 was solved recently (PDB code: 3QLE; **Qian *et al.* 2011**). In the Tim50^{CC} crystal structure, it was shown to adopt a globular conformation. Likewise, the SAXS analysis of the Tim50^{core} domain displayed a parabolic pairwise distribution plot consistent for a globular structure, and the *ab initio* reconstruction of the molecular envelope of the core region confirmed its globular appearance as well (**Figure 4.9A and 4.9C; Table 4.2**). The normalized spatial discrepancy (NSD) for the 10 independent reconstructions from DAMMIF was calculated to be a resonably low value of 0.468, suggesting very high similarity between independent reconstructions. Moreover, the Tim50^{core} envelope displayed an excellent fit to the solved crystal structure of Tim50^{CC} (χ^2=1.14) (**Figure 4.9B**).

Table 4.2 *Experimental Parameters for SAXS Sampling of the Tim50^{core}*

Concentration (mg/ml)	R_g[a] (Å)	R_g[b] (Å)	D_{max} (Å)	MW I(0) (kDa)
0.25	19.2	20.4	74.4	20.7

R_g[a] = R_g from Guinier analysis

R_g[b] = R_g from *p(r)* distribution analysis (Real Space)

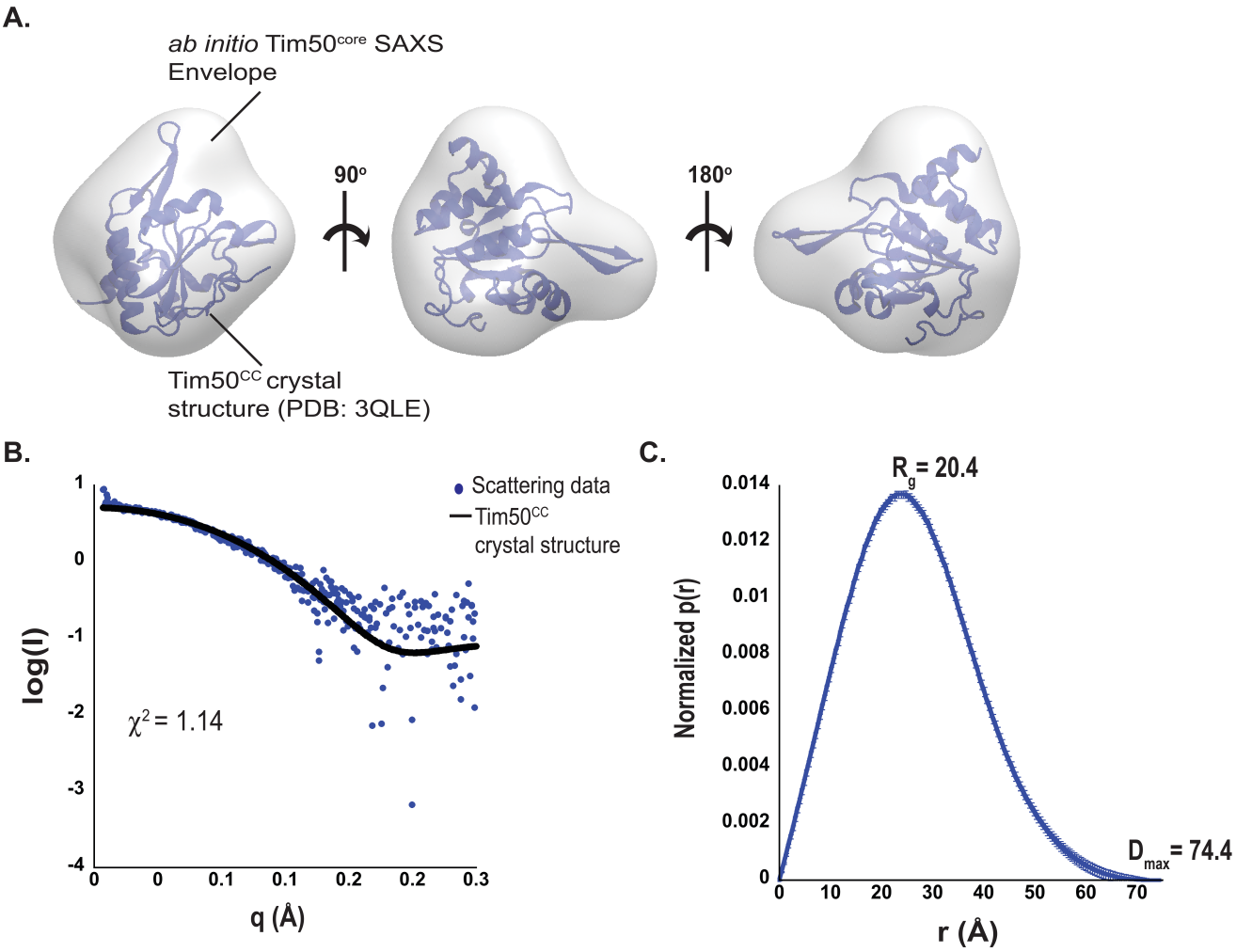

Figure 4.9 *SAXS Analysis of the Tim50^{core}*

A. SAXS-derived molecular envelope for the Tim50^{core} domain. The crystal structure of Tim50^{CC} (PDB: 3QLE, **Qian *et al.*, 2011**) was aligned with the Tim50^{core} SAXS envelope using SITUS **(Wriggers & Chacón, 2001)**. The normalized spatial discrepancy (NSD) for the 10 independent reconstructions from DAMMIF was calculated to be 0.468. The figures are rotated 90° relative to each other (Figure of the Tim50^{CC} crystal structure aligned with the Tim50^{core} SAXS envelope provided by Prof. Eric May, University of Connecticut).
B. The fit of the scattering data of 0.25 mg/ml Tim50^{core} from the experimental values (blue) displays a good fit to the theoretical scattering profile for the crystal structure of Tim50^{core} (black) **(Qian et al., 2011)**. The fit was performed using the program CRYSOL (Svergun et al., 1995), and gave an acceptable χ^2 value of 1.14.
C. *p(r)* distribution curve for the 0.25 mg/ml Tim50^{core} computed from the experimental data by GNOM **(Svergun, 1992)** indicating the R_g and D_{max} positions.

4.4 Discussion and Future Directions

Cardiolipin-Mediated Tim23-Tim50 Interactions

At present, the TIM23 complex contains 11 identified subunits. Both inter- and intra-molecular protein-protein interactions within the complex have been well characterized using various biochemical and biophysical approaches *in vivo*, *in organello*, and *in vitro*. Even with such a wealth of information at our disposal, the role of the physical and chemical features of the native mitochondrial IM on protein-protein interactions within the complex remains poorly understood. Indeed, there have been some efforts in that direction, where studies focusing on the effect of the membrane potential ($\Delta\Psi_m$) across the IM on protein-protein interactions **(Alder et al., 2008b; Bauer et al., 1996)** and on the structure of channel-forming Tim23 **(MALHOTRA et al.,**

2013) have revealed the role of membrane energetics on the structure of membrane proteins and their interactions. Moreover, studies focusing on the effect of the IM lipid profile on the assembly of the TIM23 complex have implicated the IM-resident phospholipid CL for the proper assembly of the complex **(Gallas et al., 2006; Kutik et al., 2008; Tamura et al., 2006; Tamura et al., 2009a; van der Laan et al., 2007)**. It has been demonstrated that matrix-facing Tam41p (translocator assembly and maintenance protein 41), plays an important role in maintaining the integrity and protein import activity of the TIM23 complex **(Gallas et al., 2006; Tamura et al., 2006)**. Interestingly, the same protein was also found to be involved in the cardiolipin biosynthesis pathway at the level of CDP-DAG synthase, where deletion of *tam41* gene resulted in deficiency of CL and its precursor PG **(Kutik et al., 2008)**. Consistent with these findings, two IMS proteins Ups1p and Ups2p were found to regulate cardiolipin levels in an antagonistic manner in mitochondria, and were also shown to affect protein import and integrity of the TIM23 complex **(Tamura et al., 2009a).** Thus, it is clear from various reports that a normal cardiolipin background is essential for maintaining the integrity and functioning of the TIM23 complex.

However, information on the effect of cardiolipin on individual protein-protein interactions within the TIM23 complex is rather limited and have mostly relied on the use of detergent-based techniques, where it was shown that depleting cardiolipin levels affects association between the TIM23 translocase and constituents of the motor machinery on the matrix-facing side of the IM; the same side where cardiolipin biosynthesis is accomplished **(Gallas et al., 2006; Kutik et al., 2008; Tamura et al.,**

2006; Tamura et al., 2009a). It has been also claimed that depleting cardiolipin levels has an effect on the assembly of the core constituents of the TIM23 complex, where based on co-immunoprecipitation analysis with increasing concentration of Triton X-100, it was shown that in cardiolipin-deficient mitochondria the interaction of Tim23 with Tim17 and Tim21, but not with Tim50, is affected **(Tamura et al., 2009a)**. The drawback of such kind of analysis is that it does not provide accurate and complete information on the site-specific interactive sites between two protein constituents, and as has been pointed earlier, relies on the stability of these assemblies in the presence of harsh detergents.

In this study, we look at the effect of cardiolipin on the interaction of Tim50 with the individual domains of Tim23. Using a chemical crosslinking-based approach, both *in organello* and in a model-membrane system, we show that CL modulates Tim23-Tim50 interaction in a site-specific manner, where the absence of CL leads to a decrease in Tim50's interaction with the channel-facing TMSs. Moreover, we show that in CL-deficient mitochondria, the interaction between the respective receptor domains of Tim23 and Tim50 increases. This finding that the Tim50 receptor interacts with different regions of Tim23 in a lipid-dependent manner has implications on various identified roles played by the Tim23-Tim50 interaction. Tim50, via its interaction with Tim23 has been shown to gate the Tim23 channel, such that in the absence of substrate, it closes the channel and helps maintain the $\Delta\Psi_m$ across the IM **(Meinecke, 2006)**. Even then, mutating the coiled-coil region in $Tim23^{IMS}$, the only Tim50 interactive site known on Tim23 yet, did not have any effect on the $\Delta\Psi_m$ across the IM **(Gevorkyan-Airapetov et**

al., 2009). Our finding that the CL-rich IM provides an additional interactive surface to hold the Tim50-channel interaction together even in the presence of mutations that abrogate its interaction with the Tim23 receptor domain suggests how Tim50 is still able to gate the Tim23 channel. Thus, these results suggest that cardiolipin, besides being involved in maintaining the $\Delta\Psi_m$ across the IM via interactions with the respiratory chain complexes **(Böttinger et al., 2012; Pfeiffer et al., 2003; Schwall et al., 2012)**, also contributes towards maintaining the electrochemical gradient across the bilayer by regulating Tim50-Tim23 channel interactions.

The lack of CL is known to inhibit the TIM23 complex mediated import **(Gallas et al., 2006; Jiang et al., 2000; Kutik et al., 2008; Tamura et al., 2006; Tamura et al., 2009a)**. The interaction between the Tim23 channel and Tim50 receptor is essential for mediating early stages of preprotein translocation. Moreover, our data suggest that in the presence of substrate, Tim50 maintains its interaction with the channel region of Tim23 (see Chapter 6). Our finding that CL is essential for maintaining interaction between Tim50 and the channel-facing TMSs suggest that the CL-mediated Tim50-Tim23 channel interactions might play an important role in mediating efficient protein transport across the IM by direct interaction between different regions during specific stages of the protein import reaction. In any case, this hypothesis needs to be experimentally tested by carrying out crosslinking-based Tim23-Tim50 interaction analysis in the presence of substrate in CL-deficient mitochondria (see Chapter 6 for discussion). Moreover, there is a need to investigate the role of increased interaction observed between the respective receptor domains of Tim23 and Tim50 in CL-

compromised mitochondria. Interestingly, compromising the $\Delta\Psi_m$ across the IM has been shown to lead to a similar increase in interaction between the receptor domains of Tim23 and Tim50 **(Alder et al., 2008b)**. Deficiency of CL is also known to decrease the $\Delta\Psi_m$ across the IM **(Jiang et al., 2000)**. This suggests that a decrease in local potential across the IM might play an important role in regulating the $Tim23^{IMS}$-$Tim50^{IMS}$ interaction. Whether or not decrease in $\Delta\Psi_m$ across the IM leads to a decrease in Tim50-Tim23 channel interactions as seen in CL-deficient mitochondria (this study) remains to be investigated. The implications of a depolarized IM on the structure of Tim23 channel region have already been discussed (see chapter 3). Overall, for the very first time this study sheds light on the role played by the IM-resident phospholipid CL in regulating key interactions between the two essential protein components of the TIM23 complex in a site-specific manner.

$Tim50^{IMS}$ Binds to Cardiolipin-Containing Membrane Bilayers

Based on lipid-binding studies, we know so far that the matrix-facing protein Tim44 and the IMS-facing receptor domain of Tim23 ($Tim23^{IMS}$) within the TIM23 complex, have inherent affinities for CL-containing membrane bilayers **(Bajaj et al., 2014b; Marom et al., 2009; Weiss et al., 1999)**. In this study, we provide the first evidence of a membrane-bound state of the IMS-facing domain of Tim50 in a CL-dependent manner. Further, by using CL variants with differing chemical and physical properties combined with lipid-binding studies in the presence of increasing salt

concentration, we show that hydrophobic Tim50^{IMS}-CL interactions comprise a significant part of this interaction. Indeed, we see a positive influence of the presence of salt within the physiological range on the interaction between Tim50^{IMS} and CL-containing bilayers. This effect has been amply demonstrated for other peripheral membrane proteins and their interaction with lipid bilayer **(Bustad et al., 2012; Vogel et al., 2001)**. Salts, especially those of the "kosmotropic" class, may participate in protein-membrane interactions by either increasing the interfacial tension between protein and solvent thereby promoting the hydrophobic effect **(Zhang & Cremer, 2006)**, or by screening the unfavorable charged residues **(Cacace, Landau, & Ramsden, 1997)**. Different salts can also have varying effects on the structure of proteins. Moreover, Tim50^{IMS} has been shown to bind to divalent cations **(Zhang et al., 2012)**. In future, one could probe the salt-mediated effect on the membrane-binding of Tim50^{IMS} in more detail by carrying out similar analysis as performed in this study with salts of different composition, including looking at their effect on the structure of Tim50^{IMS} using techniques like circular dichroism and fluorescence spectroscopy.

Our MD analysis has provided critical insights on the involvement of specific residues within the conserved β-hairpin of Tim50^{IMS} in mediating contacts with CL-containing membrane bilayers. By site-specific labeling of a cysteine residue engineered at the β-hairpin tip with NBD fluorophore we show using steady-state fluorescence measurements prominent NBD emission intensity changes in the presence of CL-containing membrane bilayers. This indicates the transitioning of NBD fluorophore from a polar environment in soluble unbound Tim50^{IMS} to a region with

relatively low polarity in the presence of CL-containing bilayers. Whether or not NBD fluorophore on the Tim50^{IMS} β-hairpin is reaching to a hydrophobic milieu dominated by acyl chains can be tested by carrying out NBD fluorescence quenching studies, where quenching moieties (*e.g.* nitroxide spin labels) are positioned at different depths within a bilayer **(Johnson, 2005)**. Such analysis could also inform us of depth of insertion of β-hairpin in the Tim50^{IMS}. Moreover, by carrying out mutational analysis of the residues identified to make contacts with CL in lipid bilayers, we confirmed the involvement of the Tim50^{IMS} β-hairpin in mediating the interaction between Tim50^{IMS} and CL-containing bilayers. Interestingly, a recent structural analysis of the Tim50 "conserved core" domain found the same CL-interacting tryptophan residues, W207 and W213 (identified in this study) to be involved in making hydrophobic contacts with an adjacent helix of monomeric Tim50 "conserved core" domain **(Li & Sha, 2015)**. Surprisingly, the authors of that study attribute those residues likely to be involved in mediating non-polar contacts with the hydrophobic face of an amphipathic presequence moiety since those two residues are found close to a presequence-binding groove. However, the study offered no experimental evidence to back their claim. On the contrary, results from this study that combines *in vitro* and *in silico* (included as a part of manuscript) analysis strongly suggest the involvement of conserved residues on a β-hairpin loop in mediating contacts between Tim50^{IMS} and CL-containing bilayers. Whether or not the same CL-interacting residues also make contacts with presequence-carrying preproteins needs to be further investigated. In any case, involvement of the β-hairpin of the core region of Tim50^{IMS} in Tim50-CL interaction is intriguing as the same structural element was also found to be involved in mediating Tim50's interaction with Tim23 **(Qian et al., 2011)**.

This ties well to the experimental evidence provided in this study that demonstrated the involvement of CL in mediating Tim50's interaction with the channel-region of Tim23, and probably does so by recruiting the $Tim50^{IMS}$ to lipid bilayer (see working model). Finally, the presence of the β-hairpin containing $Tim50^{core}$ alone or also containing the C-terminus, did not show any preferential binding to CL-containing bilayers. This is in accordance to the different MD models, which suggest preferential involvement of the N-terminus along with β-hairpin in binding to CL-containing membrane bilayers. Nevertheless, in the future, a more rigorous mutational analysis needs to be undertaken to identify the involvement of different residues within the three domains (N-terminus, core and C-terminus) of $Tim50^{IMS}$ to identify their importance in recruiting CL-containing membrane bilayers.

SAXS Model of the IMS Domain of Tim50

Since the discovery of Tim50 in 2002 demonstrating its strict requirement in mediating preprotein transport across the IM **(Geissler et al., 2002; Mokranjac et al., 2003; Yamamoto et al., 2002)**, there has been only a limited knowledge on structure of the functional domain of Tim50. The only structural information known to now is a crystal structure of a protease-protected conserved core region **(Li & Sha, 2015; Qian et al., 2011)**. The hurdles presented in gaining high resolution structural information is not surprising given that the $Tim50^{IMS}$ domain is riddled with regions having flexible propensity according to the various disorder prediction programs. Small-angle X-ray

scattering is a widely used technique to gather low-resolution structural information of well folded as well as intrinsically disordered proteins **(Jeffries & Svergun, 2015)**. This study for the first time presents SAXS analysis of the full-length $Tim50^{IMS}$ as well as $Tim50^{core}$, and uses that information to generate first *ab inito* envelope structures of the two domains. Interestingly, the SAXS analysis of $Tim50^{IMS}$ suggests presence of a rod-like density sticking out of the molecular surface. Moreover, fitting of a homology model of the $Tim50^{IMS}$ (performed by Prof. Eric May) through energy minimization, gives the best fit of the extended C-terminus to a rod-like density. This has implications for the transport function of $Tim50^{IMS}$, where it has been suggested that the $Tim50^{IMS}$ C-terminus is positioned close to the TOM complex of the OM, and is the first segment of the IMS to receive preproteins from the OM **(Qian et al., 2011; Rahman et al., 2014)**. This is followed by transfer of preproteins to the "presequence binding domain" of $Tim50^{core}$ **(Rahman et al., 2014)**. We speculate that while the N-terminus and core domain of $Tim50^{IMS}$ are involved in binding to CL-rich IM, the C-terminus is positioned at an angle from the plane of IM to reach out to the TOM complex of the OM and receive incoming preproteins (see working model). Interestingly, the homology model also predicts the presence of coiled-coil structures in the C-terminus of $Tim50^{IMS}$. This is in alignment with the various coiled-coil prediction programs that show a high propensity for the residues in C-terminus to form coiled-coil conformations. Some of the unpublished results from our laboratory have also indicated that mutations in the coiled-coil region of $Tim23^{IMS}$ (Y70A L71A) abrogate interactions of Tim23 with presequence-carrying preproteins. In light of that observation, it will be interesting to see an outcome

of similar analysis done with the C-terminal region of $Tim50^{IMS}$ by mutating residues involved in coiled-coil formation, especially on preprotein import activity across the IM.

4.5 Materials and Methods

Plasmids and Yeast strains

Library of Tim23C variants was generated as described **(Alder et al., 2008b)**. Mitochondria were isolated as described previously **(Daum et al., 1982)** from yeast strains YPH499. Yeast strains harboring deletions in the cardiolipin biosynthesis pathway were provided by Prof. D. Mokranjac (LMU Munich).

Translation, Import, Chemical Cross-Linking, and Immunoprecipitation

All the procedures were carried out as described previously **(Alder et al., 2008b)**. Immunoprecipitation assays were carried out using polyclonal anti-mouse antibodies against Tim50 synthesized in the laboratory of Prof. D. Mokranjac (LMU Munich) and have been described previously **(Mokranjac et al., 2009)**.

[^{35}S]Tim23-ND Assembly and Crosslinking with Tim50^{IMS}

Membrane scaffolding protein (MSP1E3D1) was synthesized and purified as described **(Ritchie et al., 2009; Appendix A.3)**. Briefly, chloroform stocks of phospholipids (Avanti Polar Lipids Inc., Alabaster, AL) were dried under nitrogen stream and kept O/N in a vacuum desiccator to remove traces of chloroform. The lipid film was solubilized in cholate (59 mM) containing MSP buffer (20 mM Tris-HCl, 100 mM NaCl, 0.5 mM EDTA, pH 7.4) and added to reaction mixture of MSP1E3D1 and *in vitro* translated [^{35}S]Tim23 to a final ratio of 120:1:12.5% (v/v), corresponding to Phospholipid:MSP1E3D1:Tim23. Protease inhibitor cocktail (200X) (Sigma-Aldrich, St. Louis, MO) was added to the reaction mix to a final concentration of 8X. The ND reaction mix was incubated at RT for 30 min, followed by 2h incubation with pre-hydrated hydrophobic adsorbent Bio-beads SM (Bio-Rad Laboratories Inc, Hercules, CA) to remove traces of detergent and allow ND self-assembly to proceed. Following bead removal and incubation with nickel-nitriloacetic acid-agarose (Ni^{2+}-NTA agarose) column, samples were subjected to step gradients of MSP buffer and imidazole (up to 400 mM) to isolate ND with Histidine-tagged MSP. The first two elution fractions were combined (ND) and dialyzed into crosslinking buffer (20 mM HEPES, pH 7.5, 200 mM NaCl, 5 mM $MgCl_2$, 50 mM KCl, 5% (v/v) glycerol) followed by concentration to a final volume of 500 µl using Amicon® Ultra centrifugal filters (3 ml; 3,000-50,000 MWCO).

Crosslinking reactions containing [^{35}S]Tim23-ND [46% (v/v)], 1 µM Tim50^{IMS}, 50 µM bismaleimidoethane (BMOE) [ThermoFisher Scientific, Waltham, Massachusetts] were incubated at RT for 1 h. The reactions were stopped by adding equal volume of 2X SDS- and –dithiothreitol (DTT)-sample buffer ($[DTT]_{final}$ = 0.12 M). For immunoprecipitation after crosslinking, the reactions were transferred to a new tube, and protein A-sepharose beads (Sigma-Aldrich, St. Louis, MO) precoupled with antibody (6-10 µl) were added. After rocking at RT for 2h, beads were washed three times with RIPA buffer [50 mM Tris, pH 7.4, 150 mM NaCl, 1 mM EDTA, 1% (v/v) NP-40, 0.25% (v/v) Na-deoxycholate], once in 1 ml of 10 mM of Tris-HCl, pH 7.5, and eluted with 30 µl of SDS-sample buffer. The crosslinked adducts were separated by SDS-PAGE using 12% acrylamide and visualized by autoradiography after washing the acrylamide gel two times with destain solution [10% Acetic acid, 40% Methanol in dH_2O (v/v)] for 10 min followed by two 5 min dH_2O washes. The bands were quantified using Image lab 3.0 software (Bio-Rad, Hercules, CA).

TMM(PEG)$_{12}$ labeling of [^{35}S]Tim23-ND

[^{35}S]Tim23-ND with a single cysteine positioned at a specific site on Tim23 was purified and assembled as described above. To carry out labeling of a site-specific cysteine using a thiol-reactive hydrophilic reagent, TMM(PEG)$_{12}$ (Thermo Fisher Scientific, Waltham, MA) was added to a final concentration of 5 mM to a 50 µl reaction containing 23 µl of purified and concentrated [^{35}S]Tim23-ND in crosslinking buffer. The reaction was incubated for 5 min at RT followed by quenching by adding DTT [$(DTT)_{final}$

= 0.2 M] and incubating at RT for 5 min. For pre-DTT samples, DTT was added prior to addition of TMM$(PEG)_{12}$ and incubated at RT for 5 min. Equal volume of 2X SDS-sample buffer was added and the bands were separated by SDS-PAGE using 12% acrylamide and visualized by autoradiography as described above. The bands were quantified using Image lab 3.0 software (Bio-Rad, Hercules, CA). The percentage labeling was calculated using equation 1:

Equation 1:

$$\% \text{ labeling} = \frac{\text{Labeled } [^{35}S]\text{Tim23} - \text{Unlabeled } [^{35}S]\text{Tim23}}{\text{Labeled } [^{35}S]\text{Tim23}} \times 100\%$$

Purification of Tim50 Constructs

BL21(DE3) cells (Invitrogen, Carlsbad, CA) transformed with Tim50-containing plasmid were grown for ~6 h at 37°C in 2L of YT medium containing 50 µg/ml kanamycin. Upon reaching an A_{600} of 0.8, the temperature was lowered to 26°C and protein expression was induced with 1 mM isopropyl β-D-1-thiogalactopyranoside. Bacteria were collected by centrifugation at 6,000 RPM for 10 min and were resuspended in resuspension buffer [50 mM $NaH_2PO_4.H_2O$, pH 7.5, 300 mM NaCl, 5 mM imidazole, 1.25 mg/ml lysozyme, 0.025 mg/ml DNase, 0.1 mM phenylmethylsulfonyl fluoride (PMSF)]. After incubation on ice for 30 min, the bacteria were disrupted by sonication. Insoluble material was removed by centrifugation at 30,000 g for 30 min at 4°C. The soluble fraction was loaded onto a Ni^{2+}-NTA agarose column (10 ml) (Qiagen,

Hilden, Germany) pre-equilibrated with resuspension buffer. The column was subjected to step gradients of buffer 1 (50 mM $NaH_2PO_4.H_2O$, pH 7.5, 300 mM NaCl) and imidazole (up to 400 mM). The fractions enriched with protein were pooled and dialyzed against dialysis buffer (20 mM Tris-HCl, pH 7.4, 100 mM NaCl, 0.5 mM EDTA), followed by treatment with TEV protease (Sigma-Aldrich, St. Louis, MO) (TEV:protein, 1:20 w/w) O/N at 16°C. The protein was then passed over a second Ni^{2+}-NTA agarose column to remove His-tagged TEV protease and uncleaved Tim50. Fractions enriched with protein were loaded onto a Superdex 200 10/300 GL column (Amersham Biosciences) pre-equilibrated with Buffer B (10 mM HEPES, pH 7.4, 100 mM NaCl, 100 mM KCl) and collected at a flow-rate of 0.5 ml/min.

Liposome Preparation and Co-sedimentation Analysis

Chloroform stocks of lipids (Avanti Polar Lipids Inc, Alabaster, AL) were dried under nitrogen stream and kept O/N in a vacuum desiccator. Dried lipid film was rehydrated in 1 ml Buffer A (10 mM Na-HEPES, pH 7.4, 500 mM sucrose), and passed 17 times through 0.1 µM polycarbonate membranes using a mini-extruder. The liposome stock was diluted to 4 ml by adding Buffer B (10 mM Na-HEPES, pH 7.4, 100 mM NaCl, 100 mM KCl) and aliquoted proportionally into four 1.5 ml polycarbonate centrifuge tubes. The liposomes were centrifuged at *137,000 x g* for 1 h at 22°C in S120-AT2 rotor. Each liposome pellet was finally reconstituted in 100 µl of Buffer B. The liposomes were pooled and their concentration measured using ammonium ferrothiocyanate colorimetric analysis at A_{488} **(Stewart, 1980)**.

For co-sedimentation analysis, purified Tim50^{IMS} (1 µM) in Buffer B was added to 150 µl reactions containing varying concentration of liposomes. The reactions were incubated at RT for 1 h followed by centrifugation for 1 h at *137,000 x g* at 22°C. The supernatant was discarded, and the pellets were resuspended in 40 µl 2X SDS-sample buffer. The samples were run on a SDS PAGE followed by staining with SYPRO Orange protein stain (Molecular Probes, Eugene, OR). The bands were visualized and quantified using Bio-Rad PharosFXPlus Imager and Image lab 3.0 software respectively.

Transmission electron microscopy of LUVs

Samples of each LUV type were imaged by negative staining (uranyl acetate) transmission electron microscopy after 20x or 40x dilution in Hydration Buffer. Images were collected at 23,000x magnification on a Tecnai Biotwin G2 Spirit electron microscope.

IANBD Labeling of the Tim50^{IMS}

500 µl of Tim50^{IMS} stock in Buffer B (pH 7.4) was mixed with 100X IANBD amide (Invitrogen, Carlsbad, CA) and incubated at RT for 2 h with continuous rotation followed by addition of 20 mM DTT to quench the reaction. To separate the unbound dye from

the labeled protein, the reaction mix was passed through a ~5 ml econocolumn (Bio-Rad Laboratories Inc, Hercules, CA) packed with G25 resin (Sigma-Aldrich, St. Louis, MO) containing Buffer B with no salt (10 mM Na-HEPES, pH 7.4). The fractions were collected and readings at A_{280} (Protein) and A_{481} (IANBD) were recorded to measure the labeling efficiency using equation 2.

Equation 2:

$$\% \text{ labeling efficiency} = \frac{A_{280}/\varepsilon_{Tim50IMS}}{A_{481}/\varepsilon_{IANBD}} \times 100\%$$

Where $\varepsilon_{Tim50IMS}$ = 52,830 M^{-1} cm^{-1} and ε_{IANBD} = 23,700 M^{-1} cm^{-1}

Fluorescence Spectroscopy

Steady-state measurements of IANBD-labeled $Tim50^{IMS}$ (λ_{ex} = 470 nm, 5 nm band pass; λ_{em} = 500-600 nm, 5 nm band pass) were performed with a Fluorolog 3-22 spectrofluorometer (HORIBA Jobin-Yvon) equipped with photon-counting electronics, double grating excitation and emission monochromators and a 450-W xenon lamp. To look at changes in the emission intensity of NBD-$Tim50^{IMS}$ in the presence of liposomes, LUV's with different lipid composition were prepared as described above, except the dried lipid film was reconstituted directly in 1 ml Buffer B (no salt) followed by extrusion. For each course measurement, 0.5 µM IANBD-labeled $Tim50^{IMS}$ was incubated alone or with varying concentrations of LUVs in Buffer B (no salt) in a total volume of 300 µl for

10 min at RT. All fluorescence measurements (averaging 3 measurements) were performed in quartz cuvettes with 1 cm path length at RT with continuous stirring. Changes in maximum fluorescence intensity for a given concentration of lipid (F/F0) were calculated by averaging the fluorescence intensity from 530 nm – 535 nm followed by final averaging for 3 separate measurements (F), and normalizing to the fluorescence intensity when no LUV's are present (F0). All the data points were fit using KaleidaGraph (Synergy Software, PA).

Limited Proteolysis

Tim50^{IMS} (1 μM) was incubated in Buffer B with or without LUVs (1 mg/ml) for 0.5 h at RT in a total volume of 180 μl. After incubation, 25 μl of reaction was added to tubes containing indicated concentrations of Proteinase K and incubated on ice for 0.5 h. The reactions were quenched by adding 2.8 mM PMSF and analyzed by SDS-PAGE using SYPRO Orange staining. The proteolyzed were visualized using Bio-Rad PharosFXPlus Imager.

SAXS Data Collection

Scattering data were acquired at CHESS beamline G1, operating at 11.75 keV (1.055 Å, the tantalum edge). Protein samples were centrifuged at 14,000 RPM for 10 minutes prior to data collection and protected from radiation damage by oscillating the X-ray beam using a computer-controlled syringe pump. All data was collected at 4 degrees. The X-ray beam was collimated to 250 x 500 μm^2 and images were collected with a Dual Pilatus 100 K-S detector with momentum transfer interval of 0.007 $Å^{-1}$ <q< 0.7 $Å^{-1}$. Sample-to-detector distance was calibrated using silver behenate powder (The Gem Dugout, State College, PA). Ten exposures of 2s were averaged and the data were subtracted from Buffer B and reduced using BioXTAS RAW software **(Nielsen et al., 2009)**. *p(r)* curves and values for I_0, R_g and D_{max} were obtained using the program GNOM. R_g values calculated from the GNOM were consistent with those estimated from the Guinier region **(Guinier and Fournet, 1955)**. The intensity of a standard (lysozyme, 4.14 mg/ml) at zero scattering angle I_0 was determined by Guinier analysis and used to estimate molecular weight by comparison **(Mylonas & Svergun, 2007)**. The theoretical scattering data from the homology model and the crystal structure for comparison with the experimental scattering data were calculated using the CRYSOL program **(Svergun et al., 1995; Svergun & Koch, 2003)**. Using the scattering data, *ab initio* molecular envelope was generated by averaging 10 independent DAMMIF **(Franke & Svergun, 2009)** runs (with no imposed symmetry) using the program DAMAVER **(Volkov & Svergun, 2003)**. Final refinement was performed using DAMMIN **(Svergun, 1999)**.

Tim50^{IMS} Homology Model Generation (Provided by Prof. Eric May, University of Connecticut)

A model for the full-length Tim50^{IMS} domain was constructed by combining the known coordinates of the core region residues, with homology modeled structures of the N-terminal and C-terminal regions. Given the conserved core structure (residues: 176-361) has been solved by X-ray crystallography, we chose to homology model the terminal regions independently, rather than generate a complete homology model for the entire IMS sequence. The sequence of the N-terminal region (residues: 133-195) and the C-terminal regions (residues: 343-476), were supplied to the I-TASSER **(Zhang, 2008)** webserver to generate models of those regions. The terminal region models contained overlapping regions with the conserved core to facilitate structural alignments, when constructing the full-length Tim50^{IMS} model. The top-ranking model for both the N-terminus and C-terminus were built onto the crystal structure coordinates (PDB code: 3QLE) of the conserved core. The model building was accomplished in CHARMM **(Brooks et al., 2009)** by performing a local alignment of residues 176-180 between the core and N-terminus and then copying in the coordinates of residues 132-175. Similarly, the C-terminal coordinates were generated by aligning residues 355-361 and then copying in the coordinates of residues 362-476 into the full model. Hydrogen atoms were constructed with the HBuild command and steepest descent (SD) minimization was performed in the GBSW implicit solvent model **(Im et al., 2003)**. During the minimization the backbone atoms of residues 132-360 were harmonically

restrained with a force constant of 50 kcal/mol*Å^2 for 500 steps, followed by 500 steps of unrestrained minimization.

When this initial model was compared with the SAXS envelope it was evident that this model was too elongated and extended outside of the SAXS envelope. In an attempt to generate model, which was more consistent with the experimentally derived SAXS envelope, we replaced the C-terminal region with the second ranked homology model from I-TASSER. The difference between the first and second ranking models was the top-ranking model predicted a dimeric coiled-coil structure whereas the second model predicted a trimeric coiled-coil structure. The trimeric C-terminal model was minimized in the GBSW implicit solvent model while the backbone atoms of residues 132-360 were harmonically restrained. The restraint force constant was set to 200 kcal/mol*Å^2 and 500 SD steps were performed, followed by 500 steps of Adopted Basis Newton-Raphson (ABNR) minimization. The restraint force was lowered to 100 kcal/mol*Å^2 and another 500 steps of SD followed by 500 steps of ABNR were performed. This model when compared to the SAXS envelope displayed an angular architecture, which was not consistent with the linear SAXS envelope. To improve the agreement between the model and the SAXS envelope, the model was manually manipulated with the UCSF Chimera program **(Pettersen et al., 2004)** to alter the backbone angles in residues 359-360 to generate a more linear conformation. Following the modifications in Chimera the model was again minimized in CHARMM using GBSW solvent while restraining backbone atoms in residues 132-358 with an initial force constant of 200 kcal/mol*Å^2 for 500 SD steps followed by 500 ABNR steps. The

restrains were reduced to 100 kcal/mol*$Å^2$ and 500 steps of SD and ABNR were performed. Finally, all restrains were released and 500 steps of SD and ABNR minimization were performed.

Chapter 5

Structural Changes in the Mitochondrial Tim23 Channel are Coupled to the Proton-Motive Force

Derived from: Malhotra K., Sathappa M., Landin J.S., Johnson A.E., and Alder N.N. (2013) Structural changes in the mitochondrial Tim23 channel are coupled to the proton-motive force. *Nat. Struct. Mol. Biol.* 20(8): 965-72, doi: 10.1038/nsmb.2613.

5.1 Abstract

Tim23, the central subunit of the TIM23 protein-translocation complex, forms a voltage-gated channel in the mitochondrial inner membrane (IM), an energy-conserving membrane that generates a proton-motive force to drive vital processes. Using high-resolution fluorescence mapping of a channel-facing transmembrane segment (TMS2) of Tim23 from *Saccharomyces cerevisiae*, we demonstrate that changes in the energized state of the IM cause marked structural alterations in the channel region. In an energized membrane, TMS2 forms a continuous α-helix that is inaccessible to the aqueous intermembrane space (IMS). Upon depolarization, the helical periodicity of TMS2 is disrupted, and the channel becomes exposed to the IMS. Kinetic measurements confirm that changes in TMS2 conformation coincide with depolarization. These results reveal how the energized state of the membrane drives functionally relevant structural dynamics in membrane proteins coupled to processes such as channel gating.

5.2 Introduction

Many biological membranes establish chemiosmotic ion gradients to power vital processes. The IM, for example, uses the potential energy of the proton-motive force (PMF) to drive endergonic processes such as ATP synthesis by the F_0F_1 ATP synthase enzyme, which supplies most of the metabolic energy for eukaryotic cells. However, the way in which the energized state of a lipid bilayer may modulate the structure of membrane proteins and protein complexes is poorly understood. To address this issue, we have analyzed the coupling between the magnitude of the PMF and the structure of the translocase of the inner mitochondrial membrane 23 (TIM23) transport complex of the IM.

The IM houses respiratory-chain complexes whose redox-coupled proton-pumping activity creates a proton electrochemical potential ($\Delta\mu_{H+}$) that is parsed as a proton gradient (ΔpH) and a transmembrane electric potential ($\Delta\Psi_m$). In actively respiring mitochondria, the dominant $\Delta\Psi_m$ component is on the order of -150 mV (matrix negative), and the ΔpH is ~0.5 pH units (matrix alkaline) **(Loew et al.,1993)**. Among different biomembranes, the $\Delta\Psi_m$ is known to regulate membrane protein function, most notably at the voltage-gated channels of excitable membranes **(Hille, 2001)**. It is therefore likely that the $\Delta\Psi_m$ has a general role in regulating structural changes of proteins and complexes embedded within energy-coupling membranes.

The TIM23 complex is a multifunctional complex mediating both the matrix translocation and the lateral integration of nuclear-encoded proteins in a manner requiring an energized membrane **(Chacinska et al., 2009; Endo et al., 2011; Gebert et al., 2011; Maromet al., 2011a)**. Substrates of the TIM23 complex are synthesized on cytosolic ribosomes as precursor proteins containing cleavable N-terminal targeting signals termed presequences. These precursors reptate across the mitochondrial outer membrane (OM) through the translocase of the outer mitochondrial membrane (TOM) complex and engage the TIM23 complex in an unfolded conformation **(Rassow et al., 1990)**. The TIM23 complex consists of a core of membrane-bound subunits Tim23 and Tim17, which share a homologous polytopic membrane region, and Tim50, which functions as a precursor receptor **(Geissler et al., 2002; Marom et al., 2011b; Mokranjac et al., 2003; Schulz et al., 2011; Truscott et al., 2001; Yamamoto et al., 2002)**. The Tim21 subunit, in cooperation with the recently identified Mgr2 **(Gebert et al., 2012)**, regulates the interaction of the TIM23 complex with the TOM complex **(Chacinska et al., 2005; 2010; Mokranjac et al., 2005; Tamura et al., 2009b)** and with respiratory-chain complexes III and IV **(van der Laan et al., 2006; Wiedemann et al., 2007)**. Precursor membrane proteins contain stop-transfer sorting signals downstream of the presequence that are recognized within the TIM23 complex as transmembrane segments and are laterally released into the inner membrane **(Botelho et al., 2011; Glick et al., 1992; van der Laan et al., 2007)**. In contrast, the translocation of soluble polypeptides across the IM requires the matrix-facing ATPase-import motor (presequence translocase associated motor (PAM) complex). The import and sorting of all precursor proteins by the TIM23 complex is strictly dependent on the $\Delta\Psi_m$

component of the PMF; however, the ΔpH appears to be dispensable **(Martin et al., 1991)**. Whereas the $\Delta\Psi_m$ alone is sufficient to drive the lateral integration of membrane proteins by the TIM23 complex, soluble matrix-directed precursors use the $\Delta\Psi_m$ in an initial step to drive the presequence across the IM before substrate engagement with the ATPase motor.

The molecular basis of this $\Delta\Psi_m$ dependence of TIM23-complex activity appears to be two-fold. First, the transmembrane potential modulates the channel-gating activity of the complex. The central subunit, Tim23, consists of a soluble receptor domain in the IMS and a membrane-bound domain that constitutes a membrane-spanning aqueous channel **(Alder et al., 2008a)**. Electrophysiological measurements on mitochondrial membranes **(Lohret et al., 1997)** and purified Tim23 **(Truscott et al., 2001)** have shown that Tim23 forms a cation-selective and voltage-gated multiconductance channel. Tim17 may also be involved in forming a cooperatively gated twin pore complex **(Martinez-Caballero et al., 2007)**. The precise mechanism of gating remains elusive but may involve a combination of $\Delta\Psi_m$-coupled dimerization of the Tim23 IMS domain **(Bauer et al., 1996)**, voltage sensing by Tim17 **(Meier, 2004)** and regulation of channel opening by Tim50 **(Meinecke, 2006)**. Second, the $\Delta\Psi_m$ has been proposed to exert an electrophoretic pull that drives the positively charged presequence across the channel **(Lohret et al., 1997)**. This driving force, in fact, is strong enough to promote the unfolding of mature protein domains **(Huang et al., 2002)**. Notably, in addition to its role in driving precursor import, the $\Delta\Psi_m$ modulates the quaternary structure of the TIM23 complex. This was demonstrated by cross-linking studies, which revealed reversible

changes in the proximity between distinct regions of Tim23 and other subunits (Tim17 and Tim50) as the membrane potential is collapsed and then re-established **(Alder et al., 2008b)**.

Hence, it is known that changes in the $\Delta\Psi_m$ regulate Tim23 gating and interactions with other subunits; however, there is no information on the $\Delta\Psi_m$-coupled structural changes in Tim23 that may underpin these processes. Do changes in the $\Delta\Psi_m$ cause conformational alterations in the Tim23 channel region or alter the exposure of the channel lumen to the aqueous IMS compartment? How do the kinetics of $\Delta\Psi_m$-coupled changes compare with the kinetics of changes in the $\Delta\Psi_m$ itself? To address these questions, we used a recently developed fluorescence-based experimental strategy **(Alder et al., 2008a)** to directly measure structural changes in the channel region of Tim23 that correspond with the energized state of the IM.

5.3 Results

Experimental Design

Using a high-resolution fluorescence mapping approach it was shown earlier that TMS2 of Tim23 faces a protein-conducting channel in the IM, with one helical face oriented towards the aqueous lumen that interacts with presequence-carrying preproteins **(Alder et al., 2008a)**. Using the same approach with the channel-facing TMS2 we

investigated the $\Delta\Psi_m$-coupled structural changes in the channel region of Tim23. *In vitro* translated monocysteine mutants of *S. cerevisiae* Tim23 encoding for site-specific cysteine were subjected to labeling with the small, uncharged environment-sensitive probe 7-nitrobenz-2-oxa-1,3-diazole (NBD) during translation reactions that included the fluorescent aminoacyl-tRNA analog NBD-[^{14}C]Cys-tRNA^{Cys}. NBD is used as an excellent reporter of the microenvironment of the probe. The spectral properties of NBD depend on the polarity and hydrogen bonding capacity of the solvent, where NBD displays a lower fluorescence lifetime, a lower steady-state emission intensity, a red-shift in its wavelength of maximum emission ($\lambda_{em\ max}$), and a red-shift in absorbance (quantified by the emission yields at two different excitation wavelengths ('excitation ratio') in a polar environment relative to when it is in a nonpolar environment **(Alder et al., 2008a; Crowley et al., 1994; Lancet & Pecht, 1977)**. *In vitro* translated NBD-Tim23 has been shown in an earlier study to integrate into the IM with a proper toplogy. Moreover, it assembled with endogeneous TIM23-complex subunits into functional presequence-interactive complexes **(Alder et al., 2008a)**.

To modulate the $\Delta\Psi_m$ of mitochondria containing NBD-Tim23, we used selective additions of respiratory substrate, nucleoside di- and triphosphates and uncouplers. State 4 respiration (high $\Delta\Psi_m$ and low respiration rate) in mitochondria was introduced by incubation with respiratory substrates, malate and pyruvate, along with ATP. This was followed by selectively decreasing the $\Delta\Psi_m$ by two separate means: (i) addition of the protonophore carbonyl cyanide m-chlorophenyl hydrazone (CCCP), which depolarizes the IM by transporting H^+ across the membrane, and (ii) induction of state 3

respiration by the addition of ADP, which stimulates H^+ flux into the matrix through F_0F_1 ATP synthase to drive ATP production (**Figure 5.1A-B**).

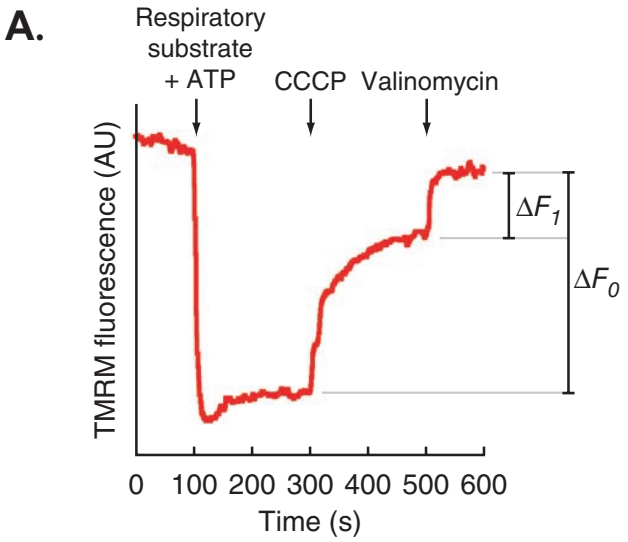

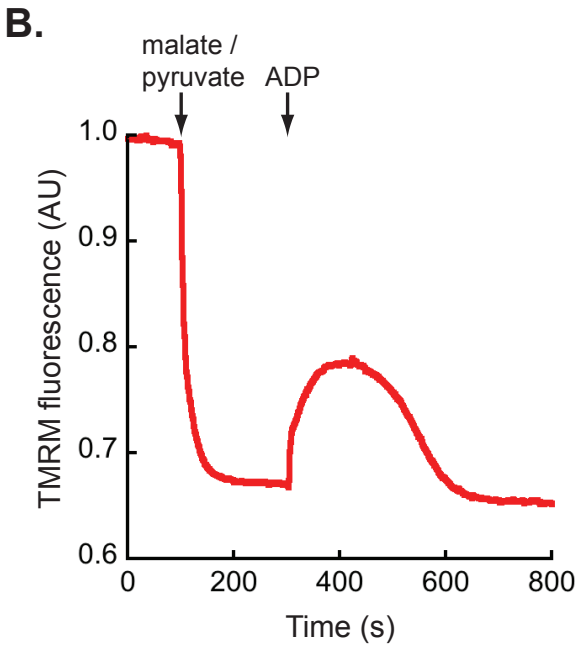

Figure 5.1 *CCCP- and ADP-Coupled Changes in the $\Delta\Psi_m$*

A. TMRM-detected changes in the $\Delta\Psi_m$ induced by CCCP addition. Representative time trace of TMRM emission with isolated mitochondria (0.1 mg ml^{-1}) after sequential additions of respiratory substrate (2.5 mM malate and 2.5 mM pyruvate) with 2 mM ATP, CCCP and 1 µM valinomycin to cause the complete collapse of the $\Delta\Psi_m$ as indicated. Relative $\Delta\Psi_m$ in the presence of CCCP is the ratio of the magnitude of TMRM quenching after CCCP addition (ΔF_1) to that of fully energized mitochondria (ΔF_0). AU, arbitrary units.
B. TMRM-detected changes in the $\Delta\Psi_m$ induced by ADP addition. Representative time trace of TMRM emission with isolated mitochondria (0.1 mg ml^{-1}) after sequential additions of respiratory substrate (2.5 mM malate and 2.5 mM pyruvate) and then ADP (pH 7.5) as indicated. The state 4 to state 3 transition caused by the addition of 75 µM ADP was detected as a transient depolarization, which was followed by a return to state 4 respiration.

The Tim23 Channel Undergoes $\Delta\Psi_m$-Coupled Structural Changes

We investigated $\Delta\Psi_m$-coupled structural changes in the Tim23 channel region by positioning NBD probes sequentially along TMS2 and monitoring several spectral parameters in the absence and presence of CCCP. As pointed out in the previous section, NBD fluorescence is sensitive to the polarity and hydrogen-bonding capacity of the environment and displays specific solvent effects. Moreover, fluorescence-quenching studies can provide an additional parameter to probe the microenvironment of the NBD fluorophore **(Johnson, 2005)**. Soluble fluorescence-quenching agents (for example, iodide ions) added to mitochondrial samples equilibrate across the OM but do not cross the ion-tight barrier of the IM. The rates of collision between probe and quencher (quantified as the bimolecular quenching constant, k_q) then provide an index of accessibility of a given NBD probe to the IMS as has been shown earlier **(Alder et al., 2008a)**.

Consistent with the previous study **(Alder et al., 2008a)**, within an energized IM, the spectral parameters of NBD probes that were incorporated along Tim23 TMS2 [**Figure 5.2**; specifically the $\lambda_{em\ max}$ (**Figure 5.2A**), normalized emission intensity (**Figure 5.2B**) and excitation ratio values (**Figure 5.2C**) all revealed periodic oscillations between a polar and a nonpolar microenvironment. Whereas the $\lambda_{em\ max}$ values increased with greater exposure to the aqueous environment, the emission intensity and excitation ratio values both decreased with aqueous solvation of the probe. Fits of these data to harmonic wave functions (**Figure 5.2A–C**) revealed a periodicity between 3.6 and 3.8 residues per turn, results consistent with a canonical α-helix in an amphipathic environment, with one face toward a nonpolar region and the opposing face toward an aqueous region (the channel lumen). Fourier transform power spectra of these data (**Figure 5.2E–G**) confirmed the α-helical periodicity of this transmembrane segment (primary peaks 92°–96°). Helical wheel projections of these data confirmed that the vector sums of these spectral parameters orient toward the polar-facing ($\lambda_{em\ max}$) and the nonpolar-facing (emission yield, excitation ratio and fluorescence lifetime) sides of the helix, respectively (**Figure 5.3A–D**). Finally, as shown before, under energized conditions, the channel lumen was virtually inaccessible to the IMS, on the basis of iodide collisional quenching measurements that revealed low k_q values at all sites (**Figure 5.2D**); hence, we detected no periodic trend for this parameter (**Figure 5.2H**).

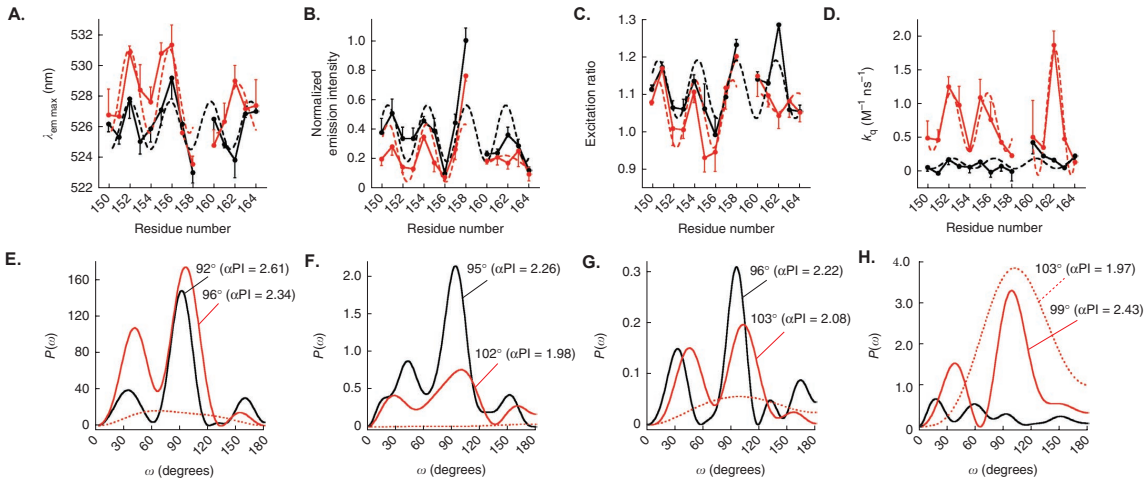

Figure 5.2 *Fluorescence Properties of Probes Along the Tim23 TMS2 Helical Axis*

(A-C) Fluorescence parameters, shown for NBD probes located along Tim23 TMS2 sites in mitochondria either fully energized (black) or depolarized with 50 μM CCCP (red). Dashed traces, nonlinear least-squares fits to a harmonic wave function. Data for energized samples are fit to a constant sinusoid; data for depolarized samples are separated into N-terminal (positions 150–158) and C-terminal (positions 160–164) regions of TMS2. Data are means ± s.d. (n > 3 independent measurements). Measured fluorescence parameters are: fluorescence emission maximum ($\lambda_{em\ max}$) (A.), normalized emission intensity (emission yield per probe) (B.) and excitation ratio (ratio of emission with λ_{ex} at 468 nm to that at 491 nm) (C.). (D.) Bimolecular quenching constant ($k_q = K_{SV}/\tau_0$, where K_{SV} is the Stern–Volmer constant and τ_0 the unquenched fluorescence lifetime). (E-H) Discrete Fourier transform power spectra (P(ω)) as a function of angular frequency (ω) for fluorescence data in the corresponding figures above for energized samples (black) and depolarized samples separated into N-terminal (red solid) and C-terminal (red dotted) regions. Peak frequencies and α-periodicity index (αPI) values are indicated where α-helical patterns are detected. αPI >2 indicates an α-helix.

Conducting the same comprehensive fluorescence analysis after treatment with 50 μM CCCP, we observed marked changes in the microenvironments of NBD probes along TMS2 (**Figure 5.2A–D**). We interpret these changes as major structural alterations that can be divided into two types. The first change was that, upon addition of CCCP, the transmembrane helix moved toward a more polar environment. For the N-terminal region of TMS2 (sites 150–158), there was a pronounced red shift in $\lambda_{em\ max}$ (**Figure 5.2A**) and reduction in both emission yield and excitation ratios (**Figure 5.2B-C**), particularly for sites that face the channel lumen under energized conditions (sites 152, 153, 155 and 156), results indicating a greater exposure to polar solvent upon depolarization. Helical wheel representations of the TMS2 N-terminal region confirm that the vector sums of NBD spectral parameters were oriented toward the same face after depolarization as they were under energized conditions (**Figure 5.3E–H**); hence, this region appeared to maintain the same orientation relative to the channel lumen after $\Delta\Psi_m$ collapse. Moreover, on the basis of iodide quenching, these same channel-facing sites that were shielded from the IMS within an energized IM became highly accessible to the IMS after addition of CCCP (**Figure 5.2D**). We note that the highest k_q values measured for NBD at TMS2 sites following $\Delta\Psi_m$ collapse (~1.5 M^{-1} ns^{-1}) were consistent with values measured previously for NBD probes in the IMS domain of Tim23, results underscoring the strong exposure of these channel sites to the IMS upon membrane depolarization. Power spectra of these data confirmed the α-helical conformation of the N-terminal half of TMS2 after depolarization (**Figure 5.2E–H**).

The second change was the apparent break in helical periodicity along TMS2 after CCCP addition. Within an energized membrane, the probe parameters revealed a constant sinusoid throughout all sites of the helix (**Figure 5.2A–C**). After CCCP addition, this periodicity remained for the N-terminal part of the helix; however, it was disrupted within the C-terminal region (sites 160–164), as shown by both solvent effects (**Figure 5.2A–C**) and iodide quenching (**Figure 5.2D**). Analysis of these measurements under depolarized conditions clearly shows that for all fluorescence parameters, values for the C-terminal sites do not conform to the periodicity maintained by the N-terminal sites (**Figure 5.3**). This break in helical periodicity may be attributable to either a phase shift resulting from helical twisting or a disruption of backbone hydrogen-bonding pattern due to local unfolding.

TMS2 (entire sequence)
energized IM

TMS2 (N-terminal region)
depolarized IM

A.

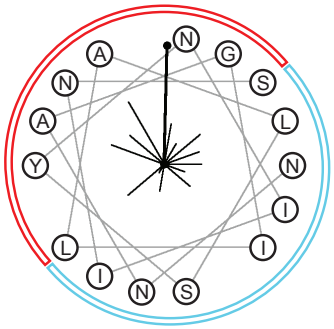

E.

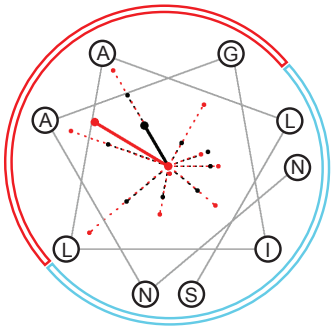

$\lambda_{em\ max}$

B.

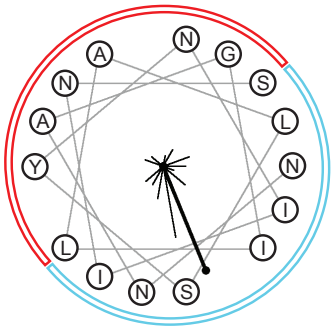

F.

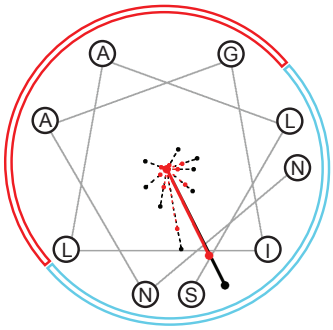

Emission intensity

C.

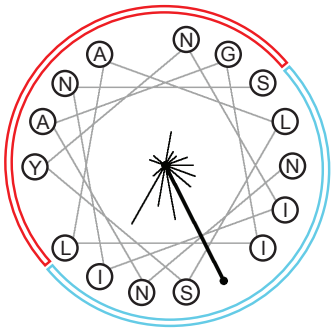

G.

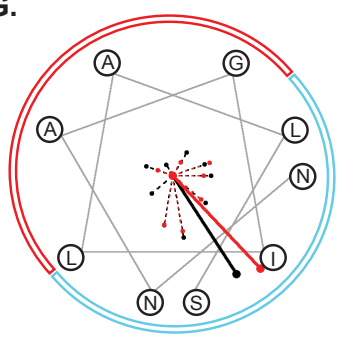

Excitation ratio

D.

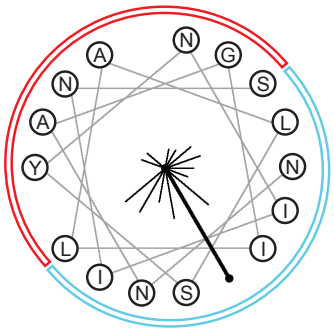

H.

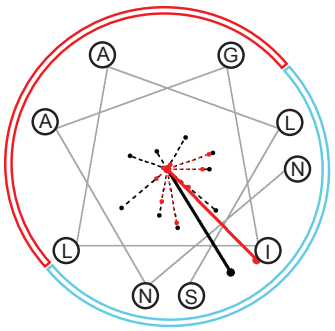

Mean fluorescence lifetime

Figure 5.3 *Helical Wheel and Vector Representations of Tim23 TMS2 NBD Spectral Parameters*

TMS2 helical wheels as viewed from the matrix side of the inner membrane are shown with the helical face oriented toward the aqueous channel lumen (red outer arc) and the face oriented toward the more nonpolar environment (blue outer arc). (A-D) The entire sequence of TMS2 with parameters measured under energized conditions, including $\lambda_{em\ max}$ (A.), emission intensity (B.), excitation ratio (C.), and fluorescence lifetime (D.). Mean values for individual sites are depicted as vectors with thin lines; the vector sum for each parameter is shown as a thick line and solid circle. (E-H) The N-terminal region of TMS2 (positions 150 to 158) with vector representations (dotted lines) of (E.) $\lambda_{em\ max}$, (F.) emission intensity, (G.) excitation ratio, and (H.) fluorescence lifetime in energized (black) and depolarized (red) mitochondria. Vector sums for each parameter are shown as closed circles and solid lines in representative colors.

TMS2 Spectral Changes Vary With the Extent of $\Delta\Psi_m$ Reduction

Based on TMRM fluorescence quenching measurements, 50 μM CCCP resulted in almost a complete collapse of the $\Delta\Psi_m$ (**Figure 5.1A**). To check whether changes in the NBD fluorescence, which in turn inform us of structural changes in Tim23, vary with different concentrations of CCCP and to determine the end point of these structural changes we monitored the spectral properties (emission intensity and $\lambda_{em\ max}$) of NBD at position 162 at different concentrations of CCCP. This site faces a relatively nonpolar environment in an energized membrane and shifts to a more polar IMS-exposed environment upon depolarization (**Figure 5.2A-D**). The addition of 10 μM CCCP to samples containing an NBD probe at position 162 (**Figure 5.4A**) resulted in spectral changes (31% decrease in emission intensity and 4-nm red shift in $\lambda_{em\ max}$) comparable to those observed with 50 μM CCCP (**Figure 5.2A-B**), thus suggesting that the full extent of the structural change had been nearly effected by this magnitude of

depolarization. To look at the effect of CCCP in more detail we measured emission spectra over a range of CCCP concentrations below 10 μM. Upon increasing CCCP concentration, we observed both a progressive decrease in the relative emission intensity and an increase in the $\lambda_{em\ max}$ (red shift) of the NBD reporter probe at position 162 (**Figure 5.4B**). These spectral parameters changed markedly as CCCP concentration was titrated up 10 μM; however, with a higher CCCP concentration (50 μM) the spectral parameters changed comparatively little. We conclude that our NBD-detected structural changes varied with the extent of depolarization (rather than a 'all-or-none' response) and that the point at which we detected near-complete collapse of the $\Delta\Psi_m$ (50 μM CCCP) also approached the endpoint of these structural changes.

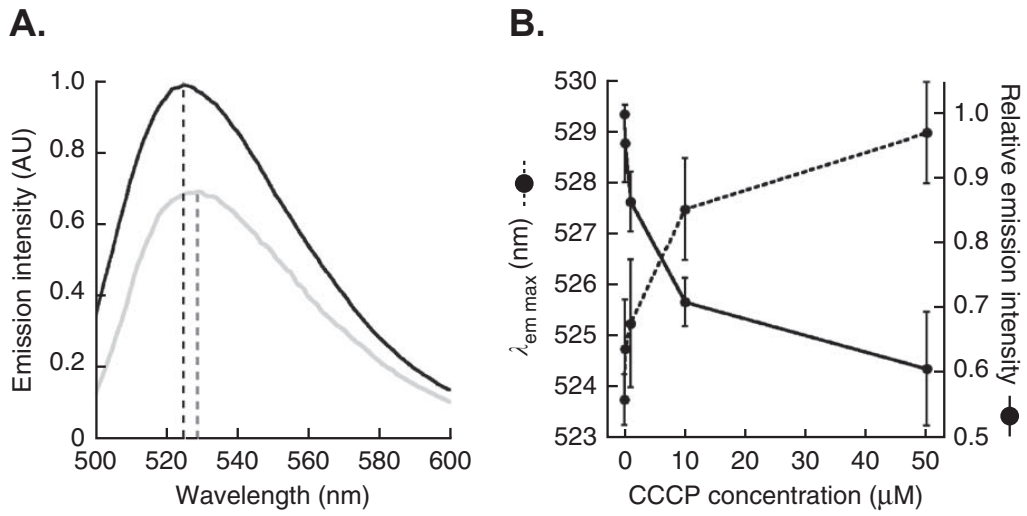

Figure 5.4 *Analysis of NBD-Detected Structural Changes With Increasing Depolarization*

A. Representative emission spectra of mitochondria containing Tim23 labeled with NBD at position 162 under fully energized (black) or partially depolarized (10 μM CCCP, gray) conditions. Dashed lines denote $\lambda_{em\ max}$ values of each spectrum. AU, arbitrary units.

B. Mean changes in emission intensity (solid line) and $\lambda_{em\ max}$ (dotted line) of NBD at position 162 with increasing CCCP concentration.

Changes in TMS2 Structure Coincide with Depolarization

One of the key features of our experimental approach is that spectral changes can be monitored as they occur in real time. Using this approach, we compared the kinetics of NBD spectral shift with the kinetics of $\Delta\Psi_m$ dissipation to check whether the fluorescence-detected structural changes in the channel region were indeed coupled to the changes is the $\Delta\Psi_m$. We therefore performed TMRM time-course measurements of the relative changes in the $\Delta\Psi_m$ in parallel with changes in the fluorescence of an NBD probe at position 152 of the Tim23 channel. Membrane depolarization was induced either by the addition of limiting CCCP concentrations or by the addition of ADP to induce state 3 respiration. ADP, even at high concentrations, did not collapse the $\Delta\Psi_m$ to the same extent as did CCCP (**Figure 5.5A-B**). We therefore analyzed the kinetics of NBD-detected structural changes following $\Delta\Psi_m$ dissipation by either 5 μM CCCP (which induced near-complete depolarization) or 4.5 mM ADP (which induced near-maximal depolarization by inducing state 3 respiration) (**Figure 5.6A-B**). The decrease

in TMRM-detected $\Delta\Psi_m$ after addition of CCCP (**Figure 5.7A**) and ADP (**Figure 5.7B**) was 92% and 71%, respectively, and in each case the rate of depolarization followed first-order kinetics, consistent with previous reports **(Baracca et al., 2003)**. Concurrently, the emission intensity of the NBD probe at position 152 decreased by 17% after CCCP addition (**Figure 5.7A**) and by 5% after ADP addition (**Figure 5.7B**), indicating a shift to a more polar environment. In both cases, the kinetics of the NBD change closely matched that of the $\Delta\Psi_m$ reduction. We therefore conclude that the structural changes in the Tim23 channel domain coincided with depolarization and that the structural change occurred irrespective of whether the $\Delta\Psi_m$ collapse was caused by a pharmacological agent (CCCP) or by a physiological substrate (ADP).

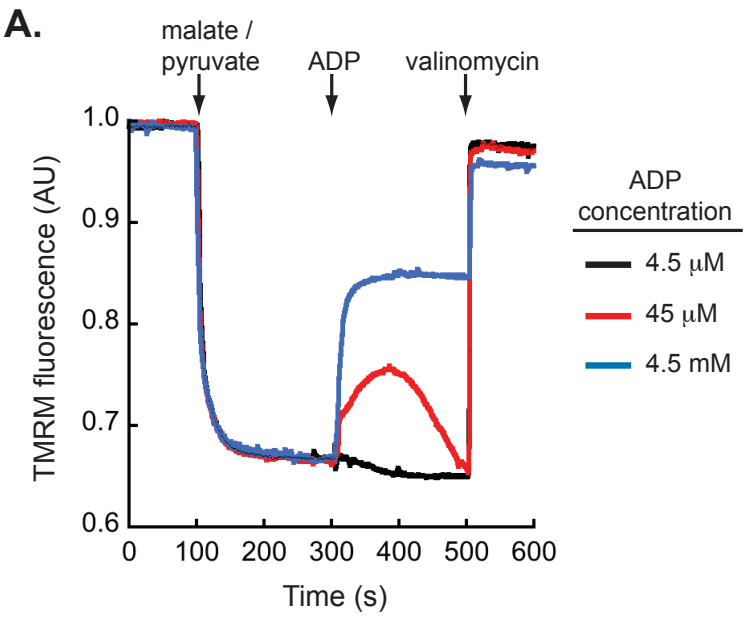
A.
malate /
pyruvate
ADP
valinomycin
TMRM fluorescence (AU)
1.0
0.9
0.8
0.7
0.6
0
100
200
300
400
500
600
Time (s)
ADP
concentration
4.5 μM
45 μM
4.5 mM

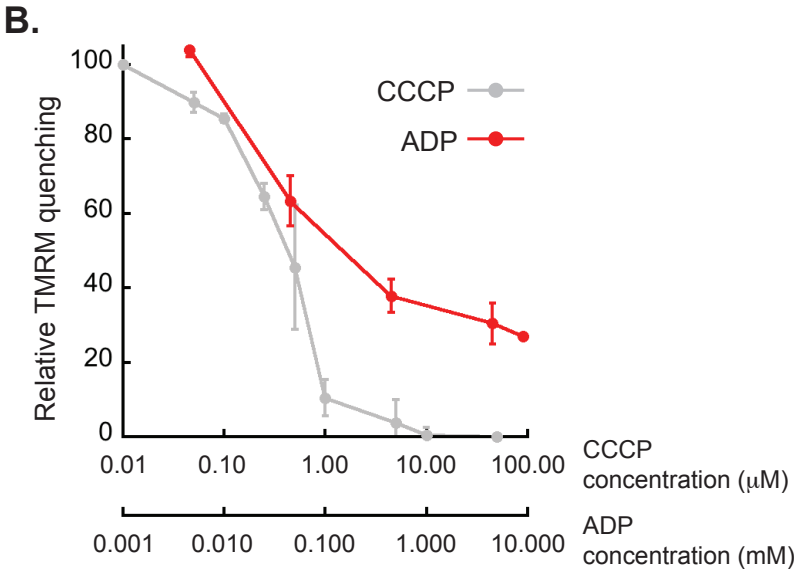
B.
Relative TMRM quenching
100
80
60
40
20
0
CCCP
ADP
0.01
0.10
1.00
10.00
100.00
CCCP
concentration (μM)
0.001
0.010
0.100
1.000
10.000
ADP
concentration (mM)

Figure 5.5 *TMRM-Detected Changes in the $\Delta\Psi_m$ Induced by Different Concentrations of ADP*

A. TMRM-detected changes in the $\Delta\Psi_m$ induced by ADP addition. The indicated concentrations of ADP were added as shown. The addition of 1 µM valinomycin caused complete $\Delta\Psi_m$ collapse.

B. Relative TMRM emission quenching elicited by the addition of the indicated concentrations of ADP (red) and CCCP (grey). Error bars, s.d. (n>3 independent measurements). The extent of ADP-induced depolarization was near maximal with addition of ~4.5 mM ADP.

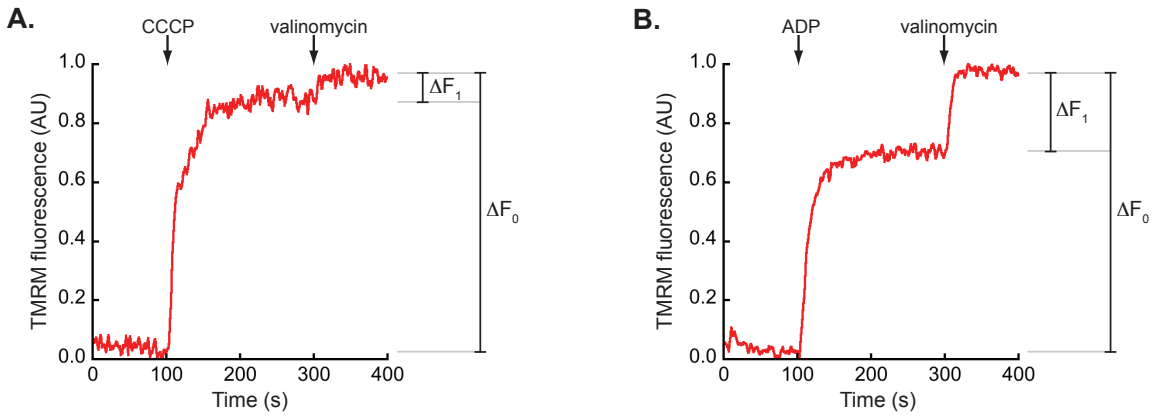

Figure 5.6 *TMRM-Detected Changes in the $\Delta\Psi_m$ Induced by CCCP and ADP*

Relative changes in membrane potential detected by TMRM quenching under conditions used for NBD-detected structural changes. Under the experimental conditions used for measuring time-dependent changes in NBD-Tim23 fluorescence, the $\Delta\Psi_m$ was partially collapsed by the addition of 5 µM CCCP (A.) or 4.5 mM ADP (B.).

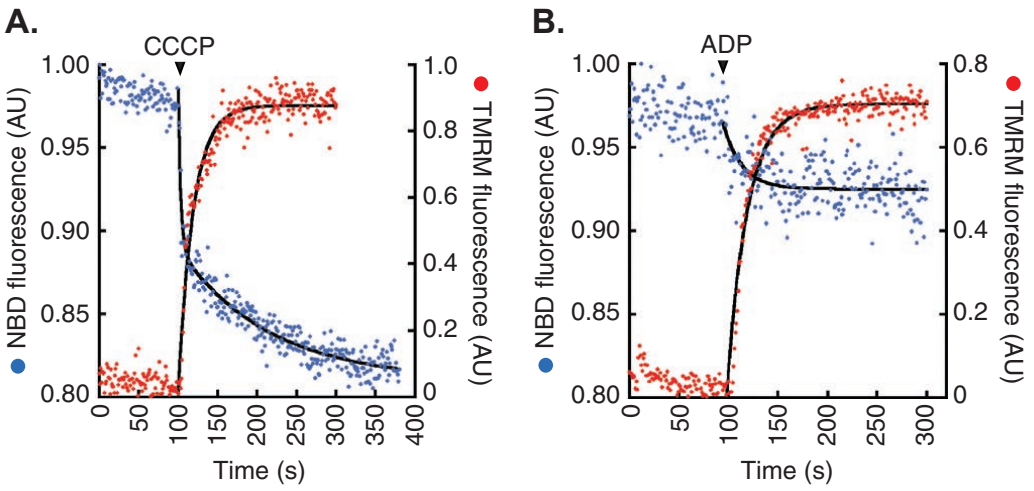

Figure 5.7 *NBD- and TMRM-Detected Changes in Tim23 and the $\Delta\Psi_m$ Induced by CCCP and ADP*

Time-course measurements of NBD-detected structural changes and membrane depolarization. Samples are energized mitochondria containing Tim23 with NBD probes at position 152 in TMS2 subjected to additions of 5 μM CCCP (A.) or 4.5 mM ADP (B.) at 100 s. Fits to the kinetic data are shown as black traces. TMRM fluorescence intensity data (red) were fit as monoexponential increases (rate constant k_1 of 0.052 s^{-1} and 0.048 s^{-1} for CCCP and ADP addition, respectively). NBD fluorescence intensity data (blue) were fit to a biexponential decay function for CCCP addition (k_1 of 0.305 s^{-1} and k_2 of 0.009 s^{-1}) or a monoexponential decay function for ADP addition (k_1 of 0.053 s^{-1}). AU, arbitrary units.

5.4 Discussion and Working Model

Constituents of lipid bilayer are known to influence the structure and function of membrane proteins. The mitochondrial IM also acts as an energy conserving membrane, where the $\Delta\Psi_m$ is known to modulate a number of mitochondrial processes, including protein transport. Normally, structural techniques such as X-ray crystallography and NMR are the two widely used techniques to gain residue-level information of different proteins. However, their use is rather limited to soluble proteins, where requirement for a specialized bilayer environment in case of membrane proteins has hampered their applicability in the field of membrane biology. Moreover, it is difficult to monitor structural changes in real time using traditional structural approaches. Our fluorescence-based approach is ideally suited for investigating the $\Delta\Psi_m$ dependence of Tim23 protein structure because, as has been shown previously, NBD-Tim23 integrates into the IM of active mitochondria with the proper topology, and it assembles into complexes with endogenous TIM23 subunits to form substrate-interactive complexes **(Alder et al., 2008a)**. We are therefore able to directly monitor this electromechanical coupling in the context of a native biomembrane whose $\Delta\Psi_m$ can be precisely modulated.

Using this approach it was previously identified that TMS2 of Tim23 is a part of the polypeptide-conducting channel with one side of TMS2 in a nonpolar environment and the opposite side facing the aqueous channel lumen. Furthermore, it was shown that within energized mitochondria, the channel is sealed off from the IMS, regardless of whether the complex is inactive **(Alder et al., 2008a and this study)** or in a translocation competent state **(Alder et al., 2008a)**. The present study revealed many $\Delta\Psi_m$-coupled changes in TMS2. The first noticeable change was that upon depolarization, channel lumen-facing sites in the N-terminal region of TMS2 became exposed to a much more polar environment in an aqueous continuum with the IMS (**Figure 5.2**). Notably, although these sites exist within a transmembrane helix, both solvent effects (**Figure 5.2A-C**) and quenching data (**Figure 5.2D**) revealed that upon depolarization, they shifted to a microenvironment that was as water exposed and accessible to the IMS as were sites within the Tim23 receptor domain **(Alder et al., 2008a)**. This strong IMS exposure extended deep into the channel (toward the N-terminal end of TMS2), suggesting that upon $\Delta\Psi_m$ collapse the channel opens up to a wide vestibule. This dynamic behavior of TMS2 is consistent with the previously reported $\Delta\Psi_m$-dependent exposure of Tim23 TMS1 to the IMS **(Alder et al., 2008b)**. Whether other TMSs or the sites on matrix-facing loops of Tim23 also gain exposure to the IMS upon depolarization needs to be investigated.

The second $\Delta\Psi_m$-coupled change we observed was a break in the regular α-helical hydrogen-bonding along TMS2, detected by the helical pattern in NBD-probe parameters. In a fully energized membrane, TMS2 NBD probes revealed a constant sinusoidal pattern along the axis from sites 150 to 164 (roughly 4.2 helical turns) (**Figure 5.2A-C**). Upon depolarization, this α-helical pattern was maintained in the N-terminal region of TMS2 (sites 150 to 158), on the basis of nonlinear least-squares fits to the data (**Figure 5.2A-C**) and Fourier transforms (**Figure 5.2E-G**). However, this pattern was disrupted in the C-terminal part of TMS2 (sites 160 to 164) when the $\Delta\Psi_m$ was collapsed (**Figure 5.2 and 5.3**). This altered pattern in NBD spectral parameters may have resulted due to different interactions of the C-terminal region with nearby proteins. However, given the substantial depolarization-coupled change in microenvironments, particularly at site 162 (from a nonpolar-facing site to complete IMS exposure), it is likely that this region underwent a pronounced internal structural change. Upon depolarization, the C-terminal segment may have retained an α-helical (or other regular) hydrogen-bonding pattern that fell out of register with the N-terminal part of TMS2 because of helical twisting. Such breaks or bends are common in the TMSs of membrane proteins and often serve as sites for hinge-like conformational flexibility **(Hall et al., 2009; Langelaan et al., 2010; Screpanti & Hunte, 2007)**, as observed in other voltage-gated channels **(Chakrapani et al., 2010)**. Even with the limited sample set of this region (five sites), a more uniform amphipathic pattern would be predicted from our multiple independent parameters if a regular hydrogen-bonding periodicity were present. Thus, it is also possible that upon depolarization the C-terminal end of TMS2 underwent a complete loss of secondary structure. The breaking of amide hydrogen

bonds incurs a high thermodynamic penalty in the low dielectric environment of a bilayer hydrocarbon core **(White & Wimley, 1999)**. However, the increased exposure of this region to water after depolarization would effectively weaken backbone hydrogen bonds, thus allowing for the disruption of the regular secondary structure. Indeed, many helical-bundle proteins contain extended peptides without regular hydrogen-bonding. The sarcoplasmic Ca^{2+} ATPase, for example, contains TMSs with extended regions of polypeptide that assume multiple alternate backbone hydrogen-bonding patterns during the transport cycle **(Møller, Olesen, & Winther, 2010)**. Such distortion of backbone hydrogen bonds during the catalytic cycle of a membrane protein may be associated with relatively small energetic costs **(Cao & Bowie, 2012)**. In any event, the present work shows that changes in the $\Delta\Psi_m$ can drive major structural alterations within the Tim23 channel region.

Significant drops in the mitochondrial $\Delta\Psi_m$ are associated with processes such as the opening of the permeability transition pore and induction of the apoptotic pathway **(Hüser & Blatter, 1999; Hüser et al., 1998; Ly et al., 2003; Zorov et al., 2009)**. The mitochondrial $\Delta\Psi_m$ may also fluctuate strongly under normal physiological conditions. Using potentiometric probes and real-time imaging, several groups have independently shown that mitochondria undergo spontaneous and reversible depolarizations of variable duration and potentially of high magnitude (reported up to 100 mV) **(Buckman & Reynolds, 2001; O'Reilly et al., 2003; Schwarzländer et al., 2012)**. Because these fluctuations in the $\Delta\Psi_m$ appear to be a common feature of mitochondria, the

conformational changes that we report probably represent the normal temporal dynamics of many voltage-sensitive, IM-resident proteins.

Finally, our work provides insights into the structural changes accompanying the voltage gating of the Tim23 channel during its operation (summarized in our working model, **Figure 5.8**). Under conditions of high $\Delta\Psi_m$, the Tim23 channel in isolation assumes a multiconductance state with a high open probability **(Truscott et al., 2001)**. However, interaction with the IMS domain of Tim50 promotes closure of the channel in a voltage-dependent fashion **(Meinecke, 2006)**. This state is likely to correspond to our measurements under energized conditions in which the channel lumen is sealed off from the IMS (**Figure 5.8**). Upon depolarization, the soluble receptor domain of Tim23 has been shown to reversibly alter its interactions with receptor domains of other Tim23 molecules and with the IMS region of Tim50 **(Alder et al., 2008b)**. This state probably corresponds to our measurements under depolarized conditions in which the channel lumen is exposed to the IMS (**Figure 5.8**). Hence, $\Delta\Psi_m$-coupled changes in the interactions of Tim23 and $Tim50^{IMS}$ domains are accompanied by large structural changes in the channel region. During import, a $\Delta\Psi_m$ is required for the transfer of incoming polypeptide from Tim50 to the channel **(Tamura, et al., 2009b)**. Presequences of TIM23-complex substrates have been shown to act antagonistically to Tim50-mediated channel closure, inducing rapid gating transitions within the channel **(Meinecke, 2006; Schulz et al., 2011)**. The $\Delta\Psi_m$-coupled structural rearrangements that we observe in Tim23 may represent structural states associated with these gating transitions. The mechanistic implications of the structural changes in the C-terminus of

TMS2 remain speculative, but one possibility is that membrane potential–induced folding of this region is important for mediating interactions between Tim23 and other complex subunits that regulate voltage gating and import activity.

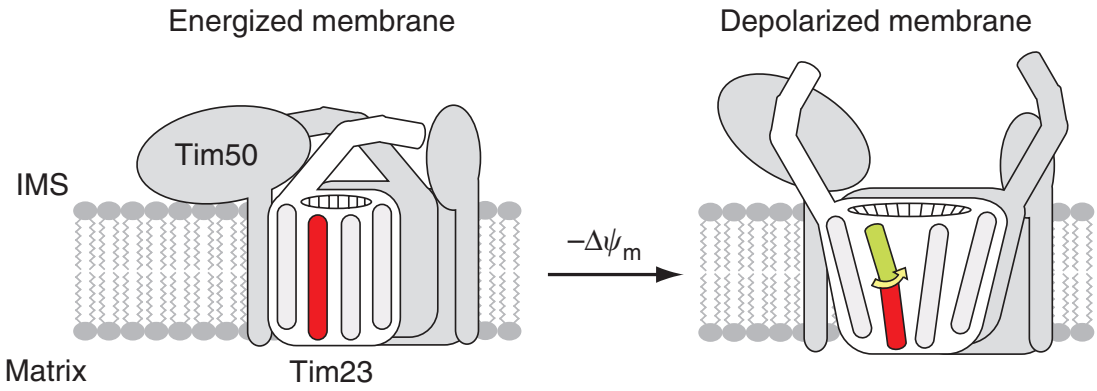

Figure 5.8 *Working Model for the $\Delta\Psi_m$-Coupled Structural Changes in Tim23*

In an energized state of the IM, TMS2 (red) forms a continuous helix with the channel-facing site gated from the IMS probably via Tim50 (Meinecke, 2006). Upon depolarization, the channel opens up into a wide vestibule toward the IMS, and the C-terminal region of TMS2 (green) undergoes a disruption in the helical pattern.

5.5 Materials and Methods

Plasmids, mRNA and mitochondria

The SP6-based plasmid library of Tim23 monocysteine mutants has been previously described **(Alder et al., 2008a; Alder et al., 2008b)**. mRNA was transcribed from PCR-generated DNA fragments with 5′ and 3′ oligonucleotides complementary to the plasmid SP6 promoter and Tim23 sequences downstream of the stop codon. PCR products were transcribed *in vitro* with SP6 polymerase at 37 °C for 1.5 h in reactions containing 100 mM HEPES-KOH, pH 7.5, 20 mM $MgCl_2$, 2.5 mM spermidine, 12 mM dithiothreitol (DTT), 4 mM each of ATP, CTP and UTP, 0.4 mM GTP, 0.013 U μl^{-1} G(5′)ppp(5′)G RNA cap analog (New England BioLabs), 0.5 U μl^{-1} RNase inhibitor and 6 U nl^{-1} pyrophosphatase, then supplemented with 4 mM GTP and allowed to proceed for an additional 0.5 h. mRNA was precipitated overnight at −20 °C in ethanol and 90 mM sodium acetate, pH 5.2, washed in 70% (v/v) ethanol and reconstituted in TE buffer (10 mM Tris-HCl and 1 mM EDTA, pH 7.5).

For the preparation of active mitochondria, the wild-type *S. cerevisiae* strain D273-10B was cultivated at 30 °C to mid-log phase in lactate medium, and mitochondria were isolated by the lysis of spheroplasts and differential centrifugation as described **(Daum et al., 1982)**.

In vitro translation

Tim23 mRNA was translated in 20 mM HEPES-KOH, pH 7.5, 100 mM potassium acetate, pH 7.5, 1.5–3.0 mM magnesium acetate, 1 mM DTT, 200 μM spermidine, 8 μM S-adenosylmethionine, protease inhibitors (0.25 μg ml^{-1} each of leupeptin, chymostatin, antipain and pepstatin A and 0.025% (v/v) aprotinin), 0.2 U μl^{-1} RNase inhibitor, 1.2 mM ATP, 1.2 mM GTP, 64 mM creatine phosphate, 9.6 U nl^{-1} creatine phosphokinase, 30 μM of amino acids (but lacking cysteine for incorporation of NBD-[^{14}C]cysteine) and 20% (v/v) wheat germ extract prepared as described **(Erikson & Blobel, 1983)**. Translation reactions were incubated at 26 °C for 5 min before the addition of mRNA and either 0.6 μM [^{14}C]Cys-$tRNA^{Cys}$ (for synthesis of blank samples in fluorescence experiments) or 0.6 μM NBD-[^{14}C]Cys-$tRNA^{Cys}$ (for synthesis of NBD-labeled samples in fluorescence experiments). Reactions then continued at 26 °C for 40 min. The preparation of the aminoacyl-tRNA analog NBD-[^{14}C]Cys-$tRNA^{Cys}$ has been described **(Alder et al., 2008a)**. This tRNA analog recognizes the unique in-frame 5′-UGC-3′ codon on each Tim23 monocysteine construct mRNA and specifically incorporates an NBD probe at that site.

Assessment of the mitochondrial membrane potential ($\Delta\Psi_m$)

To assess the $\Delta\Psi_m$ of isolated mitochondria, the lipophilic cationic dye tetramethylrhodamine methyl ester (TMRM; Molecular Probes), which accumulates in mitochondria in accordance with a Nernstian distribution, was used in quench mode. Two-milliliter samples of mitochondria (0.1 mg mitochondrial protein per milliliter) in MEB containing 100 nM TMRM (from methanol stocks, final methanol concentration 1.0% (v/v)) were added to stirred cuvettes. TMRM emission (λ_{ex} of 547 nm; λ_{em} of 570 nm; slits at 4 nm) was measured over a time course that included the successive addition of: (i) respiratory substrate (2.5 mM malate and 2.5 mM pyruvate) with or without 2 mM ATP, pH 7.5; (ii) either CCCP or ADP, pH 7.5, in various concentrations and (iii) 1 µM valinomycin to completely dissipate the potential. The difference in fluorescence signal between fully energized and valinomycin-depolarized mitochondria (ΔF_0) represented a relative measure of $\Delta\Psi_m$. The difference in the stabilized signal after the addition of CCCP or ADP and that after complete depolarization (ΔF_1) was used to calculate the fractional depolarization ($\Delta F_1/\Delta F_0$) X 100.

Mitochondrial import and fluorescence analysis of NBD-Tim23 within mitochondria

All import reactions (26 °C, 20 min) were conducted in import buffer (IMB; 20 mM HEPES-KOH, pH 7.5, 0.25 M sucrose, 80 mM KCl, 5 mM $MgCl_2$, 2 mM potassium phosphate, pH 7.5, and 3 mg ml^{-1} bovine serum albumin (BSA; fatty-acid free) supplemented with respiratory substrate (3.0 mM malate and 3.0 mM pyruvate). For the preparation of mitochondria containing NBD-Tim23, import reactions (3 X 800 µl per Tim23 construct per experiment) were conducted with mitochondria at 0.03 mg ml^{-1} and 10% (v/v) translation reaction. After import, mitochondria were prepared for spectral analysis by washing in MEB, sedimentation and resuspension in MEB to 0.27 mg mitochondrial protein per milliliter. Samples for all spectral analyses were supplemented with respiratory substrate (3.0 mM malate and 3.0 mM pyruvate) with or without ATP, pH 7.5, as indicated in the figure legends.

Steady-state fluorescence measurements were made with a Spex Fluorolog 3-22 spectrofluorometer equipped with photon-counting electronics, double-grating excitation and emission monochromators and a 450-W xenon lamp. Unless otherwise indicated, measurements were performed with samples in 4 X 4–mm quartz microcells with a 4-nm bandpass. In all cases, fluorescent samples were measured in parallel with blank samples (lacking the dye but otherwise identical to the fluorescent sample) used to obtain the emission originating from the probe by subtraction. Normalized fluorescence intensity (emission intensity per probe) was calculated for each NBD-Tim23 variant as the emission intensity at $\lambda_{em\ max}$ (in photons s^{-1}) divided by the total membrane-bound

^{14}C c.p.m. determined by liquid scintillation counting after spectral measurements **(Crowley et al., 1994; Crowley et al., 1993)**.

Time-resolved fluorescence measurements were made with an ISS Model K2-002 phase-modulation spectrofluorimeter equipped with a laser diode (λ_{ex} of 471 nm) and a 495-nm long-pass filter in the emission path as described **(Alder et al., 2008a)**. The fluorescence lifetime (τ) of NBD-Tim23 was measured in the frequency domain (15 frequencies, 2–200 MHz) against a reference of fluorescein in 0.1N NaOH (τ of 4.05 ns). The phase-modulation data from mitochondria lacking NBD-Tim23 were used for background subtraction. Frequency domain data were analyzed with GLOBALS-WE software with a sum of two discrete exponential lifetimes (τ1 and τ2) that were intensity-weighted (f1 and f2, where f1 + f2 = 1), and goodness of fit was assessed by χ^2.

Description of steady-state fluorescence parameters

(i) Emission spectra. Emission scans for mitochondria containing NBD-Tim23 (λ_{ex} = 470 nm; λ_{em} = 490 to 590 nm) were taken with 2 s integration times and the wavelength of maximal emission ($\lambda_{em\ max}$) was calculated from the first derivative of these spectra. Independent spectral measurements of mitochondria containing NBD-Tim23 constructs were taken in the presence and absence of CCCP. To confirm that CCCP itself does not affect the spectral properties of NBD in a manner independent of its effect on the electric field, we measured

spectra of NBD-labeled soluble protein in the presence and absence of 50 μM CCCP and found no alteration of the probe fluorescence characteristics.

(ii) Excitation ratio. NBD absorption displays a solvatochromic red shift in solvents of increasing polarity **(Lancet & Pecht, 1977; Lin & Struve, 1991)**. Due to the low extinction coefficient of NBD (~25,000 $M^{-1}cm^{-1}$) and the low concentration of labeled Tim23 (1–5 nM) in our mitochondrial samples, the absorbance of NBD-Tim23 could not be directly measured. We therefore performed excitation scans of mitochondria containing NBD-Tim23 (λ_{ex} = 450 to 500 nm; λ_{em} = 530 nm) to quantify shifts in the excitation spectrum (and hence absorbance) as a measure of the local polarity of different probe sites. We thus define the excitation ratio as the ratio of emission intensities (λ_{em} = 530 nm) resulting from two well-separated excitation (absorption) wavelengths (λ_{ex} = 468 nm and λ_{ex} = 491 nm).

(iii) Collisional quenching. Potassium iodide titrations were performed as before **(Alder et al., 2008a; Crowley et al., 1993; Crowley et al., 1994)** by the addition of 0, 20, 40, and 60 mM KI to separate samples (supplementing with KCl to maintain ionic strength) and 1 mM $Na_2S_2O_3$ to prevent iodide oxidation. Emission scans were performed as above to quantify the quencher-dependent decrease in the emission yield at $\lambda_{em\ max}$ for each probe site. Blank samples (mitochondria not containing NBD-Tim23) were treated identically in parallel and their background fluorescence and light scattering signals were subtracted from NBD-Tim23 containing samples to obtain the net emission intensity of NBD probes. Steady-state data were analyzed graphically according to the Stern-Volmer equation:

$F_O/F = 1+K_{SV}[Q]$

where F_O/F is the ratio of fluorescence intensities in the absence and presence of iodide ions, and the Stern-Volmer constant (K_{SV}) is determined as the slope of F_O/F versus quencher concentration ([Q], iodide ion concentration in this case).Because the observed extent of quenching is greater when the probe has a longer unquenched fluorescence lifetime (τ_0), accurate measurements of

quencher accessibility for different probe sites must be based on the bimolecular

quenching constant (k_q), defined as:

$kq=KSV/<\tau_0>$

where $<\tau_0>$ is the mean unquenched lifetime of each probe.

(iv) Kinetics measurements. Mitochondria containing NBD-Tim23 (2 ml samples) were added to stirred cuvettes and emission intensities (λ_{ex} = 470 nm; λ_{em} = 530 nm) were measured at 1 s intervals.

Evaluation of periodicity

Based on measured fluorescence parameters, the helical periodicity of the Tim23

TMS2 structural element was evaluated by two means:

(i) Least-squares fit to the harmonic wave function:

$$y(x) = a \cdot \sin\left(2\pi\left(\frac{x+b}{p}\right)\right) + c$$

where a is the amplitude; b is the phase; p is the period; c is the offset value and

x is the residue position. Optimal fits to the data were made using a least-square

curve fitting procedure (KaleidaGraph, version 4.03).

(ii) Calculation of the Fourier transform power spectrum (P(ω)), calculated as:

$$P(\omega) = \left[X(\omega)^2 + Y(\omega)^2\right]$$

where:

$$X(\omega) = \sum_{j=1}^{n}\left[(V_j - \langle V\rangle)\sin(j\omega)\right] \qquad \text{and} \qquad Y(\omega) = \sum_{j=1}^{n}\left[(V_j - \langle V\rangle)\cos(j\omega)\right]$$

and ω is the angular frequency, n is the number of residues in a segment, V_j is the measured fluorescence parameter at a given position, and $\langle V_j \rangle$ is the average value of the parameter for the segment **(Cornette et al., 1987; Ma et al., 2009; Silberberg, Chang, & Swartz, 2005)**. P(ω) is analyzed for the value of ω that maximizes the function. The α-periodicity index (αPI) is the average value of P(ω) from 80° to 120° relative to the average value of P(ω) over the entire power spectrum, defined as:

$$\alpha\text{PI}\left[P(\omega)\right] = \frac{\frac{1}{40}\int_{80^\circ}^{120^\circ} P(\omega)\partial(\omega)}{\frac{1}{180}\int_{0^\circ}^{180^\circ} P(\omega)\partial(\omega)}$$

Because canonical α-helices have 3.6 residues per turn, a peak angular frequency of 100° indicates an ideal α-helix. Values of αPI>2 are generally considered indicative of an α-helix.

Chapter 6

Future Directions: Cardiolipin-Mediated Structural Changes in Tim50 and Substrate Modulated Tim23-Tim50 Interactions *In Vitro* and *In Organello*

6.1 Introduction

Mitochondrial biogenesis is dependent on the efficient import of proteins from their cytoplasmic origin to the mitochondrion. The vast number of pre-proteins to be imported to different mitochondrial sub-compartments, each with a distinct microenvironment, requires dedicated pathways to carry out protein localization. One such pathway called the presequence translocase pathway is involved in transporting preproteins across the mitochondrial inner membrane into the matrix **(Chacinska et al., 2009; Harbauer et al., 2014)**. The presequence translocase machinery or the TIM23 complex comprises the component of this pathway that is localized to the inner membrane. The IMS exposed domain of the central subunit of this machinery, Tim23, co-ordinates with the corresponding domain of the central receptor, Tim50, to carry out the initial stages of pre-protein translocation *i.e.*, transport of pre-proteins from the TOM complex of the outer membrane to the inner membrane. However, the mechanism by which these two subunits of the TIM23 complex co-ordinate remains controversial. Some reports have suggested that $Tim50^{IMS}$ alone receives preproteins from the TOM complex, and transfers them to the intermembrane space domain of Tim23, which finally directs substrate to the inner membrane channel **(Li & Sha, 2015; Lytovchenko et al., 2013; Schulz et al., 2011)**. This preprotein translocation is rendered unidirectional by the higher affinity for the preproteins on the *trans* side of the inner membrane channel **(Lytovchenko et al., 2013; Marom et al., 2011b)**. On the other hand, some studies suggest that $Tim23^{IMS}$ and $Tim50^{IMS}$ together form a more permanent translocation-competent receptor complex for transporting preproteins across the aqueous intermembrane space milieu **(Gevorkyan-Airapetov et al., 2009;**

Mokranjac et al., 2009; Tamura et al., 2009b).

Both Tim23 and Tim50 have been shown to be able to interact with presequence-containing proteins independently. Structural and functional studies have so far suggested two presequence binding sites on the receptor domain of Tim50; one on the protease-resistant core domain (residues: 165-361) and a second one on the fungi specific C-terminal domain (residues: 395-476) **(Li & Sha, 2015; Marom et al., 2011b; Qian et al., 2011; Rahman et al., 2014; Schulz et al., 2011).** Interestingly, the two domains were also found to interact with each other, suggesting the basis of preprotein transfer from one substrate-binding domain to another **(Rahman et al., 2014)**. To date, there has been no information on the involvement of the matrix-exposed domain or the predicted transmembrane (TMS) segment of Tim50 on preprotein recognition and transport. Presequence binding sites on Tim23 have been mapped to its intrinsically disordered receptor domain, as well as to TMS1 and TMS2 **(Alder et al., 2008a; Alder et al., 2008b; Bauer et al., 1996; la Cruz et al., 2010; Marom et al., 2011b; Pareek et al., 2013; Truscott et al., 2001).** By using fluorescence spectroscopy based approaches, TMS2 was found to line the aqueous channel **(Alder et al., 2008a)**. Intriguingly, the presequence binding sites on Tim23 lie in the same regions identified to bind to the $Tim50^{IMS}$ **(Alder et al., 2008a; Bauer et al., 1996; la Cruz et al., 2010; Schulz et al., 2015).** Moreover, the crystal structure of the Tim50 core domain suggested the presence of a substrate-binding groove close to the Tim23 interactive β-hairpin **(Li & Sha, 2015; Qian et al., 2011)**. The idea of the presence of a ternary complex comprising Tim23-Tim50-presequence has been refuted based on experimental evidence **(Schulz et al., 2011)**. Based on all the facts available, a critical

missing piece of information is how the Tim23-Tim50 interaction modulates presequence binding and, conversely, how presequence binding mediates the Tim23-Tim50 interaction. Most importantly, there is a need to address the structural details of the receptor complex (Tim23-Tim50) in a translocation competent state.

Cardiolipin (CL) is the signature phospholipid of the mitochondrial IM. Its unique physiochemical properties impart many structural characteristics, which make cardiolipin indispensable for multiple mitochondrial processes **(Claypool & Koehler, 2012; Lewis & McElhaney, 2009; Schlame et al., 2000)**. Cardiolipin is known to be involved in maintaining the structure and function of various mitochondrial inner membrane proteins and complexes, which include peripheral (cytochrome c, Tim44) as well as integral (AAC, Complex IV) membrane proteins **(Planas-Iglesias et al., 2015)**. The stability of the TIM23 complex has also been shown to be cardiolipin-dependent **(Gallas et al., 2006; Kutik et al., 2008; Tamura et al., 2006; Tamura et al., et al., 2009b; van der Laan et al., 2007)**. The work presented herein, we have demonstrated the role played by cardiolipin in mediating receptor-channel interactions within the TIM23 complex via its interactions with the receptor domain of Tim50 **(Chapter 4 of this study)**. But how does cardiolipin affect the structure of $Tim50^{IMS}$? Does the conformation of the receptor domain differ between its aqueous and its membrane-bound state? These are some of the questions whose answers will not only shed light on the mechanism of preprotein transport across the IM, but will also provide us the structural basis of multiple Tim50-mediated interactions within the complex.

In this chapter, we discuss some preliminary data that will help provide insights into the structural state of the receptor complex in a translocation-competent and a lipid-dependent state. Specifically, we show that the IM resident phospholipid cardiolipin modulates the structure of the receptor domain of Tim50. Moreover, by comparing Tim23-Tim50 interaction in model membranes and *in organello*, we show that the inner membrane properties help keep the receptor-channel interactions intact in a translocation active state.

6.2 Results

Cardiolipin-Mediated Structural Changes in the Tim50^{IMS}

To determine if Tim50^{IMS} undergoes a structural change in the presence of cardiolipin-containing membrane bilayers, we undertook a cysteine accessibility approach wherein the accessibility of the only native cysteine (C268) present in the core region was tested under different conditions. The cysteine in Tim50^{IMS} is fortuitously located close to both the Tim23 interactive β-hairpin loop as well as to the putative presequence binding acidic groove of the core domain **(Alder et al., 2008b; Qian et al., 2011)**. Hence, any conformational change in that region concomitant with cardiolipin interaction will inform us of the basis of Tim50's interaction with Tim23 and preproteins in its membrane bound state. To analyze the changes in cysteine accessibility, Tim50^{IMS} was treated with a soluble thiol-reactive trimethyl and maleimide derivative of polyethylene glycol, TMM(PEG)$_{12}$, in the presence and absence LUVs (**Figure 6.1A**). Increasing concentrations of POPC (PC) LUVs with and without 20% CL (mol/mol) were

used to monitor the effect of different lipids on the Tim50^{IMS} structure. In the absence of any LUVs, Tim50^{IMS} was labeled with ~35% efficiency (**Figure 6.1B and 6.1C,** lanes 1 and 6). This shows that in solution, the cysteine is only partially accessible to the aqueous milieu. The addition of increasing concentrations of PC LUVs did not induce any systematic change in the labeling efficiency of the Tim50^{IMS} (**Figure 6.1B,** lanes 2-5). However, upon incorporation of PC+CL LUVs, Tim50^{IMS} showed a much higher labeling efficiency than when it is present in solution by itself (**Figure 6.1C,** lanes 7-10). This shows that interaction with CL induces local conformational changes in the core region of Tim50^{IMS}, which makes the only cysteine present in the sequence more accessible to the aqueous environment.

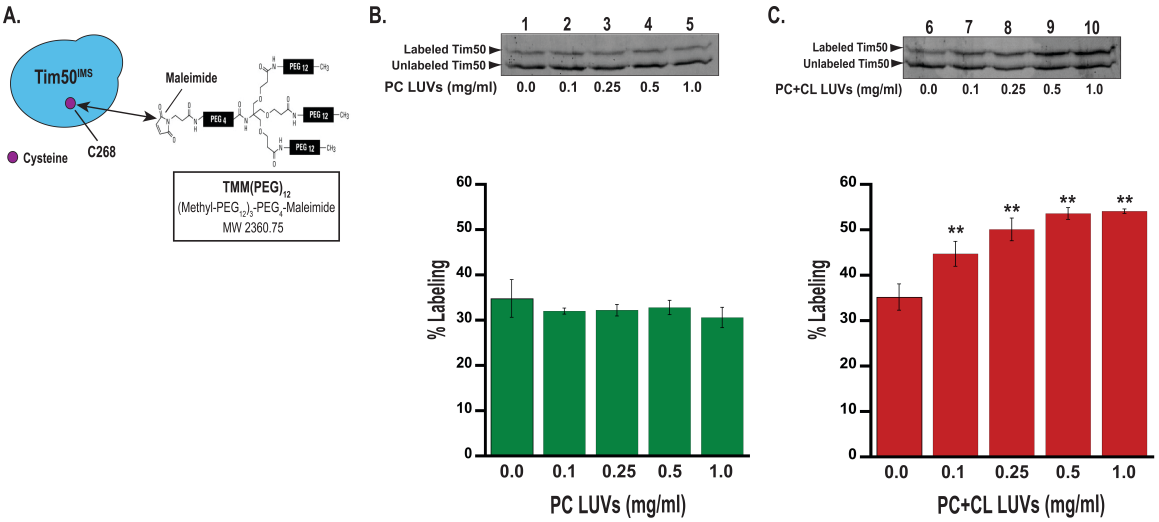

Figure 6.1 *Tim50^{IMS} Cysteine Accessibility in the Presence of LUVs*

A. Schematic representation of the Tim50^{IMS} (cyan) with a single cysteine (C268, magenta) conjugated to thiol-reactive TMM(PEG)$_{12}$.

B. and C. Labeling of Tim50^{IMS} in the presence and absence of different concentrations of LUVs; PC (lanes 2-5) and PC+20% CL mol/mol (lanes 7-10). Tim50^{IMS} labeled with TMM(PEG)$_{12}$ migrates slower on SDS-PAGE and is resolved from the unlabeled species (Top). Percentage labeling of Tim50^{IMS} as a function of the concentration of LUVs (Bottom). The percentage of labeling was calculated as follows: Intensity of labeled product / Intensity of (labeled + unlabeled product) * 100. The mean values and standard deviations of relative band intensities for three independent experiments are shown. * indicates significant difference in comparison to results from control (0 mg/ml LUVs) by student's t-test (*$p<0.05$, **$p<0.01$).

To examine the CL-mediated conformational changes in more detail, the cysteine in Tim50^{IMS} was labeled with thiol-reactive BODIPY fluorophore and subjected to limited proteolysis by proteinase K in the presence of LUVs (**Figure 6.2A**). Fluorescent labeling of Tim50^{IMS} ensured increased sensitivity in the detection of proteolyzed bands that might otherwise go undetected using regular protein staining procedures following SDS-PAGE. Fluorescent labeling of the cysteine in Tim50^{IMS} also ensured that we focus on the structural changes associated with the core domain in the presence of membrane bilayers, in continuation with our cysteine accessibility studies. The proteolysis profile of the Tim50^{IMS} displayed characteristics of a well-folded protein, with incomplete proteolysis seen even at the highest proteinase K concentration (**Figure 6.2B,** lane 5). Consistent with our thiol-labeling studies, incorporation of PC LUVs did not have any effect on the proteolysis of Tim50^{IMS} (**Figure 6.2B,** lanes 7-10). On the other hand, upon interaction with CL-containing bilayers, new proteolyzed bands were observed for the low proteinase K concentrations, diagnostic of structural changes and increased

conformational flexibility **(Fontana et al., 2004; 2012)** (**Figure 6.2B,** lanes 12-14). Based on these results, we conclude that Tim50^{IMS} undergoes conformational changes in a cardiolipin-dependent manner.

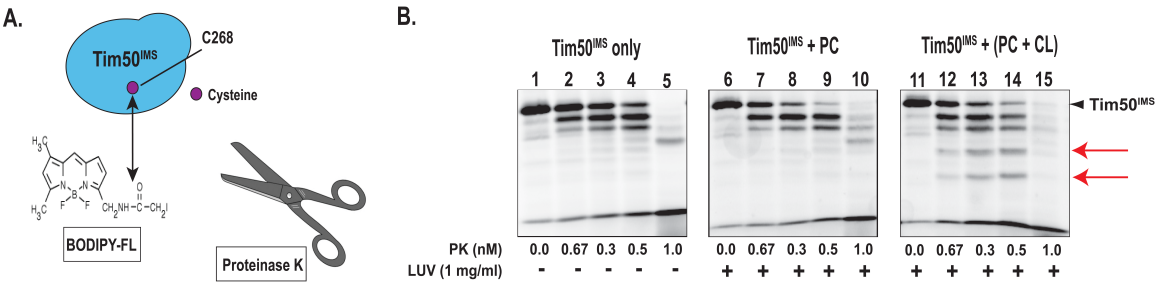

Figure 6.2 *Limited Proteolysis of BODIPY-Tim50^{IMS}*

A. Schematic representation of the Tim50^{IMS} (cyan) with a single cysteine (C268, magenta) conjugated to thiol-reactive BODIPY-FL. Limited proteolysis of BODIPY-Tim50^{IMS} is carried out in the presence of limited concentrations of proteinase K that cut the protein only at solvent-exposed recognition sites.

B. Treatment of BODIPY-Tim50^{IMS} (1 μM) with increasing concentrations of proteinase K, in the absence and presence of LUVs (1 mg/ml) containing either 100% PC (lanes 6-10) or 80% PC + 20% CL mol/mol (lanes 11-15). The band corresponding to the intact Tim50^{IMS} is indicated by an arrowhead. Generation of unique bands in the PC+CL-containing lanes is indicated by red arrows.

Substrate-Mediated Tim23-Tim50 Interactions

Tim50 has been shown to interact with both the IMS domain as well as the membrane-bound TMS1 of Tim23. Depolarization of the inner membrane is known to increase the interaction between the receptor domains of Tim23 and Tim50 **(Alder et al., 2008b)**. But how the presence of a presequence-carrying substrate might modulate Tim50's interaction with the receptor and the channel region of Tim23 remains unknown. To identify the effect of the presence of substrate on the Tim23-Tim50 interaction, we utilized our crosslinking-based approach in PC-nanodiscs as well as *in organello* **(Chapter 4 of this study)**. Nanodiscs provide a native-like membrane environment without the complexity of *in organello* system. The use of both nanodiscs and *in organello* systems offers an opportunity to look at the direct effect of a substrate on the interaction between the two essential proteins at individual domain level in our reductionist system, and compare it with the native environment of the inner membrane. The TIM23 substrate we used to analyze the effects on crosslinking was the widely used pSu9-DHFR, a fusion protein between the first 69 amino acids of subunit 9 of mitochondrial F_O-ATPase and mouse dihydrofolate reductase **(Rapaport, Künkele, & Dembowski, 1998)**. For our *in organello* system, the substrate was pre-incubated with methotrexate to induce folding of its DHFR domain, and lock it on the OM to form a translocation intermediate spanning the TIM23 complex (**Figure 6.3A**). Interestingly, the presence of substrate had an opposite effect on the Tim23-Tim50 interaction seen in the two systems. Whereas the Tim50-TMS1(F114C) interaction remained stable in the presence of substrate at a concentration of up to 4 μM *in organello* (**Figure 6.3B**), the same interaction lost its stability in our nanodiscs system as the substrate concentration

was increased (**Figure 6.4B**). This reversal of interaction was also visualized for the receptor domains in the two systems, where $Tim23^{IMS}$(S80C)-$Tim50^{IMS}$ interaction remained stable in our PC-nanodiscs system even at the highest substrate concentration (**Figure 6.4B**), the proximity between the two receptor domains kept decreasing as the concentration of substrate was increased *in organello* (**Figure 6.3B**). Interestingly, the presence of substrate in increasing amounts had a mutually exclusive effect on Tim50's interaction with the two domains of Tim23 in both our systems. These results suggest that certain factors in the inner membrane environment keep the $Tim50^{IMS}$ receptor domain proximal to the channel region of Tim23 in an active translocation state. This finding has implications on the role of $Tim50^{IMS}$ to act as a membrane barrier and prevent the diffusion of ions across the IM when the channel is engaged with substrate.

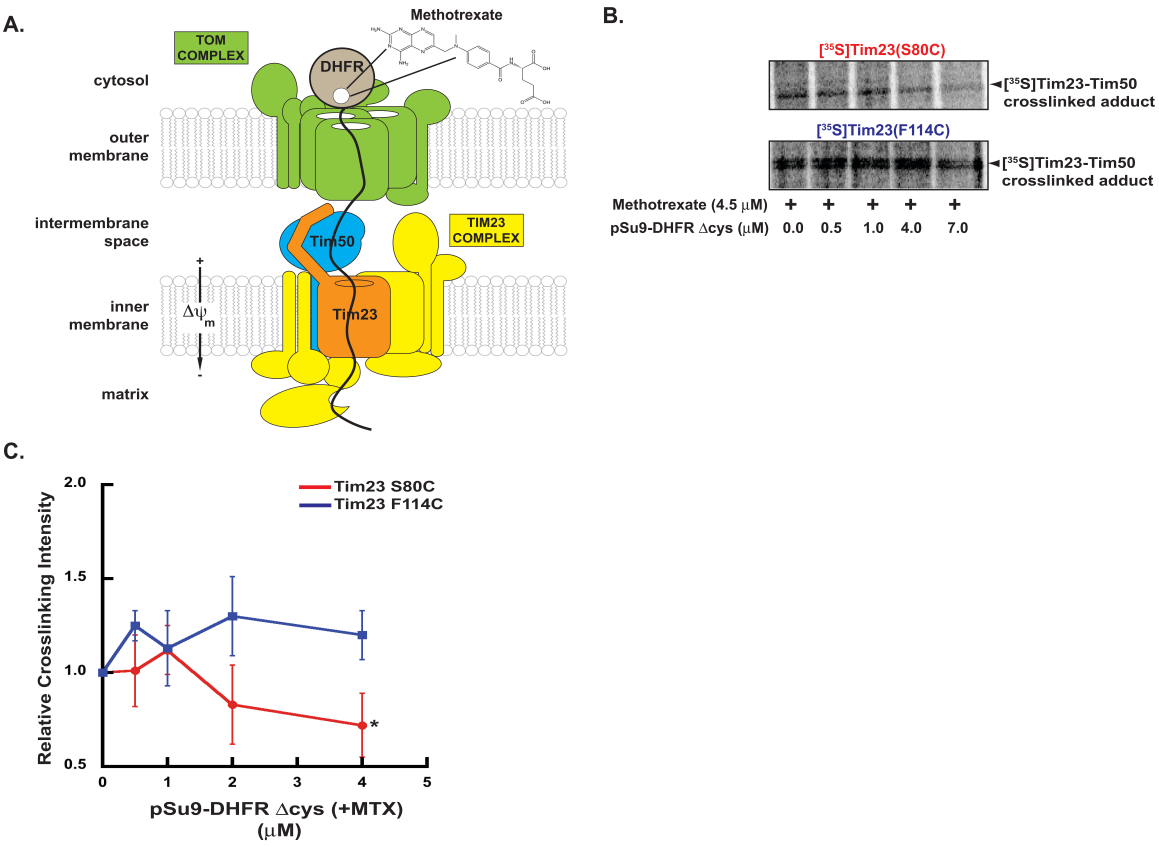

Figure 6.3 *Effect of the Presence of Substrate on Tim23-Tim50 Interactions In Organello*

A. Schematic representation of the TOM (green) and TIM (yellow) translocases with model substrate, pSu9-DHFR. Tim23 is shown in orange and Tim50 is depicted in cyan. Addition of MTX to pSu9-DHFR stabilizes the folded state of DHFR domain (gray) and blocks it from traversing the OM. Meanwhile, the presequence, pSu9 (69 amino acids; string) forms a translocation intermediate by engaging with the TIM23 complex **(Eilers & Schatz, 1986)**.

B. Crosslinking between [^{35}S]Tim23 (S80C and F114C) and Tim50 in the presence of different concentrations of pSu9-DHFR treated with 4.5 μM MTX.

C. Relative crosslinking intensities with pSu9-DHFR-MTX titration as seen above. The mean values and standard deviations of relative band intensities for three independent experiments are shown. * indicates significant difference in comparison to results from control (no substrate) by student's t-test (*$p<0.05$)

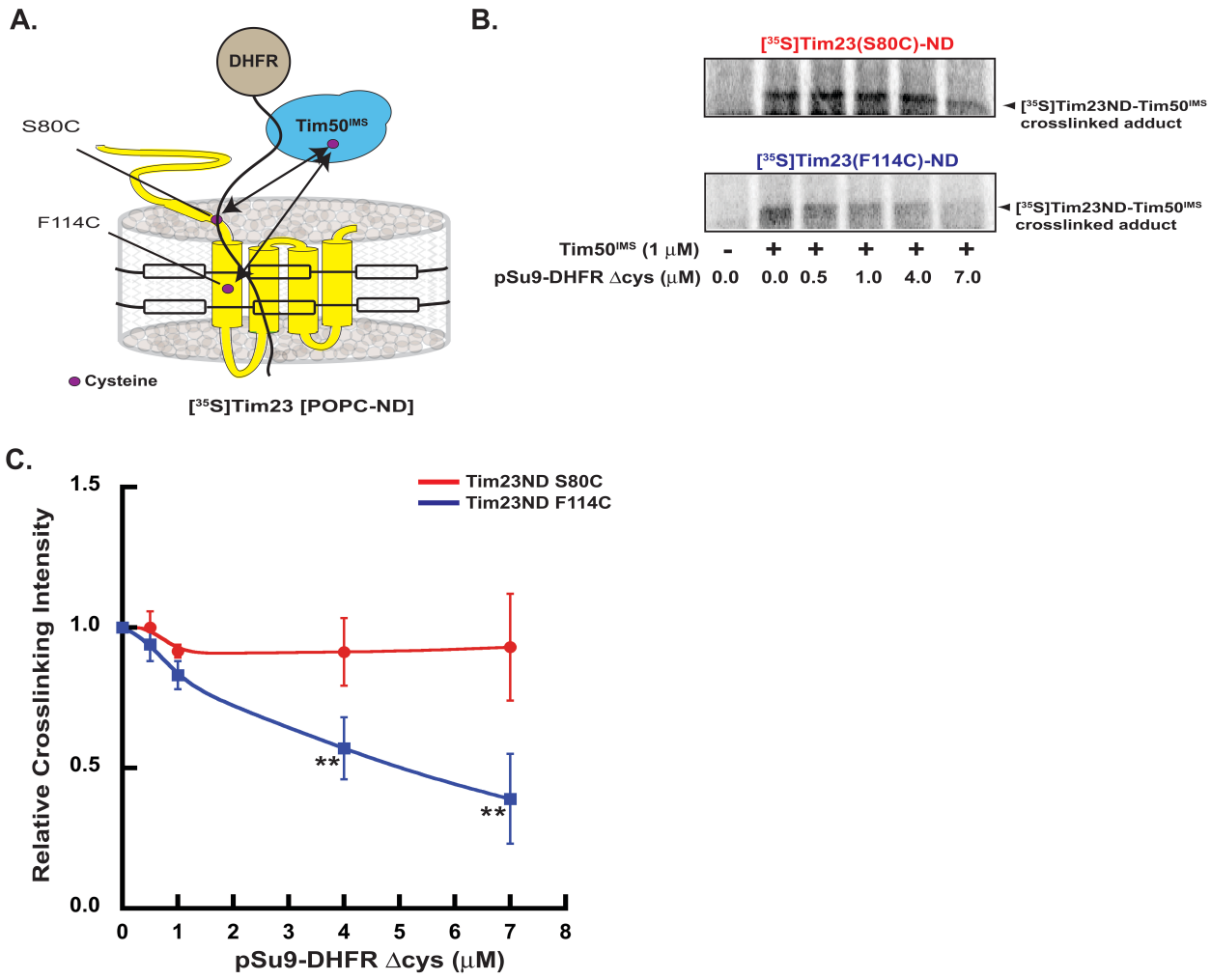

Figure 6.4 *Effect of the Presence of Substrate on Tim23-ND - Tim50^{IMS} Interactions*

A. Schematic representation of the [^{35}S]Tim23-ND (yellow) and its interaction with Tim50^{IMS} (cyan) in the presence of pSu9-DHFR (gray circle and string). Cysteine residues used for crosslinking are indicated by dots (magenta)

B. Crosslinking between [^{35}S]Tim23(S80C and F114C)-ND and Tim50^{IMS} in the presence of different concentrations of pSu9-DHFR.

C. Relative crosslinking intensities with pSu9-DHFR titration as seen above. The mean values and standard deviations of relative band intensities for three independent experiments are shown. * indicates significant difference in comparison to results from control (no substrate) by student's t-test (**p<0.01).

6.3 Discussion and Future Directions

Cardiolipin-Mediated Structural Changes in the Tim50^{IMS}

A large number of soluble proteins are known interact with membranes, which in turn impart structural changes in their membrane-interactive as well as non-interactive domains. For example, cardiolipin is well known to induce secondary and tertiary structure changes in the IMS protein cytochrome c, which in turn facilitates its peroxidase activity and leads to apoptosis **(Muenzner & Pletneva, 2014)**. In an earlier chapter of this study **(Chapter 4)**, we showed how cardiolipin influences proximity between the Tim50 receptor domain and Tim23 *via* its interactions with the Tim50^{IMS}. In this chapter, we take a step further and look at the potential structural changes that the Tim50^{IMS} undergoes in a CL-membrane bound state. We focus on the dynamics of the structurally illuminated Tim50^{core} in a CL-dependent manner, specifically of the cysteine bordering the Tim23 interactive region and the putative substrate interactive regions **(Qian et al., 2011)**. The only cysteine present in Tim50 is known to be in close contact with the IMS and TMS1 of Tim23 **(Alder et al., 2008b)**. Moreover, crosslinking analysis has found the same cysteine to be in proximity to the native cysteines present in the IMS domains of Tim23 and Tim21, triggering speculation of intermolecular disulfide linkages **(Lytovchenko et al., 2013)**. Here we show for the first time that in the presence of CL-containing membrane bilayers, the cysteine in question becomes more solvated, suggestive of local conformational changes in the core region. Further, proteolytic profile changes in the presence of CL-containing membrane bilayers suggest

enhanced backbone flexibility and unfolding of the core domain. Interestingly, a second reported crystal structure of the $Tim50^{core}$ also suggested inherent flexibility of that region **(Li & Sha, 2015)**. The implications of the CL-dependent flexibility of the $Tim50^{core}$ will be investigated in more detail in future work, but is suggestive to act as a switch between substrate-interactive and non-interactive states (see working model below). Also, in light of the flexible propensity of the cysteine in the core domain, its participation in the redox-regulated import process in the IMS and interaction with cysteine rich substrates cannot be ruled out **(Chacinska et al., 2009)**. Using complementary approaches like fluorescence spectroscopy **(Johnson, 2005)** and hydrogen-deuterium exchange mass spectrometry **(Rostislavleva et al., 2015)**, one more can precisely identify the dynamics of different domains in the $Tim50^{IMS}$ in the presence of CL-containing membrane bilayers. Additionally, the technique of Attenuated Total Reflection in conjunction with Infrared Spectroscopy (ATR-FTIR) can be used to look at the secondary structure changes in $Tim50^{IMS}$ accompanying its interaction with CL-containing vesicles. This way one can avoid the potential pitfalls of high scattering property of lipid vesicles that mars many useful spectroscopic investigations like circular dichroism **(Kong & Yu, 2007)**.

Substrate-Mediated Tim23-Tim50 Interactions

How the central components of the TIM23 complex, Tim23 and Tim50, co-ordinate with each other to carry out protein transport from the OM to the channel region in the IM remains a long standing debate in the field of mitochondrial biogenesis **(Schulz et al., 2015)**. By crosslinking analysis, the presence of presequence peptides, pALDH, was shown to increase the proximity between Tim23 and Tim50, but the study failed to dissect the peptide's effect on the individual interactions of Tim50 with the IMS domain and the channel-facing TMS1 of Tim23 **(Lytovchenko et al., 2013)**. It is also known that the presence of presequence-carrying substrate decreases Tim23-Tim23 and Tim23-Tim17 interaction, while also triggering Tim50-Tim21 dissociation **(Alder et al., 2008b; Lytovchenko et al., 2013)**. Here for the first time we investigate the effect of the presence of substrate on Tim50's interaction with the individual domains of Tim23, both in model-membrane system nanodiscs and *in organello*. Crosslinking-based analysis in both the systems revealed that Tim50 interacts with the individual domains of Tim23 in a mutually exclusive manner in the presence of substrate. This suggests shifting of interactions in an active translocation state, which is a hallmark of the highly dynamic presequence translocase pathway **(Wenz et al., 2014)**. It is intriguing to note the observed shift in the two systems, where complete opposite effects of the presence of substrate on Tim23-Tim50 interaction take place. While in our model-membrane system, $Tim50^{IMS}$ loses its hold of the TMS1 as the substrate concentration is increased; *in organello*, Tim50 is seen to maintain its proximity to the channel region under similar conditions. Also, $Tim50^{IMS}$ was observed to maintain its Tim23 receptor bound state even at the highest substrate concentration in the reductionist system,

whereas the opposite trend was observed *in organello*. The disparity in Tim23-Tim50 interactions seen between the two systems suggests a functional role played by one or more components of the IM to keep the Tim50-channel interaction intact that are missing from our reductionist system. It also points to the significance of maintaining Tim50-channel interactions in an active translocation state seen *in organello*, probably working to maintain the membrane barrier across the IM while transporting substrate across the channel. By systematically adding in lipids and proteins to our reductionist system and making it more like a native IM environment, one can identify the factors essential for Tim50-channel interaction when the substrate is present. In this study we show that CL plays an important role in mediating interaction between Tim50 and the channel region of Tim23. Repeating the experimental procedures of this chapter *in organello* with mitochondria isolated from yeast strains deficient in CL can suggest whether CL is involved in mediating the said Tim50-channel interaction in the presence of a substrate. To avoid any secondary effects of not having CL around, one can recapitulate the CL content of the IM in our reductionist system and then look at Tim50-channel interactions in the presence of substrate. One can also speculate on the role played by the TMS of Tim50 in maintaining contacts with the channel. This can also be analyzed by incorporating purified full-length Tim50 and Tim23 in nanodiscs followed by crosslinking-based proximity experiments. To ascertain the role played by the membrane potential across the IM, one can repeat the crosslinking experiments *in organello* after inducing depolarization across the IM **(Alder et al., 2008b)**. Additionally, using crosslinking-based analysis one can also investigate the interaction of substrate with different Tim23 domains, and how are they affected in the presence of the IMS

domain of Tim50. Experiments towards the above stated directions have already been initiated in our laboratory and are being currently explored.

6.4 Materials and Methods

pSu9-DHFR purification

The gene encoding for the recombinant protein, pSu9-DHFR, comprising the first 69 amino acids of subunit 9 of the F_O-ATPase fused to full-length dihydrofolate reductase with a C-terminal hexahistidine tag was cloned into the pET30a(+)vector (Novagen, Madison, WI). Monocysteine and cysteine-less variants of the construct were created using site-directed mutagenesis (Stratagene, San Diego, CA). For expression, the plasmid was then transformed into BL21 Star (DE3) cells (Invitrogen, Carlsbad, CA) and the cells were grown to A_{600} of 0.4-0.6. The cells were then induced with 1 mM IPTG for 2.5 h, and pelleted at 6,000 RPM for 20 min. Pelleted cells were then disrupted by resuspending the cells in lysozyme-containing resuspension buffer (50 mM $NaH_2PO_4.H_2O$, 300 mM NaCl, 5 mM Imidazole, 1.25 mg/ml lysozyme, pH 7.5) followed by sonication. The protein was purified from cell lysate on a Ni^{2+}-NTA matrix using an imidazole gradient [Wash 1- 25 mM, Wash 2- 60 mM, Elution 1- 200 mM, Elution 2- 400 mM] (Stan, Ahting, Dembowski, & Künkele, 2000).

Crosslinking in the presence of substrate

In organello and nanodiscs crosslinking between Tim23 and Tim50 was performed as described in Chapter 5. To look at the effect of substrate *in organello*, different concentrations of pSu9-DHFR were incubated with 4.5 µM Methotrexate (MTX) at 4°C for 10 min. Import of pSu9-DHFR + MTX was performed with 0.25 mg/ml mitochondria + [^{35}S]Tim23 at RT for 20 min. For crosslinking reactions performed in nanodiscs, reactions containing [^{35}S]Tim23-ND, 1 µM Tim50^{IMS}, and different concentrations of pSu9-DHFR were incubated at RT for 10 min followed by addition of crosslinker BMOE (50 µM). The crosslinking reactions were quenched and visualized as described in Chapter 5.

TMM(PEG)$_{12}$ labeling of Tim50^{IMS}

Purified Tim50^{IMS} (1 µM) was incubated at RT for 15 min in the presence or absence of different concentrations of PC and PC+CL LUVs. This was followed by addition of 2 mM TMM(PEG)$_{12}$ (Thermo Fisher Scientific, Waltham, MA) and incubation at RT for another 5 min. The reactions were quenched by adding 0.2 M DTT, and loaded on SDS-PAGE after adding equal volume of 2X sample buffer. The bands were visualized by SYPRO Orange staining. The gels were visualized and quantified using Bio-Rad PharosFXPlus Imager and Image lab 3.0 software respectively. The percentage of labeling was calculated as follows: Intensity of labeled product / Intensity of (labeled + unlabeled product) * 100.

BODIPY®-labeling and limited proteolysis

For BODIPY® labeling of $Tim50^{IMS}$, similar procedure was followed as for NBD labeling (Chapter 5). To carry out the labeling procedure, thiol-reactive BODIPY® FL iodoacetamide was used (Thermo Fisher Scientific, Waltham, CA). Limited proteolysis and visualization of proteolyzed bands was performed as described in Chapter 5.

Chapter 7

Working Model

In this chapter we synthesize our results from **Chapters 4 and 6** of this study and propose a working model on the Tim23-Tim50-substrate interactions in a native mitochondrial environment. Implicit in this model is our proposal that the soluble receptor domain of Tim50 is actually a peripheral membrane binding domain, which binds to the IM in a CL-dependent manner (**Figure 7.1A**). Mutational analysis as well as MD simulations have identified the importance of N-terminal region and specific residues on the conserved β-hairpin in $Tim50^{IMS}$ to be essential for mediating interaction between $Tim50^{IMS}$ and CL-containing membrane bilayers (**Figure 7.1A**). Moreover, by performing steady-state fluorescence measurements and lipid-binding analysis, we show that the β-hairpin in $Tim50^{IMS}$ samples hydrophobic milieu in the presence of CL-containing membrane bilayers. The first SAXS analysis of $Tim50^{IMS}$ also offered a glimpse into its *ab initio* envelope structure, which revealed a rod-like density sticking out from the molecular surface. Fitting of a $Tim50^{IMS}$ homology model into the envelope revealed that the best fit for the C-terminal end of $Tim50^{IMS}$ is a rod-like protrusion from the core domain. Importantly, $Tim50^{IMS}$ has been shown to be in close contact with the TOM complex of the OM where it is assumed that the $Tim50^{IMS}$ C-terminus is positioned close to the exit of Tom40 channel **(Mokranjac et al., 2009; Qian et al., 2011; Rahman et al., 2014; Shiota et al., 2011; Tamura et al., 2009b)**. This puts the C-terminal end of $Tim50^{IMS}$ in our working model to be positioned proximal to the TOM complex machinery, where the suggested presequence binding domain on the C-terminus (PBD1) **(Lytovchenko et al., 2013; Rahman et al., 2014; Schulz et al., 2011)** lies at the exit of Tom40 channel, whereas the N-terminus and β-hairpin of $Tim50^{IMS}$ are bound to the CL-rich IM (**Figure 7.1A-B**). Moreover, if we look at this model dimensionally, the

calculated distance between the IM-bound N-terminal end and a region close to the exit of Tom40 channel in our $Tim50^{IMS}$ homology model is ~ 11 nm (**Figure 7.1A**). The closest reported distance between the OM and the IM is ~12 nm, which is equal to the sum of reported width of the two membranes **(Reichert and Neupert, 2002)** (**Figure 7.1A**). In fact, the two membranes are known to be in close contact with each other in the presence of substrate **(Donzeau., et al., 2000)**. This puts our working model with the N-terminus of $Tim50^{IMS}$ bound to the IM and the C-terminus close to the OM within the range of reported values of distance beween the two membranes. However, it is worthy to note that this state might represent just one of the many possible conformations for $Tim50^{IMS}$ in the IMS, varying with different stages of protein translocation. For example, the state depicted in **Figure 7.1A-B** might represent the early translocation stage, where the PBD1 of $Tim50^{IMS}$ is optimally positioned to receive substrates from the TOM complex (see below).

Further, this model has implcations for the interactions between Tim50 and the channel-facing TMSs (TMS1 and TMS2) of Tim23, where our crosslinking-based proximity analysis with Cys268 near the β-hairpin and presquence binding domain of $Tim50^{core}$ (PBD2) has suggested that both, CL and the coiled-coil region of $Tim23^{IMS}$, mutually reinforce the interaction between $Tim50^{IMS}$ and the channel region of Tim23 (**Figure 7.1B**). Moreover, we find that basic residues in the $Tim50^{IMS}$ β-hairpin, identified in a previous study to be important for mediating Tim23-Tim50 interactions **(Qian et al., 2011),** are also invloved in $Tim50^{IMS}$ binding to CL-containing bilayers. Combined with our studies on CL-mediated $Tim50^{IMS}$ structural changes and substrate-mediated

Tim23-Tim50 interactions, this working model also offers insights into the mechanism of substrate transport. Presequence-carrying substrate upon its exit from the Tom40 channel encounters the first presequence binding domain (PBD1) on the C-terminal end of $Tim50^{IMS}$ (**Figure 7.1A-B**). The $Tim50^{core}$ is also suggested to have a second presequence binding site (PBD2) **(Qian et al., 2011; Li and Sha, 2015)**. Moreover, binding of $Tim50^{core}$ to PBD1 is thought to facilitate the transfer of preproteins from PBD1 to PBD2, suggestive of a flexible $Tim50^{core}$ domain **(Rahman et al., 2014)**. Limited preoteolysis and labeling data from this study suggests that CL promotes structural rearrangements within the $Tim50^{core}$, which could facilitate binding of $Tim50^{core}$ to PBD1 of the C-terminus. The presequence-containing preprotein is then transferred to the receptor domain of Tim23, which in turn directs preprotein into the channel region of IM formed in part by TMS1 and TMS2 of Tim23 in a $\Delta\Psi_m$-dependent manner **(Alder et al., 2008a; Pareek et al., 2013)**. Moreover, in this study, we show that in the presence of substrate the $Tim50^{IMS}$ loses its hold over the IMS-facing receptor module of Tim23 while still maintaining contacts with the channel region of Tim23. By maintaining its interaction with the channel region of Tim23, $Tim50^{IMS}$ makes sure that the sanctity of the IM permeability barrier is maintained to avoid any changes in the electrochemical gradient across the IM while carrying out translocation of preproteins **(Meinecke, 2006)**. Overall, this model provides the structural and mechanistic basis of Tim23-Tim50 interactions mediated by the IM-resident phospholipid cardiolipin, and its implications in substrate transport and maintainance of the $\Delta\Psi_m$ across the IM.

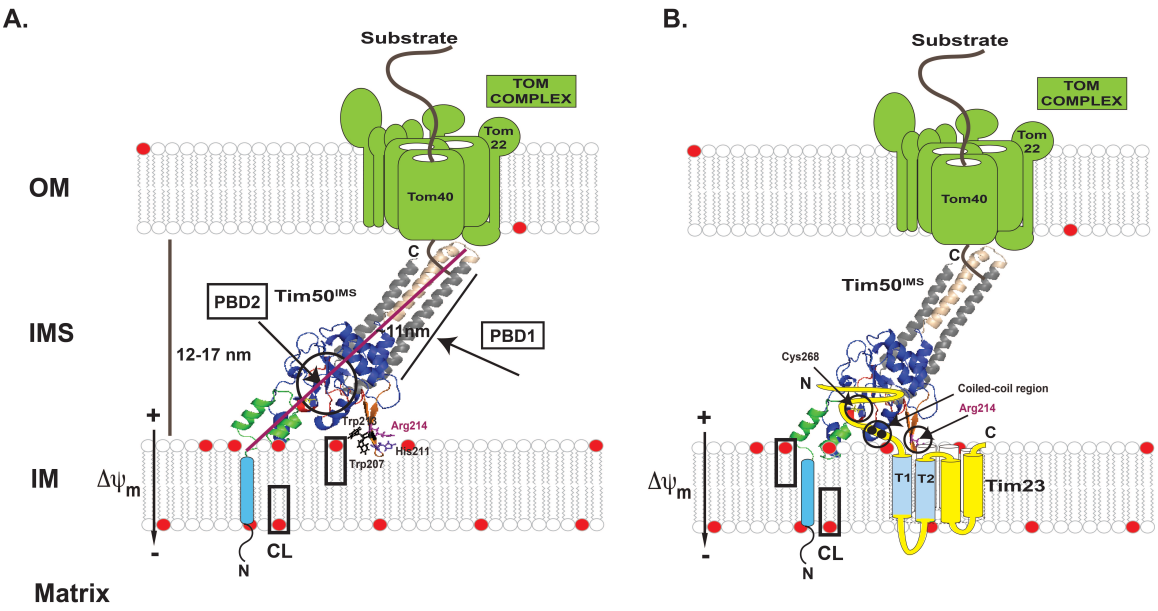

Figure 7.1 *Working Model for Cardiolipin- and Substrate-Mediated Interactions of the Mitochondrial Presequence Translocase*

A. Homology model of the full-length Tim50^{IMS} with different regions highlighted; N-terminus (green), core (blue), β-hairpin (orange), presequence binding domain 1 (gray, "PBD1") and presequence binding domain 2 (red, "PBD2"). The Tim50^{IMS} is depicted to be anchored in the inner membrane ("IM") by an N-terminal transmembrane segment (cyan) preceded by a matrix-facing loop. The cardiolipin (red circles) interacting residues on a β-hairpin are marked and depicted as sticks. TOM complex of the OM is depicted in green with Tim50^{IMS} proximal subunits (Tom40 and Tom22) highlighted **(Shiota et al., 2011; Tamura, et al., 2009b)**. The reported distance between the OM and the IM (~12-17 nm) is shown by straight line (brown) **(Reichert and Neupert, 2002)**. The calculated distance between the extreme N-terminus of Tim50^{IMS} and a residue close to PBD1 (~11 nm) is shown by a slanted line (purple). The distance between the two residues in Tim50^{IMS} homology model was calculated using PyMol.
B. Tim23 (yellow) with an IMS-facing N-terminus and four transmembrane segments is shown to be anchored in the IM. The Tim50 interactive coiled-coil region in Tim23^{IMS} is highlighted with Y70 and L71 residues (black circles). Channel-facing transmembrane segments, TMS1 (T1) and TMS2 (T2) of Tim23 are highlighted (blue). The cysteine at position 268 (Cys268) in Tim50^{IMS} used for crosslinking-based proximity analysis with Tim23 in this study is highlighted and depicted as stick (yellow), alongwith CL- and –Tim23 interactive arginine at position 214 (Arg214). For clarity purposes, only Tim23 and Tim50 of the TIM23 complex are depicted. We do acknowledge that other subunits within the complex could be important for mediating Tim23-Tim50 interactions.

Appendix A: Stepwise Protocol for the Reconstitution of Cell-Free Translated Tim23 Into Nanodiscs

A.1 Preparation of Wheat Germ Extract

A.1.1 Summary

The protocol for making wheat germ extract is modified from Erickson and Blobel (Erickson & Blobel, 1983). First, the wheat germ is floated, which enriches viable and intact embryos. Subsequently, the extract is prepared in three steps: homogenization of the floated germ, homogenate centrifugation, and gel filtration of the supernatant.

A.1.2 Materials and Solutions

1. Wheat germ, untreated (Sigma W-0125).

2. Mortar and pestle, six inch.

3. Floatation Solvent: carbon tetrachloride and cyclohexane (600:200, v/v).

4. Homogenization Buffer: 40 mM HEPES-KOH, pH 7.5, 100 mM KOAc, 1 mM $Mg(OAc)_2$, 2 mM $CaCl_2$, and 4 mM DTT.

5. Column Buffer: 40 mM HEPES-KOH, pH 7.5, 100 mM KOAc, 5 mM $Mg(OAc)_2$, and 4 mM DTT.

6. Buchner funnel and Whatman filter paper # 1.

7. Centrifuge and 50 ml centrifuge tubes.

8. Column (2.5 cm wide x 28 cm length; bed volume 140 ml) packed with gel filtration medium (Sephadex G-25, fine) and equilibrated with Column Buffer.

9. Fraction collector.

10. 1% (v/v) SDS.

11. Absorbance spectrophotometer and 1 ml quartz cuvette.

A.1.3 Methods

A.1.3.1 Floatation of Wheat Germ

1. Prepare floatation solvent in a 1 L beaker in a ventilated hood. Stir with a glass rod until no schlieren lines are visible.

2. Carefully pour 50 g of wheat germ to the top of the solution and gently stir. During the 2-3 minute separation process, damaged embryos will settle and intact, viable embryos will float.

3. Decant the floating embryos into a Buchner funnel fitted with Whatman filter #1 and dry the wheat germ embryos by pulling air through the funnel for 30 min.

4. Spread the dried wheat germ onto sterile foil to continue drying in fume hood.

5. Repeat steps 1-4 with another 50 g of wheat germ.

6. Combine and weigh the dried embryos. The target yield of the floated wheat germ is 30-40% (w/w).

A.1.3.2 Preparation of Wheat Germ Extract

1. Place dried wheat germ in a pre-chilled 6 in. mortar, cover with liquid N_2, and grind wheat germ to a fine powder with a pestle. The total grinding time should be about 2 min. Add the dried powder to a sterile sheet of foil.

2. Add Homogenization Buffer to the mortar at a sufficient volume to saturate the powder, slowly add powdered wheat germ, and grind until a thick paste is obtained.

3. Transfer the homogenate into two 50 ml pre-chilled centrifuge tubes using sterile rubber policemen. Centrifuge at 23,000 x g at 4°C for 10 min.

4. Transfer the supernatant to fresh 50 ml centrifuge tubes using a sterile Pasteur pipette.

5. Repeat centrifugation step (23,000 x g at 4°C for 10 min) and transfer the supernatants to a fresh tube. Measure the exact volume.

6. Perform gel filtration of the extract by adding supernatant to the G-25 column and elute with Column Buffer under gravity flow. Collect eluate in 1 ml fractions.

7. Measure the absorbance of each fraction at 260 and 280 nm by adding 5 µl fraction to 1 ml of 1% (v/v) SDS in a quartz cuvette with a spectrophotometer blanked with 5 µl of column buffer and 1 ml of 1% (v/v) SDS.

8. Pool the most turbid fractions into a sterile 50 ml centrifuge tube, aliquot into microfuge tubes, flash freeze in liquid N_2, and store at -80°C.

A.2 *In Vitro* Transcription

A.2.1 Summary

We used *in vitro* transcription to generate single stranded mRNA fragments to be used for the translation reaction. In this protocol, we used PCR to linearize the template DNA plasmid instead of restriction endonuclease(s).

A.2.2 Materials and Solutions

1. SP6 promoter-containing vector with gene of interest (in our case Tim23 from *S. cerevisiae*).

2. Primers for DNA amplification of the ORF. The upstream (5') oligonucleotide is complementary to the plasmid SP6 promoter and the downstream (3') oligonucleotide is complementary to the gene sequence downstream of the stop codon.

3. DNA polymerase (Bio-Rad # 170-8870) and dNTP mix (Bio-Rad # 170-8874).

4. PCR cleanup kit (QIAquick PCR purification kit, Qiagen # 28106).

5. PCR thermal cycler and thin-walled PCR tubes.

6. Refrigerated microcentrifuge.

7. Transcription Buffer (10X Master Mix): 1M HEPES-KOH, pH 7.5, 200 mM $MgCl_2$, and 25 mM spermidine.

8.100 mM DTT.

9. Ribonucleotide (rNTP) solution mixture: 100 mM each of ATP, GTP, UTP and CTP in 20 mM Tris-HCl, pH 7.5.

10. 0.1 U/µl diguanosine triphosphate [G(5')ppp(5')G] (New England Biolabs # S1407).

11. 20 U/µl Ribonuclease Inhibitor (RNasin).

12. 0.05 U/µl pyrophosphatase.

13. SP6 RNA Polymerase.

14. 3M NaOAc, pH 5.2.

15. 100% Ethanol.

16. TE Buffer (10 mM Tris, pH 7.5, 1 mM EDTA, pH 7.5).

17. Rotary evaporator.

A.2.3 Methods

A.2.3.1 PCR Amplification of DNA Fragments

1. Assemble the PCR reaction mixture (**Table A.1**) in a PCR tube.

2. Add the reaction to a PCR thermal cycler programmed as follows first denature (94°C, 4 min); 30 cycles of amplification (denature 94°C, 20 s; anneal 54°C, 20 s; extension 72°C, 30 s); final extension (72°C, 4 min). Optimal annealing temperature and time lengths will vary for different constructs.

3. Purify the amplified DNA fragment using the QIAquick PCR purification kit and elute with 50 µl of RNase-free H_2O.

Table A.1 ***PCR Protocol***

Component	Volume (µl)	Final concentration
Nuclease-free dH_2O	80.5	n/a
10X PCR buffer	10.0	1X
10 mM dNTP mix	2.0	0.2 mM, each dNTP
50 mM $MgCl_2$	4.0	2 mM
50 µM forward primer	1.0	0.5 µM
50 µM reverse primer	1.0	0.5 µM

100 ng/µl DNA template	1.0	1 ng/µl
DNA polymerase (5U/µl)	0.5	0.013 U/µl
Total	**100.0**	

A.2.3.2 In Vitro Transcription Reaction

1. Assemble the *in vitro* transcription mixture (**Table A.2**) in a 1.5 ml microfuge tube and incubate the reaction at 37°C for 1.5 h.

2. Isolate and purify RNA by adding reaction to 340 µl of 100% ethanol and 13.3 µl of 3M NaOAc (pH 5.2) and precipitating mRNA on ice for 2 h; pelleting samples at maximum speed in a microfuge (4°C) and carefully aspirating supernatant; washing pellet with 1 ml 70% (v/v) ethanol, re-centrifuging and aspirating supernatant; drying pellet in a rotary evaporator for 5 min; and resuspending mRNA pellet in 100 µl TE (pH 7.5).

3. Aliquot mRNA in volumes of 25 µl each, flash-freeze in liquid N_2 and store at - 80°C.

Table A.2 ***In Vitro Transcription Protocol***

Component	Volume (µl)	Final concentration
Nuclease-free d_2H_2O	43.3	n/a
10X transcription buffer	10.0	100 mM HEPES, pH 7.5 20 mM $MgCl_2$ 2.5 mM spermidine
100 mM DTT	10.0	10 mM
100 mM rNTP mixture	4.0	4 mM, each rNTP
0.1 U/µl (5')ppp(5')G	13.0	0.013 U/µl
20 U/µl RNasin	2.0	0.4 U/µl
PCR product DNA	13.0	variable
SP6 RNA polymerase	3.5	variable
0.5 U/µl Pyrophosphatase	1.2	0.006 U/µl
Total	**100.0**	

A.3 MSP Preparation

A.3.1 Summary

Several variants of MSP have been described (Denisov et al., 2004). Among them, plasmids comprised of the pET28a vector with the MSP coding sequence are available in the Addgene repository. These contain an N-terminal 6XHistag, which can be used to purify Target protein-ND assembly using Ni^{2+}-NTA chromatography. In this protocol we describe purification of a MSP variant, MSP1E3D1.

A.3.2 Materials and Solutions

1. YT Culture Media: 0.5% (w/v) yeast extract, 0.8% (w/v) tryptone, 80 mM NaCl.
2. YT-Agar Selective Media: 0.5% (w/v) yeast extract, 0.8% (w/v) tryptone, 80 mM NaCl, 0.75% (w/v) agar, 25 µg/ml kanamycin.
3. SOC Media: 0.5% (w/v) yeast extract, 2% (w/v) tryptone, 8.5 mM NaCl, 2.5 mM KCl, 10 mM $MgCl_2$, 20 mM D-glucose.
4. 20% (w/v) D-glucose, filter sterilized with 0.22 µm filter.
5. BL21 (DE3) Star competent *E. coli* cells (Invitrogen).
6. pET28a:MSP1E3D1 plasmid DNA.
7. 50 mg/ml kanamycin.
8. 1M isopropyl-β-D-thiogalactopyranoside (IPTG) in H_2O.
9. 500 mM phenylmethanesulfonylfluoride (PMSF) in 100% ethanol.
10. 10% (v/v) TritonX-100.
11. Ni^{2+}-NTA agarose.

12. Resuspension Buffer: 20 mM Na-phosphate, pH 7.5.

13. Column Wash 1 Buffer: 40 mM Tris-HCl, pH 8.0, 300 mM NaCl, 1% (v/v) TritonX-100.

14. Column Wash 2 Buffer: 40 mM Tris-HCl, pH 8.0, 300 mM NaCl, 20 mM imidazole, 50 mM Na-cholate.

15. Column Wash 3 Buffer: 40 mM Tris-HCl, pH 8.0, 300 mM NaCl, 50 mM imidazole.

16. Column Elution Buffer: 40 mM Tris-HCl, pH 8.0, 300 mM NaCl, 400 mM imidazole.

17. Dialysis Buffer: 20 mM Tris-HCl, pH 7.5, 100 mM NaCl, 0.5 mM EDTA.

A.3.3 Methods

A.3.3.1 MSP1E3D1 Expression

1. Transform pre-chilled BL21 (DE3) Star cells with 25 ng pET28a:MSP1E3D1 plasmid DNA by incubation on ice for 30 min, heat shock at 42°C for 45 s, and recovery at 37°C in 0.95 ml SOC Media for 1 h.

2. Plate 100 µl transformed cells on kanamycin-selective plates and incubate overnight at 37°C.

3. Prepare 100 ml growth medium (100 ml YT culture medium, 0.2% (w/v) filter-sterilized glucose, 25 µg/ml kanamycin), divide into several 5 ml aliquots in culture tubes, inoculate each with individual colonies from transformation plate and grow overnight (37°C, 250 rpm).

4. Prepare 4 x 500 ml growth medium (500 ml YT culture medium, 0.2% (w/v) filter-sterilized glucose, 25 µg/ml kanamycin), inoculate each with 1 ml overnight culture and

grow (37°C, 250 rpm) to OD_{600} = 0.8 to 1.0.

5. Induce expression by reducing growth temperature to 26°C, adding 1 mM IPTG, and continuing incubation for 3 h.

6. Harvest cells by centrifugation (4,000 x g for 20 min), decant medium, flash freeze pellets in liquid N_2 and store at -80°C.

A.3.3.2 *MSP1E3D1 Purification*

1. Thaw pellets from each 500 ml culture on ice and resuspend each pellet in 20 ml Resuspension Buffer with 1 mM PMSF. Add TritonX-100 to a final concentration of 1% (v/v).

2. Disrupt cells by ultrasonication in an ice bath using a microtip (50% amplitude, 60 s, total, five times). Clarify the lysate by centrifugation (30,000 x g for 30 min) and combine supernatants.

3. Equilibrate Ni-NTA agarose column (matrix bed 8 ml) with several column volumes (CV) of Column Wash 1 Buffer; load clarified lysate supernatant onto column and wash the column with 5 CV Column Wash 1 Buffer, 5 CV Column Wash 2 Buffer, 5 CV Column Wash 3 Buffer.

4. Elute MSP1E3D1 with Column Elution Buffer (10x~ 1 ml fractions). Pool protein-containing fractions, add to dialysis cassette (MWCO 2,000) and dialyze overnight at 4°C in 3 l Dialysis Buffer with one buffer exchange.

5. Measure MSP concentration by A280 and known molar extinction coefficients (Figure 2). Aliquot stocks into 250 µl, flash freeze in liquid N_2 and store in -80°C.

Table A.3 ***Lipid-Only Biomimetic Nanodiscs Assembly Reaction***

Component	Volume (µl)	Final concentration
20.5 mM lipid blend	590	4.8 mM POPC 1.2 mM TOCL
200 µM MSP1E3D1	0	n/a
ND-Buffer A	1410	n/a
Total	**2000**	

A.4 Assembly of Nanodiscs with Tim23

A.4.1 Summary

In this step we incorporate *in vitro* translated Tim23 into nanodiscs using either pre-formed discs or adding the translation reaction into a nanodisc-forming mix comprising of desired lipids and MSP.

A.4.2 Materials and Solutions

1. Pyrex 50 ml round-bottom centrifuge tube.

2. Rotary evaporator.

3. Source of compressed nitrogen gas.

4. Stocks of synthetic lipids in chloroform, including: a) 1-hexadecanoyl-2-(9Z-octacecenoyl)-*sn*-glycero-3-phosphocholine (POPC; Avanti #850457C); b) 1,1′,2,2′-

tetra-(9Z-octadecenoyl) cardiolipin (TOCL; Avanti #710335C).

5. ND Buffer A: 20 mM Tris-HCl, pH 7.5, 100 mM NaCl, 0.5 mM EDTA.

6. ND Buffer B: 20 mM Tris-HCl, pH 7.5, 100 mM NaCl, 0.5 mM EDTA, 59 mM Na-cholate.

7. ND Column Buffer 1: 40 mM Tris-HCl, pH 8.0, 300 mM NaCl.

8. ND Column Buffer 2: 40 mM Tris-HCl, pH 8.0, 300 mM NaCl, 400 mM imidazole.

9. ND Storage Buffer: 20 mM HEPES-KOH, pH 7.5, 200 mM NaCl, 50 mM KOAc, 5 mM $Mg(OAc)_2$, 5% (v/v) glycerol.

10. Laboratory vortex mixer.

11. Bath sonicator.

12. 15 ml conical tubes.

13. Laboratory rotisserie.

14. BioBeads SM-2 (Bio-Rad) hydrophobic adsorbents.

15. Column with Ni^{2+}-NTA agarose matrix.

16. Amicon Ultra Centrifugal filter Units (Millipore), 3,000 MWCO, 5 ml capacity.

17. Translation Buffer (10X): 200 mM HEPES-KOH, pH 7.5, 1 M KOAc, pH 7.5, 25 mM $Mg(OAc)_2$, 2 mM spermidine, 0.08 mM S-adenosylmethionine.

18. Protease Inhibitor Mixture (200X): 50 µg/ml each of Antipain, Chymostatin, Leupeptin, Pepstatin A and 5% (v/v) of Aprotinin.

19. Energy Generating System and Amino Acid Mixture (EGS): 90 mM HEPES-KOH, pH 7.5, 15 mM ATP, pH 7.5, 15 mM GTP, pH 7.5, 120 mM creatine phosphate, 0.12 U/µl creatine phosphokinase, 0.38 mM each of 20 common L-amino acids except for methionine in case of *in vitro* translation of [^{35}S]Tim23 and cysteine in case of *in vitro*

translation of NBD-Tim23.

20. Wheat germ extract (prepared as in Step A.1)

21. L-[^{35}S]-methionine or NBD-Cys-tRNA^{cys}.

A.4.3 Methods

A.4.3.1 Preparation of Solubilized Lipids

1. Assemble the desired lipid blend by combining chloroform stocks of lipids in a 50 ml round bottom tube using a Hamilton syringe. To assemble POPC and TOCL lipid combination (80 mol% POPC, 20 mol% TOCL), add 0.4 ml of POPC and 0.2 ml of TOCL.

2. Evaporate the chloroform under a gentle nitrogen stream in a fume hood.

3. Cover the tube with parafilm with small hole on top and place in vacuum dessicator for a minimum of two hours to remove all traces of organic solvent.

4. Hydrate the lipid film by adding 0.8 ml of ND Buffer B (the concentration of cholate should be at least twice the concentration of lipid), vortexing lipids into solution, and placing in a bath sonicator for a total of four x one minute cycles until suspension is clear.

A.4.3.2 Assembly of Lipid-Only Nanodiscs (for Co-Translational Assembly Only)

1. Prepare a 2 ml lipid-only nanodisc assembly reaction in a 15 ml conical tube by assembling cholate-solubilized lipids (from Section 4.3.1) and MSP (from Section A.3) at optimized molar ratios and adjusting the volume with ND Buffer A as shown in **Table A.3**. Incubate assembly for 30 min.

2. Prepare BioBeads by adding 1.5 g of dry beads to a 15 ml conical tube and hydrating with 1.0 ml of ND Buffer A on laboratory rotisserie for 30 min. Carefully remove buffer by pipetting.

3. Initiate the self-assembly reaction by adding the nanodisc assembly mixture to the conical vial containing pre-hydrated BioBeads. Incubate reaction on laboratory rotisserie for 2 h.

4. Affinity purify assembled nanodiscs via batch purification with Ni^{2+}-NTA agarose by adding 1 ml of Ni^{2+}-NTA beads (equilibrated with ND-Buffer A) to the assembly reaction and incubating for 45 min; adding slurry to chromatography column (approx. 0.8 cm wide x 4 cm length); preparing wash and elution buffers (**Table A.4**) and adding: 2 CV of Wash 1 Buffer, 2 CV of Wash 2 Buffer, 2 CV

of Wash 3 Buffer, and eluting with Elution Buffer in four-one ml fractions.

5. Perform nanodisc concentration and buffer exchange by adding elution fractions to 5 ml Millipore Centrifugal unit (3,000 MWCO), pre-equilibrated with ND Storage Buffer. Perform the following four times: centrifuge sample at 3,500 x g for 15-20 min at 4°C, discard eluate, add 3.0 ml ND Storage Buffer to nanodiscs sample in filter device. Finally, concentrate the sample to approximately 0.5 ml.

6. Purified nanodiscs can be used immediately in translation reactions. Alternatively,

they may be stored long-term by flash freezing in liquid N_2 and storage at -80°C.

Table A.4 ***Nanodiscs Affinity Purification Buffers***

	ND Column Buffer 1	ND Column Buffer 2
Buffer	Volume (ml)	Volume (ml)
Wash1 (no imidazole)	25.0	0.0
Wash2 (20 mM imidazole)	23.75	1.25
Wash3 (50 mM imidazole)	21.87	3.13
Elution (400 mM imidazole)	0	25.0

A.4.3.3 Co-translational Assembly of Tim23 into Nanodiscs

1. Assemble Translation Reaction with Nanodiscs (**Table A.5**) in a 1.5 ml microfuge tube and incubate the reaction at 26°C for 40 min.

2. Centrifuge the reaction mixture at 20,000 x g for 10 min to pellet precipitated protein, and transfer clarified supernatant containing nanodiscs with Tim23 protein to a new microfuge tube.

3. To re-purify and concentrate the [^{35}S]Tim23-containing nanodiscs, the sample can be subjected to a second round of Ni^{2+}-NTA based chromatography, exactly as detailed in Section 4.3.2, steps 4 and 5.

A.4.3.4 Post-translational Assembly of Tim23 into Nanodiscs

1. Assemble Translation Reaction without Nanodiscs (**Table A.5-6**) in a 1.5 ml centrifuge tube and incubate the reaction at 26°C for 40 min.

2. Prepare a 2 ml Tim23-nanodisc assembly reaction in a 15 ml conical tube by assembling cholate-solubilized lipids (from Section 4.3.1) and MSP (from Section A.3) at optimized molar ratios and adjusting the volume with ND Buffer A as shown in **Table A.3**. Incubate assembly for 30 min.

3. Prepare BioBeads by adding 1.5 g of dry beads to a 15 ml conical tube and hydrating with 1.0 ml of ND Buffer A on laboratory rotisserie for 30 min. Carefully remove buffer by pipetting.

4. Initiate the self-assembly reaction by adding the nanodiscs assembly mixture to the conical vial containing pre-hydrated BioBeads. Incubate reaction on laboratory rotisserie for 2 h.

5. Affinity purify assembled nanodiscs via batch purification with Ni^{2+}-NTA agarose by adding 1 ml of Ni^{2+}-NTA beads (equilibrated with ND-Buffer A) to the assembly reaction and incubating for 45 min; adding slurry to chromatography column (approx. 0.8 cm width x 4 cm length); preparing wash and elution buffers (**Table A.4**) and adding: 2 CV of Wash 1 Buffer, 2 CV of Wash 2 Buffer, 2 CV

of Wash 3 Buffer, and eluting with Elution Buffer in four-one ml fractions.

6. Perform nanodiscs concentration and buffer exchange by adding elution fractions to 5 ml Millipore Centrifugal unit (3,000 MWCO), pre-equilibrated with ND Storage Buffer. Perform the following four times: centrifuge sample at 3,500 x g for 15-20 min at 4°C, discard eluate, add 3.0 ml ND Storage Buffer to nanodisc sample in filter device. Finally, concentrate the sample to approximately 0.5 ml.

Table A.5 ***Translation Reaction***

	With Nanodiscs	No Nanodiscs	
Component	Volume (µl)	Volume (µl)	Final Concentration
Nuclease-free d_2H_2O	146.4	146.4	n/a
10X translation buffer	50	50	20 mM $HEPES^{7.5}$ 100 mM $KOAc^{7.5}$ 2.5 mM $Mg(OAc)_2$ 200 µM spermidine 8 µM S-adenosylmethionine
100 mM DTT	5.0	5.0	1 mM
200X protease inhibitors	2.6	2.6	1X

20 U/µl RNasin	2.6	2.6	0.1 U/µl
EGS	40	40	7.2 mM HEPES7.5 1.2 mM ATP7.5 1.2 mM GTP7.5 9.6 mM creatine phosphate 9.6 U/ml creatine phosphokinase 47.5 µM each amino acid
Wheat germ extract	100	100	20% (v/v)
10 µCi/µl [^{35}S]methionine	13.4	13.4	0.25µCi/µl
Tim23 mRNA	40	40	8% (v/v)
Purified nanodiscs	100	n/a	20% (v/v) nanodiscs
ND storage buffer	n/a	100	20% (v/v) buffer
Total	**500**	**500**	

Table A.6 *NBD-Tim23 Translation Reaction*

Component	Volume (µl)	Final Concentration
Nuclease-free d_2H_2O	139.8	n/a
10X translation buffer	50	20 mM $HEPES^{7.5}$ 100 mM $KOAc^{7.5}$ 2.5 mM $Mg(OAc)_2$ 200 µM spermidine 8 µM S-adenosylmethionine
100 mM DTT	5.0	1 mM
200X protease inhibitors	2.6	1X
20 U/µl RNasin	2.6	0.1 U/µl
EGS	40	7.2 mM HEPES7.5 1.2 mM ATP7.5 1.2 mM GTP7.5 9.6 mM creatine phosphate 9.6 U/ml creatine phosphokinase 47.5 µM each amino acid

Wheat germ extract	100	20% (v/v)
15 μM NBD-Cys-tRNA^{cys}	20	0.6 μM
Tim23 mRNA	40	8% (v/v)
ND storage buffer	100	20% (v/v) buffer
Total	**500**	

A.5 Gel-Based Analysis

A.5.1 Summary

In this step we prepare samples for visualization by performing SDS-PAGE. SDS-PAGE is followed by autoradiography to screen for [^{35}S]Tim23, and coomassie blue staining to detect the presence of MSP in our fractions.

A.5.2 Materials and Solutions

1. Mini-PROTEAN Tetra Cell (Bio-Rad 165-8004).
2. PowerPac Universal Power Supply (Bio-Rad 164-5070).
3. Mini-Protean TGX Precast Gel (Bio-Rad 456-1044S).

4. Electrophoresis running buffer (25 mM Sigma 7-9 buffer, 0.2 M glycine, 0.1 (w/v) sodiumdodecyl sulfate, 0.045% (w/v) bromophenol blue, 0.1 M DTT).

5. SDS-PAGE Sample Buffer (125 mM Tris-Base, 18%(v/v) glycerol, 3.6%(w/v) sodium dodecylsulfate, 0.045%(w/v) bromophenol blue, 0.1M DTT).

6. Destain solution (50%(v/v) methanol, 10%(v/v) acetic acid).

7. Coomassie stain solution (50%(v/v) methanol, 10%(v/v) acetic acid, 0.5%(w/v) Coomassie G-250).

8. Gel imaging system capable of imaging radiolabeled samples.

9. Gel drying apparatus (Bio-Rad 165-1789 Hydrotech system including Model 583 gel dryer and vacuum pump).

10. Imaging screen-K, 20 x 25 cm phosphor imaging screen (Bio-Rad 170-7843) and exposure cassette-K (Bio-Rad 170-7861).

11. ^{14}C-methylated protein molecular weight markers (Perkin-Elmer #NEC81100).

12. Precision Plus All Blue Prestained Standards (Bio-Rad 161-0373).

A.5.3 Methods

1. Set up the electrophoresis apparatus according to the manufacturer's instructions.

2. In separate microfuge tubes, pre-mix 5 µl nanodisc purification fractions (flow through, wash steps, elution steps, and concentrated samples) with an equal volume of SDS-PAGE Sample Buffer and heat at 65°C for 10 min prior to gel loading. For gels in radioisotope scans, add 5 µl of radiolabeled molecular weight markers to an equal volume of SDS-PAGE Sample Buffer; for coomassie gels, add 5 µl of all blue markers to an equal volume of SDS-PAGE Sample Buffer.

Quantitatively load all samples onto gel.

3. Run gels at 125 V until the bromophenol blue dye front reaches the bottom of the separating gel.

4. Prepare gels used for radioisotope scans by washing in 100 ml of Destain Solution for 10 min followed by two 10 min washes in water. Dry gels for 40 min at 80°C and place on phosphor imaging screen. Perform radioisotope scan on the molecular imager using the appropriate settings.

5. Prepare gels used for Coomassie stain by washing in 100 ml of coomassie Stain Solution for 30 min followed by multiple 20 min washes in 100 ml Destain Solution. Continue destain solution until signal from protein bands are sufficiently contrasted with background.

Table A.7 ***Tim23-Biomimetic Nanodiscs Assembly Reaction***

Component	Volume (µl)	Final concentration
20.5 mM lipid blend	590	4.8 mM POPC 1.2 mM TOCL
200 µM MSP1E3D1	500	50 µM
Tim23 translation	250	12.5% (v/v)
200X protease inhibitors	20	2X
ND-Buffer A	640	
Total	**2000**	

References

Acehan, D., Malhotra, A., Xu, Y., Ren, M., Stokes, D. L., & Schlame, M. (2011). Cardiolipin affects the supramolecular organization of ATP synthase in mitochondria. Biophysical Journal, 100(9), 2184–2192. doi:10.1016/j.bpj.2011.03.031

Alder, N.N. (2011). Biogenesis of lipids and proteins within biological membranes. in *The Structure of Biological Membranes* (ed. Yeagle, P.L.) 315-377 (CRC, 2011)

Alder, N. N., Jensen, R. E., & Johnson, A. E. (2008a). Fluorescence Mapping of Mitochondrial TIM23 Complex Reveals a Water-Facing, Substrate-Interacting Helix Surface. Cell, 134(3), 439–450. doi:10.1016/j.cell.2008.06.007

Alder, N. N., Sutherland, J., Buhring, A. I., Jensen, R. E., & Johnson, A. E. (2008b). Quaternary structure of the mitochondrial TIM23 complex reveals dynamic association between Tim23p and other subunits. Molecular Biology of the Cell, 19(1), 159–170. doi:10.1091/mbc.E07-07-0669

Allegrini, P. R., Pluschke, G., & Seelig, J. (1984). Cardiolipin conformation and dynamics in bilayer membranes as seen by deuterium magnetic resonance. Biochemistry.

Andersen, O. S., & Koeppe, R. E. (2007). Bilayer thickness and membrane protein function: an energetic perspective. Annual Review of Biophysics and Biomolecular Structure, 36, 107–130. doi:10.1146/annurev.biophys.36.040306.132643

Arias-Cartin, R., Grimaldi, S., Arnoux, P., Guigliarelli, B., & Magalon, A. (2012). Cardiolipin binding in bacterial respiratory complexes: structural and functional implications. Biochimica Et Biophysica Acta, 1817(10), 1937–1949. doi:10.1016/j.bbabio.2012.04.005

Atkinson, D., & Small, D. M. (1986). Recombinant lipoproteins: implications for structure and assembly of native lipoproteins. Annual Review of Biophysics and Biophysical Chemistry, 15, 403–456. doi:10.1146/annurev.bb.15.060186.002155

Baile, M. G., Lu, Y.-W., & Claypool, S. M. (2014a). The topology and regulation of cardiolipin biosynthesis and remodeling in yeast. Chemistry and Physics of Lipids, 179, 25–31. doi:10.1016/j.chemphyslip.2013.10.008

Baile, M. G., Sathappa, M., Lu, Y.-W., Pryce, E., Whited, K., McCaffery, J. M., et al. (2014b). Unremodeled and remodeled cardiolipin are functionally indistinguishable in yeast. The Journal of Biological Chemistry, 289(3), 1768–1778. doi:10.1074/jbc.M113.525733

Baile, M. G., Whited, K., & Claypool, S. M. (2013). Deacylation on the matrix side of the mitochondrial inner membrane regulates cardiolipin remodeling. Molecular Biology of the Cell, 24(12), 2008–2020. doi:10.1091/mbc.E13-03-0121

Bajaj, R., Jaremko, Ł., Jaremko, M., Becker, S., & Zweckstetter, M. (2014a). Molecular basis of the dynamic structure of the TIM23 complex in the mitochondrial intermembrane space. Structure (London, England : 1993), 22(10), 1501–1511. doi:10.1016/j.str.2014.07.015

Bajaj, R., Munari, F., Becker, S., & Zweckstetter, M. (2014b). Interaction of the intermembrane space domain of Tim23 protein with mitochondrial membranes. The Journal of Biological Chemistry, 289(50), 34620–34626. doi:10.1074/jbc.M114.595702

Ban, T., Heymann, J. A. W., Song, Z., Hinshaw, J. E., & Chan, D. C. (2010). OPA1 disease alleles causing dominant optic atrophy have defects in cardiolipin-stimulated GTP hydrolysis and membrane tubulation. Human Molecular Genetics, 19(11), 2113–2122. doi:10.1093/hmg/ddq088

Banerjee, R., Gladkova, C., Mapa, K., Witte, G., & Mokranjac, D. (2015). Protein translocation channel of mitochondrial inner membrane and matrix-exposed import motor communicate via two-domain coupling protein. eLife.

Baracca, A., Sgarbi, G., Solaini, G., & Lenaz, G. (2003). Rhodamine 123 as a probe of mitochondrial membrane potential: evaluation of proton flux through F0 during ATP synthesis. Biochimica Et Biophysica Acta (BBA) - Bioenergetics, 1606(1-3), 137–146. doi:10.1016/S0005-2728(03)00110-5

Bauer, M. F., Sirrenberg, C., Neupert, W., & Brunner, M. (1996). Role of Tim23 as voltage sensor and presequence receptor in protein import into mitochondria. Cell, 87(1), 33–41.

Bayburt, T. H., & Sligar, S. G. (2003). Self-assembly of single integral membrane proteins into soluble nanoscale phospholipid bilayers. Protein Science.

Bayburt, T. H., & Sligar, S. G. (2010). Membrane protein assembly into Nanodiscs. FEBS Letters, 584(9), 1721–1727. doi:10.1016/j.febslet.2009.10.024

Bayburt, T. H., Grinkova, Y. V., & Sligar, S. G. (2002). Self-Assembly of Discoidal Phospholipid Bilayer Nanoparticles with Membrane Scaffold Proteins. Nano Letters, 2(8), 853–856. doi:10.1021/nl025623k

Bazzacco, P., Billon-Denis, E., Sharma, K. S., Catoire, L. J., Mary, S., Le Bon, C., et al. (2012). Nonionic homopolymeric amphipols: application to membrane protein folding, cell-free synthesis, and solution nuclear magnetic resonance. Biochemistry, 51(7), 1416–1430. doi:10.1021/bi201862v

Beranek, A., Rechberger, G., Knauer, H., Wolinski, H., Kohlwein, S. D., & Leber, R. (2009). Identification of a cardiolipin-specific phospholipase encoded by the gene CLD1 (YGR110W) in yeast. The Journal of Biological Chemistry, 284(17), 11572–11578. doi:10.1074/jbc.M805511200

Bergstrom, C. L., Beales, P. A., Lv, Y., Vanderlick, T. K., & Groves, J. T. (2013). Cytochrome c causes pore formation in cardiolipin-containing membranes. Proceedings of the National Academy of Sciences of the United States of America, 110(16), 6269–6274. doi:10.1073/pnas.1303819110

Blesneac, I., Ravaud, S., Juillan-Binard, C., Barret, L.-A., Zoonens, M., Polidori, A., et al. (2012). Production of UCP1 a membrane protein from the inner mitochondrial membrane using the cell free expression system in the presence of a fluorinated surfactant. Biochimica Et Biophysica Acta, 1818(3), 798–805. doi:10.1016/j.bbamem.2011.12.016

Bogdanov, M., Zhang, W., Xie, J., & Dowhan, W. (2005). Transmembrane protein topology mapping by the substituted cysteine accessibility method (SCAM(TM)): application to lipid-specific membrane protein topogenesis. Methods, 36(2), 148–171. doi:10.1016/j.ymeth.2004.11.002

Bohnert, M., Rehling, P., Guiard, B., & Herrmann, J. M. (2010). Cooperation of stop-transfer and conservative sorting mechanisms in mitochondrial protein transport. Current Biology.

Botelho, S. C., Osterberg, M., Reichert, A. S., Yamano, K., Björkholm, P., Endo, T., et al. (2011). TIM23-mediated insertion of transmembrane α-helices into the mitochondrial inner membrane. The EMBO Journal, 30(6), 1003–1011. doi:10.1038/emboj.2011.29

Böttinger, L., Ellenrieder, L., & Becker, T. (2015). How lipids modulate mitochondrial protein import. Journal of Bioenergetics and Biomembranes. doi:10.1007/s10863-015-9599-7

Böttinger, L., Horvath, S. E., Kleinschroth, T., Hunte, C., Daum, G., Pfanner, N., & Becker, T. (2012). Phosphatidylethanolamine and cardiolipin differentially affect the stability of mitochondrial respiratory chain supercomplexes. Journal of Molecular Biology, 423(5), 677–686. doi:10.1016/j.jmb.2012.09.001

Brandner, K., Mick, D. U., Frazier, A. E., Taylor, R. D., Meisinger, C., & Rehling, P. (2005). Taz1, an outer mitochondrial membrane protein, affects stability and assembly of inner membrane protein complexes: implications for Barth Syndrome. Molecular Biology of the Cell, 16(11), 5202–5214. doi:10.1091/mbc.E05-03-0256

Brooks, B. R., Brooks, C. L., & MacKerell, A. D. (2009). CHARMM: the biomolecular simulation program. Journal of ….

Buckman, J. F., & Reynolds, I. J. (2001). Spontaneous changes in mitochondrial membrane potential in cultured neurons. The Journal of Neuroscience : the Official Journal of the Society for Neuroscience, 21(14), 5054–5065.

Bustad, H. J., Skjaerven, L., Ying, M., Halskau, Ø., Baumann, A., Rodriguez-Larrea, D., et al. (2012). The peripheral binding of 14-3-3γ to membranes involves isoform-specific histidine residues. PloS One, 7(11), e49671. doi:10.1371/journal.pone.0049671

Cacace, M. G., Landau, E. M., & Ramsden, J. J. (1997). The Hofmeister series: salt and solvent effects on interfacial phenomena. Quarterly Reviews of Biophysics, 30(3), 241–277.

Callaway, E. (2015). The revolution will not be crystallized: a new method sweeps through structural biology. Nature, 525(7568), 172–174. doi:10.1038/525172a

Cao, Z., & Bowie, J. U. (2012). Shifting hydrogen bonds may produce flexible transmembrane helices. Proceedings of the National Academy of Sciences of the United States of America, 109(21), 8121–8126. doi:10.1073/pnas.1201298109

Cappuccio, J. A., Blanchette, C. D., Sulchek, T. A., Arroyo, E. S., Kralj, J. M., Hinz, A. K., et al. (2008). Cell-free co-expression of functional membrane proteins and apolipoprotein, forming soluble nanolipoprotein particles. Molecular & Cellular Proteomics : MCP, 7(11), 2246–2253. doi:10.1074/mcp.M800191-MCP200

Chaban, Y., Boekema, E. J., & Dudkina, N. V. (2014). Structures of mitochondrial oxidative phosphorylation supercomplexes and mechanisms for their stabilisation. Biochimica Et Biophysica Acta, 1837(4), 418–426. doi:10.1016/j.bbabio.2013.10.004

Chacinska, A., Koehler, C. M., Milenkovic, D., Lithgow, T., & Pfanner, N. (2009). Importing Mitochondrial Proteins: Machineries and Mechanisms. Cell, 138(4), 628–644. doi:10.1016/j.cell.2009.08.005

Chacinska, A., Lind, M., Frazier, A. E., Dudek, J., Meisinger, C., Geissler, A., et al. (2005). Mitochondrial Presequence Translocase: Switching between TOM Tethering and Motor Recruitment Involves Tim21 and Tim17. Cell, 120(6), 817–829. doi:10.1016/j.cell.2005.01.011

Chacinska, A., van der Laan, M., Mehnert, C. S., Guiard, B., Mick, D. U., Hutu, D. P., et al. (2010). Distinct forms of mitochondrial TOM-TIM supercomplexes define signal-dependent states of preprotein sorting. Molecular and Cellular Biology, 30(1), 307–318. doi:10.1128/MCB.00749-09

Chakrapani, S., Sompornpisut, P., Intharathep, P., Roux, B., & Perozo, E. (2010). The activated state of a sodium channel voltage sensor in a membrane environment. Proceedings of the National Academy of Sciences of the United States of America, 107(12), 5435–5440. doi:10.1073/pnas.0914109107

Chang, S. C., Heacock, P. N., & Clancey, C. J. (1998). The PEL1 Gene (Renamed PGS1) Encodes the Phosphatidylglycero-phosphate Synthase ofSaccharomyces cerevisiae. Journal of Biological ….

Chicco, A. J., & Sparagna, G. C. (2007). Role of cardiolipin alterations in mitochondrial dysfunction and disease. American Journal of Physiology. Cell Physiology, 292(1), C33–44. doi:10.1152/ajpcell.00243.2006

Clarke, S. L. N., Bowron, A., Gonzalez, I. L., Groves, S. J., Newbury-Ecob, R., Clayton, N., et al. (2013). Barth syndrome. Orphanet Journal of Rare Diseases, 8, 23. doi:10.1186/1750-1172-8-23

Claypool, S. M., & Koehler, C. M. (2012). The complexity of cardiolipin in health and disease. Trends in Biochemical Sciences, 37(1), 32–41. doi:10.1016/j.tibs.2011.09.003

Claypool, S. M., Oktay, Y., Boontheung, P., Loo, J. A., & Koehler, C. M. (2008). Cardiolipin defines the interactome of the major ADP/ATP carrier protein of the mitochondrial inner membrane. The Journal of Cell Biology, 182(5), 937–950. doi:10.1083/jcb.200801152

Corin, K., Baaske, P., Ravel, D. B., Song, J., Brown, E., Wang, X., et al. (2011). Designer lipid-like peptides: a class of detergents for studying functional olfactory receptors using commercial cell-free systems. PloS One, 6(11), e25067. doi:10.1371/journal.pone.0025067

Cornette, J. L., Cease, K. B., Margalit, H., Spouge, J. L., Berzofsky, J. A., & DeLisi, C. (1987). Hydrophobicity scales and computational techniques for detecting amphipathic structures in proteins. Journal of Molecular Biology, 195(3), 659–685.

Cross, T. A., Murray, D. T., & Watts, A. (2013). Helical membrane protein conformations and their environment. European Biophysics Journal.

Crowley, K. S., Liao, S., Worrell, V. E., Reinhart, G. D., & Johnson, A. E. (1994). Secretory proteins move through the endoplasmic reticulum membrane via an aqueous, gated pore. Cell, 78(3), 461–471.

Crowley, K. S., Reinhart, G. D., & Johnson, A. E. (1993). The signal sequence moves through a ribosomal tunnel into a noncytoplasmic aqueous environment at the ER membrane early in translocation. Cell, 73(6), 1101–1115.

DAMMIN, M. (1999). Svergun. Restoring low resolution structure of biological macromolecules from solution scattering using simulated annealing. Biophys J.

Das, A., & Sligar, S. G. (2009). Modulation of the cytochrome P450 reductase redox potential by the phospholipid bilayer. Biochemistry, 48(51), 12104–12112. doi:10.1021/bi9011435

Das, A., Grinkova, Y. V., & Sligar, S. G. (2007). Redox potential control by drug binding to cytochrome P450 3A4. Journal of the American Chemical Society, 129(45), 13778–13779. doi:10.1021/ja074864x

Daum, G., Böhni, P. C., & Schatz, G. (1982). Import of proteins into mitochondria. Cytochrome b2 and cytochrome c peroxidase are located in the intermembrane space of yeast mitochondria. Journal of Biological Chemistry.

Davis, A. J., Ryan, K. R., & Jensen, R. E. (1998). Tim23p contains separate and distinct signals for targeting to mitochondria and insertion into the inner membrane. Molecular Biology of the Cell, 9(9), 2577–2593.

Dekker, P. J., Martin, F., Maarse, A. C., Bömer, U., Müller, H., Guiard, B., et al. (1997). The Tim core complex defines the number of mitochondrial translocation contact sites and can hold arrested preproteins in the absence of matrix Hsp70-Tim44. The EMBO Journal, 16(17), 5408–5419. doi:10.1093/emboj/16.17.5408

Demchenko, A. P., MEly, Y., Duportail, G., & Klymchenko, A. S. (2009). Monitoring Biophysical Properties of Lipid Membranes by Environment-Sensitive Fluorescent Probes. Biophysical Journal, 96(9), 3461–3470. doi:10.1016/j.bpj.2009.02.012

Demishtein-Zohary, K., Marom, M., Neupert, W., Mokranjac, D., & Azem, A. (2015). GxxxG motifs hold the TIM23 complex together. The FEBS Journal, 282(11), 2178–2186. doi:10.1111/febs.13266

Denisov, I. G., Grinkova, Y. V., Lazarides, A. A., & Sligar, S. G. (2004). Directed Self-Assembly of Monodisperse Phospholipid Bilayer Nanodiscs with Controlled Size. Journal of the American Chemical Society, 126(11), 3477–3487. doi:10.1021/ja0393574

DeVay, R. M., Dominguez-Ramirez, L., Lackner, L. L., Hoppins, S., Stahlberg, H., & Nunnari, J. (2009). Coassembly of Mgm1 isoforms requires cardiolipin and mediates mitochondrial inner membrane fusion. The Journal of Cell Biology, 186(6), 793–803. doi:10.1083/jcb.200906098

Dienhart, M. K., & Stuart, R. A. (2008). The yeast Aac2 protein exists in physical association with the cytochrome bc1-COX supercomplex and the TIM23 machinery. Molecular Biology of the Cell, 19(9), 3934–3943. doi:10.1091/mbc.E08-04-0402

Dolezal, P., Likic, V., Tachezy, J., & Lithgow, T. (2006). Evolution of the molecular machines for protein import into mitochondria. Science, 313(5785), 314–318. doi:10.1126/science.1127895

Donzeau, M., Káldi, K., Adam, A., Paschen, S., & Wanner, G. (2000). Tim23 links the inner and outer mitochondrial membranes. Cell.

Dörr, J. M., Koorengevel, M. C., Schäfer, M., Prokofyev, A. V., Scheidelaar, S., van der Cruijsen, E. A. W., et al. (2014). Detergent-free isolation, characterization, and functional reconstitution of a tetrameric K+ channel: the power of native nanodiscs. Proceedings of the National Academy of Sciences of the United States of America, 111(52), 18607–18612. doi:10.1073/pnas.1416205112

Dörr, J. M., Scheidelaar, S., Koorengevel, M. C., Dominguez, J. J., Schäfer, M., van Walree, C. A., & Killian, J. A. (2016). The styrene-maleic acid copolymer: a versatile tool in membrane research. European Biophysics Journal : EBJ, 45(1), 3–21. doi:10.1007/s00249-015-1093-y

Dürr, U. H. N., Gildenberg, M., & Ramamoorthy, A. (2012). The magic of bicelles lights up membrane protein structure. Chemical Reviews, 112(11), 6054–6074. doi:10.1021/cr300061w

Eilers, M., & Schatz, G. (1986). Binding of a specific ligand inhibits import of a purified precursor protein into mitochondria. Nature, 322(6076), 228–232. doi:10.1038/322228a0

Eilers, M., Endo, T., & Schatz, G. (1989). Adriamycin, a drug interacting with acidic phospholipids, blocks import of precursor proteins by isolated yeast mitochondria. The Journal of Biological Chemistry, 264(5), 2945–2950.

Endo, T., & Schatz, G. (1988). Latent membrane perturbation activity of a mitochondrial precursor protein is exposed by unfolding. The EMBO Journal, 7(4), 1153–1158.

Endo, T., Eilers, M., & Schatz, G. (1989). Binding of a tightly folded artificial mitochondrial precursor protein to the mitochondrial outer membrane involves a lipid-mediated conformational change. The Journal of Biological Chemistry, 264(5), 2951–2956.

Endo, T., Yamano, K., & Kawano, S. (2011). Structural insight into the mitochondrial protein import system. Biochimica Et Biophysica Acta (BBA) - Biomembranes, 1808(3), 955–970. doi:10.1016/j.bbamem.2010.07.018

Epand, R. F., Martinou, J.-C., Fornallaz-Mulhauser, M., Hughes, D. W., & Epand, R. M. (2002). The apoptotic protein tBid promotes leakage by altering membrane curvature. The Journal of Biological Chemistry, 277(36), 32632–32639. doi:10.1074/jbc.M202396200

Erickson, A. H., & Blobel, G. (1983). Cell-free translation of messenger RNA in a wheat germ system. Methods in Enzymology, 96, 38–50.

Erikson, A. H., & Blobel, G. (1983). Cell-free translation of a messenger RNA in a wheat germ system. Methods in Enzymology (USA).

Fontana, A., de Laureto, P. P., Spolaore, B., & Frare, E. (2004). Probing protein structure by limited proteolysis. Acta Biochimica ….

Fontana, A., de Laureto, P. P., Spolaore, B., & Frare, E. (2012). Identifying disordered regions in proteins by limited proteolysis. Methods in Molecular Biology (Clifton, N.J.), 896, 297–318. doi:10.1007/978-1-4614-3704-8_20

Franke, D., & Svergun, D. I. (2009). DAMMIF, a program for rapid ab-initio shape determination in small-angle scattering. Journal of Applied Crystallography.

Friedman, J. R., Mourier, A., Yamada, J., McCaffery, J. M., & Nunnari, J. (2015). MICOS coordinates with respiratory complexes and lipids to establish mitochondrial inner membrane architecture. eLife, 4. doi:10.7554/eLife.07739

Gallas, M. R., Dienhart, M. K., Stuart, R. A., & Long, R. M. (2006). Characterization of Mmp37p, a Saccharomyces cerevisiae mitochondrial matrix protein with a role in mitochondrial protein import. Molecular Biology of the Cell, 17(9), 4051–4062. doi:10.1091/mbc.E06-04-0366

Gaspard, G. J., & McMaster, C. R. (2015). Cardiolipin metabolism and its causal role in the etiology of the inherited cardiomyopathy Barth syndrome. Chemistry and Physics of Lipids, 193, 1–10. doi:10.1016/j.chemphyslip.2015.09.005

Gebert, M., Schrempp, S. G., Mehnert, C. S., Heisswolf, A. K., Oeljeklaus, S., Ieva, R., et al. (2012). Mgr2 promotes coupling of the mitochondrial presequence translocase to partner complexes. The Journal of Cell Biology, 197(5), 595–604. doi:10.1083/jcb.201110047

Gebert, N., Joshi, A. S., Kutik, S., Becker, T., McKenzie, M., Guan, X. L., et al. (2009). Mitochondrial cardiolipin involved in outer-membrane protein biogenesis: implications for Barth syndrome. Current Biology : CB, 19(24), 2133–2139. doi:10.1016/j.cub.2009.10.074

Gebert, N., Ryan, M. T., Pfanner, N., Wiedemann, N., & Stojanovski, D. (2011). Mitochondrial protein import machineries and lipids: a functional connection. Biochimica Et Biophysica Acta, 1808(3), 1002–1011. doi:10.1016/j.bbamem.2010.08.003

Geissler, A., Chacinska, A., Truscott, K. N., Wiedemann, N., Brandner, K., Sickmann, A., et al. (2002). The mitochondrial presequence translocase: an essential role of Tim50 in directing preproteins to the import channel. Cell, 111(4), 507–518.

Gevorkyan-Airapetov, L., Zohary, K., Popov-Čeleketić, D., Mapa, K., Hell, K., Neupert, W., et al. (2009). Interaction of Tim23 with Tim50 Is essential for protein translocation by the mitochondrial TIM23 complex. The Journal of Biological Chemistry, 284(8), 4865–4872. doi:10.1074/jbc.M807041200

Glick, B. S., Brandt, A., Cunningham, K., Müller, S., Hallberg, R. L., & Schatz, G. (1992). Cytochromes c1 and b2 are sorted to the intermembrane space of yeast mitochondria by a stop-transfer mechanism. Cell, 69(5), 809–822.

Glück, J. M., Wittlich, M., Feuerstein, S., Hoffmann, S., Willbold, D., & Koenig, B. W. (2009). Integral membrane proteins in nanodiscs can be studied by solution NMR spectroscopy. Journal of the American Chemical Society, 131(34), 12060–12061. doi:10.1021/ja904897p

Gohil, V. M. (2004). Cardiolipin Biosynthesis and Mitochondrial Respiratory Chain Function Are Interdependent. The Journal of Biological Chemistry, 279(41), 42612–42618. doi:10.1074/jbc.M402545200

Gohil, V. M., & Greenberg, M. L. (2009). Mitochondrial membrane biogenesis: phospholipids and proteins go hand in hand. The Journal of Cell Biology, 184(4), 469–472. doi:10.1083/jcb.200901127

Goldsmith, B. R., Mitala, J. J., Josue, J., Castro, A., Lerner, M. B., Bayburt, T. H., et al. (2011). Biomimetic chemical sensors using nanoelectronic readout of olfactory receptor proteins. ACS Nano, 5(7), 5408–5416. doi:10.1021/nn200489j

Grinkova, Y. V., Denisov, I. G., McLean, M. A., & Sligar, S. G. (2013). Oxidase uncoupling in heme monooxygenases: human cytochrome P450 CYP3A4 in Nanodiscs. Biochemical and Biophysical Research Communications, 430(4), 1223–1227. doi:10.1016/j.bbrc.2012.12.072

Gu, Z., Valianpour, F., Chen, S., Vaz, F. M., Hakkaart, G. A., Wanders, R. J. A., & Greenberg, M. L. (2004). Aberrant cardiolipin metabolism in the yeast taz1 mutant: a model for Barth syndrome. Molecular Microbiology, 51(1), 149–158.

Guinier and Fournet (1955). Small-angle scattering of X-rays. Wiley

Gulati, S., Jamshad, M., Knowles, T. J., Morrison, K. A., Downing, R., Cant, N., et al. (2014). Detergent-free purification of ABC (ATP-binding-cassette) transporters. Biochemical Journal, 461(2), 269–278. doi:10.1042/BJ20131477

Hagn, F., Etzkorn, M., Raschle, T., & Wagner, G. (2013). Optimized phospholipid bilayer nanodiscs facilitate high-resolution structure determination of membrane proteins. Journal of the American Chemical Society, 135(5), 1919–1925. doi:10.1021/ja310901f

Haines, T. H. (1983). Anionic lipid headgroups as a proton-conducting pathway along the surface of membranes: a hypothesis. Proceedings of the National Academy of Sciences of the United States of America, 80(1), 160–164.

Haines, T. H. (2009). A new look at Cardiolipin. Biochimica Et Biophysica Acta, 1788(10), 1997–2002. doi:10.1016/j.bbamem.2009.09.008

Hall, S. E., Roberts, K., & Vaidehi, N. (2009). Position of helical kinks in membrane protein crystal structures and the accuracy of computational prediction. Journal of Molecular Graphics & Modelling, 27(8), 944–950. doi:10.1016/j.jmgm.2009.02.004

Ham, M. H., Choi, J. H., Boghossian, A. A., & Jeng, E. S. (2010). Photoelectrochemical complexes for solar energy conversion that chemically and autonomously regenerate. Nature.

Harbauer, A. B., Zahedi, R. P., Sickmann, A., Pfanner, N., & Meisinger, C. (2014). The protein import machinery of mitochondria-a regulatory hub in metabolism, stress, and disease. Cell Metabolism, 19(3), 357–372. doi:10.1016/j.cmet.2014.01.010

Henrich, E., Dötsch, V., & Bernhard, F. (2015). Screening for lipid requirements of membrane proteins by combining cell-free expression with nanodiscs. Methods in Enzymology, 556, 351–369. doi:10.1016/bs.mie.2014.12.016

Heuck, A. P., Hotze, E. M., Tweten, R. K., & Johnson, A. E. (2000). Mechanism of membrane insertion of a multimeric beta-barrel protein: perfringolysin O creates a pore using ordered and coupled conformational changes. Molecular Cell, 6(5), 1233–1242.

Hille, B. (2001). Ion channels of excitable membranes.

Horvath, S. E., & Daum, G. (2013). Lipids of mitochondria. Progress in Lipid Research.

Horvath, S. E., Rampelt, H., Oeljeklaus, S., Warscheid, B., van der Laan, M., & Pfanner, N. (2015). Role of membrane contact sites in protein import into mitochondria. Protein Science : a Publication of the Protein Society, 24(3), 277–297. doi:10.1002/pro.2625

Hovijitra, N. T., Wuu, J. J., & Peaker, B. (2009). Cell-free synthesis of functional aquaporin Z in synthetic liposomes. Biotechnology and ….

Huang, S., Ratliff, K. S., & Matouschek, A. (2002). Protein unfolding by the mitochondrial membrane potential. Nature Structural Biology, 9(4), 301–307. doi:10.1038/nsb772

Hüser, J., & Blatter, L. A. (1999). Fluctuations in mitochondrial membrane potential caused by repetitive gating of the permeability transition pore. Biochemical Journal, 343 Pt 2, 311–317.

Hüser, J., Rechenmacher, C. E., & Blatter, L. A. (1998). Imaging the permeability pore transition in single mitochondria. Biophysical Journal, 74(4), 2129–2137. doi:10.1016/S0006-3495(98)77920-2

Ieva, R., Schrempp, S. G., Opaliński, L., Wollweber, F., Höß, P., Heißwolf, A. K., et al. (2014). Mgr2 functions as lateral gatekeeper for preprotein sorting in the mitochondrial inner membrane. Molecular Cell, 56(5), 641–652. doi:10.1016/j.molcel.2014.10.010

Im, W., Lee, M. S., & Brooks, C. L. (2003). Generalized born model with a simple smoothing function. Journal of Computational Chemistry.

Jefferies, J. L. (2013). Barth syndrome. American Journal of Medical Genetics. Part C, Seminars in Medical Genetics, 163C(3), 198–205. doi:10.1002/ajmg.c.31372

Jeffries, C. M., & Svergun, D. I. (2015). High-throughput studies of protein shapes and interactions by synchrotron small-angle X-ray scattering. Methods in Molecular Biology (Clifton, N.J.), 1261, 277–301. doi:10.1007/978-1-4939-2230-7_15

Jiang, F., Ryan, M. T., Schlame, M., Zhao, M., Gu, Z., Klingenberg, M., et al. (2000). Absence of cardiolipin in the crd1 null mutant results in decreased mitochondrial membrane potential and reduced mitochondrial function. The Journal of Biological Chemistry, 275(29), 22387–22394. doi:10.1074/jbc.M909868199

Johnson, A. E. (2005). Fluorescence approaches for determining protein conformations, interactions and mechanisms at membranes. Traffic, 6(12), 1078–1092. doi:10.1111/j.1600-0854.2005.00340.x

Joshi, A. S., Zhou, J., Gohil, V. M., Chen, S., & Greenberg, M. L. (2009). Cellular functions of cardiolipin in yeast. Biochimica Et Biophysica Acta, 1793(1), 212–218. doi:10.1016/j.bbamcr.2008.07.024

Junge, F., Haberstock, S., Roos, C., Stefer, S., Proverbio, D., Dötsch, V., & Bernhard, F. (2011). Advances in cell-free protein synthesis for the functional and structural analysis of membrane proteins. New Biotechnology, 28(3), 262–271. doi:10.1016/j.nbt.2010.07.002

Kalmbach, R., Chizhov, I., Schumacher, M. C., Friedrich, T., Bamberg, E., & Engelhard, M. (2007). Functional cell-free synthesis of a seven helix membrane protein: in situ insertion of bacteriorhodopsin into liposomes. Journal of Molecular Biology, 371(3), 639–648. doi:10.1016/j.jmb.2007.05.087

Kates, M., Syz, J. Y., Gosser, D., & Haines, T. H. (1993). pH-dissociation characteristics of cardiolipin and its 2'-deoxy analogue. Lipids, 28(10), 877–882.

Katzen, F., Fletcher, J. E., Yang, J.-P., Kang, D., Peterson, T. C., Cappuccio, J. A., et al. (2008). Insertion of membrane proteins into discoidal membranes using a cell-free protein expression approach. Journal of Proteome Research, 7(8), 3535–3542. doi:10.1021/pr800265f

Khalifat, N., Rahimi, M., Bitbol, A.-F., Seigneuret, M., Fournier, J.-B., Puff, N., et al. (2014). Interplay of packing and flip-flop in local bilayer deformation. How phosphatidylglycerol could rescue mitochondrial function in a cardiolipin-deficient yeast mutant. Biophysical Journal, 107(4), 879–890. doi:10.1016/j.bpj.2014.07.015

Kim, T.-H., Zhao, Y., Ding, W.-X., Shin, J. N., He, X., Seo, Y.-W., et al. (2004). Bid-cardiolipin interaction at mitochondrial contact site contributes to mitochondrial cristae reorganization and cytochrome C release. Molecular Biology of the Cell, 15(7), 3061–3072. doi:10.1091/mbc.E03-12-0864

Klammt, C., Schwarz, D., Fendler, K., Haase, W., Dötsch, V., & Bernhard, F. (2005). Evaluation of detergents for the soluble expression of alpha-helical and beta-barrel-type integral membrane proteins by a preparative scale individual cell-free expression system. The FEBS Journal, 272(23), 6024–6038. doi:10.1111/j.1742-4658.2005.05002.x

Knowles, T. J., Finka, R., Smith, C., & Lin, Y. P. (2009). Membrane proteins solubilized intact in lipid containing nanoparticles bounded by styrene maleic acid copolymer. Journal of the ….

Kong, J., & Yu, S. (2007). Fourier transform infrared spectroscopic analysis of protein secondary structures. Acta Biochimica Et Biophysica Sinica.

Kuchler, K., Daum, G., & Paltauf, F. (1986). Subcellular and submitochondrial localization of phospholipid-synthesizing enzymes in Saccharomyces cerevisiae. Journal of Bacteriology, 165(3), 901–910.

Kusonwiriyawong, C., van de Wetering, P., Hubbell, J. A., Merkle, H. P., & Walter, E. (2003). Evaluation of pH-dependent membrane-disruptive properties of poly(acrylic acid) derived polymers. European Journal of Pharmaceutics and Biopharmaceutics : Official Journal of Arbeitsgemeinschaft Für Pharmazeutische Verfahrenstechnik E.V, 56(2), 237–246.

Kutik, S., Rissler, M., Guan, X. L., Guiard, B., Shui, G., Gebert, N., et al. (2008). The translocator maintenance protein Tam41 is required for mitochondrial cardiolipin biosynthesis. The Journal of Cell Biology, 183(7), 1213–1221. doi:10.1083/jcb.200806048

la Cruz, de, L., Bajaj, R., Becker, S., & Zweckstetter, M. (2010). The intermembrane space domain of Tim23 is intrinsically disordered with a distinct binding region for presequences. Protein Science, 19(11), 2045–2054. doi:10.1002/pro.482

Lancet, D., & Pecht, I. (1977). Spectroscopic and immunochemical studies with nitrobenzoxadiazolealanine, a fluorescent dinitrophenyl analogue. Biochemistry, 16(23), 5150–5157.

Langelaan, D. N., Wieczorek, M., Blouin, C., & Rainey, J. K. (2010). Improved helix and kink characterization in membrane proteins allows evaluation of kink sequence predictors. Journal of Chemical Information and Modeling, 50(12), 2213–2220. doi:10.1021/ci100324n

Laursen, T., Singha, A., Rantzau, N., & Tutkus, M. (2014). Single molecule activity measurements of cytochrome p450 oxidoreductase reveal the existence of two discrete functional States. ACS Chemical ….

Lee, A. G. (2004). How lipids affect the activities of integral membrane proteins. Biochimica Et Biophysica Acta (BBA) - Biomembranes.

Lewis, R. N. A. H., & McElhaney, R. N. (2009). The physicochemical properties of cardiolipin bilayers and cardiolipin-containing lipid membranes. Biochimica Et Biophysica Acta, 1788(10), 2069–2079. doi:10.1016/j.bbamem.2009.03.014

Li, J., & Sha, B. (2015). The structure of Tim50(164-361) suggests the mechanism by which Tim50 receives mitochondrial presequences. Acta Crystallographica. Section F, Structural Biology Communications, 71(Pt 9), 1146–1151. doi:10.1107/S2053230X15013102

Li, X., Romero, P., Rani, M., Dunker, A., & Obradovic, Z. (1999). Predicting Protein Disorder for N-, C-, and Internal Regions. Genome Informatics. Workshop on Genome Informatics, 10, 30–40.

Li, X.-X., Tsoi, B., Li, Y.-F., Kurihara, H., & He, R.-R. (2015). Cardiolipin and its different properties in mitophagy and apoptosis. The Journal of Histochemistry and Cytochemistry : Official Journal of the Histochemistry Society, 63(5), 301–311. doi:10.1369/0022155415574818

Liapakis, G., Simpson, M. M., & Javitch, J. A. (2001). The substituted-cysteine accessibility method (SCAM) to elucidate membrane protein structure. Current Protocols in Neuroscience / Editorial Board, Jacqueline N. Crawley ... [Et Al.], Chapter 4, Unit 4.15. doi:10.1002/0471142301.ns0415s08

Lin, S., & Struve, W. S. (1991). Time-resolved fluorescence of nitrobenzoxadiazole-aminohexanoic acid: effect of intermolecular hydrogen-bonding on non-radiative decay. Photochemistry and Photobiology, 54(3), 361–365.

Loew, L. M., Tuft, R. A., Carrington, W., & Fay, F. S. (1993). Imaging in five dimensions: time-dependent membrane potentials in individual mitochondria. Biophysical Journal, 65(6), 2396–2407. doi:10.1016/S0006-3495(93)81318-3

Lohret, T. A., Jensen, R. E., & Kinnally, K. W. (1997). Tim23, a protein import component of the mitochondrial inner membrane, is required for normal activity of the multiple conductance channel, MCC. The Journal of Cell Biology, 137(2), 377–386.

Long, A. R., O'Brien, C. C., & Alder, N. N. (2012). The cell-free integration of a polytopic mitochondrial membrane protein into liposomes occurs cotranslationally and in a lipid-dependent manner. PloS One, 7(9), e46332. doi:10.1371/journal.pone.0046332

Long, A. R., O'Brien, C. C., MALHOTRA, K., Schwall, C. T., Albert, A. D., Watts, A., & Alder, N. N. (2013). A detergent-free strategy for the reconstitution of active enzyme complexes from native biological membranes into nanoscale discs. BMC Biotechnology, 13, 41. doi:10.1186/1472-6750-13-41

Luévano-Martínez, L. A., Forni, M. F., Santos, dos, V. T., Souza-Pinto, N. C., & Kowaltowski, A. J. (2015). Cardiolipin is a key determinant for mtDNA stability and segregation during mitochondrial stress. Biochimica Et Biophysica Acta, 1847(6-7), 587–598. doi:10.1016/j.bbabio.2015.03.007

Lupas, A., Van Dyke, M., & Stock, J. (1991). Predicting coiled coils from protein sequences. Science, 252(5009), 1162–1164. doi:10.1126/science.252.5009.1162

Ly, J. D., Grubb, D. R., & Lawen, A. (2003). The mitochondrial membrane potential (deltapsi(m)) in apoptosis; an update. Apoptosis : an International Journal on Programmed Cell Death, 8(2), 115–128.

Lytovchenko, O., Melin, J., Schulz, C., Kilisch, M., Hutu, D. P., & Rehling, P. (2013). Signal recognition initiates reorganization of the presequence translocase during protein import. The EMBO Journal, 1–13. doi:10.1038/emboj.2013.23

Lyukmanova, E. N., Shenkarev, Z. O., Khabibullina, N. F., Kopeina, G. S., Shulepko, M. A., Paramonov, A. S., et al. (2012). Lipid-protein nanodiscs for cell-free production of integral membrane proteins in a soluble and folded state: comparison with detergent micelles, bicelles and liposomes. Biochimica Et Biophysica Acta, 1818(3), 349–358. doi:10.1016/j.bbamem.2011.10.020

Ma, Z., Kong, J., & Kallen, R. G. (2009). Studies of alpha-helicity and intersegmental interactions in voltage-gated Na+ channels: S2D4. PloS One, 4(11), e7674. doi:10.1371/journal.pone.0007674

MacKenzie, J. A., & Payne, R. M. (2007). Mitochondrial protein import and human health and disease. Biochimica Et Biophysica Acta (BBA) - Molecular Basis of Disease, 1772(5), 509–523. doi:10.1016/j.bbadis.2006.12.002

MacKerell, A. D., Bashford, D., Bellott, M., Dunbrack, R. L., Evanseck, J. D., Field, M. J., et al. (1998). All-atom empirical potential for molecular modeling and dynamics studies of proteins. The Journal of Physical Chemistry B, 102(18), 3586–3616. doi:10.1021/jp973084f

MacKerell, A. D., Feig, M., & Brooks, C. L. (2004). Extending the treatment of backbone energetics in protein force fields: Limitations of gas‐phase quantum mechanics in reproducing protein conformational …. Journal of Computational ….

MALHOTRA, K., & Alder, N. N. (2014). Advances in the use of nanoscale bilayers to study membrane protein structure and function. Biotechnology & Genetic Engineering Reviews, 30(1-2), 79–93. doi:10.1080/02648725.2014.921502

MALHOTRA, K., Sathappa, M., Landin, J. S., Johnson, A. E., & Alder, N. N. (2013). Structural changes in the mitochondrial Tim23 channel are coupled to the proton-motive force. Nature Structural & Molecular Biology, 20(8), 965–972. doi:10.1038/nsmb.2613

Malyshka, D., & Pandiscia, L. A. (2014). Cardiolipin containing liposomes are fully ionized at physiological pH. An FT-IR study of phosphate group ionization. Vibrational ….

Marom, M., & Azem, A. (2013). The use of cardiolipin-containing liposomes as a model system to study the interaction between proteins and the inner mitochondrial membrane. Methods in Molecular Biology (Clifton, N.J.), 1033, 147–155. doi:10.1007/978-1-62703-487-6_10

Marom, M., Azem, A., & Mokranjac, D. (2011a). Understanding the molecular mechanism of protein translocation across the mitochondrial inner membrane: still a long way to go. Biochimica Et Biophysica Acta, 1808(3), 990–1001. doi:10.1016/j.bbamem.2010.07.011

Marom, M., Dayan, D., Demishtein-Zohary, K., Mokranjac, D., Neupert, W., & Azem, A. (2011b). Direct interaction of mitochondrial targeting presequences with purified components of the TIM23 protein complex. The Journal of Biological Chemistry, 286(51), 43809–43815. doi:10.1074/jbc.M111.261040

Marom, M., Safonov, R., Amram, S., Avneon, Y., Nachliel, E., Gutman, M., et al. (2009). Interaction of the Tim44 C-terminal domain with negatively charged phospholipids. Biochemistry, 48(47), 11185–11195. doi:10.1021/bi900998v

Marsh, D. (2007). Lateral pressure profile, spontaneous curvature frustration, and the incorporation and conformation of proteins in membranes. Biophysical Journal, 93(11), 3884–3899. doi:10.1529/biophysj.107.107938

Martin, J., Mahlke, K., & Pfanner, N. (1991). Role of an energized inner membrane in mitochondrial protein import. Delta psi drives the movement of presequences. The Journal of Biological Chemistry, 266(27), 18051–18057.

Martinez-Caballero, S., & Grigoriev, S. M. (2007). Tim17p regulates the twin pore structure and voltage gating of the mitochondrial protein import complex TIM23. Journal of Biological ….

McKenzie, M., Lazarou, M., Thorburn, D. R., & Ryan, M. T. (2006). Mitochondrial respiratory chain supercomplexes are destabilized in Barth Syndrome patients. Journal of Molecular Biology, 361(3), 462–469. doi:10.1016/j.jmb.2006.06.057

Mehnert, C. S., Rampelt, H., Gebert, M., Oeljeklaus, S., Schrempp, S. G., Kochbeck, L., et al. (2014). The mitochondrial ADP/ATP carrier associates with the inner membrane presequence translocase in a stoichiometric manner. The Journal of Biological Chemistry, 289(39), 27352–27362. doi:10.1074/jbc.M114.556498

Meier, S. (2004). Conserved N-terminal Negative Charges in the Tim17 Subunit of the TIM23 Translocase Play a Critical Role in the Import of Preproteins into Mitochondria. The Journal of Biological Chemistry, 280(9), 7777–7785. doi:10.1074/jbc.M412158200

Meinecke, M. (2006). Tim50 Maintains the Permeability Barrier of the Mitochondrial Inner Membrane. Science, 312(5779), 1523–1526. doi:10.1126/science.1127628

Mick, D. U., Dennerlein, S., Wiese, H., Reinhold, R., Pacheu-Grau, D., Lorenzi, I., et al. (2012). MITRAC Links Mitochondrial Protein Translocation to Respiratory-Chain Assembly and Translational Regulation. Cell, 151(7), 1528–1541. doi:10.1016/j.cell.2012.11.053

Mileykovskaya, E., & Dowhan, W. (2009). Cardiolipin membrane domains in prokaryotes and eukaryotes. Biochimica Et Biophysica Acta, 1788(10), 2084–2091. doi:10.1016/j.bbamem.2009.04.003

Mileykovskaya, E., & Dowhan, W. (2014). Cardiolipin-dependent formation of mitochondrial respiratory supercomplexes. Chemistry and Physics of Lipids, 179, 42–48. doi:10.1016/j.chemphyslip.2013.10.012

Mokranjac, D., & Neupert, W. (2010). The many faces of the mitochondrial TIM23 complex. Biochimica Et Biophysica Acta, 1797(6-7), 1045–1054. doi:10.1016/j.bbabio.2010.01.026

Mokranjac, D., Paschen, S. A., Kozany, C., Prokisch, H., Hoppins, S. C., Nargang, F. E., et al. (2003). Tim50, a novel component of the TIM23 preprotein translocase of mitochondria. The EMBO Journal, 22(4), 816–825. doi:10.1093/emboj/cdg090

Mokranjac, D., Popov-Čeleketić, D., Hell, K., & Neupert, W. (2005). Role of Tim21 in mitochondrial translocation contact sites. The Journal of Biological Chemistry, 280(25), 23437–23440. doi:10.1074/jbc.C500135200

Mokranjac, D., Sichting, M., Popov-Čeleketić, D., Mapa, K., Gevorkyan-Airapetov, L., Zohary, K., et al. (2009). Role of Tim50 in the transfer of precursor proteins from the outer to the inner membrane of mitochondria. Molecular Biology of the Cell, 20(5), 1400–1407. doi:10.1091/mbc.E08-09-0934

Montessuit, S., Somasekharan, S. P., Terrones, O., Lucken-Ardjomande, S., Herzig, S., Schwarzenbacher, R., et al. (2010). Membrane remodeling induced by the dynamin-related protein Drp1 stimulates Bax oligomerization. Cell, 142(6), 889–901. doi:10.1016/j.cell.2010.08.017

Moritani, Y., Nomura, S. M., Morita, I., & Akiyoshi, K. (2010). Direct integration of cell-free-synthesized connexin-43 into liposomes and hemichannel formation. FEBS Journal.

Muenzner, J., & Pletneva, E. V. (2014). Structural transformations of cytochrome c upon interaction with cardiolipin. Chemistry and Physics of Lipids, 179, 57–63. doi:10.1016/j.chemphyslip.2013.11.002

Murakami, T. (2012). Phospholipid nanodisc engineering for drug delivery systems. Biotechnology Journal, 7(6), 762–767. doi:10.1002/biot.201100508

Mylonas, E., & Svergun, D. I. (2007). Accuracy of molecular mass determination of proteins in solution by small-angle X-ray scattering. Journal of Applied Crystallography.

Møller, J. V., Olesen, C., & Winther, A. (2010). The sarcoplasmic Ca 2+-ATPase: design of a perfect chemi-osmotic pump. Quarterly Reviews of ….

Neupert, W., & Herrmann, J. M. (2007). Translocation of proteins into mitochondria. Annual Review of Biochemistry, 76, 723–749. doi:10.1146/annurev.biochem.76.052705.163409

Ng, K. K., Lovell, J. F., Vedadi, A., Hajian, T., & Zheng, G. (2013). Self-assembled porphyrin nanodiscs with structure-dependent activation for phototherapy and photodiagnostic applications. ACS Nano, 7(4), 3484–3490. doi:10.1021/nn400418y

Nielsen, S. S., Toft, K. N., & Snakenborg, D. (2009). BioXTAS RAW, a software program for high-throughput automated small-angle X-ray scattering data reduction and preliminary analysis. Journal of Applied ….

Numata, M., Grinkova, Y. V., Mitchell, J. R., Chu, H. W., Sligar, S. G., & Voelker, D. R. (2013). Nanodiscs as a therapeutic delivery agent: inhibition of respiratory syncytial virus infection in the lung. International Journal of Nanomedicine, 8, 1417–1427. doi:10.2147/IJN.S39888

Nymeyer, H., & Zhou, H.-X. (2008). A method to determine dielectric constants in nonhomogeneous systems: application to biological membranes. Biophysical Journal, 94(4), 1185–1193. doi:10.1529/biophysj.107.117770

O'Reilly, C. M., Fogarty, K. E., Drummond, R. M., Tuft, R. A., & Walsh, J. V. (2003). Quantitative Analysis of Spontaneous Mitochondrial Depolarizations. Biophysical Journal, 85(5), 3350–3357. doi:10.1016/S0006-3495(03)74754-7

Olofsson, G., & Sparr, E. (2013). Ionization constants pKa of cardiolipin. PloS One, 8(9), e73040. doi:10.1371/journal.pone.0073040

Orwick, M. C., Judge, P. J., & Procek, J. (2012). Detergent-Free Formation and Physicochemical Characterization of Nanosized Lipid–Polymer Complexes: Lipodisq. Angewandte Chemie ….

Orwick-Rydmark, M., Lovett, J. E., & Graziadei, A. (2012). Detergent-free incorporation of a seven-transmembrane receptor protein into nanosized bilayer Lipodisq particles for functional and biophysical studies. Nano ….

Osman, C., Haag, M., Wieland, F. T., Brügger, B., & Langer, T. (2010). A mitochondrial phosphatase required for cardiolipin biosynthesis: the PGP phosphatase Gep4. The EMBO Journal, 29(12), 1976–1987. doi:10.1038/emboj.2010.98

Osman, C., Voelker, D. R., & Langer, T. (2011). Making heads or tails of phospholipids in mitochondria. The Journal of Cell Biology, 192(1), 7–16. doi:10.1083/jcb.201006159

Öjemyr, L. N., Ballmoos, von, C., Gennis, R. B., & Sligar, S. G. (2012). Reconstitution of respiratory oxidases in membrane nanodiscs for investigation of proton-coupled electron transfer. FEBS Letters.

Paradies, G., Paradies, V., De Benedictis, V., Ruggiero, F. M., & Petrosillo, G. (2014). Functional role of cardiolipin in mitochondrial bioenergetics. Biochimica Et Biophysica Acta, 1837(4), 408–417. doi:10.1016/j.bbabio.2013.10.006

Pareek, G., Krishnamoorthy, V., & D'Silva, P. (2013). Molecular insights revealing interaction of Tim23 and channel subunits of presequence translocase. Molecular and Cellular Biology, 33(23), 4641–4659. doi:10.1128/MCB.00876-13

Pettersen, E. F., Goddard, T. D., Huang, C. C., Couch, G. S., Greenblatt, D. M., Meng, E. C., & Ferrin, T. E. (2004). UCSF Chimera--a visualization system for exploratory research and analysis. Journal of Computational Chemistry, 25(13), 1605–1612. doi:10.1002/jcc.20084

Pfeiffer, K., Gohil, V., Stuart, R. A., Hunte, C., Brandt, U., Greenberg, M. L., & Schägger, H. (2003). Cardiolipin stabilizes respiratory chain supercomplexes. The Journal of Biological Chemistry, 278(52), 52873–52880. doi:10.1074/jbc.M308366200

Planas-Iglesias, J., Dwarakanath, H., Mohammadyani, D., Yanamala, N., Kagan, V. E., & Klein-Seetharaman, J. (2015). Cardiolipin Interactions with Proteins. Biophysical Journal, 109(6), 1282–1294. doi:10.1016/j.bpj.2015.07.034

Popot, J.-L. (2010). Amphipols, nanodiscs, and fluorinated surfactants: three nonconventional approaches to studying membrane proteins in aqueous solutions. Annual Review of Biochemistry, 79, 737–775. doi:10.1146/annurev.biochem.052208.114057

Popov-Čeleketić, D. S. A., Mapa, K., Neupert, W., & Mokranjac, D. (2008). Active remodelling of the TIM23 complex during translocation of preproteins into mitochondria. The EMBO Journal. doi:10.1038/emboj.2008.79

Postis, V., Rawson, S., Mitchell, J. K., Lee, S. C., Parslow, R. A., Dafforn, T. R., et al. (2015). The use of SMALPs as a novel membrane protein scaffold for structure study by negative stain electron microscopy. Biochimica Et Biophysica Acta, 1848(2), 496–501. doi:10.1016/j.bbamem.2014.10.018

Powell, G. L., & Jacobus, J. (1974). The nonequivalence of the phosphorus atoms in cardiolipin. Biochemistry, 13(19), 4024–4026.

Powell, G. L., & Marsh, D. (1985). Polymorphic phase behavior of cardiolipin derivatives studied by 31P NMR and X-ray diffraction. Biochemistry, 24(12), 2902–2908.

Proverbio, D., Roos, C., Beyermann, M., Orbán, E., Dötsch, V., & Bernhard, F. (2013). Functional properties of cell-free expressed human endothelin A and endothelin B receptors in artificial membrane environments. Biochimica Et Biophysica Acta, 1828(9), 2182–2192. doi:10.1016/j.bbamem.2013.05.031

Puthenveetil, R., & Vinogradova, O. (2013). Optimization of the design and preparation of nanoscale phospholipid bilayers for its application to solution NMR. Proteins, 81(7), 1222–1231. doi:10.1002/prot.24271

Qian, X., Gebert, M., Höpker, J., Yan, M., Li, J., Wiedemann, N., et al. (2011). Structural basis for the function of Tim50 in the mitochondrial presequence translocase. Journal of Molecular Biology, 411(3), 513–519. doi:10.1016/j.jmb.2011.06.020

Rahman, B., Kawano, S., Yunoki-Esaki, K., Anzai, T., & Endo, T. (2014). NMR analyses on the interactions of the yeast Tim50 C-terminal region with the presequence and Tim50 core domain. FEBS Letters, 588(5), 678–684. doi:10.1016/j.febslet.2013.12.037

Rapaport, D., Künkele, K. P., & Dembowski, M. (1998). Dynamics of the TOM complex of mitochondria during binding and translocation of preproteins. … And Cellular Biology.

Raschle, T., Hiller, S., Yu, T.-Y., Rice, A. J., Walz, T., & Wagner, G. (2009). Structural and functional characterization of the integral membrane protein VDAC-1 in lipid bilayer nanodiscs. Journal of the American Chemical Society, 131(49), 17777–17779. doi:10.1021/ja907918r

Rassow, J., Hartl, F. U., Guiard, B., Pfanner, N., & Neupert, W. (1990). Polypeptides traverse the mitochondrial envelope in an extended state. FEBS Letters, 275(1-2), 190–194.

Reichert, A.S. and Neupert W. (2002) Contact sites between the outer and the inner membrane of mitochondria-role in protein transport. Biochimica Et Biophysica Acta, 1592(1), 41–59.

Ritchie, T. K., Grinkova, Y. V., Bayburt, T. H., Denisov, I. G., Zolnerciks, J. K., Atkins, W. M., & Sligar, S. G. (2009). Chapter 11 Reconstitution of Membrane Proteins in Phospholipid Bilayer Nanodiscs. In Methods in Enzymology (Vol. 464, pp. 211–231). Elsevier. doi:10.1016/S0076-6879(09)64011-8

Roos, C., Zocher, M., Müller, D., Münch, D., Schneider, T., Sahl, H.-G., et al. (2012). Characterization of co-translationally formed nanodisc complexes with small multidrug transporters, proteorhodopsin and with the E. coli MraY translocase. Biochimica Et Biophysica Acta, 1818(12), 3098–3106. doi:10.1016/j.bbamem.2012.08.007

Rostislavleva, K., Soler, N., Ohashi, Y., Zhang, L., Pardon, E., Burke, J. E., et al. (2015). Structure and flexibility of the endosomal Vps34 complex reveals the basis of its function on membranes. Science, 350(6257), aac7365. doi:10.1126/science.aac7365

Sachse, R., Dondapati, S. K., Fenz, S. F., Schmidt, T., & Kubick, S. (2014). Membrane protein synthesis in cell-free systems: from bio-mimetic systems to bio-membranes. FEBS Letters, 588(17), 2774–2781. doi:10.1016/j.febslet.2014.06.007

Sahu, I. D., McCarrick, R. M., Troxel, K. R., Zhang, R., Smith, H. J., Dunagan, M. M., et al. (2013). DEER EPR measurements for membrane protein structures via bifunctional spin labels and lipodisq nanoparticles. Biochemistry, 52(38), 6627–6632. doi:10.1021/bi4009984

Sanders, C. R., & Myers, J. K. (2004). Disease-related misassembly of membrane proteins. Annual Review of Biophysics and Biomolecular Structure, 33, 25–51. doi:10.1146/annurev.biophys.33.110502.140348

Schlame, M., & Haldar, D. (1993). Cardiolipin is synthesized on the matrix side of the inner membrane in rat liver mitochondria. The Journal of Biological Chemistry, 268(1), 74–79.

Schlame, M., Ren, M., Xu, Y., Greenberg, M. L., & Haller, I. (2005). Molecular symmetry in mitochondrial cardiolipins. Chemistry and Physics of Lipids, 138(1-2), 38–49. doi:10.1016/j.chemphyslip.2005.08.002

Schlame, M., Rua, D., & Greenberg, M. L. (2000). The biosynthesis and functional role of cardiolipin. Progress in Lipid Research, 39(3), 257–288.

Schmidt, O., Pfanner, N., & Meisinger, C. (2010). Mitochondrial protein import: from proteomics to functional mechanisms. Nature Reviews Molecular Cell Biology, 11(9), 655–667. doi:10.1038/nrm2959

Schuler, M. A., Denisov, I. G., & Sligar, S. G. (2013). Nanodiscs as a new tool to examine lipid–protein interactions. Lipid-Protein Interactions: Methods ….

Schulz, C., & Rehling, P. (2014). Remodelling of the active presequence translocase drives motor-dependent mitochondrial protein translocation. Nature Communications, 5, 4349. doi:10.1038/ncomms5349

Schulz, C., Lytovchenko, O., Melin, J., Chacinska, A., Guiard, B., Neumann, P., et al. (2011). Tim50's presequence receptor domain is essential for signal driven transport across the TIM23 complex. The Journal of Cell Biology, 195(4), 643–656. doi:10.1083/jcb.201105098

Schulz, C., Schendzielorz, A., & Rehling, P. (2015). Unlocking the presequence import pathway. Trends in Cell Biology, 25(5), 265–275. doi:10.1016/j.tcb.2014.12.001

Schwall, C. T., Greenwood, V. L., & Alder, N. N. (2012). The stability and activity of respiratory Complex II is cardiolipin-dependent. Biochimica Et Biophysica Acta (BBA) - Bioenergetics, 1817(9), 1588–1596. doi:10.1016/j.bbabio.2012.04.015

Schwarzländer, M., Logan, D. C., Johnston, I. G., Jones, N. S., Meyer, A. J., Fricker, M. D., & Sweetlove, L. J. (2012). Pulsing of membrane potential in individual mitochondria: a stress-induced mechanism to regulate respiratory bioenergetics in Arabidopsis. The Plant Cell, 24(3), 1188–1201. doi:10.1105/tpc.112.096438

Screpanti, E., & Hunte, C. (2007). Discontinuous membrane helices in transport proteins and their correlation with function. Journal of Structural Biology, 159(2), 261–267. doi:10.1016/j.jsb.2007.01.011

Seddon, A. M., Curnow, P., & Booth, P. J. (2004). Membrane proteins, lipids and detergents: not just a soap opera. Biochimica Et Biophysica Acta (BBA) - Biomembranes, 1666(1-2), 105–117. doi:10.1016/j.bbamem.2004.04.011

Seelig, A., & Seelig, J. (1974). The dynamic structure of fatty acyl chains in a phospholipid bilayer measured by deuterium magnetic resonance. Biochemistry, 13(23), 4839–4845.

Segrest, J. P., Jones, M. K., Klon, A. E., Sheldahl, C. J., Hellinger, M., De Loof, H., & Harvey, S. C. (1999). A detailed molecular belt model for apolipoprotein A-I in discoidal high density lipoprotein. The Journal of Biological Chemistry, 274(45), 31755–31758.

Shaw, A. W., McLean, M. A., & Sligar, S. G. (2004). Phospholipid phase transitions in homogeneous nanometer scale bilayer discs. FEBS Letters, 556(1-3), 260–264. doi:10.1016/S0014-5793(03)01400-5

Shenkarev, Z. O., & Lyukmanova, E. N. (2010). Lipid− protein nanodiscs as reference medium in detergent screening for high-resolution NMR studies of integral membrane proteins. Journal of the ….

Shiota, T., Mabuchi, H., Tanaka-Yamano, S., Yamano, K., & Endo, T. (2011). In vivo protein-interaction mapping of a mitochondrial translocator protein Tom22 at work. Proceedings of the National Academy of Sciences of the United States of America, 108(37), 15179–15183. doi:10.1073/pnas.1105921108

Silberberg, S. D., Chang, T.-H., & Swartz, K. J. (2005). Secondary structure and gating rearrangements of transmembrane segments in rat P2X4 receptor channels. The Journal of General Physiology, 125(4), 347–359. doi:10.1085/jgp.200409221

Sloan, C. D. K., Marty, M. T., Sligar, S. G., & Bailey, R. C. (2013). Interfacing lipid bilayer nanodiscs and silicon photonic sensor arrays for multiplexed protein-lipid and protein-membrane protein interaction screening. Analytical Chemistry, 85(5), 2970–2976. doi:10.1021/ac3037359

Song, J., Tamura, Y., Yoshihisa, T., & Endo, T. (2014). A novel import route for an N-anchor mitochondrial outer membrane protein aided by the TIM23 complex. EMBO Reports.

Stan, T., Ahting, U., Dembowski, M., & Künkele, K. P. (2000). Recognition of preproteins by the isolated TOM complex of mitochondria. The EMBO ….

Stewart, J. (1980). Colorimetric determination of phospholipids with ammonium ferrothiocyanate. Analytical Biochemistry.

Svergun, D. I. (1992). Determination of the regularization parameter in indirect-transform methods using perceptual criteria. Journal of Applied Crystallography, 25(4), 495–503. doi:10.1107/S0021889892001663

Svergun, D. I., & Koch, M. (2003). Small-angle scattering studies of biological macromolecules in solution. Reports on Progress in Physics.

Svergun, D., Barberato, C., & Koch, M. (1995). CRYSOL–a program to evaluate X-ray solution scattering of biological macromolecules from atomic coordinates. Journal of Applied ….

Swainsbury, D., Scheidelaar, S., & van Grondelle, J. R. (2014). Antoinette Killian, Michael R. Jones, Bacterial Reaction Centers Purified with Styrene Maleic Acid Copolymer Retain Native Membrane Functional …. … Chemie International Edition.

Tamura, Y., Endo, T., Iijima, M., & Sesaki, H. (2009a). Ups1p and Ups2p antagonistically regulate cardiolipin metabolism in mitochondria. The Journal of Cell Biology, 185(6), 1029–1045. doi:10.1083/jcb.200812018

Tamura, Y., Harada, Y., Nishikawa, S.-I., Yamano, K., Kamiya, M., Shiota, T., et al. (2013). Tam41 is a CDP-diacylglycerol synthase required for cardiolipin biosynthesis in mitochondria. Cell Metabolism, 17(5), 709–718. doi:10.1016/j.cmet.2013.03.018

Tamura, Y., Harada, Y., Shiota, T., Yamano, K., Watanabe, K., Yokota, M., et al. (2009b). Tim23-Tim50 pair coordinates functions of translocators and motor proteins in mitochondrial protein import. The Journal of Cell Biology, 184(1), 129–141. doi:10.1083/jcb.200808068

Tamura, Y., Harada, Y., Yamano, K., Watanabe, K., Ishikawa, D., Ohshima, C., et al. (2006). Identification of Tam41 maintaining integrity of the TIM23 protein translocator complex in mitochondria. The Journal of Cell Biology, 174(5), 631–637. doi:10.1083/jcb.200603087

Tarahovsky, Y. S., Arsenault, A. L., & MacDonald, R. C. (2000). Electrostatic control of phospholipid polymorphism. Biophysical Journal.

Ting, S.-Y., Schilke, B. A., Hayashi, M., & Craig, E. A. (2014). Architecture of the TIM23 inner mitochondrial translocon and interactions with the matrix import motor. The Journal of Biological Chemistry, 289(41), 28689–28696. doi:10.1074/jbc.M114.588152

Tonge, S. R., & Tighe, B. J. (2001). Responsive hydrophobically associating polymers: a review of structure and properties. Advanced Drug Delivery Reviews, 53(1), 109–122.

Truscott, K. N., Kovermann, P., Geissler, A., Merlin, A., Meijer, M., Driessen, A. J. M., et al. (2001). Nature Structural Biology, 8(12), 1074–1082. doi:10.1038/nsb726

Turakhiya U., von der Malsburg K., Gold V.A., Guiard B., Chackinska A., van der lann M. & Ieva R. (2016). Protein Import by the Mitochondrial Presequence Translocase in the Absence of a Membrane Potential. Journal of Molecular Biology, (in press). doi: 10.1016/j.jmb.2016.01.020.

Uhlemann, E.-M. E., Pierson, H. E., Fillingame, R. H., & Dmitriev, O. Y. (2012). Cell-free synthesis of membrane subunits of ATP synthase in phospholipid bicelles: NMR shows subunit a fold similar to the protein in the cell membrane. Protein Science : a Publication of the Protein Society, 21(2), 279–288. doi:10.1002/pro.2014

van den Brink-van der Laan, E., Killian, J. A., & de Kruijff, B. (2004). Nonbilayer lipids affect peripheral and integral membrane proteins via changes in the lateral pressure profile. Biochimica Et Biophysica Acta, 1666(1-2), 275–288. doi:10.1016/j.bbamem.2004.06.010

van der Laan, M., Hutu, D. P., & Rehling, P. (2010). On the mechanism of preprotein import by the mitochondrial presequence translocase. BBA - Molecular Cell Research, 1–8. doi:10.1016/j.bbamcr.2010.01.013

van der Laan, M., Meinecke, M., Dudek, J., Hutu, D. P., Lind, M., Perschil, I., et al. (2007). Motor-free mitochondrial presequence translocase drives membrane integration of preproteins. Nature Cell Biology, 9(10), 1152–1159. doi:10.1038/ncb1635

van der Laan, M., Wiedemann, N., Mick, D. U., Guiard, B., Rehling, P., & Pfanner, N. (2006). A role for Tim21 in membrane-potential-dependent preprotein sorting in mitochondria. Current Biology : CB, 16(22), 2271–2276. doi:10.1016/j.cub.2006.10.025

Vogel, R., Fan, G. B., Sheves, M., & Siebert, F. (2001). Salt dependence of the formation and stability of the signaling state in G protein-coupled receptors: evidence for the involvement of the Hofmeister effect. Biochemistry, 40(2), 483–493.

Volkov, V. V., & Svergun, D. I. (2003). Uniqueness of ab initio shape determination in small-angle scattering. Journal of Applied Crystallography.

Wadsäter, M., Laursen, T., Singha, A., Hatzakis, N. S., Stamou, D., Barker, R., et al. (2012). Monitoring shifts in the conformation equilibrium of the membrane protein cytochrome P450 reductase (POR) in nanodiscs. The Journal of Biological Chemistry, 287(41), 34596–34603. doi:10.1074/jbc.M112.400085

Wallin, E., & Heijne, von, G. (1998). Genome-wide analysis of integral membrane proteins from eubacterial, archaean, and eukaryotic organisms. Protein Science : a Publication of the Protein Society, 7(4), 1029–1038. doi:10.1002/pro.5560070420

Wang, Y., Carrie, C., Giraud, E., Elhafez, D., Narsai, R., Duncan, O., et al. (2012). Dual Location of the Mitochondrial Preprotein Transporters B14.7 and Tim23-2 in Complex I and the TIM17:23 Complex in Arabidopsis Links Mitochondrial Activity and Biogenesis. The Plant Cell, 24(6), 2675–2695. doi:10.1105/tpc.112.098731

Watanabe, Y., Tamura, Y., Kawano, S., & Endo, T. (2015). Structural and mechanistic insights into phospholipid transfer by Ups1-Mdm35 in mitochondria. Nature Communications.

Weiss, C., Oppliger, W., Vergères, G., Demel, R., Jenö, P., Horst, M., et al. (1999). Domain structure and lipid interaction of recombinant yeast Tim44. Proceedings of the National Academy of Sciences of the United States of America, 96(16), 8890–8894.

Wenz, L.-S., Opaliński, L., Schuler, M.-H., Ellenrieder, L., Ieva, R., Böttinger, L., et al. (2014). The presequence pathway is involved in protein sorting to the mitochondrial outer membrane. Nature Publishing Group, 15(6), 678–685. doi:10.1002/embr.201338144

White, S. H. (2001). How Membranes Shape Protein Structure. Journal of Biological Chemistry, 276(35), 32395–32398. doi:10.1074/jbc.R100008200

White, S. H., & Wimley, W. C. (1999). Membrane protein folding and stability: physical principles. Annual Review of Biophysics and ….

Wiedemann, N., van der Laan, M., Hutu, D. P., Rehling, P., & Pfanner, N. (2007). Sorting switch of mitochondrial presequence translocase involves coupling of motor module to respiratory chain. The Journal of Cell Biology, 179(6), 1115–1122. doi:10.1083/jcb.200709087

Wriggers, W., & Chacón, P. (2001). Using Situs for the registration of protein structures with low-resolution bead models from X-ray solution scattering. Journal of Applied Crystallography.

Xu, Y., Kelley, R. I., Blanck, T. J. J., & Schlame, M. (2003). Remodeling of cardiolipin by phospholipid transacylation. The Journal of Biological Chemistry, 278(51), 51380–51385. doi:10.1074/jbc.M307382200

Xu, Y., Malhotra, A., Ren, M., & Schlame, M. (2006). The enzymatic function of tafazzin. The Journal of Biological Chemistry, 281(51), 39217–39224. doi:10.1074/jbc.M606100200

Yamamoto, H., Esaki, M., Kanamori, T., Tamura, Y., Nishikawa, S.-I., & Endo, T. (2002). Tim50 is a subunit of the TIM23 complex that links protein translocation across the outer and inner mitochondrial membranes. Cell, 111(4), 519–528.

Yang, J.-P., Cirico, T., Katzen, F., Peterson, T. C., & Kudlicki, W. (2011). Cell-free synthesis of a functional G protein-coupled receptor complexed with nanometer scale bilayer discs. BMC Biotechnology, 11, 57. doi:10.1186/1472-6750-11-57

Yu, F., He, F., Yao, H., Wang, C., Wang, J., Li, J., & Qi, X. (2015). Structural basis of intramitochondrial phosphatidic acid transport mediated by Ups1-Mdm35 complex. Embo ….

Yu, T.-Y., Raschle, T., Hiller, S., & Wagner, G. (2012). Solution NMR spectroscopic characterization of human VDAC-2 in detergent micelles and lipid bilayer nanodiscs. Biochimica Et Biophysica Acta, 1818(6), 1562–1569. doi:10.1016/j.bbamem.2011.11.012

Zhang, Y. (2008). I-TASSER server for protein 3D structure prediction. BMC Bioinformatics.

Zhang, Y., & Cremer, P. S. (2006). Interactions between macromolecules and ions: The Hofmeister series. Current Opinion in Chemical Biology, 10(6), 658–663. doi:10.1016/j.cbpa.2006.09.020

Zhang, Y., Deng, H., Zhang, X., & Li, S. J. (2012). Interaction of divalent metal ions with human translocase of inner membrane of mitochondria Tim50. Biochemical and Biophysical Research Communications, 428(3), 365–370. doi:10.1016/j.bbrc.2012.10.060

Zorov, D. B., Juhaszova, M., Yaniv, Y., Nuss, H. B., Wang, S., & Sollott, S. J. (2009). Regulation and pharmacology of the mitochondrial permeability transition pore. Cardiovascular Research, 83(2), 213–225. doi:10.1093/cvr/cvp151